Enhancing Fracture Toughness of Ultrahigh Strength Aerospace Components made by Additive Manufacturing

Submitted by **Hamza Hassn Ramadan Alsalla**

to the University of Exeter as a thesis for the degree of

Doctor of Philosophy in Engineering

In August 2017

I certify that all material in this thesis which is not my own work has been identified and that no material has previously been submitted and approved for the award of a degree by this or any other University

.....

Abstract

Direct Metal Laser Sintering (DMLS) and Selective Laser Melting (SLM) are an Additive Manufacturing (AM) technique that produces complex three- dimensional parts by adding layer upon layer of powder materials from bottom to top. Recently, AM has received a significant amount of press and is set to have an enormous impact such as decreasing the cost of production, fast and flexible, design freedom and increase the innovation opportunities. The powder base nature allows these techniques to process a variant of materials as well as produce complex composite parts and develop new materials system for Aerospace industries.

The biggest problems in the process is limited surface quality, and residual porosity in SLM and DMLS parts that are undesirable for some applications where fatigue resistance and high strength are essential. This research aims to improve the fracture toughness, ductility and fatigue for the metallic components, which is essential to be able to exploit the potential of the SLM and DMLS of these alloys for aerospace applications. In additional development of the AM technology is not only limited to new machines but also processes, new materials, and methods, as it offers high mechanical properties and performance.

This research focuses on DMLS and SLM of titanium and stainless steel alloys to investigate the effect of processes parameter and different build direction on toughness and fatigue crack growth property to change the physical and mechanical properties. Also, manipulate the process parameters and their effect on strength, fracture toughness and quality for both bulk and cellular lattice structure parts. The novelty in this study lies in using additive manufacturing process to evaluate the local failure mechanism of 316L bulk and cellular lattice structures made by SLM under uniaxial tension and three-point bending load. The effect of different build directions of the 316L lattice structure on the fracture toughness properties is compared to the Ashby and Gibson models. The findings demonstrate that the build direction does have an effect on the microstructure of parts, which subsequently has an effect upon mechanical properties and the surface quality of manufactured parts.

Results found in this study will enable the designer to understand the important factors which affect the SLM and DMLS process and quality of final parts at different build direction. The comparison between micromechanics model and experimental results will help the designer to predict fracture toughness of AM cellular structures without need of experimental tests. Finally the results of mechanical properties of these bulk and lightweight parts will give a confidence to the designer to use and tailor their properties to specific applications.

DEDICATION

For my parents

My loving mother, wife and sons

Acknowledgments

Firstly, I wish to give all praise to Almighty God for giving me the strength to complete this research.

I would like to express my deepest gratitude to my supervisors, Professor Christopher Smith, Stephen Eichhorn and Dr Liang Hao for supervision. They have been always there, patience, ready and happy to help. Their suggestions, guidance, encouragement and helpful advice comments in all aspects of this research enabled me to gain a good experience and to develop an understanding of the subject.

For help I would like to thank Exeter Advanced Technology centre (x-at) for providing environment and wonderful time in the lab.

For grateful collaboration, I would like to thank ES Technology Ltd for their excellent service

I wish to thank my whole extended family for the honest support and the supporting environment they provided.

Last but not least, this study would not have been possible without the financial support of my sponsor, the Ministry of Higher Education in Libya. I wish to express my gratitude for giving me this opportunity to learn.

List of Publications

Alsalla, H., Hao, L., & Smith, C. (2016). Fracture toughness and tensile strength of 316L stainless steel cellular lattice structures manufactured using the selective laser melting technique. Materials Science and Engineering: A, 669, 1-6. (published)

Alsalla, H., Hao, L & Smith. C. (2016). Fatigue and fracture of high strength low alloy steel processed by additive manufacturing. The Britch society of strain measurement, BSSM. (published)

Alsalla, H Smith, C. W., &. Hao, L., (2017). Effect of build orientation on the surface quality, microstructure and mechanical properties of selective laser melting 316L stainless steel. Rapid prototyping journal. Vol:24, iss:2 (Accepted)

Alsalla, H, Hao, L &.Smith, C. W., (2017). The Effect of Different Building Orientation on the Consolidation, Tensile and Fracture Toughness Properties of Direct Metal Laser Sintering Ti-6Al-4V. Rapid prototyping journal. Vol:24, iss:2 (Accepted)

Alsalla, H., Hao, L., & Smith, C. (2016). Effect of different cell size and build direction on fracture toughness and strength of lightweight 316L stainless steel cellular lattice structures processed by selective laser melting. Journal of Engineering Manufacture (Submitted)

Conferences

I participated in the first Conference for Renewable Energies and Water Desalination in Tripoli (2008). I also participated in the Twelfth Deliberation Association of Science and Knowledge Conference, titled; Causes of Corrosion in Oil Pipelines and Methods of Prevention. This took place in Misrata, Libya in 2009.

Effect of different building direction on fracture toughness of Ti-6Al-4V and 316L stainless steel aerospace components made by SLM and DMLS processes. 2nd International Conference and Exhibition on Industrial Engineering November 16-18, 2015 Dubai, UAE

Effect of different building direction on fracture toughness of ultra-high strength aerospace components made by additive manufacturing. 3rd International Conference and Exhibition on Mechanical & Aerospace Engineering October 05-07, 2015 San Francisco, USA

Fracture toughness and tensile strength of 316L stainless steel cellular lattice structures manufactured using the selective laser melting technique. International Conference on Design and Production Engineering July 25-26, 2016 Berlin,Germany

Fatigue and fracture of high strength low alloy steel processed by additive manufacturing. The BSSM's 11th International Conference on Advances in Experimental Mechanics, 5th to 7th September 2016, Exeter, UK.

Effect of different cell size and build direction on mechanical properties of lightweight 316L stainless steel cellular lattice structures processed by selective laser melting. The Second Postgraduate Experimental Mechanics (PGEM) Conference, 14th December 2016 - 16th December 2016, University of Oxford, UK.

Table of Contents

List of Figures

List of Tables

Introduction

The aerospace industry uses many materials and it is critical to consider all the possible advantages and disadvantages of such materials. Improvements in manufacturing processes for aerospace have led to better aircrafts, which in turn has contributed to the massive changes seen in the last 20 years in medium and long distance air travel. Recently, many developments in the aerospace sector have been in materials. These improvements have stimulated the development of new technologies such as composite bodied aircraft, and processes such as near final shape manufacturing. There are lot of materials used in aerospace applications, the best of which combine low density and a competitive pricing; for example, titanium, stainless steel, and aluminum alloys. New methods of manufacture using such materials have become more widespread and commercially competitive, such as Additive Manufacturing (AM). In the AM process layers of material are built up sequentially into a near final shape component.

Additive Manufacturing is defined by the American Society for Testing and Materials (ASTM) as "The process of joining materials to make objects from 3D model data usually layer upon layer, as opposed to subtractive manufacturing technologies such as traditional machining." (ASTM, 2014). The recent growth of AM in aerospace is in part because of its potential i) for the manufacture of components with complex geometries, ii) its competitiveness for small volumes of parts, iii) the lack of requirement for specialist tooling – one AM machine can produce many kinds of parts. On the other hand, it is apparent that the capability for a broad range of materials lacks for some aerospace parts. Therefore, many researchers in industry and academia are attempting to enhance the AM process and its materials capability. The work described herein uses an AM process which has the ability for use with a wide range of materials attractive to the aerospace industry (Bradbury, 2012, Johns, 2009).

Rapid fabrication of prototypes has been the aim of much new technology development in the last 30 years. Previously, rapid prototyping (RP) was a generic name to produce prototype parts via AM techniques, and this then developed in the late 1980s into processes such as stereolithography (SLA). Later, this technology was extended to manufacture functional tools and dies (i.e. not just prototypes for testing), and it was renamed rapid tooling. Finally, rapid manufacturing (RM) has become a popular term to describe processes used to produce functional products mostly in AM techniques (Levy *et al.*, 2003). This technology has

advanced quickly since and is now in use across many industrial and medical domains. Along the way different names have been given to this technology, for instance: digital manufacturing, 3D printing, additive fabrication, additive techniques, additive layer manufacturing (ALM), and free form fabrication (Choi *et al*., 2011, Dahotre and Harimkar, 2008, ASTM, 2012). These different names have arisen because the technology has passed beyond its original purpose.

Many technologies have been developed following stereolithography; 3D printing, fused deposition modeling (FDM), selective laser sintering (SLS), selective laser melting (SLM), electron beam melting (EBM) and laminated object modelling (LOM). However, some of these technologies are no longer used whereas some are still in use and are present in the market today. Furthermore, most of the metal AM based processes, for instance, laser engineering net shape (LENS), SLM and EBM, are used to produce dies and moulds for die casting and injection moulding, or for tooling processes (Zhang, 2014).

Selective Laser Melting, one of the AM methods, is possibly the technology that best fits the particular needs of the aerospace sector (Peters *et al*., 2003). This is mainly because the process can produce fully melted high density materials, and thus strong parts, at the same time as offering great design freedom (Williams *et al*., 2005). SLM has advanced from SLS. It has the capability to manufacture high value, low volume and end use parts (Santos *et al*., 2006). Selective laser melting can create three-dimensional parts from metals and metal matrix composites (Dadbakhsh and Hao, 2012). In essence, it works by building up the required geometry layer-over-layer from a powder material (Alsalla *et al*., 2016). The greatest advantage of SLM is its flexibility in the choice of materials, which has stimulated much research on new compatible materials. Selective laser melting is capable of fully consolidating metals;, parts can be fabricated with specific properties, for instance, strength, hardness, and ductility. Furthermore, the time and effort invested in aerospace materials for SLM seem to be the most efficient regarding cost for current research, with shorter development times owing to the ease of mixing elements (Olakanmi *et al*., 2015). Selective Laser Melting is now one of the most commonly used AM processes, and it has presented the aerospace industry with the potential to produce lightweight and high-strength near net-shaped aerospace components.

Recently, a trend has been observed in material improvements for the SLM process, of process development for use with necessary materials. This has been developed to either allow application into new parts or to improve the physical properties of the materials themselves (Hao *et al*., 2009, Dadbakhsh *et al*., 2012b). Developments such as these allow

weight reduction of parts without sacrificing performance, the lowering of production costs, or a blend of both. Early investigations have been undertaken by colleagues from the University of Exeter, for instance, adapting existing SLM machines so they can produce titanium and stainless steel parts. Powders of such metals are relatively easy to use in SLM processes. Various publications describe work on these metals in the SLM process, investigating the effects of parameter processes, environment, and post-processing treatment on the parts produced. Also, the influence of adding alloying elements, and their composition in the consolidation, has been investigated. The effect of the process parameters and consolidation on the different cell sizes of the periodic cellular structure (Dadbakhsh *et al*., 2012b, Yan *et al*., 2014b, Hussein *et al*., 2013). However, one of the major problems that have been noted is the limited surface quality and residual porosity in SLM parts. This may be undesirable for some applications where fatigue resistance and high strength are essential (Lewandowski and Seifi, 2016). Titanium has been extensively researched owing to its excellent corrosion and oxidation resistance, its low density and high melting temperature. However, its behaviour under cyclic loading and its high cycle hence fatigue behaviour is not well covered in the literature and thus requires some attention. Similarly, stainless steel has not been widely used in SLM technology, despite the fact it is cost effective, non-hazardous to health, and easy to process. Furthermore, there are economic drivers to encourage the reduction of carbon dioxide and other emissions and to increase engine efficiency, both of which are well-served by the weight reductions possible via AM of aerospace components (Chris Carey, 2013).

The work described in this thesis investigates the effect of the build direction of AM produced parts on their mechanical properties. This will investigate the capability of AM, such as the SLM technique, to improve the mechanical properties of aerospace components vs existing methods. The critical mechanical properties of these AM produced aerospace components, specifically fracture toughness and fatigue life, have not been well described in the literature, and few have been qualified for flight on commercial aircraft. This thesis will characterise and demonstrate enhancement of the fracture toughness and fatigue life of SLM manufactured aerospace components. The study will involve analysis of materials, experimental investigation and theoretical development of the SLM titanium alloy (Ti6Al4V) and stainless steel 316L, as well as an investigation of failure mechanisms of an example 316L stainless steel cellular structure.

In terms of 316L stainless steel cellular structure, fracture toughness, testing was conducted to evaluate the effect of different cell sizes and build directions in the 316L AM cellular parts

on fracture toughness. These data are then compared with the Ashby and Gibson models for such cellular solids. The tensile strength and elongation of the 316L stainless steel cellular lattice structure and bulk material were also addressed. Scanning Electron Microscopy (SEM), X-ray Computed Tomography (CT) scanning and optical microscopy (OM) was used to examine the microstructural changes in both tensile test samples and Single Edge Notch Bend (SENB) samples during fracture.

Regardless of recent advances in SLM manufacturing of metal alloys, there is still a lack of understanding about the consolidation behaviour of these alloys and their mechanical properties regarding fracture toughness, ductility and fatigue crack growth. These aspects still require more data and ought to be addressed in more detail. Therefore, this work focuses on mechanical properties and performance of these metals made via SLM. The research data here on mechanical properties and any enhancements via AM fabrication will hopefully help extend the capacity of the SLM process for the production of high performance, lightweight components for commercial application in the aerospace sector.

Background and Literature Review

Chapter 1: Additive Manufacturing

The aim of this chapter is to provide the important background regarding AM. This necessary background includes general over view on AM technology, which is addressed in Section 1.1, and the benefit and limits of the AM technology are outlined in Section 1.2. Section 1.3 discusses the environmental impact of AM processes and energy consumption, both in the fabrication processes and through their capability to produce lightweight parts for the aerospace application. The state of the art about the metal AM processes is discussed in Section 1.4. Section 1.5 explained the capability of AM technology to fabricate lightweight and complex components that can be used in aerospace application. Section 1.6 summaries the main conclusion of this chapter.

1.1 General over view

Additive manufacture is a name that describes the technology that builds 3D objects by adding layer upon layer of material, whether it is metal, ceramic or plastic. Additive manufacture technology has received a significant amount of press in recent times and is set to have an enormous impact on the way future products are made, decreasing the cost of production and increasing the innovation opportunities (Elahinia *et al*., 2016).

Additive Manufacturing is also known as ALM, RM, and RP, in addition to other names that are currently presented since the ASTM group F42 has been in existence (ASTM, 2016). Moreover, AM has the capability to manufacture complex geometries completely without the need for tooling, which results in a reduction in the manufacturing times; this is hugely significant for the overall production costs for such items. Additive manufacturing will allow fast, flexible, reconfigurable processing and distribution of a component including economic low volume production, increased flexibility and conductivity, and design freedom (Gebhardt *et al*., 2010), more details about metal AM process in section 1.4.

The AM manufacturing process begins to consolidate the layer of material deposited using a scanning laser. After the cross section of the component that corresponds to the layer, height position is fully consolidated, the platform on which the model rests moves down one layer thickness and the next layer of material is deposited for consolidation. This layer adheres to the previous one once the process has been finished. Any consolidated material and supporting structure are then removed. Post process procedures that may have to be used to improve the surface roughness are then applied.

1.2 The benefits and limits of AM technology

Metal AM technologies offer many key benefits as follows (Gong *et al*., 2014, Sacristán *et al*., 2014, Shapiro *et al*., 2016):

- No tooling is needed, unlike other conventional metallurgy processes. These typically need forming and removal tools.
- Additive manufacturing increases design freedom in comparison to conventional machining and casting.
- Enables the designing of parts where the material is only where it needs to be, without other constraints.
- Enables the production of lightweight structures by use of lattice structure designs.
- Helps create complex parts built in one step thus reducing the number of assembly processes such as brazing and welding.
- Net shape and less material consumption; up to 25 times less than machining.
- Save production times for complex parts over conventional metallurgy processes which can often take several months

Figure 1.1 shows some examples of complex parts that have been produced by AM

It is important to be aware of some limitations and disadvantages of AM technologies, such as the following (Steen, 1991):

- Surface roughness and internal pores, consequently, AM parts often require post-processing machining or polishing.
- Expensive lasers are required to provide high power and better beam quality.
- The part sizes are limited to the powder bed size. For instance, standard powder bed systems are typically square 250 × 250 × 300 mm. However, greater parts' sizes can be fabricated with laser metal deposition processes, but it takes a long time to build tall parts due to the small thickness of powder layers
- Removal of the support structure is needed in case of overhang angle is below 45°, discussed in section 3.2.
- Material properties of AM parts tend to show anisotropy in the z-axis (building direction) and are anisotropic between the in-plane and out of plane direction discussed in section 3.3.

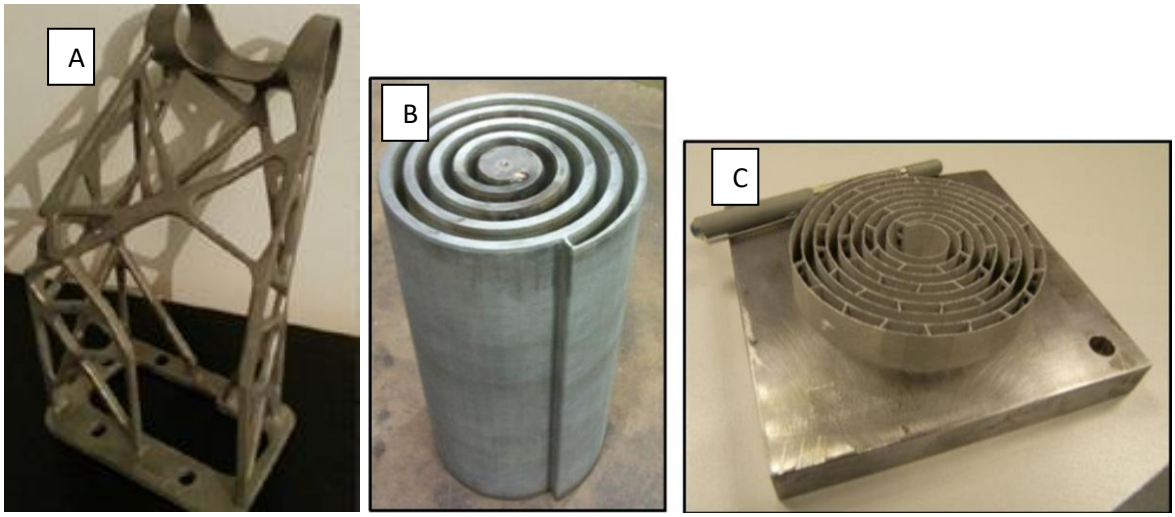

Fig1.1: Some typical complex parts made by AM. (a) A Ti6Al4V lightweight support part to a satellite antenna made by EBM, (b and c) 316L stainless steel vacuum permeators produced by SLM, which is impossible to produce by conventional processes. Reproduced from (Shapiro *et al*., 2016, Sacristán *et al*., 2014)

1.3 Environment, Energy Consumption, and Carbon Footprint

Different studies have been carried to measure the environmental impact of AM processes. Morrow *et al*. examined the environmental impact of laser based AM versus conventional manufacturing for the production of dies and tools (Morrow *et al*., 2007). Many case studies have been approached and quantitative analysis undertaken of the emissions produced and energy consumed during these processes. It has been found that the ALM of tooling had the greatest potential for reducing environmental impact and production costs (Morrow *et al*., 2007). Kellens *et al*. have studied the energy efficiencies of the SLM and SLS processes. The method they employed was a cooperative effort on process emissions in manufacturing initiatives. They found that the detailed information required for energy consumption and emissions is very limited (Kellens *et al*., 2011).

Frazier has examined the variety of environmental impacts of AM. Their study defined the system level boundaries for which environmental impacts are measured. “The energy efficiency is the ratio of output energy content of the Product/the total energy used in fabrication. For these processes, it found that the energy efficiency was 8.6% into the part. While this is an excellent approach at the system level, it does not provide for a holistic life cycle assessment” (Frazier, 2014). Dupont has investigated the efficiency of the Laser Engineered Net Shaping process (LENS) applied to the manufacture of copper and tool steel

powder deposits. The measured efficiency of laser energy transfer ranged from 30-50%. They report that the maximum deposition efficiency is 14% (Unocic and DuPont, 2004). Bourell and Sreenivasan investigated the energy used by the SLS process. The average power used was 19.6 kW, and the primary sources of energy used were the laser 16%, the stepper motors 26%, the chamber heater 36%, and the roller drives 16%. They found that the SLS process consumed little energy and had minimal waste products. These findings mean that SLM was a sustainable system.

Up to date AM leads to a reduction in the carbon footprint due to a decrease in the material waste and design optimisation. The ATKINS project found that good design could result in a material and weight saving of up to 40% (ATKINS, 2007). Also, their investigations revealed that over the lifetime of the aircraft, reducing of 100 kg of an airplane mass results in a 2.5 m dollar saving in fuel and a 1.3 $MtCO_2$ was saving. This project is set to develop how the components for the aerospace and automotive sectors are made, leading to reduction in weight, wastage and CO2 emissions both at the manufacturing period and throughout use. The aim of the project is to apply an additive manufacturing approach, especially SLM of metal components, to ensure the production, and design of fully improved aerospace components that are more sustainable and with a reduced carbon footprint (ATKINS, 2009).

The components designed to achieve the unique weight savings characteristics of AM have greatest potential to reduce environmental impact. However, more research needs to be conducted to capture the real benefit and possible pitfalls of using AM technologies.

1.4 Metallic additive manufacturing systems

Metal AM systems may be categorized regarding the build volume; material feedstock, energy source, etc. The production systems are divided into three categories (although there is much more such as VAT Photopolymerisation, Sheet Lamination binder jetting): (i) wire feed systems, (ii) powder feed systems, (iii) powder bed systems.

1.4.1 Wire feed systems

The energy source for these systems can include a laser beam, an electron beam, and plasma arc, and the feedstock is a wire. Initially, a single wire of material is deposited, and upon subsequent passes, this is built upon to develop a three-dimensional structure. They are well suited for high deposition rate processing and can produce large volumes such as in electron beam freeform fabrication (EBF), but the processed product requires more machining than the

powder feed and powder bed systems (Frazier, 2014). Figure 1.2 shows the EBF process (Ding *et al*., 2015).

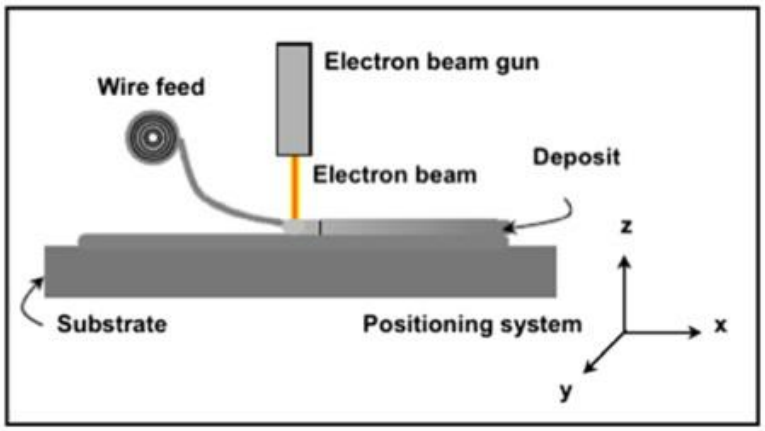

Fig 1.2: Schematic of the EBF system components (Ding *et al*., 2015)

1.4.2 Powder feed systems

These systems use focused thermal energy to fuse materials by melting as the material is being deposited; such as Direct Energy Deposition (DED) including LENS and laser cladding (LC). These systems can build enormous volumes, for instance; > 1.2 m^3 for the Optomec LENS 850-R unit. These systems lend themselves more readily to create more major volume scales compared to powder bed systems. In the powder feed systems, powders are transferred through a nozzle onto the build surface. A laser is used to melt a monolayer or more of the powder into the shape desired, and the process is repeated to produce a solid three-dimensional part (see Figure 1.3). There are two types of processes; (i) the deposition head moves and the workpiece remains fixed. (ii) The workpiece is moved, and the deposition head remains fixed. This type of system can build large volumes and can be used to repair damaged or refurbish worn components (Frazier, 2014, Liao *et al*., 2006).

1.4.3 Powder bed systems

Figure 1.4 shows a diagram of a primary powder bed system. The build volumes of this equipment are dependent on the manufacturing and requirements. A powder bed is created by taking the powder across the work area. These systems have two energy sources (laser beam, electron beam), which are programmed to deliver energy power to the bed surface by sintering or to melt the powder into the pre-selected shape. The additional powder is raked across the work area, and the process repeated to manufacture a three-dimensional part. The

benefits of these systems are its ability to manufacture complex and high resolution features and to maintain dimensional control and internal passages. The resolution depends on the feature size and material, which mean accuracy is better with features that are > 0.5 mm (PartNet, 2009). The powder bed system is divided into three processes as following:

Selective Laser Melting (SLM) or Direct Metal Laser Sintering (DMLS)

The SLM process was commercialised by the MTT technology group of Stones in 2003. It is similar to the SLS process technique, but in the SLM process the laser does not sinter but melts the powder. In the SLM process, a metal powder is melted by the laser on a powder bed and the parts built are produced, layer upon layer, until the part is completely formed (Hopkinson *et al*., 2006). The ranges of materials that can be used in this process are aluminum alloys, titanium alloys, stainless steel and tool steel. SLM can produce fully dense parts that contribute to improving the bulk materials' properties (Osakada and Shiomi, 2006).

Direct metal laser sintering, is a registered trademark of Electron Optical System (EOS) GmbH (Germany), its use would donate a specific vendor, not a process. It is an AM technology that produces components fully dense in a layer-by-layer process by selectively fusing and consolidation of thin layers of powders with a scanning laser beam. DMLS and SLS are essentially the same things, whereas DMLS refers to the process as applied to metal alloys. However, in a DMLS process, the laser is sintering apart from melting, in which the sintering processes do not fully melt the powder, but heat it to the point that the single powder grains (crystals) can fuse together on an atomistic scale. After the DMLS process has completed, the manufactured parts are left to cool, and then excess powder can be removed from the build chamber and recycled (Ghosh and Saha, 2011).

Electron Beam Melting (EBM)

Electron beam melting is an AM process that is very similar to SLM. The main difference between two techniques is that EBM uses electron beam rather than a laser to melt the metal powder. The EBM process is based on a high power electron beam that generates the energy required for a high melting capacity and productivity. It produces models that are very dense. The EBM process takes place in a vacuum and at high temperature, resulting in stress relieved parts. The electron beam heats the entire powder bed for each layer to an optimal ambient temperature, specific for the type of material used. The parts produced by the EBM process approximately have a microstructure free from a martensitic structure and free from residual stress (Murr *et al*., 2012a).

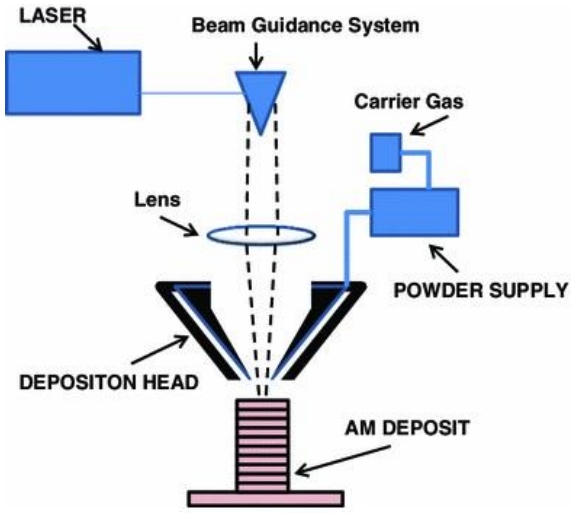

Fig 1.3: Schematic showing the generic illustration of an AM powder feed system (Frazier, 2014)

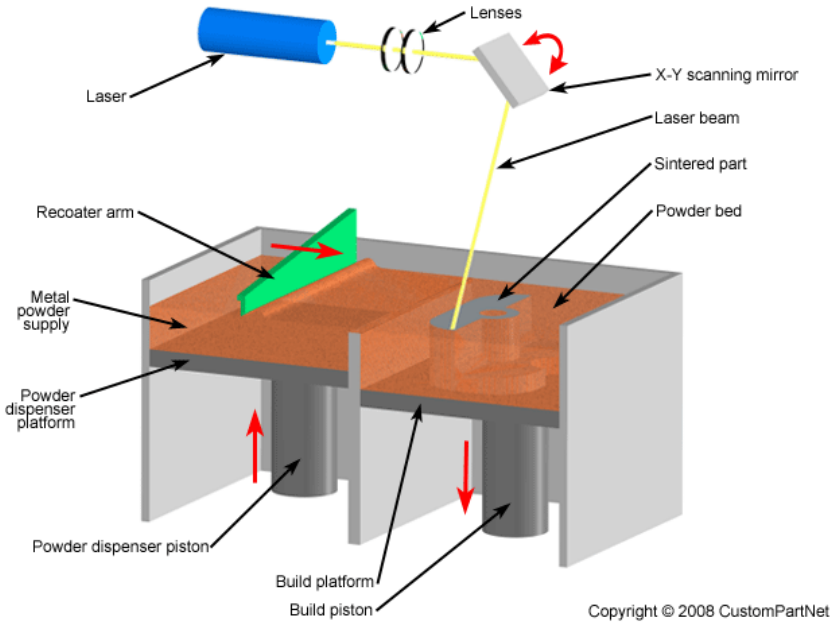

Fig 1.4: Schematic of powder bed system (PartNet, 2009)

Main process steps

Figure 1.5 presents a schematic flowchart of the metal components manufacturing with AM technologies starting with 3D modelling designed by Computer Aided Design (CAD) software. Then data preparation is carried out and organized, such as the positioning of the

support structure, part orientation definition and the model slicing. After manufacturing of the part, post processing procedures are carried out, if needed, for some applications.

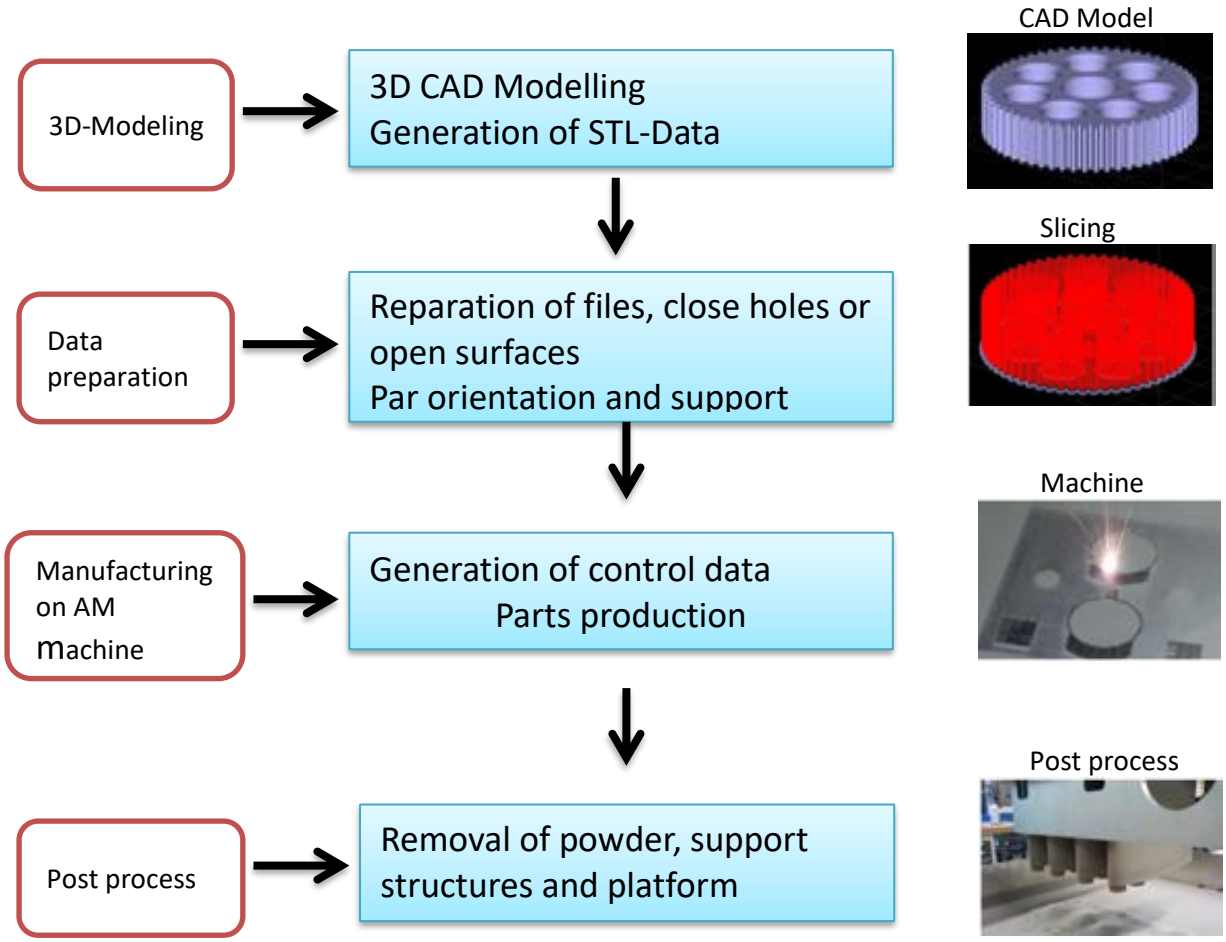

Fig 1.5: Schematic flow diagram of a typical AM process.

1.5 Additive manufacturing in aerospace industry

Aerospace industries are increasingly using AM for functional aircraft components. The primary interest in using AM or 3D printing to produce parts for the aerospace sectors is to reduce weight through the ability to manufacture complex parts and light weight structures. A reduction in weight leads to reduced fuel consumption, which leads to a decrease in cost and carbon emissions. AM allows for rapid prototyping, conceptual design review, and validation, and also one can go straight to finished parts without the need for tooling. Currently, the limited use of AM in aerospace applications is due to the lack of a proven track record, which requires more studies from the AM aerospace engineers to make changes. For

instance, AM uses are limited to applications where a potential failure is not of concern in the components. The following examples illustrate the use of AM for aerospace applications.

Fuel Nozzles GE LEAP engine

In early 2016, the new LEAP engines were using up to 20 AM fuel nozzles (Fig 1.6), and GE will need to manufacture around 25,000 annually within the next three years. The AM technology has been chosen by GE to manufacture the nozzles, because it uses less material than a conventional product and there is an opportunity in reducing weight, which would otherwise require more steps, i.e., welding about twenty small pieces together. AM reduces the cost of production and makes the parts lighter, which leads to significant fuel saving and thus saves money for the airlines. Other divisions of GE make gas and wind turbines. These parts have already been identified and can be done using the AM process (Seifi *et al*., 2016b, Herderick, 2016).

Fig 1.6: Fuel Nozzle made by AM (Seifi *et al*., 2016b)

F/A-18E/F Super Hornet cooling duct

The US Navy has wanted to reduce the cost of manufacturing and to service as well as into import new systems in the F/A-18 section. The additional systems require extra cooling ducts that would comply with the limited boundaries of the aircraft. These ducts are not structural components but need a guarantee of minimum material strength. They also have to be accurate enough to fit correctly into the aircraft.

The advantages of AM technology in manufacturing ducts is; i) assemblies that would have to be produced as two or three parts by conventional manufacturing that can be merged into one part, ii) it can simply manufacture a complex geometry to fit the cooling ducts around the obstructions, iii) the parts can be modified, or updated and weight saving achieved, if compared to conventional products. Figure 1.7 shows the duct components made by SLS (Hopkinson *et al*., 2006).

Fig 1.7: Cooling ducts for the F/A-18E/F Super Hornet manufactured from Duraform PA, produced using SLS (Hopkinson *et al*., 2006)

Airbus A380 bracket made of stainless-steel using 3D printing

Researchers at North-western University have used design optimization and AM to reduce the weight of an airplane bracket. This is a new way to help airline companies save money and the environment by using 3D printing to manufacture aircraft parts. According to their case study, using AM to make a bracket from stainless steel as a replacement for the standard cast steel reduces its weight from 1.09 kilograms to 380 grams (see Figure 1.8). The case study showed that if the possible AM components are used to their full potential, the airplane's fuel consumption could be reduced by as much as 6.4 percent. Furthermore, their life-cycle analysis found that the AM components use as little as one-third to one-half of the energy that is presently employed by the conventional methods (Van Noort, 2012, Thompson *et al*., 2016).

Fig 1.8: Typical AM parts of an optimised Airbus A380 bracket made of stainless-steel powder (Thompson *et al*., 2016)

1.6 Summary

Metal AM especially powder bed systems such as DMLS, SLM and EBM are capable of fabricating nearly/fully dense aerospace components directly from computer-aided design (CAD) models using arrange of metallic powders. The primary interest in using AM to fabricate aerospace components is to reduce weight during the ability to produce complex and lightweight structure. A reduction in weight of aerospace components leads to reduce fuel consumption, which leads to save money and reduce carbon emissions.

Chapter 2: Material consolidation processes

Chapter 2 provides a review of the metal AM process and defects to validate the relevance of this research. The most common materials used in aerospace have to withstand harsh environmental are addressed in Section 2.1. In section 2.2, the essential process parameters used in SLM and DMLS are discussed which are needed to optimise the interaction between the materials and laser to achieve an appropriate quality and properties of the aerospace AM components are addressed. The principle of laser melting of powders and the melt pool formation also explained in Section 2.2. Section 2.3 discusses the common issues that can be found in DMLS and SLM metallic parts resulting from incorrect process parameters such as insufficient powder quality, laser parameter, build strategies, etc. The summary of this chapter is given in Section 2.4

2.1 Metals used within aerospace additive manufacturing

The aerospace industry uses many materials for parts. It is critical to take into account all of the possible advantages and disadvantages of these different materials (Barrington and Black, 2001). Metals intended for the aerospace industry must have the right chemical and physical properties to withstand the harsh environments, i.e. they should be strong, fatigue resistant, creep resistant, stiff, lightweight and resistant to corrosion. Several metal such as titanium, stainless steel, nickel and aluminium alloys possess these qualities and are thus often the top choice for aerospace applications (Contrepois and Lecomte-Beckers, 2011, Nakai and Eto, 2000). A subset of these alloys is available for use in AM machines due to limited availability in powder form. More information including of some examples for each of these alloys now follows:

Nickel base superalloys such as Inconel 625, 718, etc. have significant mechanical strength, high performance at high temperatures and can operate under load bearing conditions at 85% of their melting temperatures (Campbell Jr, 2011). The properties of superalloys are corrosion resistance, creep, fatigue, high strength and withstanding high temperatures for long periods. On the other hand, superalloys have the disadvantage that they are difficult to machine, due to their relatively high density and high strength. This is however offset by their other outstanding properties at elevated temperatures. However, many of these obstacles may be circumvented during the use of AM, for components which would conventionally large

quantities of material to be removed by subtractive machining. AM has been known by many as a promising fabrication route for nickel alloy parts with complex geometries or short production runs (Carter *et al*., 2012) using these difficult to process materials (Jia and Gu, 2014). Nickel base superalloys are often used in aerospace engines, high temperature recuperates, power generation turbine components (Boyer, 1996), and Fuel Nozzle as shown in Section 1.5 figure 1.6.

Aluminium alloys are considered to be primary materials for use in aerospace applications because of their useful features such as low cost, high specific strength, high thermal and electrical conductivity, and ease of fabrication. Also, aluminium alloys have excellent corrosion resistance, since they naturally form an oxide layer instantaneously when exposed to oxygen.

Aluminium alloys perform well in structural aerospace applications because of their strength, the fact that they are lightweight and their flexibility. The primary uses of some aluminium alloys in the aerospace application are structural. Some examples of common alloys are (Dursun and Soutis 2014):

- 2024 alloy is the most typical of the high strength aluminium alloys and used for the fuselage.
- 6061 alloys had an excellent corrosion resistance and used for aircraft landing mats, structural components, truck bodies and frames
- Other aluminium alloys also used for structural applications such as 5052, 3003 and 7075 series (Nakai and Eto, 2000, Murr *et al*., 2010).

Additive manufacturing of aluminium alloys has raised increasing research interest most recently due to its lightweight property and relative low cost (Brandl *et al*., 2012, Buchbinder *et al*., 2011). There are a number of difficulties in the SLM processing of aluminium powder such as poor flowability of aluminium powder especially in the presence of moisture, the high reflectivity of aluminium increases the laser power for melting, and the major problem in processing of aluminium is reported to be oxidation and thin oxide films on both solid and molten materials. The oxide layers reduce the wettability and act as a barrier for diffusion (Louvis *et al*., 2011).

Titanium alloys are corrosion resistant, have good fatigue strength, high specific strength, and high operating temperatures. They are known for their high strength-to-weight ratios and

are extremely resistant to heat and wear. Titanium does not corrode in chlorine or sea water, so they can be taken into consideration as being suitable for aerospace applications. They are used in numerous applications, such as structural airframes including wing structures, hydraulic tubing, landing gear components and parts requiring low pressures and temperatures in engine turbines. They have a relatively high cost, because of their excellent properties and difficulties in removing and cleaning parts made from them. (Caron and Staley, 1997).

Presently titanium alloys often make up to 10% of an aircraft's weight, such as for the Boeing 777. The Ti6Al4V alloy also known as grade 5, as used in this work, is the most commonly used titanium alloy in aerospace applications for general purpose because it is stronger than other commercial titanium alloys and pure titanium materials. It is also still retaining the same excellent thermal properties and stiffness as well as resistance to corrosion and high strength-to-weight ratio. These promising properties make Ti6Al4V of considerable interest for the AM process, and as such have been intensively investigated (Peters *et al*., 2003, Khanna and Davim, 2015, Inagaki *et al*., 2014). The alloy Ti6Al4V processed by SLM has been demonstrated with approximately 240 HV hardness, which is higher than that of wrought version of the alloy, and can have comparable fatigue strength if the post treatment hot isostatic pressing (HIP) is used (Santos *et al*., 2004). Microstructural investigation on Ti6Al4V components revealed a significant influence of SLM conditions (i.e. fast cooling from high temperature) on microstructure characteristics such as orientation of grains, morphology of phases, and secondary phases which explained in more details below (Thijs *et al*., 2010). More information about the chemical composition, material powder, and mechanical properties of SLM Ti6Al4V are explained in chapter 4 section 4.1.1 and chapter 3 Section 3.3, respectively. On the other hand, Ti6Al4V ELI (grade 23) is a popular alloy where medium strength and good ductility are required.

Of note is the Ti6Al4 ELI grade which is also used in aerospace applications and is usually specified for seawater and medical applications. Titanium Grade 23 is similar to Grade 5 but with lower oxygen, nitrogen and iron content, with lower strength but better ductility and fracture toughness(Yavari *et al*., 2013). The Ti6Al4V ELI alloys are among the most widely used alloys in SLM for medical application due to their high toughness(Wauthle *et al*., 2015, Krakhmalev *et al*., 2016). Previous reports in the literature on SLM of Ti6Al4 ELI, have focused on the influence of process parameters on the microstructure and related mechanical properties (Thijs *et al*., 2010, Vrancken *et al*., 2012).

In general, the alloying behaviour of elements with titanium is defined by their effects on the α (hexagonal-close-packed hcp crystal structure) and β (body-centred-cubic bcc crystal structure) phases. Elements such as aluminium and zirconium added to titanium increase or maintain the temperature range of stability of α phase and are called α-stabilizers. Elements that stabilize the β phase are called β-stabilizers and include vanadium, iron and molybdenum. Oxygen and hydrogen are also important impurity elements, where oxygen is an α-stabilizer and hydrogen is a β-stabilizer. Oxygen and hydrogen occur as interstitial atoms because their atomic sizes are such that they fit in the spaces between the crystallographic positions of the metal atoms in the both the β and α phases.

Based on the two phases, titanium alloys are classified into four categories; α-alloys, near-α alloys, α-β alloys, and β-alloys. The mechanical properties of titanium alloys depend on the distribution and relative amounts of the α and β phases (Wanhill, 2011). However, the α+β alloys contain limited amount of β-stabilizers, the majority of which cannot strengthen the α phase.

These variations in phases are controlled by processing and heat treatment. Figure 2.1 shows the phase diagram of Ti6Al4V (α+β alloy), above the β transus the alloy is 100% β and the amount of α is increased by decreasing the temperature. The mechanical properties of α+β alloys depend on the relative amounts and distribution of α and β phases (Leyens, 2003) and these will depend strongly on the thermal processing and heat treatment temperatures in the (α + β) phase field.

Since vanadium is a β stabilizer, the higher the temperature the more readily β transform to α through cooling after thermal processing. When the β transforms to α, the morphology after the transformation is different from that of the primary α, as shown in Figure 2.2, which shows the prior β grains have transformed to co-oriented α lamellae separated by ribs of retained β (Wanhill, 2012).

Stainless steel is a combination of steel and different metal elements such as nickel, chromium, carbon, etc., that improves certain properties of the base material, such as strength, formability, and corrosion resistance. Stainless steels are iron alloys with a minimum of 10.5% chromium. It comes in different grades and has a long history of use in the aerospace industry because of its low-cost, availability, high temperature oxidation, and it maintains its mechanical properties over a wide temperature range. Stainless steel is usually divided into five types, the last of which austenitic is used in this work.

(i) **Ferritic** - these steels are based on chromium with carbon contents less than 0.1%. They are often chosen for their resistance to stress corrosion cracking. Ferritic steels are magnetic but not formable as austenitic stainless steels. Ferritic steels have different grades such as 430,439, 409, etc.

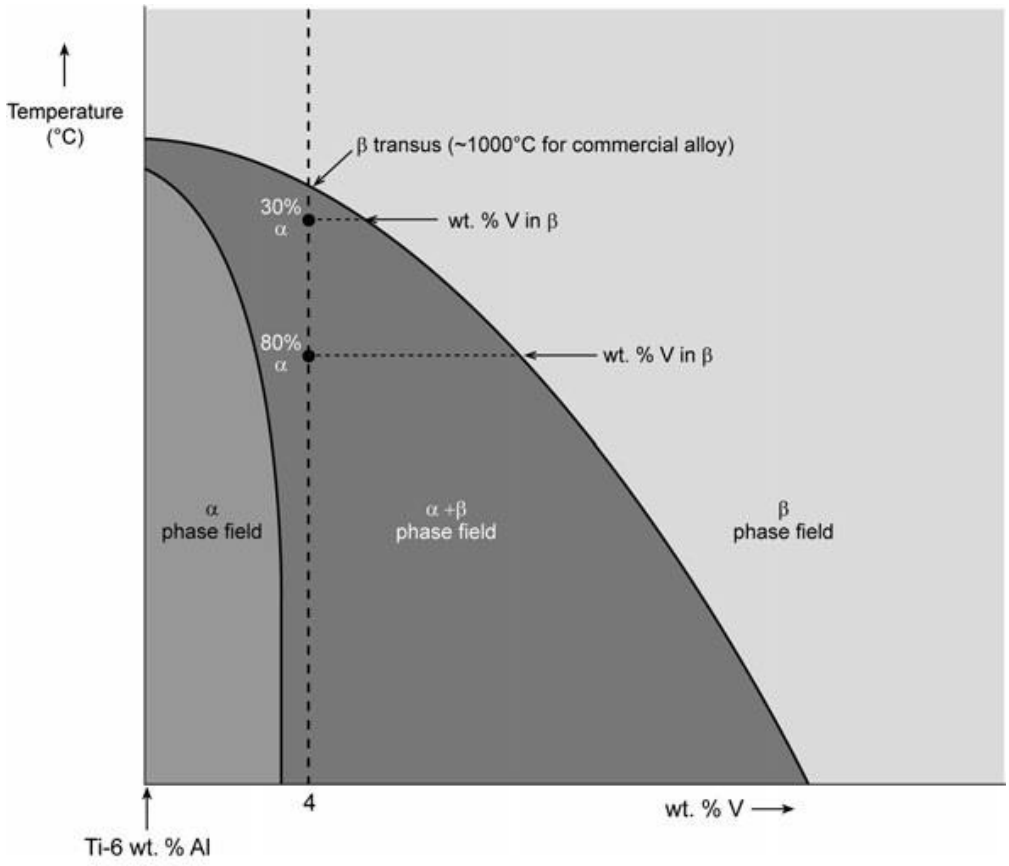

Fig 2.1: Pseudo-binary equilibrium phase diagram (schematic) for Ti6Al4V (Leyens, 2003)

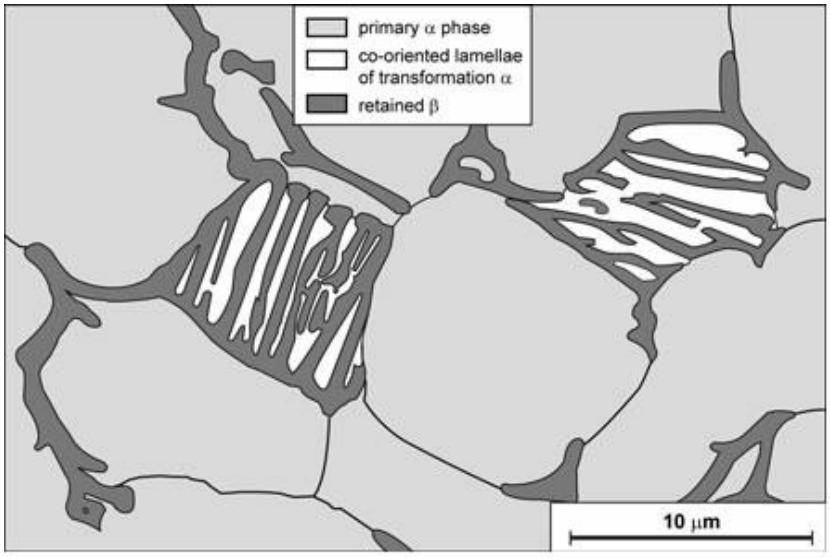

Fig 2.2: Illustration of an α-β titanium alloy microstructure, showing more or less equiaxed grains of primary α and transformed β. The transformation of β results in co-oriented α lamellae (transformation α) separated by ‘‘ribs’’ of retained β (Wanhill, 2012)

(ii) **Martensitic** - these steels are magnetic and have higher levels of carbon (up as high as 1% and 12% of chromium). They are used where moderate corrosion resistance and high strength are required but have low formability and weldability. Martensitic steels have different grades such as 2205, (Baddoo, 2008).

(iii) **Duplex** - they have a microstructure which is around 50% austenitic and 50% ferritic. This microstructure gives them a higher strength than austenitic or ferritic steels. Duplex steels are magnetic but not as much as martensitic and ferritic materials due to the 50% of an austenitic phase. They are weldable and are used where high strength and stress corrosion cracking are required.

(iv) **Precipitation hardening** - these steels can achieve great strength by adding elements like copper, aluminium and niobium to the steels but their corrosion resistance is similar to standard austenitic steels. They have different grades such as 15-5PH, 17-4PH, and 15-7PH (Villanueva *et al*., 2006).

(v) **Austenitic** - these common steels have the useful property of being able to be work hardened to high strength levels whilst retaining a significant level of toughness and ductility. They also have increased resistance to corrosion cracking due to a high degree of nickel and corrosion resistance can be improved by adding chromium, molybdenum, and nitrogen. Austenitic stainless steels are nominally non-magnetic steels and have austenite as the primary phase (face centred cubic crystal) (Takeda *et al*., 2006). Table 2.1 reports some

austenite stainless steels used in aerospace applications. This combination of strength and toughness, and corrosion resistance is the primary reason for its widespread use in AM. There are many studies which have tried to improve the density of 316L stainless steel, for instance, it has been reported that the lower scan sped, higher laser power, thinner layer thickness, and narrower hatch spacing could enable a much smoother melting surface and higher densification (Sun *et al*., 2014, Shang *et al*., 2017). There have been some efforts to improve functionability during the SLM of steel powder mixtures such as an experimental study on the SLM of austenitic and martensitic stainless steel powder mixtures with varying composition ratios has discussed in next Section 2.2.2.1 (Jerrard *et al*., 2009). More details about why used this material in this work here in, and the exact composition are given in chapter 4 Section 4.1.2. Further discussion regarding the mechanical properties of 316L stainless steel parts fabricated by AM are explained in chapter 3 Sections 3.3 and 3.4.

Table 2.1: Austenitic stainless steel grades and their aerospace applications (Xavior and Adithan, 2009[1], Tiamiyu *et al*., 2016, Sathyajith, 2015).

Aerospace Application/Use	**Austenitic Stainless Steel grade**
Fuel tanks[1]	(AISI* 304) (AISI 304L)
Exhaust components, high temperature engine and structural parts	(AISI 309) (AISI 310) (AISI 321) (AISI 316) (AISI 316L) *American iron and steel institute

2.2 Process parameters

The process parameters are imperative to operate the interaction between the laser and the materials and to ensure a suitable quality and good properties of the AM parts. This section illustrates the parameters used in the SLM and DMLS processes, the effect of environmental conditions on those processes and the powder materials used.

2.2.1 Principle of laser melting of metal powders

Throughout laser beam melting, a beam with a chosen diameter locally melts the upper powder layer on the powder bed. The laser is absorbed by the metal powder particles creating a melted pool which solidifies rapidly, as shown in Figure 2.3a. In SLM, the metal powder is applied free of fluxing agents and binders. The metal powder is heated by the laser beam to

its melting temperature. The laser powder typically varies, and the energy of the laser beam is selective in such a way that the metal powder layer is fully molten. On the other hand, in the SLS process, the mechanism is a partial melting and then fusing of the powdered materials, as shown in Figure 2.3 b. (Hunt *et al*., 2015, Fu and Guo, 2014).

The melted zone diameter is usually higher than the laser diameter, especially in the SLM process, so it is necessary to recover the dimensional error and must shift the laser beam by half the width from the contour to the inside to confirm that the contour of the next part will agree to the original data entered. This correction of the position is known as the Beam Offset value (BO), (see Figure 2.4). If this BO value is less or higher than the correct value, the powder particles in the irradiated zone might be over-melted or partially/not melted. During hatching, the laser beam moves line after line several times until it completely melts the designated areas. The distance between the scan lines are known as the hatching distance or spacing (h_d) (Aumund-Kopp and Petzoldt, 2008).

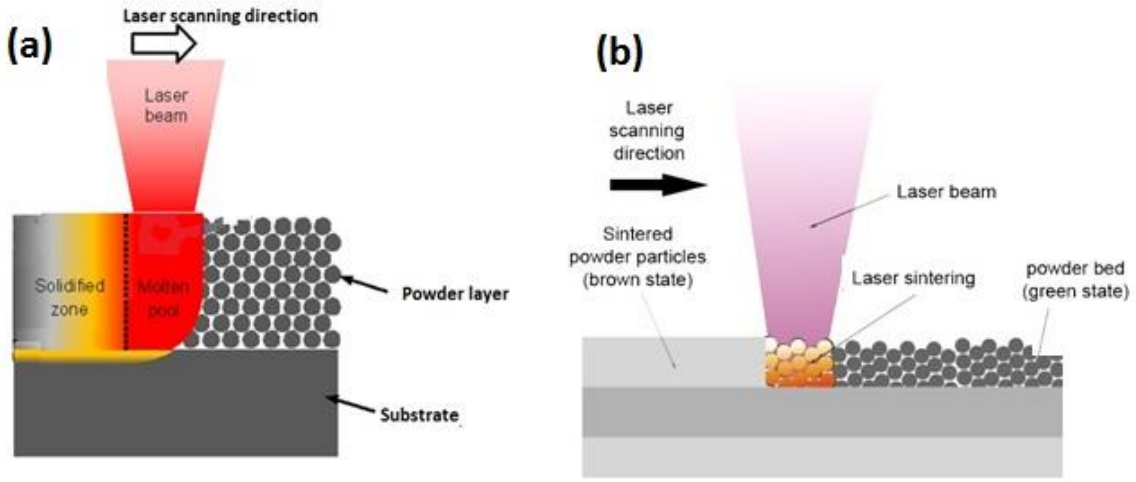

Fig 2.3: The fundamental consolidation mechanisms during (a) laser beam melting, and (b) laser beam sintering. Taken from (Fu and Guo, 2014)

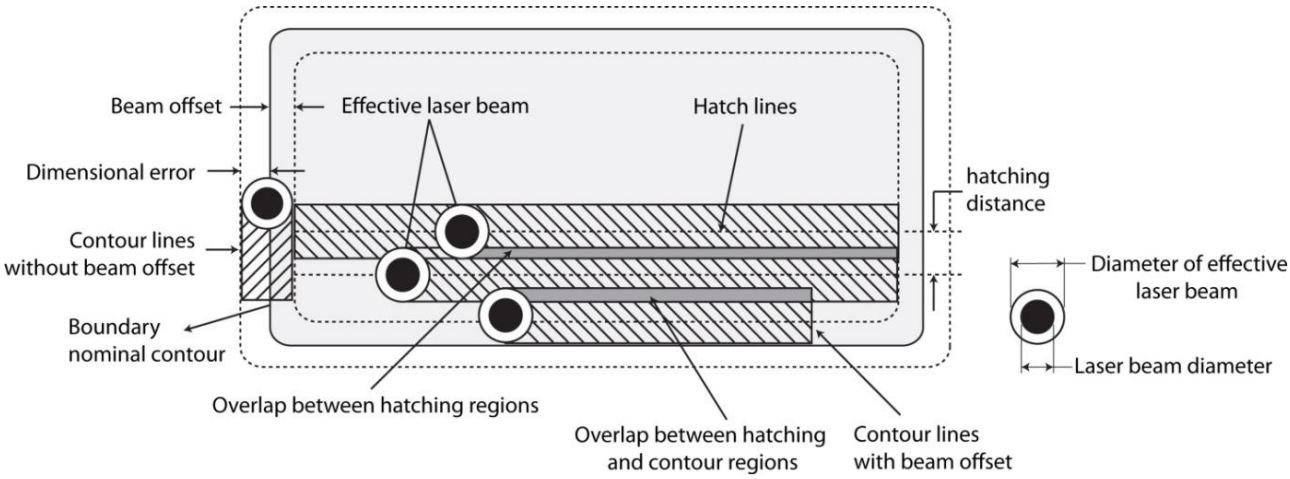

Fig 2.4: Diagram showing exposer strategy of laser pattern scanning. Taken from (Aumund-Kopp and Petzoldt, 2008)

2.2.2 Material parameters

Metal powder plays a paramount role in the AM processes. Indeed, the quality of the metal powder applied will have a major effect on mechanical properties, production of defect-free parts and manufacturing defects on the surface. Key metal powder characteristics for AM can be classified in three categories; chemical composition, powder size distribution, and physical properties. There are other useful existing standards to consider when selecting metal particles for AM processes such as their storage, health and safety, and their reusability after AM cycles (Wei *et al*., 2015).

2.2.2.1 Chemical composition of metal powders

Few metals powders are used in their pure state. Other elements are typically added to pure metals to convert them into alloys and for improving their mechanical properties. The alloying elements usually dissolve in the pure essential metal to form a solid solution; their solubility can change depending on different elements (Jones and Ashby, 2005). These elements can also affect the mechanism of bonding and the alloys' microstructure.

In the laser beam melting process, dissolved elements sometimes cause a solidification problem due to their significant influence on the material in the melt pool; for instance solidification cracks and delamination (Rombouts *et al*., 2006). Moreover, the differences in the melting temperatures of each element and the interaction between these elements can result in the formation of a heterogeneous microstructure. Some elements have an adverse effect on the densification due to the high reflectivity of the laser beam. Some elements can

also influence the behaviour of the melt pool resulting in porosity and roughness on the top surface of the components. For instance, Rombouts *et al* studied the effects of elements such as oxygen, carbon, silicon, titanium and copper on the quality of iron based objects. They found that titanium and silicon have a negative effect on the surface quality of Fe-based parts, both elements increase the irregular porosity due to their high tendency to form carbides and oxides. Copper has a negative effect on the densification if added as pure powder because pure Cu is highly reflective for Nd:YAG laser radiation, but there is a positive effect if the Cu is added in pre-alloyed form. Also, they found that the oxygen in the atmosphere of the SLM chamber increase the melt volume formed during SLM, and this was attributed to exothermic oxidation of Fe, which deteriorates the surface quality of parts (Rombouts *et al*., 2006, Schaffer *et al*., 2001). Jerrard *et al* investigated the effects of varying the ratio of austenitic and martensitic powder mixtures on the laser consolidation of steel parts see Figure 2.5. Specimens were fabricated by SLM processing from 316L austenitic and 17-4PH martensitic stainless steel powder mixtures with varying composition ratios. Mechanical and magnetic properties of the specimens were assessed by micro-hardness testing and comparison of 'magnetic adherence' forces. The composition ratios of the mixed powders have been found to influence the laser consolidation mechanisms and the resulting microstructures in the specimens (Jerrard *et al*., 2009).

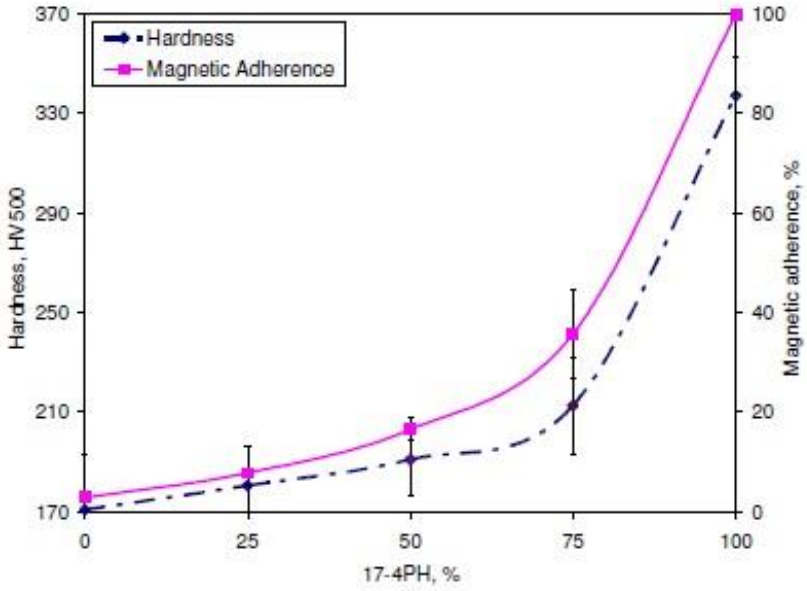

Fig 2.5: shows the influence of austenitic stainless steel (316L) mixed with different martensitic stainless steel (17-4PH) on the hardness and magnetic properties (Jerrard *et al*., 2009)

2.2.2.2 Powder, size, and particle distribution

The powder shape, size, and particle distribution play a critical role in the SLM and DMLS processes. Powder size distribution has a significant influence on powder bed density and fluidity. It also affects the surface roughness, density of the components produced, energy input determination and layer thickness determination. Smaller particle sizes can fill the gaps in between larger particles resulting in a higher packing density. A different range of particle sizes may conversely lead to increase the amount of porosity as larger particles can fully or partially melt while smaller particles may vaporise (Gibson *et al*., 2010). Previous work has reported that using a particle size range of 20-50 μm can achieve the performance of parts produced, and meet basic acceptance when building fully functional high density metal components (Khaing *et al*., 2001, Hauser *et al*., 2005).

The smaller the size of the powder particle the higher surface quality on the side and top of produced parts due to the ability to deposit thinner layers (Gong *et al*., 2014, Zhou *et al*., 2015). Therefore the smaller the particle size and consequently layer thickness leads to an improvement in the accuracy of the parts as the width of the melt area and the shrinkage variance between the top and bottom of each layer is smaller (Pinkerton, 2007).

2.2.2.3 Powder flowability

Through the SLM and DMLS process, the wiper spread the powder layer uniformly. Therefore the flowability can influence the melting/sintering process, the distribution of the powder particles on the substrate and the laser energy absorption (Das, 2003). The spherical particles with smooth surfaces and same size spread and move quickly within the powder system and lead to make a uniform bed density. The small size of powder particles leads to a high flowability. However, the mixture of different particle sizes increases the powder bed density SLM (Steen and Mazumder, 2010). Therefore, for optimum processing, an excellent balance between these two parameters should be made; for instance, in some SLM process, the powder deposited by gravity during a system of valves. If the power is irregular, it will stick in the valves it this make it impossible to generate a smooth layer (see Figure 2.6) (Simchi, 2004, Kurzynowski *et al*., 2012).

The powder flowability is also affected by moisture. This means it is very important to store the powder in a dry place. Also, pre-heating the substrate can reduce the moisture through the process.

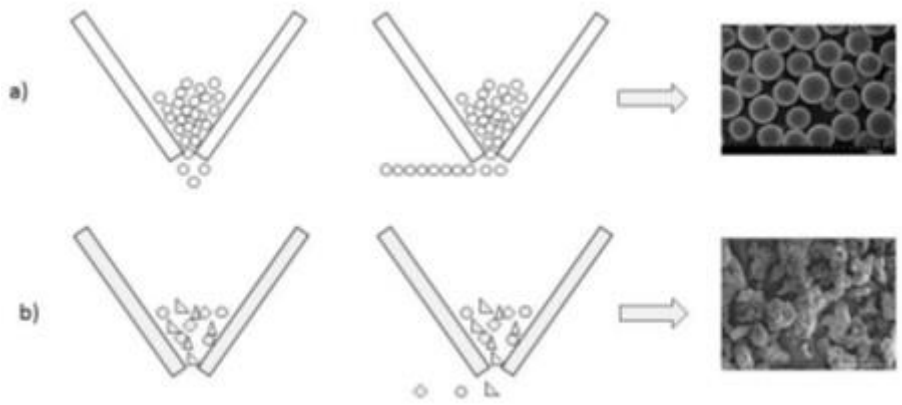

Fig 2.6: Schematic of the layer deposition process for (a) a spherical powder, and (b) an irregular powder (Kurzynowski *et al*., 2012)

2.2.3 Laser and scan parameters

2.2.3.1 Laser power, beam profile and beam energy intensity

Some factors in the powder bed process are controllable such as the laser power, the laser focus position, and the beam energy density. Some factors are, however, not controllable such as laser efficiency, focal lens properties, and laser beam profile. Today the lasers used in SLM and DMLS processes are either a short pulse or continuous waves of laser energy. The continuous wave laser (CW) has a continuous laser output through the continuous excitation of the reactive medium where the energy output is theoretically constant. In this condition, the continuous stable power input received by the powder bed to be heated and can melt the powder continuously (Yadroitsev *et al*., 2007). On the other hand, in some SLM/DMLS processes, the laser energy is emitted in a pulse mode only by adjusting the exposure time and the distance between exposures. This kind of laser energy delivery is carried out such that the melt pool width and heat build up is minimised (Huang *et al*., 2016).

In SLM and DMLS processes, the laser energy density E_ρ, is an important factor, which affects the final quality of parts produced. More details about the effect of different laser powers on parts produced will be given in Section 3.1. The laser energy density is given by the equation

$$E_\rho = \frac{P}{v\delta}\ \left(\frac{J}{mm^2}\right) \qquad 2.1$$

where P is the incident laser power (J/s), δ is the spot size of the laser beam on the powder bed (mm), and v is the laser scanning speed (mm^{-s}).

The laser power, scanning speed, and beam spot size can be controlled via the process using machine control software. Laser beam spot sizes on the powder bed are controlled by

adjusting the distance between the lenses in the beam expander and by setting the position of a lens. In addition, the change in the angle of incidence changes the laser spot geometry from circular to a large elliptical area, resulting in a reduction of the energy flux, (see Figure 2.7) (Steen and Mazumder, 2010). In some powder bed systems, the beam offset is used to compensate for the laser beam focal diameter at the scanned section boundaries, as discussed in Section 2.2.1 (Steen and Mazumder, 2010).

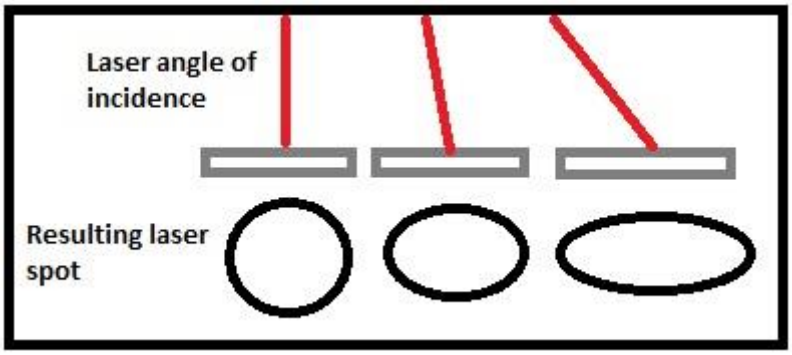

Fig 2.7: Schematic showing the change in the angle of incidence with a change in laser spot geometry. Reproduced from (Steen and Mazumder, 2010).

2.2.3.2 Process scanning strategy

The process parameters of SLM and DMLS can be controlled and varied to enhance the parts produced. Numerous studies focused on different input parameter have been carried out to improve the material properties, such as accuracy, density, mechanical properties and surface finish (Yadroitsev and Smurov, 2011). These studies' controllable input parameters include scan direction, hatch distance, powder layer thickness, laser exposer time, point distance, beam offset and others. Table 2.2 and Figure 2.4 summarise some of these parameters briefly. Different scanning strategies are possible in metal AM processes, as seen in Figure 2.8. The microstructure, porosity level, surface roughness, residual stress and cracking in the completed metal parts are influenced by the laser scanning patterns (Li *et al*., 2014, Thijs *et al*., 2013, Aboulkhair *et al*., 2014). To control the fabrication of unwrapped and uncracked layers, and at the same time control the thermal gradient through the powder heating and cooling process. Different studies (Su *et al*., 2003, Dewidar *et al*., 2003) have investigated the relationship between the scanning strategies and the properties of SLM processed parts. For instance, Dewider *et al*. discovered that the adoption of different scan patterns culminated in different times which affected the microstructures obtained for the parts produced by laser sintering (Dewidar *et al*., 2003). To make a uniform distribution of energy inputs in SLM, Su

and Yang (Su and Yang, 2012) identified three types of overlap regime: intra-layer, inter-layer and mixed, overlapping regimes with a coexistence of the first two categories (see Figure 2.9). Su and Yang found that the inter-layer overlapping regime could be found when the track space was less than 200 μm, which lead to a high relative density with the specified process parameters.

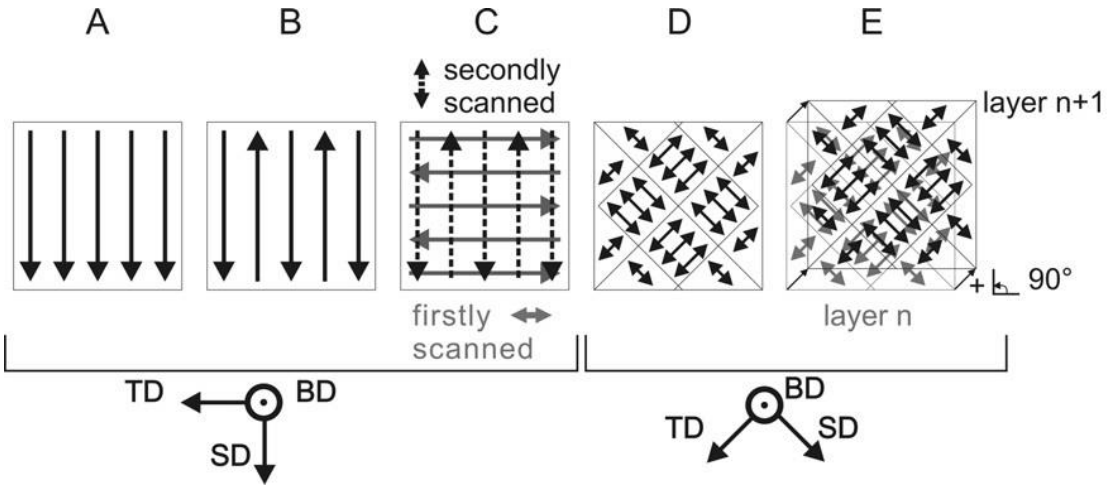

Fig 2.8: The scanning strategy used in the laser beam melting process. (a) Scanned with long unidirectional vectors. (b) Extended bidirectional vectors. (c) first scanned with long bidirectional vectors in TD and secondly scanned with long bidirectional vectors in SD (d) scanned with island strategy with 90° rotation but without shift (e) scanned with island strategy with 90° rotation and a 1 mm shift between the layers. (TD = first layer direction, SD= second layer direction, BD= bidirectional) (Thijs *et al*., 2013)

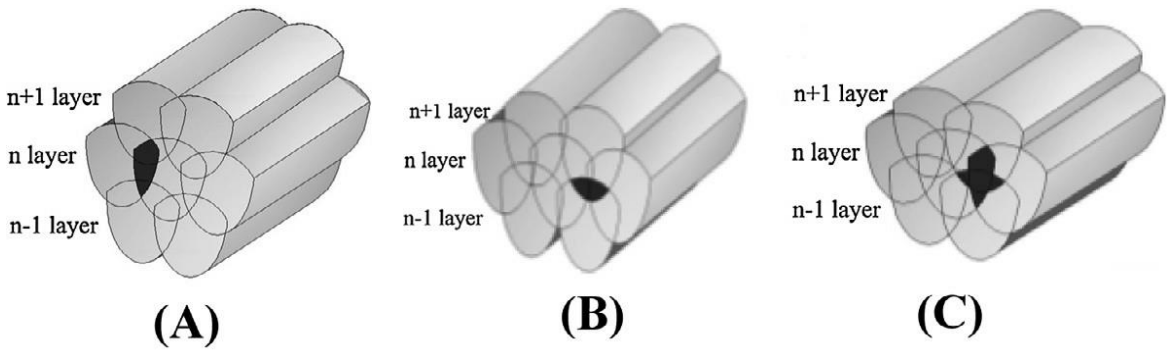

Fig 2.9: Three types of overlapping regimes. (a) The intra-layer overlapping regime, (b) inter-layer overlapping regime, (c) Mixed overlapping regime (Su and Yang, 2012).

Scanning speed and hatch distance are key factors that can affect the laser energy density. It must be mentioned that a nominal laser energy density can be produced by a range of scanning speeds and laser powers. However, the absorption and back radiation of the laser combine with the laser scanning speed and power to affect the process of particle melting (Arısoy *et al*., 2016). The most important objective when controlling the energy density is to ensure that sufficient heat is absorbed by the powder densification without over-heating. High energy inputs can cause undesirable deformation of the parts through large thermal gradients and resulting thermal stresses. This can also cause the surface powder to start vaporising before a significant depth of molten material is achieved. Reducing the energy density input can be accomplished by increasing the scanning speed, increasing the hatch distance and reducing the laser power. The melt powder layer thickness decreases with increasing hatch distance; this thickness also decreases with increasing the scanning speed because of shorter interaction times (Arısoy *et al*., 2016, Savalani and Pizarro, 2016).

Table 2.2: Summary of input process parameters for SLM and DMLS (Yadroitsev and Smurov, 2011)

Input Parameters Description	**Input Parameters Description**
Exposure time	Determines the time of laser exposure into each point.
Point distance	Each hatch line is divided into a series of points; point centres are separated by the point distance.
Scanning speed	Defines the speed of the scanning laser.
Layer thickness	Specifies the layer incremental distance during processing.
Hatch type	Controls the scanning strategy such as scanning direction, re-melting scan, etc.
Hatch distance	Controls the distance between two adjacent lines of the scan.

The process parameters are important factors that need to be considered for the wetability for preventing balling phenomena. Balling is when melting is induced by the laser beam. In this process, the molten material rapidly consolidates into spheres with diameters approximately the same as the diameter of the laser beam, instead of consolidating into the previous layer. Previous work has revealed that the spherical structures increase in number with an increase in the laser power and a decrease in the scanning speed (Makoana *et al*., 2016, Olakanmi, 2013). Dadbakhsh *et al*. also reported that the scanning speed plays a crucial role in determining or avoiding the balling phenomena shown in Figure 2.10. This process window reveals that high scan speeds combined with high laser power result in less balling attributed to the melt pool which rapidly solidifies behind the laser spot, while the length of the molten track remains to a suitable degree (Dadbakhsh *et al*., 2012a). Balling can also be reduced by appropriate high scanning speeds, even using the same energy density. More details about balling is provided in Section 2.3.2.

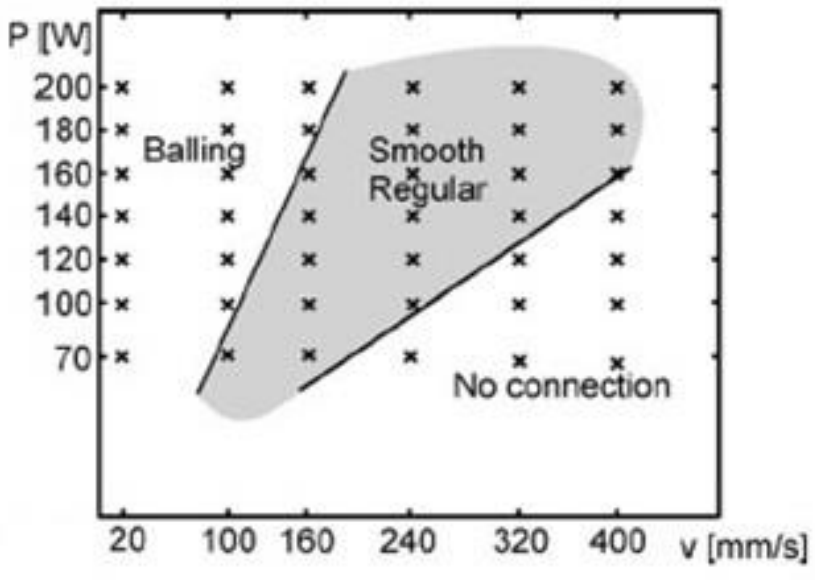

Fig 2.10: Process window for SLM of Iron-based powder in continuous wave operation (Dadbakhsh *et al*., 2012a)

A range scanning strategies can affect the melt pool behaviour and material properties of the parts produced (Guan *et al*., 2013). A re-melting strategy is also used to re-melt the part surface to reduce the residual stress, porosity and the top surface roughness (Krakhmalev *et al*., 2014). To ensure effective re-melting occurs, control of the process parameters such as

input laser power and scanning speed is required. Figure 2.11 shows the difference between SLM only and laser re-melting of 316L stainless steel. The surface roughness value reduced to 1.5 μm, the microstructure was improved, and the amount of porosity was reduced by 90% (Yasa *et al*., 2011b, Hao *et al*., 2009).

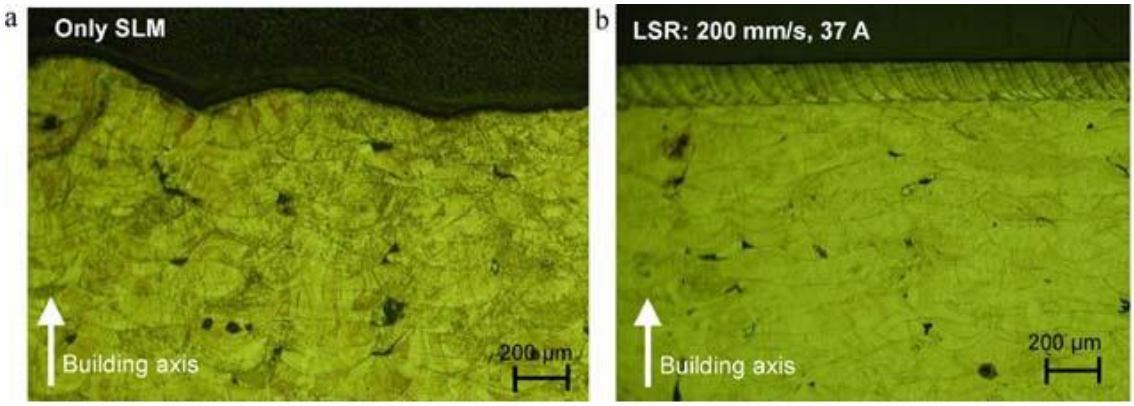

Fig 2.11: (a) Single pass melting; (b) laser re-melted part with 200 mm/s and 95 W (Yasa *et al*., 2011b)

2.2.4 Process environment

During the fabrication in the DMLS and SLM processes, the gas chamber should be filled with a protecting gas to help minimise oxidation. Oxygen (O_2) can react with the molten material causing oxidation on the surface which will influence the properties of the parts produced. Oxidation during the process leads to a reduction of the molten material's wettability, which can cause balling, porosity, tearing and delamination because of surface tension defects due to unsuccessful layer fusion (Gajalakshmi and Sriram, 2015); more details about these defects are given in Section 2.3. Some studies have focused on the effect of O_2 through the SLM process (Louvis *et al*., 2011, Van Bael *et al*., 2012, Fetoni *et al*., 2013). It is reported that the oxygen level within a SLM process should be less than 0.3% to help oxidation reduction.

Different shield gasses can be used to fill the building area such as nitrogen (N_2), helium (He) and argon (Ar). Argon is denser than air enabling an effective shielding for molten powder material (Campbell *et al*., 2013). Nitrogen can react and form nitrides with numerous elements such as chromium (Cr), manganese (Mn) and titanium (Ti) (Azman *et al*., 2014). Nitrogen cannot be used in fabricating carbon steel because it reacts with C and Fe, causing porosity in the parts produced. Helium is not usually used because it is lighter than air and it

is hard to protect molten material during the fabrication. In comparison to other gasses, Ar is widely employed in SLM processes due to its cost effectiveness and better densification results. On the other hand, Kurgan *et al*. in a study of powder metallurgy investigated the effect of the sintering atmosphere on the densification of 316L powder. They showed higher tensile strength but lower ductility were obtained with an N_2 the atmosphere at 1300 ºC (see Figure 2.12) (Kurgan, 2013).

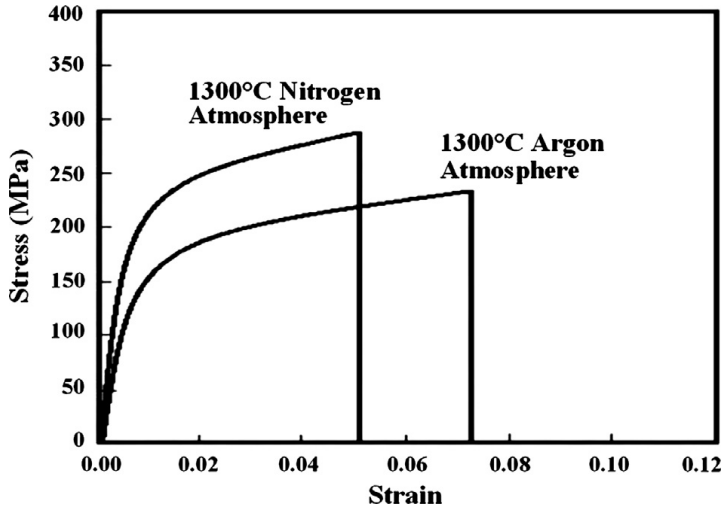

Fig 2.12: Stress-strain curves for 316L stainless steel compacts sintered in argon and nitrogen atmospheres at 1300 ºC (Kurgan, 2013)

Some previous work has reported that pre-heating the base plate can improve the surface roughness and the parts accuracy due to reduced thermal gradients and shrinkage. This is due to the requirement of less heat energy input by the laser to change the powder from a solid to liquid phase (Basak *et al*., 2016, McNutt, 2015). On the other hand, other research has indicated that pre-heating does not necessary improve the properties of parts as the pre-heating temperature is only raised up to 100-250 ºC, while the melting temperature of the metal is above 1000 ºC (McDonald, 2015). Pre-heating the building substrate typically improves the flowability of powder as it reduces the moisture content of the powder as discussed in Section 2.2.2.3.

2.3 Specific defects in materials found in metal AM process

Some common defects can be found in materials resulting from incorrect build strategies, process parameters, part orientation or insufficient powder quality, as discussed in Section 2.2. Common metallurgical defects in DMLS and SLM processed metallic parts are porosity, cracking, surface roughness, and residual stress.

2.3.1 Porosity

This is a common defect in metal AM components, and it has a negative influence on mechanical properties. Porosity occurs as result of incorrect processing, poor powder quality or a solidification artefact, as shown in Figure 2.13 (Sames et al., 2014). Regarding powder induced porosity, pores of gas may form inside the feedstock of the powder through atomization (Gong et al., 2014). These pores of gas can translate directly to the as-built parts. Numerous studies (Gong et al., 2014, Yasa et al., 2011b, Li et al., 2010) have reported that porosity formation is controlled by the techniques employed. Pores created by processing techniques or incorrect processes are formed when the input energy is insufficient for complete melting or sputter ejection take place when energy input is high. Theses pores are usually non-spherical and have different sizes (submicron to macroscopic). To avoid a range of mechanisms that can cause pores, suitable process parameters must be selected.

When the energy input applied to a region of powder is not sufficient, a lack of fusion can occur. Lack of fusion regions can be revealed by unmelted powder particles visible in or near the pore. When the energy input applied to an area of powder is too high, sputter ejection may happen in a process known as keyhole formation. In SLM, keyhole formation can be observed during the process that can produce a trail of voids over the operating region (King et al., 2014). Spatter ejection can be avoided by watching the process and adjusting the parameters while improving new processing strategies. Processed-induced porosity can also occur when the powder distributed into the processing surface has particles larger in diameter than the layer thickness, which is intended to consolidate into a layer of the correct height during the melting (Körner et al., 2013). Shrinkage porosity, sometimes known as ‘hot tearing’ occurs through solidification as a consequence of adequate metal feeding, or incomplete flow of material into the selected melt region. With optimised process parameters, process-induced porosity can be reduced to less than 1% in EBM and SLM (Vilaro et al., 2011, Frazier, 2014, Svensson, 2009b); more detail will be given on the process parameter optimisation in Section 3.1.

2.3.2 Cracking, delamination, and swelling

Defect creation depends on the process temperature. Microstructure cracking may happen through solidification or subsequent heating. Macroscopic cracks may relate to other defects such as porosity. Delamination leads to interlayer cracking. Swelling may be linked to a combination of surface tension and melt pool size when the process temperature is too high. These defects can be avoided by tightly controlling the process conditions, for more details see sections 3.1and 3.2.1. Also, microstructural cracking is material dependent, and the cracking may be unavoidable in some processing cases (Sames et al., 2014).

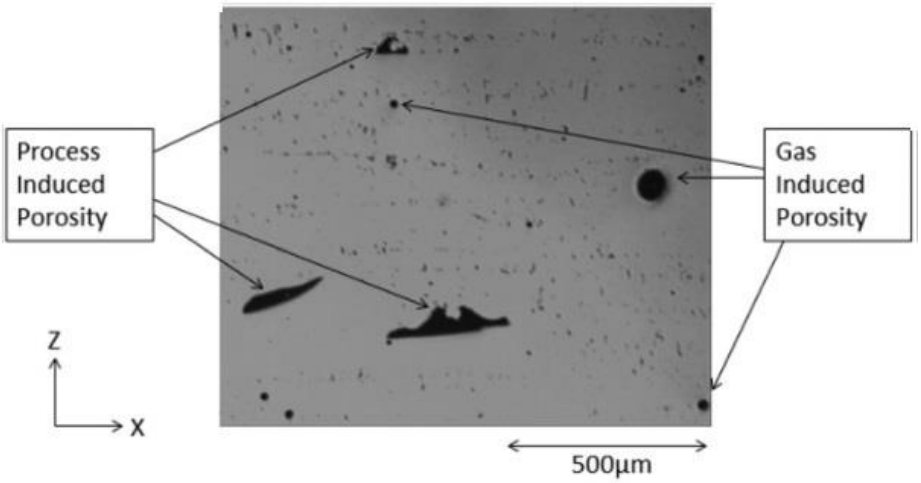

Fig 2.13: Optical micrograph showing process induced porosity which is due to lack of complete fusion, and gas induced porosity transferred from the powder feedstock (Sames *et al.*, 2014)

Various material-dependent mechanisms are leading to the formation of cracks in AM material (Carter *et al.*, 2012). Solidification cracking occurs for some materials when the input energy applied is too high and emerges from the stress induced between solidified regions of the melt pool and areas that have yet to solidify. This type of cracking is caused by high strain on the melt pool or flow obstruction by solidified grains (Rickenbacher *et al.*, 2013). Grain boundary cracking is cracking that occurs along material grain boundaries. It is dependent on the grain boundary morphology and the formation or dislocation of participate phases. Both solidification and grain boundary cracking occurs within the microstructure.

(Carter *et al*., 2012). These cracks may nucleate from other macroscopic defects such as delamination events, which are not related to excessive energy inputs (Kempen *et al*., 2013).

Delamination is the separation of adjacent layers due to a lack of melting between the layers or insufficient re-melting of the underlying solid. The lack of fusion means defects will usually be localised within the interior of the part but can be minimised with post-processing. However, delamination cracking is macroscopic and cannot be repaired by post processing (see Figure 2.14 a), it is usually reduced by using substrate heating (Kempen *et al*., 2013). Excessive laser power can lead to overheating of the material which is mostly due to overhangs in the geometry, as seen in Figure 2.14b (Hussein *et al*., 2013). Swelling 'is the rise of melted material above the plane of powder distribution, and occurs due to surface tension effects related to the melt pool geometry (see Figure 2.14c) (Sames *et al*., 2014). Recently, lattice structures have been discovered to support overhangs in geometries (Hussein *et al*., 2013). Melt ball or balling formation, as defined in Section 2.2.3.2, is the solidification of melted material into spheres instead of wetting into the underlying parts (see Figure 2.14 d). Balling occurs due to surface tension, which is directly linked to the dimensions of the melt pool (Kruth *et al*., 2004). For instance, the melt pool transition from a wetting bed to spherical balling, occurs when the ration of length (l) to diameter (d) ratio is greater than 2.1 (l/d >2.1). However, these conditions are purely conjectural; depending on assumptions such as chemical homogeneity and smooth surfaces (Zäh and Lutzmann, 2010).

Kruth *et al* proposed that the best way to address this phenomenon was by reducing the length-to-diameter ratio of the melt pool. Melt pool formation, as seen in Figure 2.14d, is a condition typically observed through material development. It occurs with higher temperatures or with lower temperatures alongside delamination (Kruth *et al*., 2004). Capillary and wetting forces have been recognised as contributors to both swelling and baling (Bauereiß *et al*., 2014). It could be difficult to identify the reasons for defects post-build, because one kind of defect may change the local heat transfer conditions and lead to the compounding of flaws. Moreover, the formation of porosity, which can lead to minimised thermal conductivity, causing swelling or melt pool formation on succeeding layers because of unexpected thermal resistance (Zäh and Lutzmann, 2010).

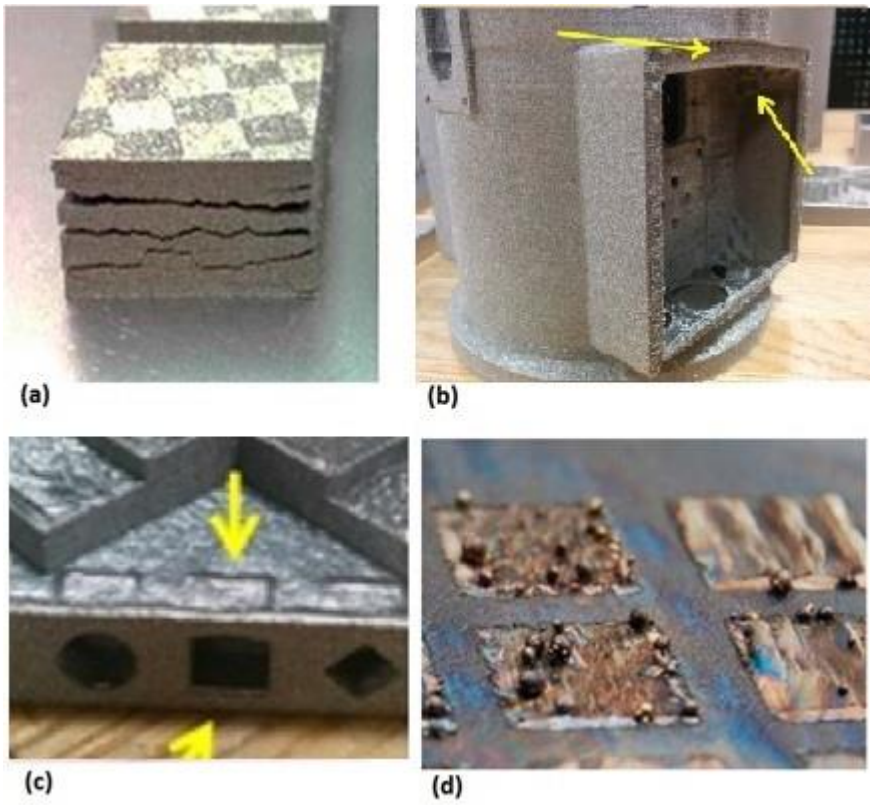

Fig 2.14: (a) Delamination cracking in SLM of tool steel (Kempen *et al*., 2013), (b) overhangs printed on the side of the Ti6Al4V part fabricated by EBM (Hussein *et al*., 2013), (c) swelling formation in SLM of 316L stainless steel (Sames *et al*., 2014), (d) balling formation in EBM 316L stainless steel (Kruth *et al*., 2004)

2.3.3 Residual stress

Residual stress is common in metal AM parts due to large thermal gradients that occur through processing, which negatively influences mechanical properties and lead to geometric distortion (Gnäupel-Herold *et al*., 2014, Sochalski-Kolbus *et al*., 2015, Brice and Hofmeister, 2013). Residual stress remains in the material after the removal of an applied stress. When the stress exceeds the local ultimate tensile stress (UTS) of material, it may cause cracking or other defects. When the stress exceeds the local yield stress (σ_s) of material, it may cause plastic deformation or warping. Residual stress occurs in metal AM either by differential heating of the solid or by differential cooling through and after solidification (see Figure 2.15) (Kruth *et al*., 2004). Accordingly, in SLM manufacturing, residual stress has an undesirable effect on the final parts. Some methods can be used to relieve residual stress, mostly multiple laser scanning of layers, the base plate and the powder bed heating, and post processing or heat treatment.

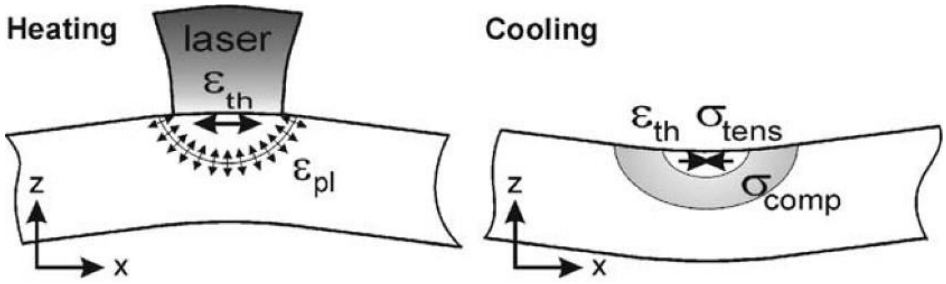

Fig 2.15: Schematic of the cause of residual stress in an SLM process. ε_{th} indicates the thermal strain, , ε_{pl} indicates the plastic strain resulting from thermal strain exceeding the yield limit, σ_{tens} indicates the tension stress, and σ_{comp} indicates the compression stress (Kruth *et al*., 2004)

Multiple scanning of laser or re-melting of one layer leads to a reduction of the remaining stress by 55% for some steels. Increasing the laser power during the second scan also relieves the stress (Manfredi *et al*., 2014, Zaeh and Branner, 2010).

Powder bed and the base plate heating contribute to a reduced cooling rate, which leads to a reduction in residual stress. Experiments have shown that the residual stress of steel parts fabricated by SLM can be reduced by 40%, if the powder material and base plate are heated to 160 °C, which is comparatively small given the high melting point of steel is approximately 1500 ˚C (Manfredi *et al*., 2014, Shiomi *et al*., 2004).

Heat treatment is another approach that is commonly used for conventionally produced parts. Heating a steel part built by SLM in the range 600 - 700 °C for an hour reduces the residual stress by approximately 70%, which can contribute to a reduction in the temperature gradients (Riemer *et al*., 2014, Manfredi *et al*., 2014). However, to apply all of these three techniques requires an increase in energy, which increases the environmental impact of a processed part.

2.3.4 Surface roughness

The surface roughness of the components typically concerns for machines operators. In some applications, however, this property is not an issue because the parts will be machined and post processed. Surface roughness has two different contributors as shown in Figure 2.16, (a) layer roughness or non-flat layer edges (b) the actual roughness of the metal surface due to unmelted/partially melted powder particles. The non-flat layer effect may be reduced by using smaller layer thicknesses. This negatively affects the build time because the layer

thickness dictates the division of the part into a number of layers. The actual roughness of a material depends upon the equipment producing the part. Direct energy deposition typically has large layer thickness, which tends to limit this technology to near net shapes. Near net shape (close to the desired part geometry) processing is different from conventional methods where the full bulk of part is machined to final geometry. PBF technology typically has finer resolution layer thickness, but is prone to satellite formation because of the sintering of powder at the edges of parts (50). SLM machines use smaller layer thickness and finer powder which lead to less surface roughness, but this may add to process time and cost, and may still require machining in critical applications. Furthermore, a smooth surface is limited by the balling formation that can happen due to laser melting (see Figure 2.14d). The balling phenomena influence the SLM process because it leads to the creation of discontinuous tracks and is responsible for the non-uniform deposition of powder on the previous layers. This induces a possible delamination and porosity between the layers (Mumtaz and Hopkinson, 2009). Also swelling formation as shown in Figure 2.14c makes the part surface rough and a non-net shape. The surface roughness is also influenced by different parameters such as laser power, build orientation, scan speed and hatch spacing (Bacchewar *et al*., 2007).

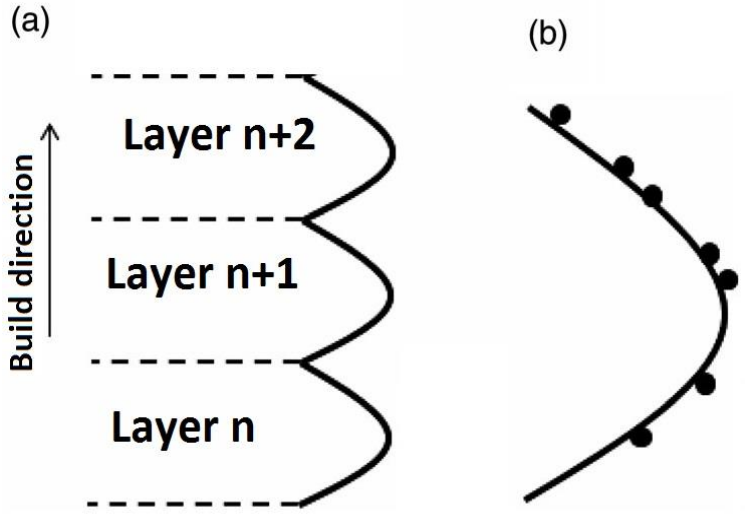

Fig 2.16: Schematics of surface roughness by (a) layer roughness and (b) actual surface roughness.

2.4 Summary

Metal AM technologies have been employed to build more advanced metallic parts using several materials such as stainless steel, aluminium, nickel, titanium alloys, etc. The 316L stainless steel is low-cost and available, as well as their excellent mechanical properties such as high temperature oxidation, strength and corrosion resistance make it one of the main and the best material to focus under the title of this thesis. Ti6Al4V alloy also have a high specific strength to weight ratios, corrosion resistance and is extremely resistant to heat and wear, so they can be taken into consideration as being suitable for aerospace applications. Ti6Al4V has relatively high cost and this issue make it the best area to focus in AM, because one of the main benefits of the AM is enabling the designing and manufacturing of parts where the material is needed to resolving in, net shape and less material consumption than machining. Thus, the Ti6Al4V powder used in the SLM process is normally recycled and reused, to reduce the amount of raw materials needed, and increasing the sustainability of the SLM process.

The controlled process parameters such as laser power, scan speed, focus position, beam energy density, etc play a critical role in the SLM and DMLS process to fabricate high quality aerospace components.some of these process are not controlable such as laser beam profile, focal lense properties and laser efficincy. The common metallurigical defects in SLM and DMLS processed metallic parts are residual stress, surface roughness, cracking and porosity, which required a suitiale process obtimisation to minimise them as discussed in chapter 3 Section 3.1.

Chapter 3: Development of Aerospace Metal Alloys Processed by AM

Development of aerospace metal alloys may generate additional properties, either, reductions in weight for some parts, with the same properties in the case of structural materials, or, greater efficiency of the engine parts, as well as resistance to higher temperatures. The property improvement for aerospace metals reflects improved efficiency and has led to the high performance of the modern aircraft sector. Very recently, an economic driver to reduce carbon dioxide emissions, such as through increasing engine efficiency and reducing the fuel burnt, has been achieved by a reduction in the weight of aircraft and the reduced drag of components (King and Carey, 2009). Moreover, the development of the processing and production of aerospace metal alloys has allowed the application of new parts and roles to improve the physical properties of these materials.

This chapter discusses the necessary guidelines to successfully fabricate lightweight and bulk aerospace components from 316L stainless steel and Ti6Al4V, and addresses the comments of previous studies on the process control parameters to fabricate these materials. To provide guidelines how to optimize the process parameters, which improve material properties, and the important guidelines that must follow through the fabrication. Section 3.1 and 3.2 give an overview of AM techniques to produce high quality parts. Also, the recent and previous studies including the mechanical properties obtained with 316L stainless steel and Ti6Al4V AM process is discussed in Section 3.3. Section 3.4 addresses the development and previous studies of lightweight cellular structures made by AM. Finally, Section 3.5 and 3.6 present the conclusion of this chapter, which puts the important findings into perspective, formulating concrete goals and guidelines about this research, respectively.

3.1 Process Parameter Optimization to Improve Material Properties

To achieve effective mechanical properties, it is important to fabricate high-density parts with an optimal surface quality and to avoid defects during the process of parameters optimization. To optimize parameters, it is common practice to fabricate simple geometries such as cubes with varying laser power, scanning speed, hatch spacing, and layer thickness. Thus, each cube is fabricated with a different energy density. Thereafter, the cubes produced are

characterized where interior density, sub-surface density, and roughness are investigated to identify the corresponding parameters and right energy window. Energy density is a key factor in the laser process which is defined in Section 2.2.3.1 and equation 2.1. Sufficient energy density is needed to fully melt the powder particles of the layer being processed and the previous layer, to assure joining between successive layers and avoid lack of fusion, porosity, and cracks; excessive energy can lead to material vaporization, creating defects.

Several studies have examined the effects of processing parameters on the part's porosity, surface roughness and mechanical properties (Dadbakhsh *et al*., 2012a, Safdar *et al*., 2012, Bourell *et al*., 2011, Strano *et al*., 2013b, Mumtaz and Hopkinson, 2009, Song *et al*., 2012, Yang *et al*., 2012a, Yang *et al*., 2012b, Hao *et al*., 2009). These reports have studied the effective factors on the SLM process of 316L and Ti6Al4V alloys, including the material properties such as: particle shape and size, particle distribution, chemical composition and so forth. They have also included laser processing parameters such as: laser power, spot size, scan line spacing, scan speed and vector length. For instance, Hao *et al* studied the effect of SLM parameters on the properties of 316L stainless steel (Figure 3.1) (Hao *et al*., 2009). The parts were manufactured using laser powers of 46.7, 53.3, 60.4, 67.2 and 73.6 W and scanning speeds of 0.125, 0.138, 0.154, 0.174 and 0.200m^{-s}. Visual inspection, hardness tests, density measurements, microstructural examination and tensile tests were conducted. Their results found that the parts' particles varied from slightly, to completely, melted in such a manner that, at a scanning speed of 0.154 m^{-s}, the particles fabricated by a power of 29.6 W were slightly melted; the parts fabricated using 39.9 W were partially melted and there were distinguishable necks between particles. The parts fabricated using 60.4 W were almost fully melted with small particles stuck on the surface.

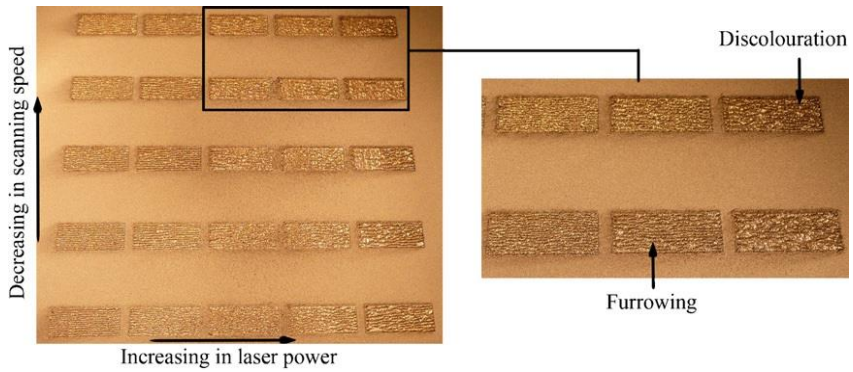

Fig 3.1: Set of 316L stainless steel samples fabricated with different laser powers and scan speeds (Hao *et al*., 2009)

Yasa *et al.* investigated the influence of different operating parameters for laser re-melting such as scan speed, laser power and scan spacing (Yasa *et al*., 2011a). Surface quality, microstructure, and density of SLM Ti6Al4V parts were also investigated. After each layer was fully molten, similar slice data were used to re-melt the layer. Their study concluded that laser re-melting is a promising method to improve the density and surface quality of SLM Ti6Al4V at a cost of longer fabrication times. Laser re-melting enhances the density by almost 100%, while the surface quality is enhanced by 90% after laser re-melting. Figure 3.2 shows an example of the average roughness Ra of a Ti6Al4V alloy with standard deviations at different laser powers and scan speeds. It is clear that there is no simple relationship between laser power and surface quality (i.e, roughness) and porosity. Since this is still one of the major defects in current AM process, it is important that further work be done on understanding these complex interactions.

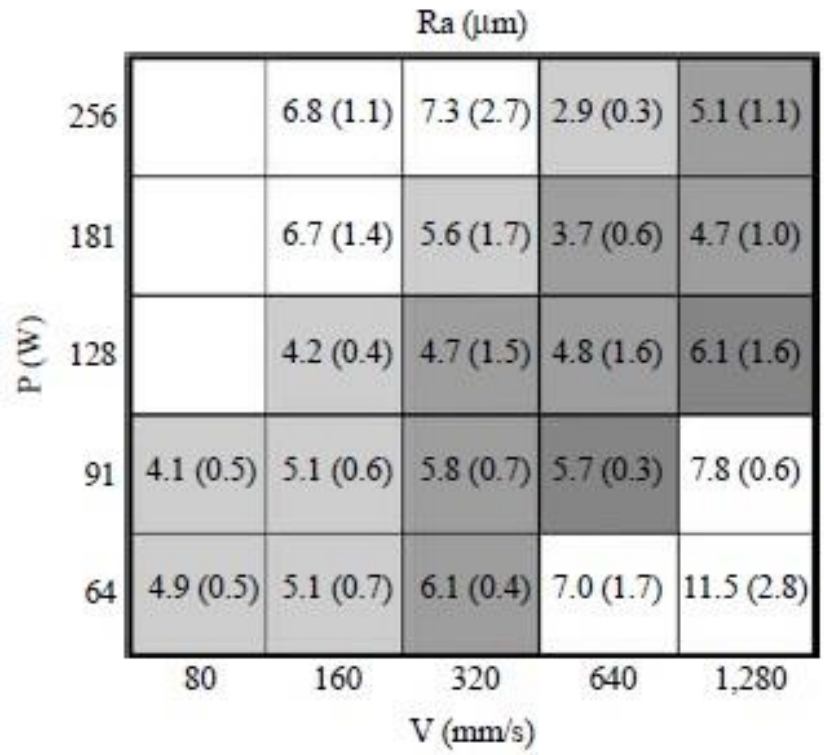

Fig 3.2: Average roughness (Ra) of a Ti6Al4V alloy with a change in different process parameters. Where (P) is a power and (V) is velocity (Yasa *et al*., 2011a)

3.2 Important guidelines to design lightweight and bulk parts for metal AM

These design guidelines are related to the SLM and DMLS processes.

3.2.1 Holes and internal channels

As mentioned in Section 2.3.2, designing holes in metal parts made by AM depends on the resolution of the metal AM machine. There are limits to the minimum and maximum hole diameters that can be built vertically and horizontally, respectively (Figure 3.3). For instance, the smallest vertical hole diameter for DMLS (EOS M 280) is 0.5 mm and for SLM (concept laser M1) it is 0.4 mm (Ghani *et al*., 2017). The acceptable range of circular horizontal hole diameters for the EOS M 280 process is from 0.5 to 6 mm without a support structure, while in the concept laser M1 process this is from 0.4 to 10 mm. For hole diameters above the maximum range, support structures are required, which can be difficult to remove in the case of non-linear holes. If the hole is not required to be circular, in this case, there is possible option to design self-support structures by modifying the hole shape such as teardrop profile or many types of self-supporting profiles to minimize the overhang area (Figure 3.3c) (Leutenecker-Twelsiek *et al*., 2016).

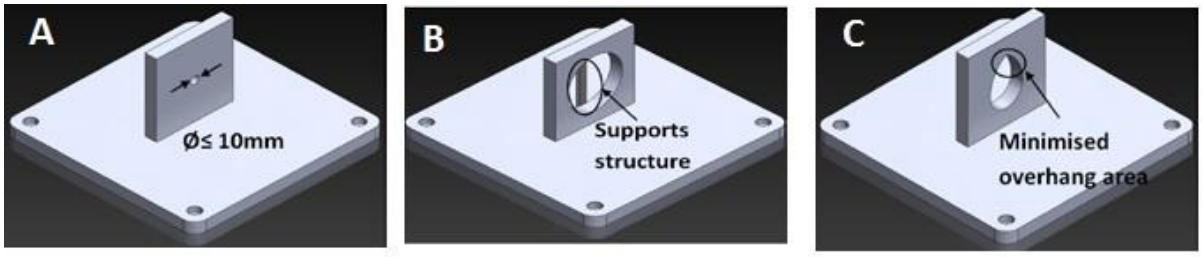

Fig 3.3: Schematics of (a) a round hole without a support structure, (b) a round hole above 10 mm diameter with a support structure, and (c) a teardrop profile to avoid support structures (Leutenecker-Twelsiek *et al*., 2016)

3.2.2 Wall thicknesses and height ratios

Minimum wall thickness can vary depending on the material, machine and powder used. If the wall section is thin and not supported, this may cause buckling in the surface. For the concept laser M1 process the recommended minimum wall thickness is 0.2 mm and for EOS M 280 it is 0.35 mm (Calignano *et al*., 2016, LLC, 2013). On the other hand, it is important

to consider the height to width or diameter ratios when designing thin vertical walls or pins to avoid buckling or distortion. The recommended height to width ratio usually does not exceed 8:1 for both SLM and DMLS processes (Adam and Zimmer, 2015).

3.2.3 Minimum strut diameter, support structures, and build orientation

Cellular lattice structures are key factors in reducing the weight of parts without reducing part strength, which is very important in aerospace and transportation industries. The minimum strut diameters for cellular lattices or support structures that can be achieved is usually 0.15 mm (Soe *et al*., 2015). Support structures have some function such as supporting the part in the case of overhangs, preventing complete failure or warping and fixing the geometry to the building platform. Figure 3.4 shows the support structures on parts, based on different positions and directions. These support structures can be difficult to remove in some cases (Strano *et al*., 2013a).

The parts' orientation in the powder bed is an important factor and must be considered for quality and cost. Certainly, part orientation affects the build time, surface roughness, and a number of the support structures. For instance, the low number of layers minimize the build time. The minimal amount of support reduces the material consumed, and easy access to supports for remove. Also, the best build orientation may reduce the surface roughness by reducing the staircase (Senthilkumaran *et al*., 2007), which is explained in more detail Section 3.2.4.

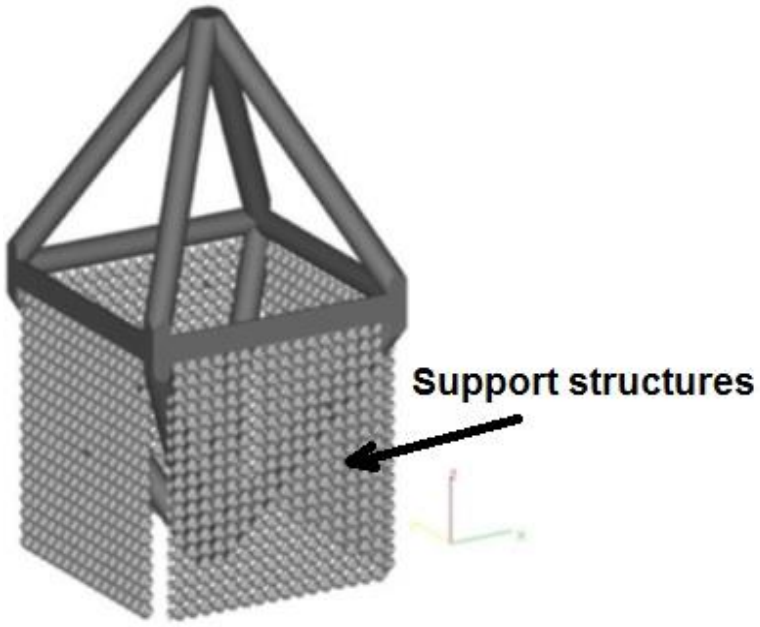

Fig 3.4: Schematic showing the support structure through an AM part (Strano *et al*., 2013a).

3.2.4 Overhangs and surface finish

Overhangs are a feature of parts without supports below them such as archways. An important rule when building parts layer-upon-layer is to avoid too low an overhang angle in the part to minimize the support structure. It is better to keep overhangs within the threshold that the machine of choice can produce if one type of overhang doesn't fit with the range of the desired machine. Another type of overhang may be be used instead such as an angular, convex, or concave type as shown in Figure 3.5. There are different limitations to these overhangs types for each machine upon which they are built. The both EOS M 280 and concept laser M1 machines are capable of producing parts with a minimum value of 45° for angular overhangs, while for concave and convex overhangs, the radius is the limiting value (Caulfield *et al*., 2007, McKown *et al*., 2008). The complete concave or convex overhangs (which complete 90° of a circle) will be lower than the minimum overhang angle either at the tip for concave or the base for convex overhangs; they are too difficult to build at large sizes. Therefore better concave or convex overhangs are produced with a smaller radius, and the design should be oriented to reduce the amount of down-facing surface as much as possible (Matsumoto *et al*., 2002, Atzeni and Salmi, 2015).

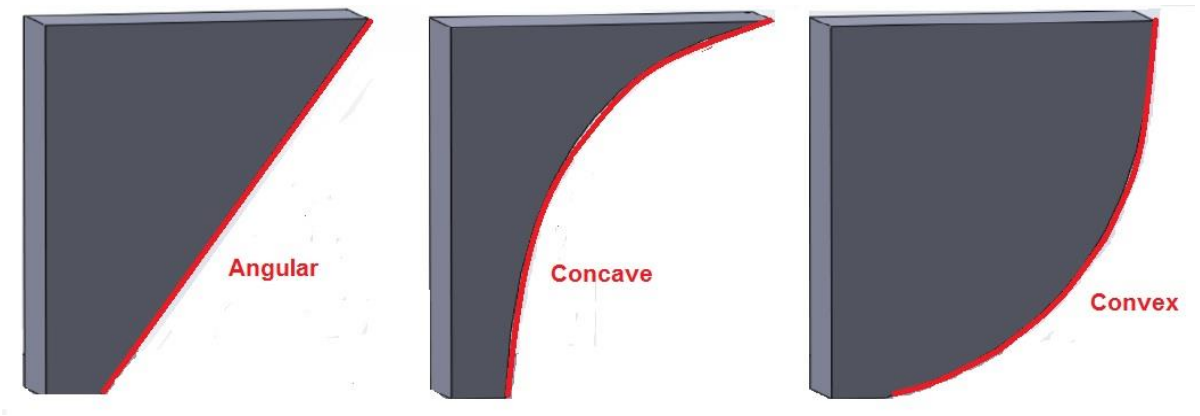

Fig 3.5: Three different types of overhangs; angular, concave and convex. Reproduced from (Caulfield *et al*., 2007)

The surface finish is also likely to be different between build materials. The worst surface finish on a part appears on the down facing surface while the better surface finish on the up facing surface, as shown in Figure 3.3c. The up facing surface is a surface that is parallel to the substrate, which has the highest quality surface finish (Calignano, 2014). On the other hand, angled or curved up facing surfaces (not parallel to the substrate) have a staircase stepping pattern in some cases as shown in Figure 3.6. These steps are related to the layer

thickness since the metal AM is typically produced by a layer upon layer process. Similar steps are created for curved or angled down facing surfaces. Down facing surfaces are also parallel to the substrate and typically overhang, which need support structures beneath them during the build process (Yan *et al*., 2014b).

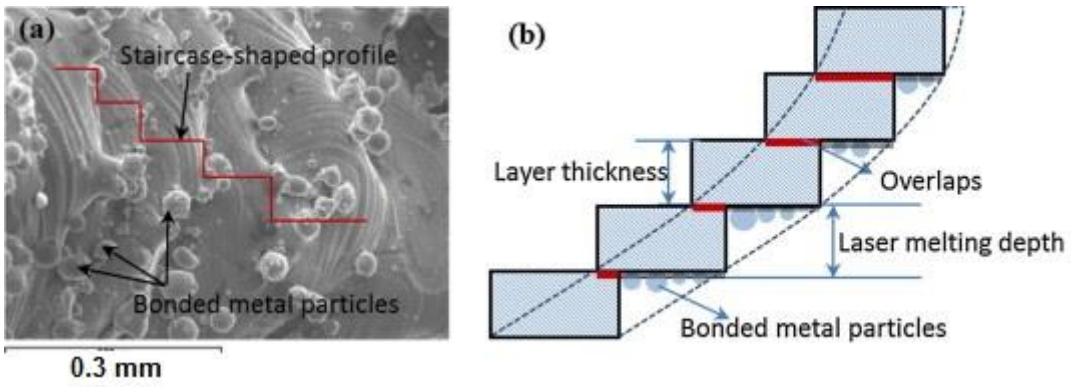

Fig 3.6: Staircase structures formed during metal AM processing; (a) SEM micrograph of the concave strut and (b) a schematic illustration of the staircase in an SLM processing of the circular strut (Yan *et al*., 2014b)

In brief, to take full advantage of AM design possibilities and limitations, design optimization is important to reduce the total number of parts, to ease fabrication, provide lightweight parts with functionality and for topological optimization, etc. For instance, topology optimization firstly minimizes the part into its basic functional requirements (functional surface, load-case). Secondly, the minimum volume of parts produced is designed to sustain the load case. This is usually achieved by using topology optimization tools, which suggest the ability of geometries to sustain the loads with minimum volume. Finally, the optimized volume is redesigned in order to comply with the above design guidelines such as machines allowance, angular, orientations, etc. (Lindemann *et al*., 2015, Douter *et al*., 2017).

3.3 Mechanical properties obtained with metal AM processes

Several studies have published mechanical properties measurements of AM metallic materials. Previous literature also shows that most of the published works have focused on density, compression, tension and hardness, (Wang *et al*., 2015, Zhao *et al*., 2015, Seifi *et al*., 2015, Challis *et al*., 2014, Facchini *et al*., 2010, Fu and Guo, 2014) with a few recent works focussing on fatigue and fracture toughness. This section will focus on the mechanical properties of powder bed fusion (PBF) processed 316L stainless and Ti6Al4V alloys using

different build strategies. The effect of specimens or build orientations on mechanical properties are documented using *x*, *y*, *z* designations according to the ASTM standard (ASTM, 2016), Different literature uses only vertical orientation (parallel to build direction) or horizontal orientation (perpendicular to build direction), while some literature uses two or three letters such as (*xy*, or *xyz*) to provide a complete orientation designation (Brif *et al*., 2015). In this terminology, the first letter designates the axis parallel to the longest overall dimension. The second letter designates the second-longest overall dimension (Lu *et al*., 2015, Markl *et al*., 2015, Mohammadhosseini *et al*., 2013). The third letter designates the third-longest overall dimension of the coupon.

3.3.1 Tensile and hardness

Given the defects, microstructure, and complex crystal orientation, parts manufactured by PBF revealed different mechanical properties than casting or wrought parts. The PBF parts achieved high tensile strength, low ductility, and anisotropy related to build orientation. The tensile properties of the parts processed by PBF are comparable with wrought parts. Table 3.1 reveals previous studies of tensile properties for 316L stainless steel and Ti6Al4V processed by PBF, and include hardness property data where obtained from the he literature. The ultimate tensile strength (UTS), yield strength, and hardness of the PBF processed 316L stainless steel and Ti6Al4V are higher than those of the cast or wrought alloys. The improvement in ultimate tensile strength, yield strength, and hardness is mainly attributed to the grain refinement in the PBF parts (Prashanth *et al*., 2014, Monroy *et al*., 2014). Conversely, ductility is slightly lower than that of the wrought or conventional product parts, and strong anisotropy is found in these two alloys. For strong anisotropy, some literature reported that the residual stress remaining in the parts causes the different mechanical properties associated with the building orientation (Vrancken *et al*., 2014). On the other hand, some literature has reported that the special microstructure of Ti6Al4V causes the anisotropy (Mertens *et al*., 2014, Shifeng *et al*., 2014, Leuders *et al*., 2014, Riemer *et al*., 2014). For instance, Mertens *et al* studied the mechanical anisotropy of two sets of Ti6Al4V specimens oriented perpendicular to each other in the deposition plan. They found the anisotropy of elongation between the *x* and *y* specimens was attributed to their microstructural difference, and to a tilt of the primary β with respect to the building orientation in the *x* samples (Mertens *et al*., 2014). Vilaro *et al* also reported that anisotropy between samples oriented in the deposition plan or along the building direction could be attributed to the very strong

anisotropy of primary β grains that where elongated parallel to the building direction (Vilaro *et al*., 201).

Table 3.1: Tensile and hardness properties of the PBF-processed and wrought 316L stainless and Ti6Al4V

Material	Machine and build direction		Yield strength/MPa	Tensile strength/MPa	Elongation/ %	Vickers Hardness	References
Ti6Al4V	Wrought		828	897	15	342	(Frazier, 2014)
	SLM		990±5	1095±10	8.1±0.3	380	(Aerospace, 2010)
	SLM	***xy***	1093±13	1200±8	6±0.7	360	(Cain *et al*., 2015)
		zx	1120±22	1216	6±0.4	351	
	EOS M280	***zx***	1017±7	1069±7	12±0.5	NA	(Greitemeier *et al*., 2016)
	Concept laser M2	***x***	1070±40	1200±40	5.5±1	NA	(Qiu *et al*., 2013)
		z	1050±40	1180±30	8.5±1.5	NA	
	Renishaw AM250	***xz***	879±5	1143±6	11.8±0.5	NA	(Simonelli *et al*., 2014b)
		zx	967±10	1117±3	8.9±0.4	NA	
		xy	1075±25	1199±25	7.6±0.5	NA	
316L Stainless steel	Wrought		170-290	480-560	40	218	(Yadroitsev I, 2009)
	Realizer M250		465	555	13.5	230	(Yadroitsev I, 2009)
	SLM	***x***	534±6	653±3	16.2±0.8	NA	(Mertens *et al*., 2014)
		y	528±4	659±3	16.6±0.4	NA	
		z	444±20	567±19	8±2.9	NA	
	EOS M270	***x-y***	624	680	31	250	(Wang, 2011)
		z	520	561	19	275	
	SLM	***x***	534±6	653±3	16.2±0.8	256	(Mertens *et al*., 2014, Liu *et al*., 2014)
		y	528±4	659±3	16.6±0.4	256	
		z	444±27	567±19	8±2.9	272	

The summary in Table 3.1 for PBF reveals orientation dependent values for ultimate tensile strength, yield strength, and elongation to failure for all of the as-built conditions. The reported elongations to failure are difficult to compare because of variances in the specimens'

gauge lengths between the different investigations. The orientation dependent variances in the texture, microstructure, and defects contribute to some of these tensile property differences (Simonelli *et al*., 2014b). They however become more important in the high cycle fatigue (HCF), fatigue crack growth (FCG), and fracture toughness studies (more details are given in Section 3.3.2).

From Table 3.1 the PBF of Ti6Al4V exhibited features are presented (machine effects, orientation dependent properties) (Aerospace, 2010, Cain *et al*., 2015, Greitemeier *et al*., 2016, Simonelli *et al*., 2014b). Highly non-equilibrium microstructures (e.g., martensite), along with essential residual stress, which increases the strength and reduces the elongation values, are possible in as-built Ti6Al4V. Also, the tensile specimens manufactured at different orientations exhibited very strong anisotropy, particularly in terms of their elongation. Previous researchers have reported the anisotropy between different build orientation specimens (Mertens *et al*., 2012). They found that mechanical anisotropy could be related to the very strong anisotropy of the primary β grains that were elongated parallel to the build direction (vertical samples) (Vilaro *et al*., 2011). Post-processing such as heat treatment and the use of a HIP can produce more desirable microstructures and reduce the amount of defects, e.g., isolated porosity, lack of fusion, residual stress, but this lead to extra cost that affects the process (Beuth *et al*., 2013, Gockel and Beuth, 2013, Gockel *et al*., 2014).

The average value of the tensile properties at three different orientations exhibited low ductility, see Table 3.1. For instance, Mertens *et al.* report that the *x* and *y* samples exhibited very similar properties, especially in ductility, whereas the *z* samples reveal lower strength and elongations (Mertens *et al*., 2014). Their study concluded that this drop in the mechanical properties in the *z* samples' orientation can be attributed to their high volume of 'lack of melting' defects, and the increased number of pores. Two different types of porosity were observed. Spherical pores associated with the gas bubbles. Larger and more elongated pores were located between melt pools corresponding to two successive layers. These elongated pores remain rare in the *x* and *y* specimens.

3.3.2 Fracture toughness

The majority of fracture toughness values that have been reported in literature are not valid because the thickness requirements for such measurements are not met for PBF of 316L stainless steel and Ti6Al4V (Seifi *et al*., 2015). For instance, equation 3.1 shows the validity

check method after the stress intensity factor K_Q is determined. If the plain strain condition is valid for the test, the fracture toughness is considered as $K_{IC} = K_Q$. This method was exactly used for the conventional material test (Marsavina and Linul, 2010), where a is the crack length, B is the thickness, W is the width (= 2B), and σ_{ys} is the yield strength.

$$a, B, (W - a) \geq 2.5 \left(\frac{K_Q}{\sigma_{ys}}\right)^2 \quad (3.1)$$

Therefore, directly comparing fracture toughness values between different works is difficult because a few of the reported fracture toughness values were valid to meet the plain strain conditions for a valid K_{IC} determination. . Measurements in the majority of studies are for a non-plane strain condition and inflate the values of K_{IC} due to a plain stress condition.

Table 3.2 summarizes some fracture toughness K_{IC} values obtained for 316L stainless steel and Ti6Al4V processed by PBF, again using different orientations *x, y, z* as discussed in Section 3.3.1. The Ti6Al4V processed by SLM reveals fracture toughness value below those of conventionally-manufactured Ti6Al4V (Seifi *et al*., 2015, Seifi *et al*., 2016a, Welsch *et al*., 1993) and exhibits orientation dependent values and strong effects of machine type. The low values of fracture toughness were due to a combination of significant residual stress, nonequilibrium microstructures, and process induced defects (Dahar *et al*., 2015). The highest reported toughness values for Ti6Al4V in Table 3.2 belonged to the EBM Arcam process (96 MPa $m^{1/2}$), while the Realizer MTT250 and EOS M280 exhibit the lowest values of toughness. This may be attributed to the ability of EBM to produce very dense parts and operate in a vacuum environment to minimize oxidation. Moreover, the preheating the powder bed in EBM processes lead to reduce the residual stress of parts (Becker *et al*., 2015, Cain *et al*., 2015, Edwards and Ramulu, 2015). In contrast, the EBM Arcam A2 process (Seifi *et al*., 2015) reveals higher toughness values for Ti6Al4V. A very recent study by Seifi *et al.* reported that texture, microstructure and the number of defects vary with different machines, build orientations, and locations, thus affecting the magnitude of fracture toughness (Seifi *et al*., 2016b). Figure 3.7 reveals the evident defects that are perpendicular to the build direction samples, which contribute to the orientation fracture toughness values. Figure 3.8 shows the large electron backscatter diffraction (EBSD) scan used to produce 3D images of the as-built sample. The microstructural variances along and perpendicular to the build direction contribute to decreasing the fracture toughness values. The defect that is evident perpendicular to the build direction in the sample likely contributes to the orientation

dependent toughness value. Figure 3.8 clearly reveals the crack path which propagated perpendicular to the β grains (Seifi *et al*., 2016b). On the other hand, the fracture toughness of 316L stainless steels manufactured by the PBF process are based on Charpy V-notch impact toughness tests because the available literature on fracture toughness of 316L stainless steel is limited. Based on the limited literature in Table 3.2, it can be seen that the 316L stainless steels manufactured by PBF generally have lower toughness compared to conventionally produced parts (Kruth *et al*., 2010, Tolosa *et al*., 2010). In conclusion, to improve the toughness values, stress relief, heat treatment or HIP post processing could enhance the toughness values by reducing residual stress, by generating preferable microstructures, and by reducing induced process defects (Zhang *et al*., 2009, Qiu *et al*., 2013).

Table 3.2: Fracture toughness of 316L stainless steel and Ti6Al4V manufactured by PBF process, * joules units

Material	**Machine and build direction**	**Fracture toughness (MPa $m^{1/2}$)**	**References**
Ti6Al4V	Annealed	75	(AMS, 2015)
	SLM ***xy***	28±2	(Cain *et al*., 2015)
	xz	23±1	
	zx	16±1	
	SLM ***xy***	66.9±2.6	(Edwards and Ramulu, 2015)
	MTT250 ***xz***	64.8±16.9	
	zy	41.8±1.7	
	EOS ***xy***	37.5±5	(Becker *et al*., 2015)
	M280		
	EBM ***xy***	96.9	(Svensson, 2009a)
	Arcam ***zx***	78.1	
	EBM ***xyz***	68.8	(Seifi *et al*., 2015)
	Arcam ***xzy***	76	
	A2 ***zxy***	79	
316L Stainless steel	Wrought	112-210	(Maloy *et al*., 2001).
	SLM	60*	(Kruth *et al*., 2010)
	SLM	56.8*	(Tolosa *et al*., 2010)

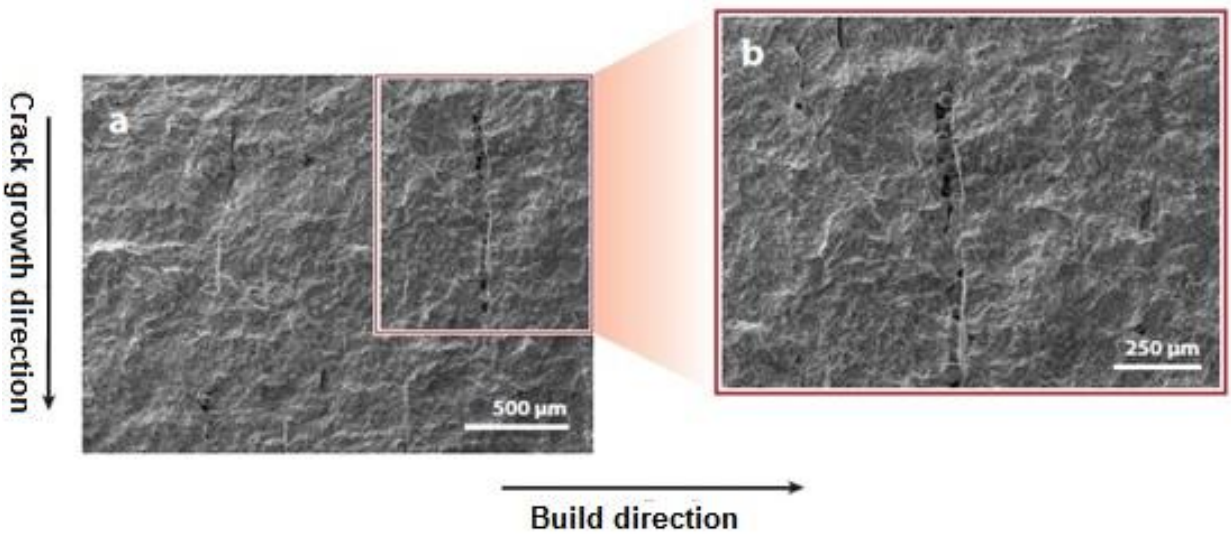

Fig 3.7: Defects evident on the fracture surface of EBM Ti6Al4V toughness specimens tested in *zx* direction; (a) low magnification (b) high magnification images (Seifi *et al*., 2016b)

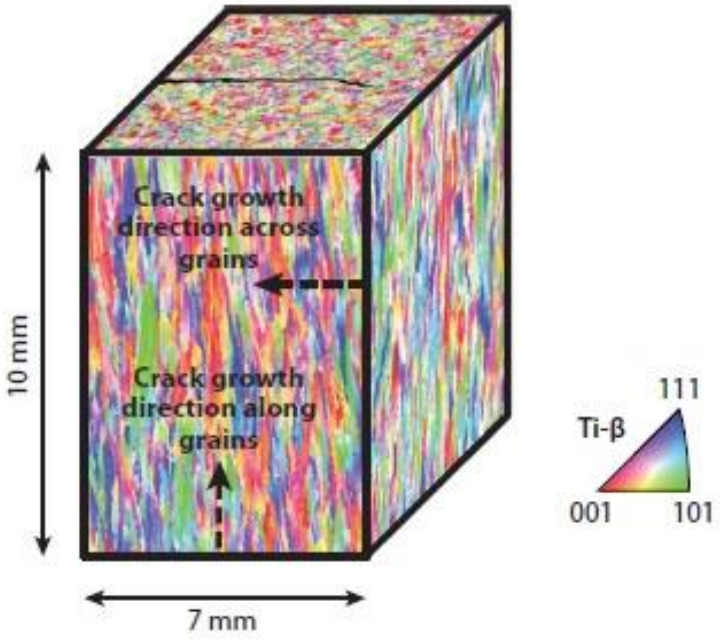

Fig 3.8: Large-area of Electron Backscatter Diffraction EBSD of a PBF (EBM) produced Ti6Al4V specimen showing crack growth direction perpendicular to β grains and build orientation. Taken from reference (Seifi *et al*., 2016b)

3.3.3 High cycle fatigue and fatigue crack growth

As discussed in Section 3.3.2, process-induced defects and microstructural variations can affect the toughness and tensile properties. However, such defects along with residual stress and surface roughness can obscure microstructural effects (Kobryn PA, 2001). They can also dominate the cyclic behavior and degrade the HCF performance by providing potent fatigue initiation sites along with harmful residual stress (Kobryn PA, 2001). A recent review summarized the stress-controlled fatigue behavior of SLM, DMLS, EBM, and DED-processed Ti6Al4V (Lewandowski, 2016). This review also covered the effects of defects (e.g., as a built vs HIP), and surface roughness (e.g., as a built vs machined) in comparison to wrought Ti6Al4V with machined surfaces by Li *et al* (Li *et al*., 2016). Li *et al* reported that Orientation dependent fatigue behavior resulted and the properties were enhanced with polished and machined surfaces. Poor performance in comparison to the data collected in their study was expected to result from defects produced during the process. In addition, Li *et al.* indicate that strong improvements in fatigue data were found by machining the as built surfaces after optimization of the PBF process for Ti6Al4V. The variance in laser process parameters generated either a fine α microstructure or martensitic microstructure. A fine α microstructure resulted in superior fatigue performance compared to martensitic microstructures (Li *et al*., 2016, Fodran E, 2015).

Figure 3.9 displays the fatigue properties of SLM manufactured 316L stainless steel and Ti6Al4V parts. The fatigue properties of SLM processed parts are lower than those of the wrought alloys by 77% (Spierings *et al*., 2013). Furthermore, the fatigue properties in different orientations of the parts yielded anisotropy. The amount of porosity in parts produced was the key contributor to the decreasing fatigue life, and the surface roughness and residual stress needed to be improved for a better fatigue performance. From Figure 3.10 K_t is the theoretical stress concentration factor and R is the ratio of minimum stress and maximum stress through the loading procedure (Spierings *et al*., 2013, Edwards and Ramulu, 2014).

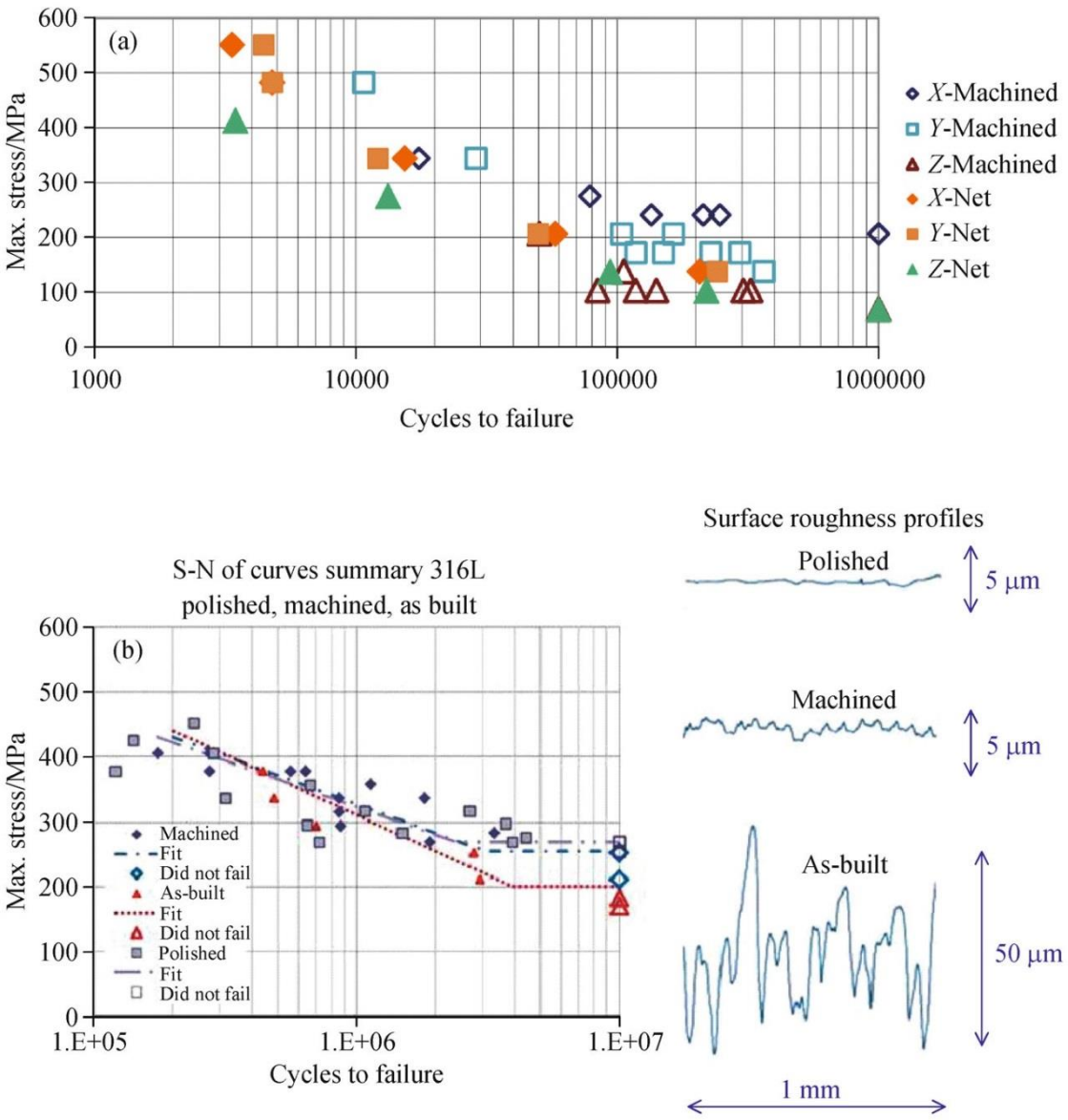

Fig 3.9: Fatigue results for SLM processes (a) max stress vs cycles to failure and S-N curve of Ti6Al4V samples built at different direction with and without post treatment (R= -0.2, K_t= 1.0) (Edwards, 2014), and (b) max stress vs cycles to failure and S-N curve of 316L stainless steel, with and without post treatment (Spierings *et al*., 2013)

3.4 Development of lightweight structures

One of the largest potential areas that can gain from AM is using a lightweight, cellular lattice structure. This is due to their low weight, the use of less material, and a reduction in the energy consumed through manufacturing. The manufacture of these lightweight cellular structures from high strength light alloys offers a high strength internal structure

accompanied by low mass (Chu *et al*., 2008). These lightweight structures can provide good energy absorption and good thermal and acoustic insulation properties (Gibson and Ashby, 1999). Recently, different types of lattice structures have been designed and manufactured using AM as seen in Figure 3.10. These structures had different cell types, sizes, and volume fractions for specific applications, as well as improving the weight to stiffness or strength ratio of the cellular structure (Evans *et al*., 1998, Hussein *et al*., 2013, Yan *et al*., 2012). For instance, Hussein *et al.* studied the mechanical properties of advanced lightweight cellular structures in 316L stainless steel SLM processes and their application as low-density support structures for internal and overhanging geometries. The most suitable cell structure for metal AM is a curved beam or strut, as it has little change in the subsequent layers through the build. This continuous curve in the strut or beam allows the part to be self-supporting through the build (see Figure 3.10) (Hussein *et al*., 2013, Yan *et al*., 2012).

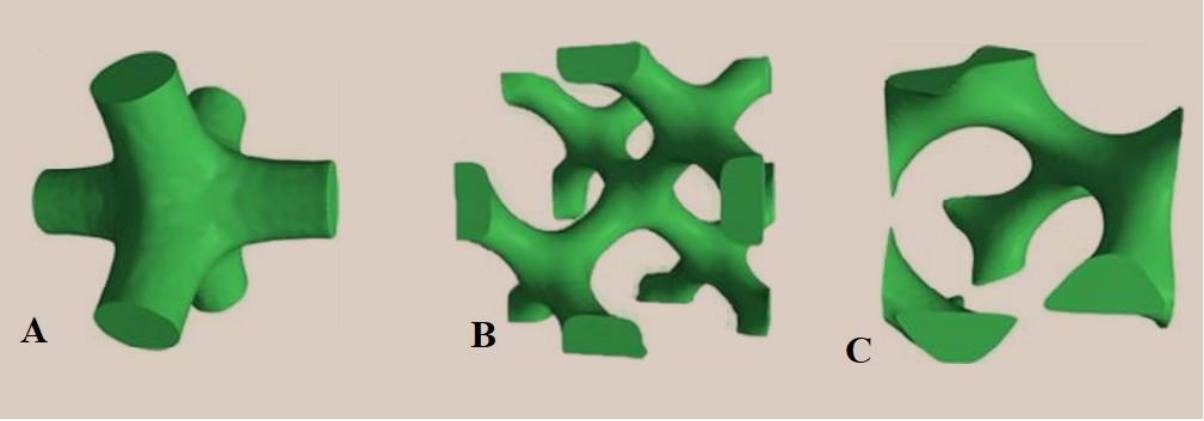

Fig 3.10: Different cell types; (a) Schwarz's Primitive (left), and (b) Diamond (centre) and (c) Schoen's Gyroid (right) (Hussein *et al*., 2013,)

3.4.1 Mechanical Properties of Lightweight Structures

The most common properties measured for lightweight structures are the yield strength, Young modulus, and energy absorption. (Yan *et al*., 2015). It may be very hard to experimentally describe the mechanical behavior of different shapes of cellular structure with a wide range of cell sizes, cell orientations, and volume fractions. A unified mathematical model that can predict the properties of large cell sizes and volume fractions and can characterize them with less experimental testing would be useful to direct the selection of cellular structures for particular applications (Marsavina and Linul, 2010). The Ashby and

Gibson model that has been developed since 1997 is the model that is most commonly used to predict the mechanical behavior of porous structures with reasonable accuracy. This model is based on the cubic unit cell, where the deformation is controlled by the bending of the individual struts within the unit cell. It is also useful when a few experimental data on the density effect are available as this can be used to improve the accuracy of the model. Of course, there are different cell shapes, often more complex than the cubic cell. If they however deform and fail by the same mechanisms, their properties can be understood using dimensional arguments which omit all of the constants arising from the specific cell geometry. The Ashby and Gibson model uses a simple dimensional approaches to characterize the mechanical behavior in terms of the strut dimensions that are related to the relative density of the cell $\frac{\rho*}{\rho_s}$, which is equivalent to the volume fraction (Gibson *et al*., 1997). Where $\rho*$ is the density of strut, and ρ_s is the density of materials.

3.4.1.1 Gibson and Ashby model comparisons with data for mechanical properties of cellular structures

In terms of fracture toughness, a brittle fracture in tension is quite low compared with that in compression. In tension, it fails due to the propagation of the single crack; in compression, the cellular or foam crushes progressively. Brittle cellular foams are linear elastic in tension right up to fracture, so tensile failure can be treated by the techniques of linear elastic fracture mechanics (Gibson *et al*., 1997). Eq 3.2 gives an expression for the fracture toughness of the foam, K_{IC} in terms of the fracture strength of the cell walls, σ_f, the relative density, $\frac{\rho*}{\rho_s}$, and C_8 a constant (= 0.65) .

$$K_{IC} = C_8 \sigma_f \sqrt{\pi l} \left(\frac{\rho*}{\rho_s}\right)^{3/2} \quad (3.2)$$

Brezny and Green also have investigated Young's modulus, strength and fracture toughness, of brittle reticulated vitreous carbon foams and compared them to the theoretical model. The fracture toughness and Young's modulus were found to be independent of the cell size. They concluded that a fracture mechanics approach (Eq 3.2) best describes the tensile properties of brittle cellular materials. The model was found to accurately describe the toughness behavior of these materials once the variation in strut strength with cell size was incorporated into the analysis (Brezny and Green, 1990). Furthermore, Kucherov and Ryvkin have studied the

brittle fracture behavior of perfect open cell Kelvin foams. The result found for mode I agreed with the experimental data and theoretical predictions of Ashby and Gibson (Kucherov and Ryvkin, 2014). In general, various studies have reported the mode I fracture toughness of carbon and aluminum foams experimentally using SENB samples. These tests were similar to ASTM E 399-90 plain strain fracture toughness experiments. The results of these tests were compared with the finite element and Ashby and Gibson micromechanics model to study the variation of fracture toughness as a function of the solidity of the foam. The studies found that a micromechanics simulation can be a powerful tool in predicting the fracture behavior and crack propagation in the foams and in other cellular solids (Olurin *et al*., 2000, Marsavina and Linul, 2010, Choi and Sankar, 2003).

On the other hand, Yan *et al.* have used the Gibson and Ashby model to estimate the compression stiffness of a different relative density of DMLS produced AlSi10Mg gyroid cellular lattice structure. They found that the model fitted perfectly with the experimental data (Yan *et al*., 2015). Different studies by Yan *et al.* and Hussein *et al.* used the Gibson and Ashby model to estimate the compressive modulus and strength of cellular lattice structure of 616L. It was found that there are small differences in theoretical and experimentally tested values, and they attributed this to the residual stress inherent to the SLM manufactured 316L stainless steel parts and the roughness of the strut surface (see Figure 3.11) (Hussein *et al*., 2013,Yan *et al*., 2014b)

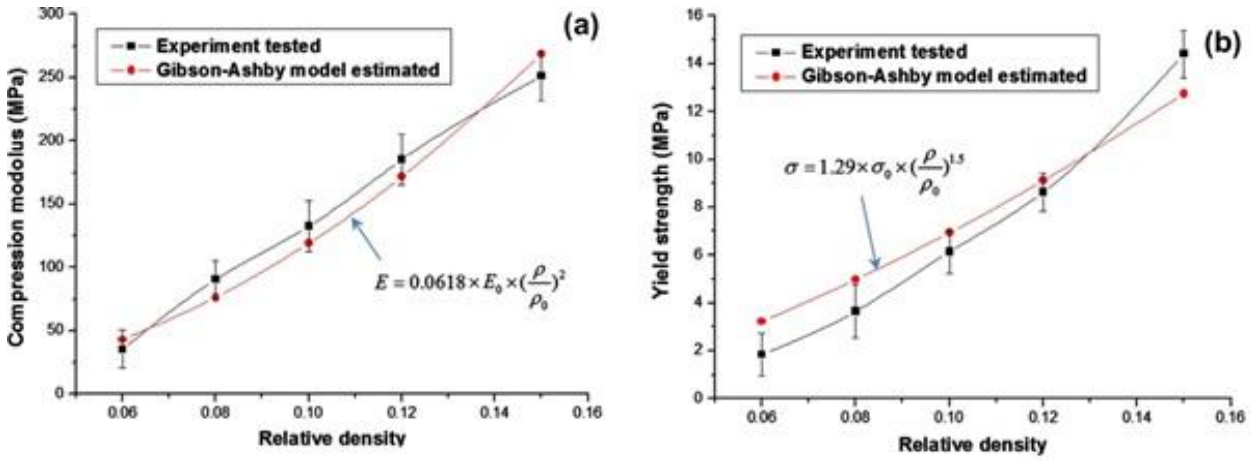

Fig 3.11: Comparison of experimentally tested and Gibson and Ashby model estimated results: (a) compressive modulus, and (b) compressive strength as a function of the relative density (Yan *et al*., 2014b)

3.5 Summary

Additive manufacturing delivers many benefits if compared to conventional production. Some of these advantages have been stated in Section 1.2. AM has great potential for manufacturing metal parts with complicated geometries, as well as being associated with rapid solidification phenomena, through the short time period of laser-material interaction and the quick movement of the laser after solidification. Current research into the SLM and DMLS processes have focused on either titanium or stainless steel alloys since these metal powders are relatively easy to use. Some work has been done on these metals and their use in the SLM/DMLS process. This has been done in order to investigate the effect of parameter processes, the environment and post-processing treatments on the parts produced. In addition, the influence of adding alloying elements and their composition on consolidation is one of the major problems that became evident during processing. These major problems are the limited surface quality and the residual porosity in SLM/DMLS parts which may be undesirable for some applications where fatigue resistance and high strength are essential.

From previous literature, some aspects of the modeling of cellular materials' methods were thus discussed and were compared to the experimental testing of foams' fracture toughness. This means that methods and procedures are available for the estimation of the mechanical behavior, especially fracture toughness of AM metal cellular structures which have not been reported previously. In additional, a limited information regarding the FCG and the fracture toughness of 316L stainless steel manufactured by AM. This information is based on Charpy V-notch impact toughness test and need to address in more details. The mechanical properties values of the previous literature on the AM parts produced need to be improved in comparison to conventional process parts produced.

3.6 Definition and Aims of the research

This research investigates the manufacturability and mechanical properties of high strength low alloy metals produced using AM. The study includes the microstructure and mechanical properties analysis of bulk and lightweight cellular structures made of Ti6Al4V and 316L stainless steel in different build directions. This study wills contribute to new knowledge on mechanical properties, especially on the fracture toughness and FCG properties of 316L stainless steel in different build directions. Additionally, the fracture toughness and tensile strength of lightweight cellular structured 316L stainless steel in different building directions and with different cell sizes will be investigated. These mechanical properties will help

designers to choose the appropriate build direction, cell size and volume fraction to suit the requirements of aerospace applications. Further this study will contribute to an understanding of the mechanical behaviour, especially in regard to the fracture toughness of cellular structures with different cell sizes and different build orientations. The fracture toughness and tensile properties of cellular structure made by SLM in different build directions will be compared with Ashby and Gibson micromechanics models. This comparison will help the researchers to use this model to predict the fracture toughness and tensile strength properties of cellular structure made by AM without need to experimental tests, and give a confidence to the designer to use and tailor their properties to specific applications.

Experimental Studies and Application

Chapter 4: Materials and Experimental Methods

This chapter describes the equipment, methods and procedures used during the experiments carried out in this research. The material powders and experimental procedures used to produce the samples by SLM and DMLS process as discussed in Section 4.1, 4.2 and 4.3, respectively. Section 4.4 illustrates the post-processing steps used for the bulk and cellular structures parts such as wire-EDM cutting, Air/bead blasting operations, and specimen's preparation. Section 4.5 also describes the setup procedures for the equipment and the tests which were applied to measure and the products' performance and the microstructure examination, which presented in Section 4.5. The conclusion is presented at the end of this chapter (Section 4.6).

4.1 Powders material

4.1.1 Ti6Al4V

The different alloys of titanium commonly available, their nomenclature and compositions are set out in Chapter 2 (Table 2.1). Titanium (Ti6Al4V) was used in this study. The decision to use Ti6Al4V alloy in this PhD project was based on the material properties that make it suitable for aerospace applications, such as withstanding high temperatures and a high strength to weight ratio (Polmear, 2006a). In addition to this, there is more research need to be done that considers how to improve the performance and mechanical properties of the material. Since the titanium powders can be manufactured by AM technology, so the AM technique was found to be suitable for producing solid parts by laser melting or sintering, this material was also deemed appropriate to this project. However, the application of titanium could be increased by an improvement in the production and manufacturing of the material, to achieve the aerospace application standards and requirements. Therefore, an additional investigation of its behaviour and properties is required.

The powdered Ti6Al4V was supplied by the AM research group in Chongqing University, China, who collaborate with the University of Exeter. They also supplied the composition data in Table 4.1, and the images in Figure 4.1 to confirm particle composition and size distributions. The diameter of the titanium powder was measured across approximatelty 150 particles in the SEM, given an average particle size of 28 μm, and as seen in Figure 4.1. The composition of the Ti6Al4V as supplied falls into the usual range (see Table 4.1).

Table 4.1: Chemical composition of Titanium (Ti6Al4V) powder (via Chongqing University)

Ti-6Al-4V	Ti	C	Fe	N	Al	O	V	H	Y	Other
Weight %	**balance**	**0.08**	**0.03**	**0.05**	**5.5-6.75**	**0.20**	**3.5-4.5**	**0.015**	**0.005**	**0.40**

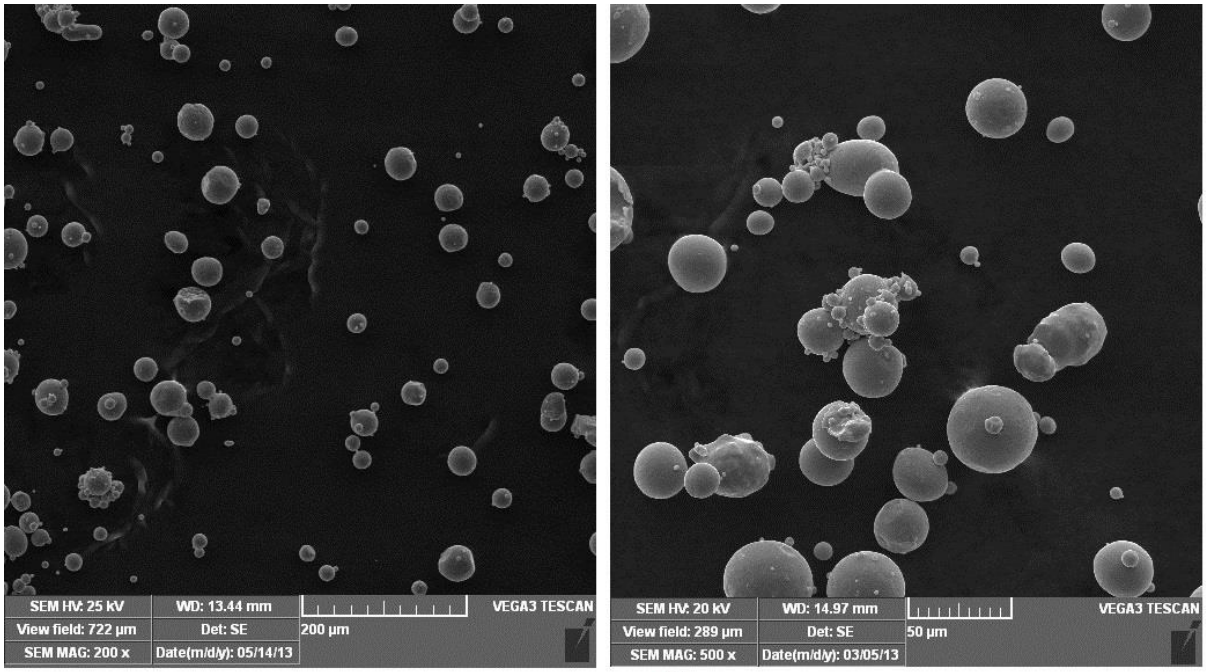

(a) (b)

Fig 4.1: Typical SEM images of Ti6Al4V powder, (a) scale bar is 200 μm, and (b) scale bar is 50 μm (courtesy of Chongqing University, China)

4.1.2 316L Stainless Steel

Recently, stainless steels have been one of the several common materials used in AM processes. This steel is also used in aerospace applications (Jerrard *et al.*, 2009, Eisen *et al.*, 1998). The decision to use stainless steel in this research because is the most material used in SLM technology recently due to its cost effectiveness, safety, and ease of processing. These advantages are key factors to investigate this material and improve their properties. Some previous research has been done on this material (see Chapter 3). On the other hand, there is still a lack of detail about the toughness properties of parts made by SLM. Some research questions also need to be addressed further, such as; new capabilities to understand

the consolidation mechanisms, the microstructures of parts produced by SLM in different building directions and their effects on their fatigue life and toughness properties. The 316L stainless steel used for this research was supplied in the form of powder (Concept Laser Ltd, German). Before the SEM was used to analyse the particle size distribution and geometry, as seen in Figure. 4.2. The particle size of the 316L stainless steel powder was analysed and measured across approximatelty 150 particles in the SEM, giving an average particle size of 25 μm. The elemental composition of the powder reported in Table 4.2 in wt.% was confirmed by Concept Laser Ltd. The powder showed no signs of agglomeration based on the SEM images (see Figure 4.2) which would prevent them from being easily deposited during the experiments.

Table 4.2: Chemical composition of 316L Stainless Steel powder (confirmed by Concept Laser Ltd, Germany)

Element	Fe	Cr	Ni	Mo	Mn	Si	P	C	S
Max	**Balance**	**18.5**	**13.0**	**2.5**	**2.0**	**1.0**	**0.045**	**0.030**	**0.030**
Typical		**16.5**	**10.0**	**2.0**	**0**	**0**	**0**	**0**	**0**

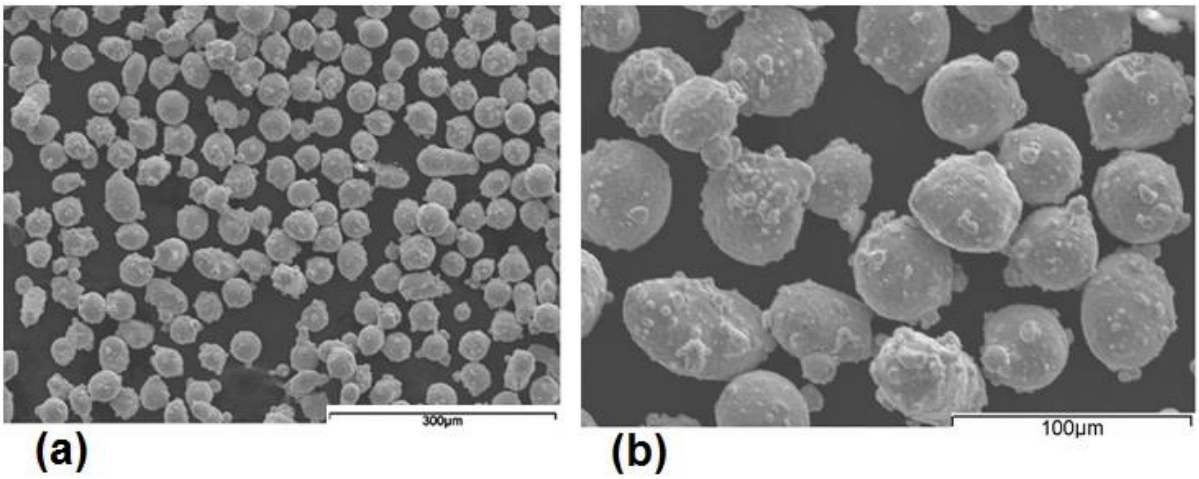

Fig 4.2: Typical SEM micrographs of 316L stainless steel powder, (a) at low magnification, and (b) high magnification

4.2 CAD software, SolidWorks, and SimpleWare

The standard manufacturing technique starts by generating a CAD model. This can be prepared by any method, so long as the file can be read or translated by the machine used. Presently, the de facto file format for AM is the STL file. STL, originally an abbreviation of 'stereolithography', is now treated as a backronym standing for 'standard triangle layout' (or an equivalent nomenclature), which is converting a CAD file into an STL translates it into an approximated surface model consisting of linked triangles. After created the CAD model, then processed by software running the AM machine. This involves digitally slicing the model into discrete layers that typically different from 20 to 100 μm (Yan and Gu, 1996); each layer then translated into machine code.

In this study, SolidWorks and SimpleWare software were used in this research to design and generate the samples. SolidWorks was utilised for the bulk materials samples, and SimpleWare was used to generate the lightweight cellular structure samples. These software packages generate high-quality 3D models from image data and are suitable for a range of design uses. The resulting models can then be exported as STL files to a 3D printing machine as mentioned above. These software packages have been used extensively for applications for different materials. All the bulk samples were designed in various *xz*, *yx* and *zx* directions in which the samples that were designed in the *zx* direction are also described as being "parallel" to the build direction. The ones in the *xz* and *yx* direction are "perpendicular", according to the ASTM for samples designation at different build direction (Brif *et al*., 2015). The lightweight samples were designed in two directions; i) parallel to the build direction and perpendicular to the build direction.

4.3 Machine setup and processing apparatus

4.3.1 EOS M280 –DMLS Machine

The SLM Ti6Al4V specimens were manufactured using a commercial DMLS machine (EOS M280, GmbH Electrooptical Systems Ltd), which melts the fine metal powder and builds up the parts layer-by-layer, as shown in Figure 4.3. More details about DMLS process were given in Section 1.4. The parameters used in these machines are specified in Chapter 5, section 5.2.

Figure 4.4a, shows a close-up view of the open processing chamber, with a build chamber area of 250 ×250 mm^2.Parts can be built to a height of 325 mm, and the EOS M 280 has a

scan speed of up to 7.0 m s^{-1}. The visual practice of the DMLS process in the act of the laser melting of samples can be seen in Figure 4.4.b.

Fig 4.3: The DMLS machine at Chongqing University

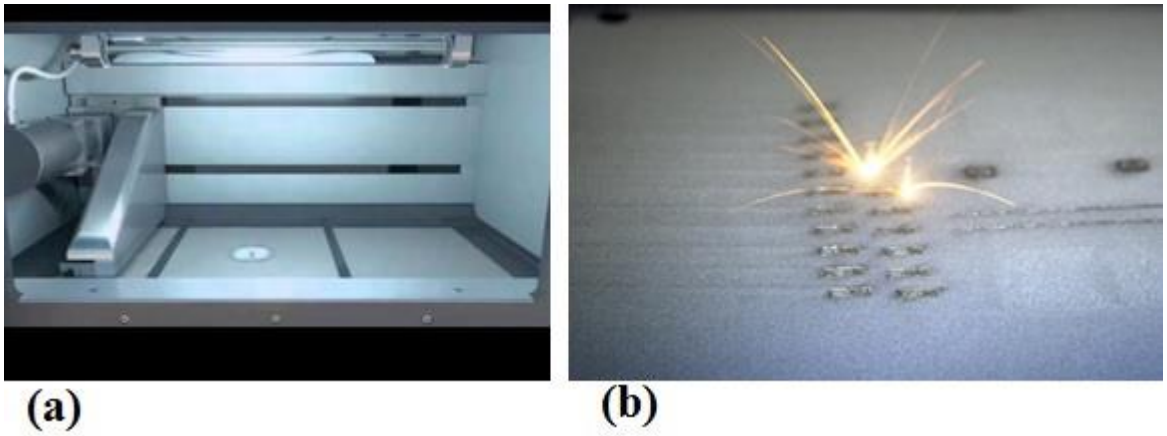

Fig 4.4: (a): Close up view of the build chamber. (b) An example of the DMLS process in the act of laser melting the samples.

Laser

The laser in the EOS M280 is a fibre laser, operating continuously at 1060-1100 nm wavelengths; pulsed modes are not available. The laser emits a laser beam which is guided by an optical fibre, a beam expander optic, the scanner mirrors and a focusing objective. All optical surfaces have special coatings to guarantee effective beam guidance. The nominal

powers are from 200 W to 400 W. The laser beam's diameter at the building area is variable from 100 μm to 500 μm, the size being manually selected depending on the material being used.

Laser scanning

A scanner is a high-speed unit comprising a precision galvanometer scanner with temperature compensation, actively cooled ultra-high reflection mirrors, integrated servo and interface electronics, digital data transfer from the system's control computer and digital signal processing. It also incorporates an integrated home-in sensor, which detects and corrects any scanner drift at regular intervals. The high positional stability of the laser beam is thereby maintained, even under varying environmental conditions or with high thermal loading due to long exposure times and large building jobs. The EOS M280 DMLS machine has a scanning strategy for separate layers that begins at the front left corner of the part and builds vertically towards the back. The routine of scan alternates, for instance; the first layer is in the x-direction and then the second layer in the y direction, and so on. The ZIGZAG scanning strategy was set up and carried out for all of the specimens to obtain parts with good metallurgical bonding, microstructure and to improve the density (Chen et al., 2017, Qi et al., 2007). Figure 4.5 shows the schematic pattern of the scanning strategy for single and additive layers. Fill line offset and scan line offset are boundary scanning parameters to improve the precision and quality of the borders. Scan line offset was used to compensate where partial milling had taken place at the boundary. Fill line offset was used to correct sample dimensions and improve the quality.

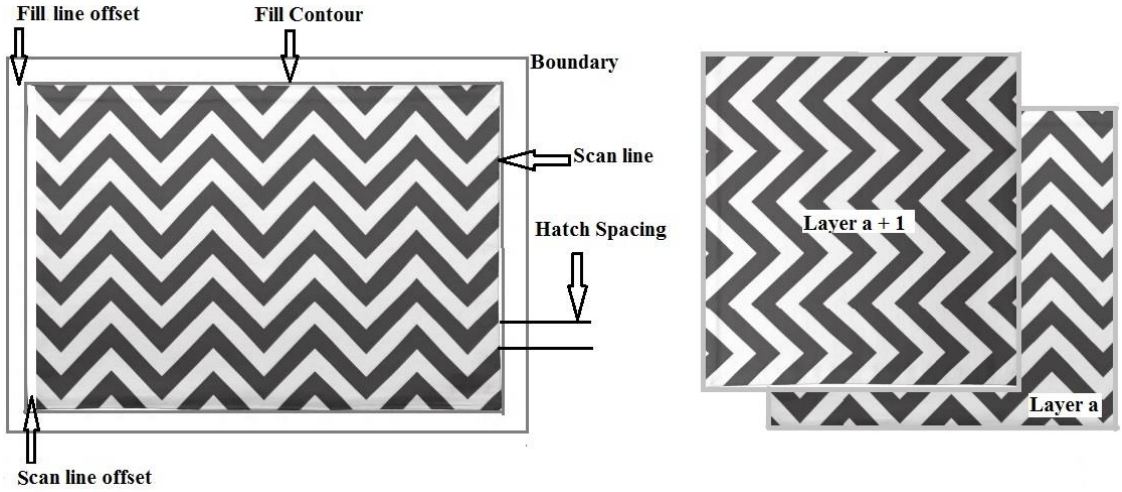

Fig 4.5: a schematic of a typical scanning strategy

4.3.2 M1 Cusing Machine

The samples for investigation were fabricated using a commercial SLM machine (M1 Cusing Metal laser melting machine available at Concept Laser – ES Technology Ltd.) see Figure 4.6. The M1 Cusing machine has a build area of 250 × 250 mm^2 and can build to a height of 250 mm.

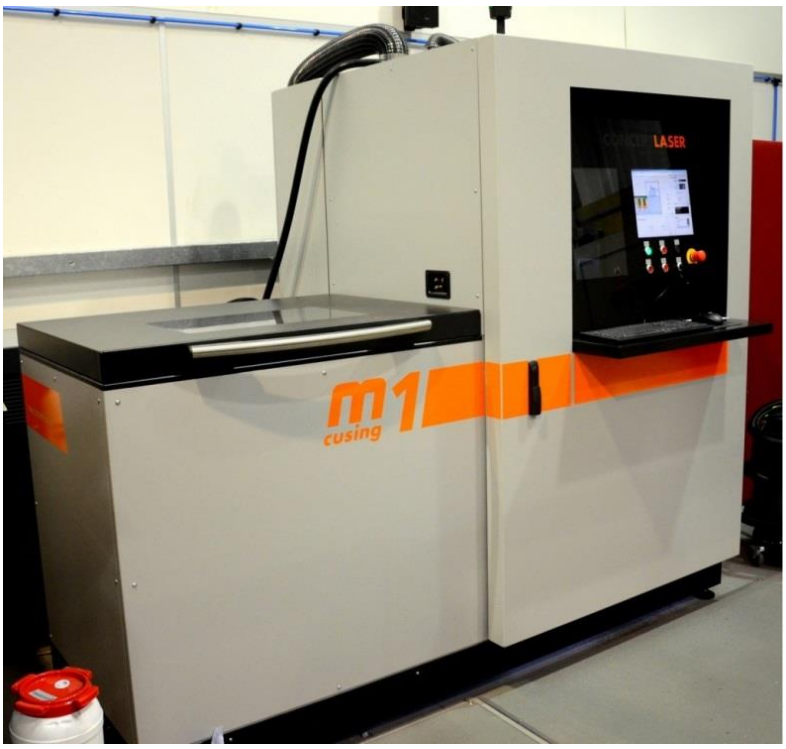

Fig 4.6: The M1 Cusing machine at ES Technology Ltd

Laser

The laser in the M1 CUSING machine is a fibre optic system, operating continuously at a wavelength of 1060 nm; pulsed modes are not available. The nominal power is 200 W, the focusing diameter is in the range 50 – 200 μm and the sizes are manually selected depending on the materials that are being used. The process parameters used for this machine are specified in Chapters 6 to 9, Sections 6.2, 7.2, 8.2, and 9.2.

Laser scanning

The M1 CUSING machine has a high-speed scanner unit comprising a precision galvanometer scanner with temperature compensation, actively cooled ultra-high reflection mirrors, integrated servo and interface electronics, digital data transfer from the system's control computer and digital signal processing. The exposure area is 250 mm × 250 mm2 and an exposure speed up to 7000 mm s-1. The M1 CUSING machine has a scanning strategy for separate layers (scanned with island strategy with 90° rotation) that begins in the front left

corner of the part and is built vertically towards the back. The routine of scanning in an alternating fashion is completed, for instance by forming the first layer in the y-direction and then the second layer in the x-direction, and so on. These scanning strategies were carried out for all specimens. The schematic pattern of the scanning strategy for single and additive layers can be seen in Figure 4.7. This strategy is better for the M1 Cusing system than the zigzag that was used in DMLS system, Section 4.3.1 because of less rippling of molten material which effected the surface roughness of the parts produced. Both strategies were used to reduce the anisotropy.

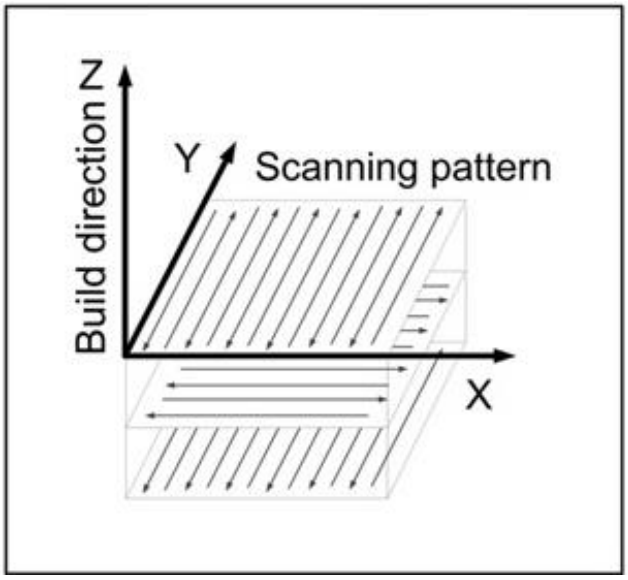

Fig 4.7: Schematic of the scanning strategy using in the M1 Cusing Machine

Inert environment control

The M1 CUSING machine uses Nitrogen gas inside the chamber, which is maintained by a simple inlet valve which can monitor the rate of gas flow, while the EOS M280 DMLS machine uses Argon gas, which is pumped into the processing chamber of the DMLS machine to reduce the air pressure. In both machines, the pressure (and the oxygen) is read by an internal sensor plus an analogue gauge that is attached to the outside of the build chamber. The internal gas was also constantly filtered to remove volatile powder particles and vaporised material. It should be noted that the oxygen level was kept below 0.8% in all circumstances.

4.4 Post Processing

4.4.1 Wire-Electric Discharge Machine (Wire – EDM)

A Wire-Electric Discharge Machine (EDM) was used to remove the samples from the base plate and the support structure. In this, a thin strand metal wire, usually brass is fed through the workpiece which is either submerged in a tank of electric fluid or electricity is supplied through the nozzle. The Wire-EDM is typically fed from a spool and is held between the lower and upper diamond guides. Through the inherent properties of the process, the wire-EDM can easily machine parts with complex shapes. The phenomenon of erosion is the same in the wire-EDM process, however; and the tool electrode takes the form of wire, typically 100 to 300 μm in diameter. Wire-EDM is used when low residual stress is desired, due to it not requiring the force needed to remove material. The dimensional accuracy of the samples will not be affected if machining takes place after heat treatment.

4.4.2 Specimens preparation

Specimen preparation comprises different steps. The first step in the sample preparation process is grinding by a number of sand papers to remove the rough surface after cutting. The second stage is polishing with very smooth cloths and different grades of liquid to polish from 9 to 1 μm. The liquid polishes help to absorb the friction heat and dilute the lapping residue of the laser during the work. Metallographic etching was carried out for the 316L samples in a solution containing 122 ml alcohol, 122 ml hydrochloric acid, and 6 ml nitric acid for 5 to 10 second. Rinsed thoroughly in clean water and blown dry with clean compressed air (etchant procedure repeated two -three times). The Ti6Al4V specimens were etched in a solution containing 2 ml hydrofluoric acid, 6 ml nitric acid and 96 ml distilled water for 1-2 minutes. Rinsed thoroughly in clean water and blown dry with clean compressed air (etchant procedure repeated two times). The etched preparation was used at room temperature according to a standard method (ASM Handbook) to characterise the surface morphology and microstructural features of the specimens (Vander *et al*., 2004, Gammon *et al.,* 2004).

4.5 Experimental Measurements and Characterisation

4.5.1 Density and porosity measurements

The densities of the samples were calculated by determining their volume and mass (mass/volume). Also, Archimedes' Principle was used to determine the density of the samples. Averages of five samples for each build direction were measured by both methods. After careful metallographic preparations were made, such as polishing, micro CT scan images were used and analysed to determine the area fraction of porosity. This can be equated to the volume fraction of porosity and equal to the porosity calculated by the actual measured density (ASM, 1998).

4.5.2 Surface roughness measurements

A Talyscan-150 (Taylor Hobson Precision Ltd.) was used to measure the surface roughness, with a non-contact laser probe to measure any vertical displacement. The roughness was tested in both 2D and 3D modes. The 2D roughness parameter of R_a was reported from an average of five samples for each build direction. At least ten tests for each sample in different positions (5 tests in perpendicular and 5 tests in parallel surface to build direction) were obtained. On the other hand, the 3D measurements were carried out on an area of 16 mm × 5 mm^2, resulting in a 3D profile and surface roughness parameter of R_a. This parameter is, in fact, the arithmetic average of the 3D and 2D roughness profiles, respectively, demonstrating the magnitude of surface roughness. Figure 4.8 shows a picture of the Talyscan-150 machine.

Fig 4.8: The Talyscan-150 surface roughness measurement equipment (at Exeter University).

4.5.3 Hardness

Hardness testing was carried out by using a Vickers' Hardness test (5 kg load was applied to 15 s). This was applied after well metallographic polishing had taken place, as mentioned in Section 4.4.2. The test was achieved by measuring the size of the indent effect on the sample and then converting it to Vickers Hardness (VH) using conversion tables recommended by the Exeter University Laboratory. The conversion table was based on Equation 4.1, where F is the load in Kg, d is the arithmetic mean of two diagonals, $d1$ and $d2$ are in mm, and 1.845 is a constant value depending on the angle between the pyramid's opposite faces, which is 136º. Mean values were determined from at least five hardness readings for each sample, and at least five samples were tested in each build direction.

$$HV = 1.845\frac{F}{d^2} \qquad (4.1)$$

4.5.4 Tensile, fracture toughness, and fatigue crack growth testing

Tensile and fracture toughness testing were carried out using an Instron Instruments Mechanical Testing Machine (3300 Dual column universal testing systems) at the University

of Exeter, to deform the specimens in tension and three point bending (Figure 4.10a). The tensile specimens were prepared and tested at a crosshead speed of 0.5 mm min^{-1} according to the ASTM-E8 standard (ASTM, 2009). The load cells used were 20 kN and 50 kN for 316L stainless steel and Ti6Al4V, respectively. Specimens was prepared and tested at crosshead speeds of 0.5 mm min^{-1} according to ASTM E399 Standard (ASTM, 2003) for both stainless steel and Ti6Al4V with the same load cells used for each tensile test.

The FCG testing was carried out using an Instron hydraulic machine (8874 25KN/100 NM-Servo-hydraulic system) at the University of Exeter, see Figure 4.10 b). This was carried to estimate the lifetime of a component produced by 3D printing, as the presence of a crack can significantly reduce the lifetime of both parts and structures. This test was performed according to ASTM E647. All the samples were designed as compact tension specimens (CT), see Figure 4.9, which are single edge notch samples and were subjected to cyclical loading and crack growth until a critical crack size is reached and causes a fracture (ASTM E647, 2016). All FCG tests were carried out at a frequency of 10 Hz, minimum load 0.6 kN, maximum load six kN, for a load cycle, and a stress intensity factor ratio of R = 0.1.

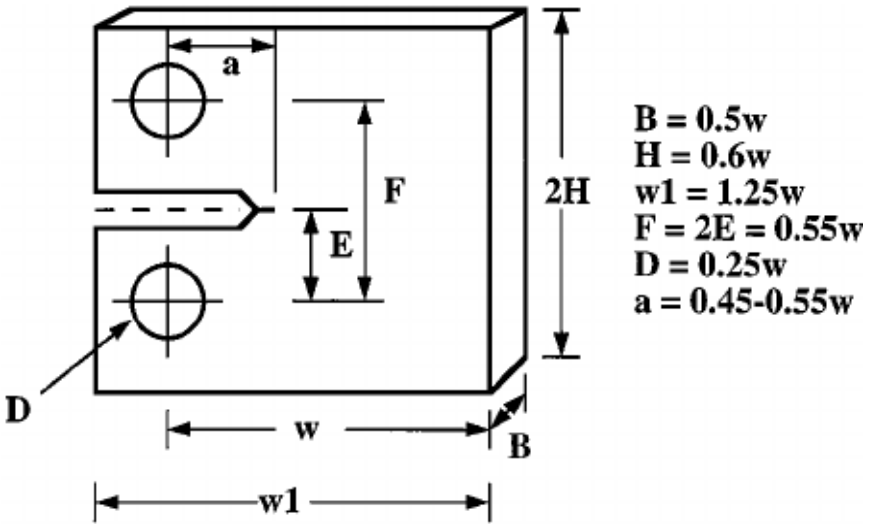

Fig 4.9: Schematic of a compact tension sample for a pre-crack fatigue test (taken from ASTM E647, 2016)

(a) (b)

Fig 4.10: The tensile testing equipment at Exeter University; (a) Instron machine for tensile testing, and (3300 Dual column universal testing systems) (b) Instron Hydraulic machine for cyclical loading (8874 25KN/100 NM- Servo-hydraulic system)

4.5.5 Metallographic Analysis

The microstructure and macrostructure analyses were carried out on the specimens by using both SEM and OM. A Hitachi S-3200 SEM, which is equipped with energy dispersive spectrometry (EDS), was utilised for the microstructural analysis. Sample cross-sections were polished and viewed both before and after the chemical etching as mentioned in Section 4.4.2. All the samples are conductive, and no coating was required before they were used except for the proper cleaning process. The optical investigation used a Zeiss Axioplan 2 OM to investigate the microstructures of the samples.

4.5.6 Micro-CT scanning

A micro-CT scanning system (Bench top CT 160Xi, x-Tek) was used to reveal the porosity formation in three dimensions of the manufactured parts. This equipment was used to calculate the samples' relative densities by the CT-scanned images following the procedure: (stet up machine, insert sample and filter, x ray on, set projection + frames, CT scan takes 2D projection/images, sample rotates 360º, repeat process then the 2D images are converted into a 3D structure automatically, checking the quality, and select area of interest). The VG Studio

MAX 2.1 software was used to reconstruct three-dimensional models of the samples using two-dimensional slice image data that was obtained from the micro-CT scans. By analysis of the three-dimensional models, the amount of internal porosity could be identified (select the whole/ 3D section, use adaptive rectangle, create a new region of interest, extract ROI, analysis and coloured bar chart to get % of material or pores in sample). All the bulk samples were of 4×4×3 mm, which were cut from a larger sample, the cellular structure samples were scanned as built. The Figure 4.11, shows the micro-CT scanner used in this research.

Fig 4.11: The micro-CT scanner at the University of Exeter.

4.6 Summary

Experiments were carried out to gain better understanding of the main factors which affect the DMLS and SLM processes. This understanding helps to optimise the DMLS and SLM processes and produce the final part's quality. The optical scanning system was examined to find the relationship between the input laser energy density and the manufactured part's physical and mechanical properties. Then Building strategies were studied to gain the knowledge of their influence on the melting process. After studying the SLM and DMLS process parameters, an experimental procedure was carried out to investigate the materials properties, especially density. The microstructure of the built parts was examined experimentally by OM, SEM and micro CT scan. Results found in this testing process gave better understanding of the laser melting process, and also were used to validate the

prediction from the mechanical properties tests. Finally, the mechanical properties experiments enable to understand the important factors which affect the SLM and DMLS process and quality of final parts at different build direction. These are the main which are discussed in more detail in chapters 5 – 10.

Chapter 5: The Effect of Different Building Orientation on the Consolidation, Tensile and Fracture Toughness Properties of Direct Metal Laser Sintering Ti6Al4V

Chapter 5 presents experimental work on DMLS of Ti6Al4V built at different directions. The work demonstrates the importance of the processing parameters in obtaining fully dense parts in Ti6Al4V by DMLS, see Section 5.2. It also investigated the effect of different build direction on density, microstructure, hardness, surface roughness, tensile strength and fracture toughness. The result and discussion of these investigations are addressed in Section 5.3, and the main findings of this study are addressed in Section 5.4. After the Ti6Al4V samples have been fabricated, the EOS M280 machine had a sudden failure. This means an alternative production process was sought for the specimens. It was found that these materials were difficult to build with alternative companies due to the high cost of the Ti6Al4V alloy. So, the specimens tested in this Chapter will be just the *xz*, *yx*, *zx* samples, for tensile and fracture toughness, as shown in Figures 5.3a and 5.3b. However, for the 316L stainless steel, all the bulk samples (*xz*, *yx*, and *zx* orientations) and cellular structure samples (vertical and horizontal orientation) were available to test as designed in the research proposal (chapters 6 to 9), due to the availability of a suitable machine for this material. For more details see section 5.2.

5.1 Introduction

Titanium alloys have been commonly used for aerospace applications due to their excellent properties, such as their resistance to high temperatures and their high strength to weight ratios. Ti6Al4V has been considered to be the most suitable of the aerospace titanium alloys, when it was used in the manufacture of airframe structural components and skins, aircraft hydraulic systems, and air engine components. A conventional processing method, casting, has been used to fabricate Ti6Al4V aerospace components. However, casting technology needs the preparation of a complex mould and is associated with risks. These risks include oxidisation, decomposition, and grain growth, which are caused by the long high temperature holding time. Furthermore, the use of this alloy faces competition from aluminium alloys on

the basis of cost. An increased adoption of titanium alloys relies on new improved and advanced material production and manufacturing technologies (Polmear, 2006b).

Recently, Direct Laser Melting Sintering (DMLS), as one of AM technique, has been extensively researched in order to consolidate titanium powder materials directly and to produce lightweight components for aerospace applications (Rehme and Emmelmann, 2010). However, there are some remaining challenges, especially regarding mechanical properties. This has an impact on the change of build direction and the relation between the microstructures produced in different manufacturing processes and their effect on the tensile, hardness and fracture toughness properties. During DMLS consolidation and melting, the edges of the parts produced are typically thicker than those in the middle; however, there is no report of this defect and its relationship with the consolidation of the quality and mechanical properties of the parts produced. As declared, DMLS may be associated with issues such as porosity, balling, and the delamination of the layers (Kruth *et al*., 2007). It is necessary to investigate the consolidation between the particles and the resulting porosity and balling phenomena, as well as their effects on the quality and mechanical properties. To meet the requirements of aerospace applications, further investigations of the properties and behaviours of the titanium material made by DMLS need to be undertaken. There is also little research on the fracture toughness and fatigue property of titanium parts made by DMLS (for more details, see Sections 3.4.2 and 3.4.3). The effect of different build directions on the fracture toughness properties of Ti6Al4V alloys made by DMLS, and especially its relationship to the microstructure has been little studied. There are a limited number of studies in this area, which are addressed in Section 3.4.2.

This chapter presents a research study that is set up to understand the working principle of the DMLS machine and to investigate the process's capabilities, the resultant shape of the parts and their properties. The work demonstrates the importance of the processing parameters in obtaining fully dense parts in Ti6Al4V by DMLS. Mechanical tests were carried out to evaluate the effect of consolidation on the mechanical performance of the DMLS specimens made with three different build directions (see Sections 5.3.3 and 5.3.4). Material analysis was carried out to investigate the microstructure of the DMLS specimens and their effects on the fracture properties will be explained in Sections 5.31, 5.32, and 5.3.4.

5.2 Experimental Procedures

5.2.1 Material design and fabrication

The Ti6Al4V powder that was used in this research has a spherical shape, and the distribution size was between 10 and 45 μm, with an average particle size of 28 μm ± 7 μm (see chapter 4 Figure 4.1). The Ti6Al4V that was received was supplied in the form of a powder, and all the samples were produced by a DMLS machine (EOSINT 280) at the University of Chongqing, China. This machine is equipped with a Yb-Fibre laser, and has a maximum power of 400 W in continuous laser mode, with a spot size of 100 to 500 μm, as explained in Section 4.3.1. Samples were made with a scanning speed ν of 1250 mm s^{-1}, hatch spacing h (distance between two scan lines) of 100 μm, a laser power of 170 W, a layer thickness (t) of 30 μm, and a spot size of 100 μm.

Layers were scanned using a continuous laser mode, and two adjacent layers that have a rotated angle of 67° with respect to each other (see Figure 5.1 for a Schematic of the scanning strategy). This rotating angle was selected so as to achieve the full density of the specimens and to minimise the anisotropy of microstructure (Chen *et al*., 2017, Qi *et al*., 2007), as explained in Section 4.3.1. The fracture toughness samples were built in different *xz*, *yx* and *zx* directions; the specimens that were built in the *zx* direction are also described as being "parallel" to the build direction. The specimens in the *xz* and *yx* direction are "perpendicular" to the build direction; more details are given in Section 4.2 for the designation of samples with different build directions according to the ASTM standard. Since the laser beam scanning direction changes with each layer, a smaller difference between the *xz* and *yx* direction of the tensile samples might be expected. However, it was decided to build and test samples with both *xz* and *yx* orientations in order to investigate what other potential factors associated with the DMLS process might contribute to the anisotropy of the resulting products. Figure 5.2 illustrates the build directions of the tensile and fracture toughness samples produced by DMLS. In each *xz*, *yx*, *zx* direction, ten samples were made to test the tensile strength and fracture toughness, respectively. As mentioned above the EOS M280 machine had a sudden failure.

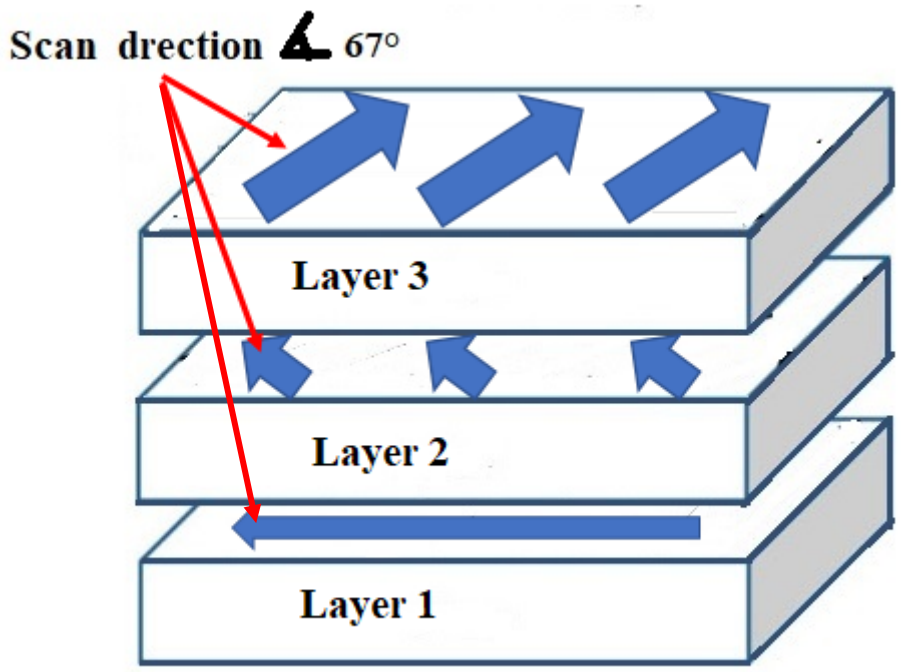

Fig 5.1: Schematic of scanning strategy

5.2.2 Mechanical and Materials Testing

After removing the 'as built' specimens (no-post treatments were applied) from the build plate, the density of the specimens was measured by two methods as explained in experimental measurements, Section 4.5. All tensile specimens (see Figure 5.2a) were deformed in tension until fracture. The fracture toughness test was carried out to determine the ability of the material to resist the growth of cracks. Figure 5.2b shows the single edge notched bend specimens. Vickers hardness testing was carried out on the specimens using a pyramidal indenter as explained in Section 4.5.3. Surface roughness and metallographic analysis were carried out to evaluate the surfaces' quality and the consolidation behaviour of the as-sintered specimens. For more details about the mechanical and material testing, see Section 4.5.

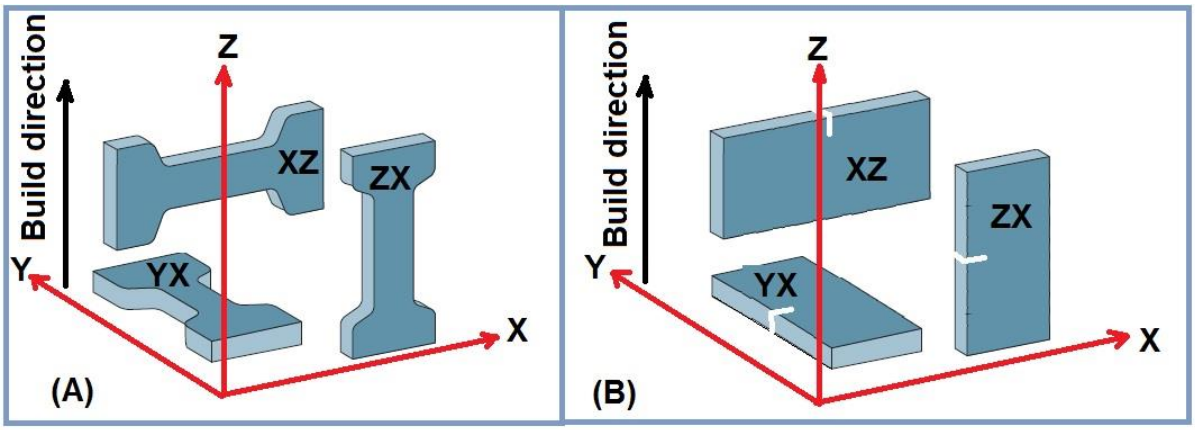

Fig 5.2: Schematics of the (a) tensile testing specimens and their build directions, and (b) the build directions for SENB specimens.

5.3 Result and discussion

5.3.1 Density analysis, surface roughness and morphology

The densities of the DMLS specimens built in different directions exhibited the same values; for the *xz*, *yx* and *zx* directions, this was a value of 4.5 g cm^{-3}, which was obtained with an average standard deviation of 0.1 g cm^{-3}, see Table 5.1. However, the influence of build direction on the density of parts becomes less apparent. The samples were built in the *zx* direction, with a large building height and several layers. The area of the layers of the *zx* sample exposed to laser sintering was smaller than the area of the layers of the *xz* and *yx* samples. After exposure and interaction with the laser beam, while scanning its external surface boundary, it is more likely to be bonded with the semi-melted particles. So, these loose particles should be removed as they have a negligible effect on the part density. The experiment results reveal no effect from the building direction on the density of metal powders in DMLS fabrication. The density value presented in this study is slightly higher than the annealed Ti6Al4V alloy, at 4.43 g cm^{-3}. This value is also higher than those of the SLM of Ti6Al4V alloys that were made in previous studies, and, as a result, there was a high number of pores and semi-melted particles due to the large hatch spacing (100 µm) (Song *et al*., 2012, Chlebus *et al*., 2011). Figure 5.3 shows the amount of porosity formed in the Ti6Al4V parts during the DMLS process, measured by CT scanning. Figure 5.3 reveals a small number of pores in all the samples with three different build directions. These pores are spherical with size approximately 6 to 8 µm and are known to be produced by escaping gas or powder induced porosity, as shown in Figures 5.9a and b. They may form inside the feedstock of the powder during the atomisation process and then translate directly to the as-

built parts. Furthermore, porosity is a common defect in AM components, which has a negative influence on the mechanical properties. A lack of fusion due to insufficient energy input can also lead to porosity in the parts. When the energy applied to an area of the powder is too high, sputter ejection may also happen in the process, known as a keyhole formation, and can produce a trail of voids (Gong *et al.*, 2014, Yasa *et al.*, 2011b, Li *et al.*, 2010)**.**

Table 5.1: Density of Ti6Al4V processed by DMLS at *xz*, *yx*, and *zx* directions

Build direction	**Density** g **cm^{-3}**	**Standard deviation g cm^{-3}**
Xz	**4.5**	**±0.04**
Yx	**4.5**	**±0.10**
Zx	**4.5**	**±0.06**

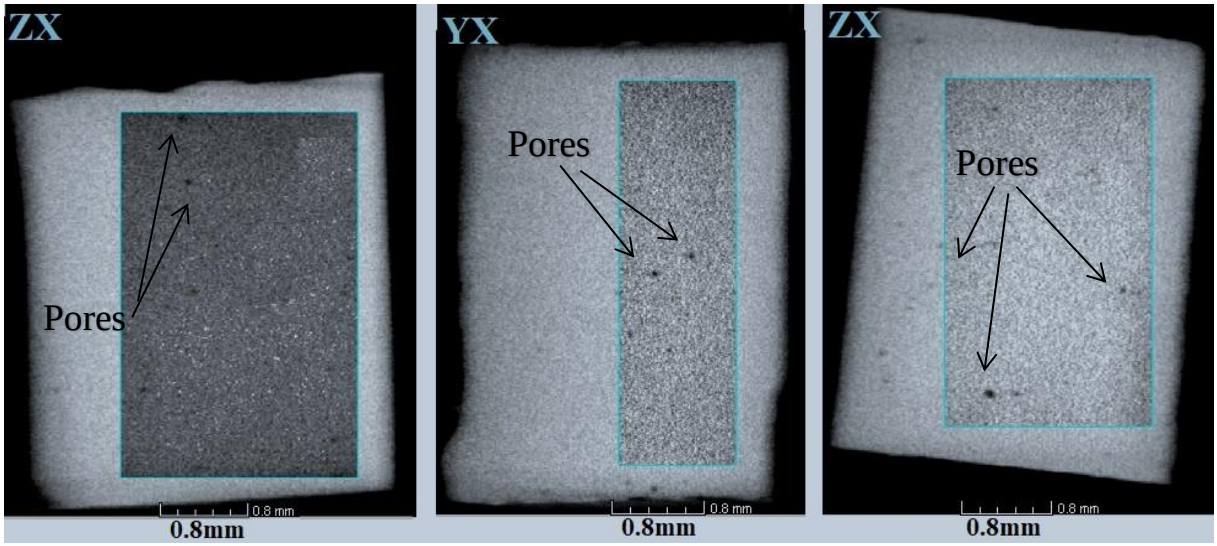

Fig 5.3: Typical 2D CT scan slices of an as built Ti6Al4V part processed by DMLS

Table 5.2 illustrates the typical surface roughness in both parallel and perpendicular directions to the build direction for *xz*, *yx*, and *zx* specimens (see Figure 5.4). An average surface roughness value (R_a) of ~7 μm (±0.3 μm) was found parallel to the build direction, and ~3 μm (±0.2 μm) to the perpendicular surface of the build directions. This difference was due to some powder particles that were stacked on the parallel surface during the melting process.

Table 5.2: Surface roughness results for the DMLS Ti6Al4V alloy built in different orientations

AS-Built Direction		Average Surface Roughness Ra	Standard deviation µm
xz	**Parallel**	**7.2 µm**	**±0.22**
	Perpendicular	**3.0 µm**	**±0.3**
yx	**Parallel**	**7.1 µm**	**±0.3**
	Perpendicular	**3.2 µm**	**±0.1**
zx	**Parallel**	**6.8µm**	**±0.39**
	Perpendicular	**2.8 µm**	**±1.47**

The roughness profiles of the as-built parts of Ti6Al4V made by DMLS are shown in Figures 5.5 and 5.6. The surface parallel to the build direction in the *zx* series sample appeared to be rougher than the perpendicular surface of the same specimen. The as-built parallel surface showed a higher amplitude value of 150 µm (A profile) than the perpendicular surface (B profile) of 80 µm.

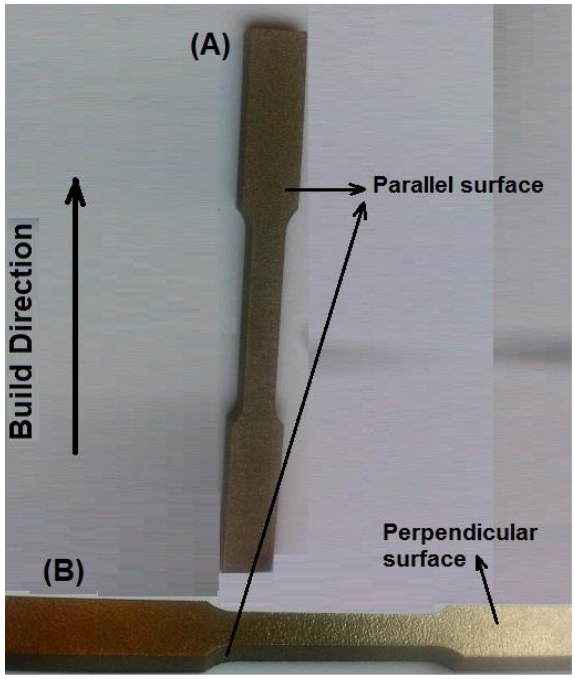

Fig 5.4: As-built Ti6Al4Vsamples produced in (a) the *zx*, and (b) the *yx* directions.

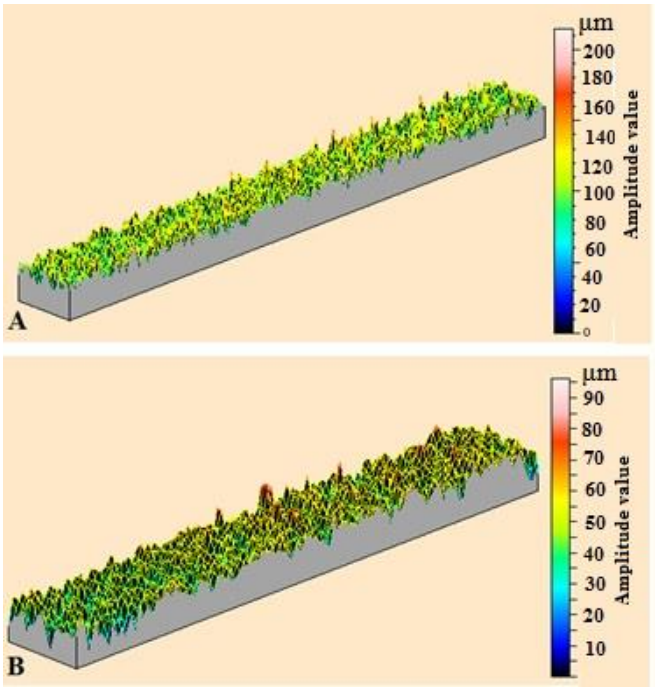

Fig 5.5: Typical 3D surface morphologies of a Ti6Al4V DMLS component produced a) parallel, and b) perpendicular to the build direction, in the *zx* orientation.

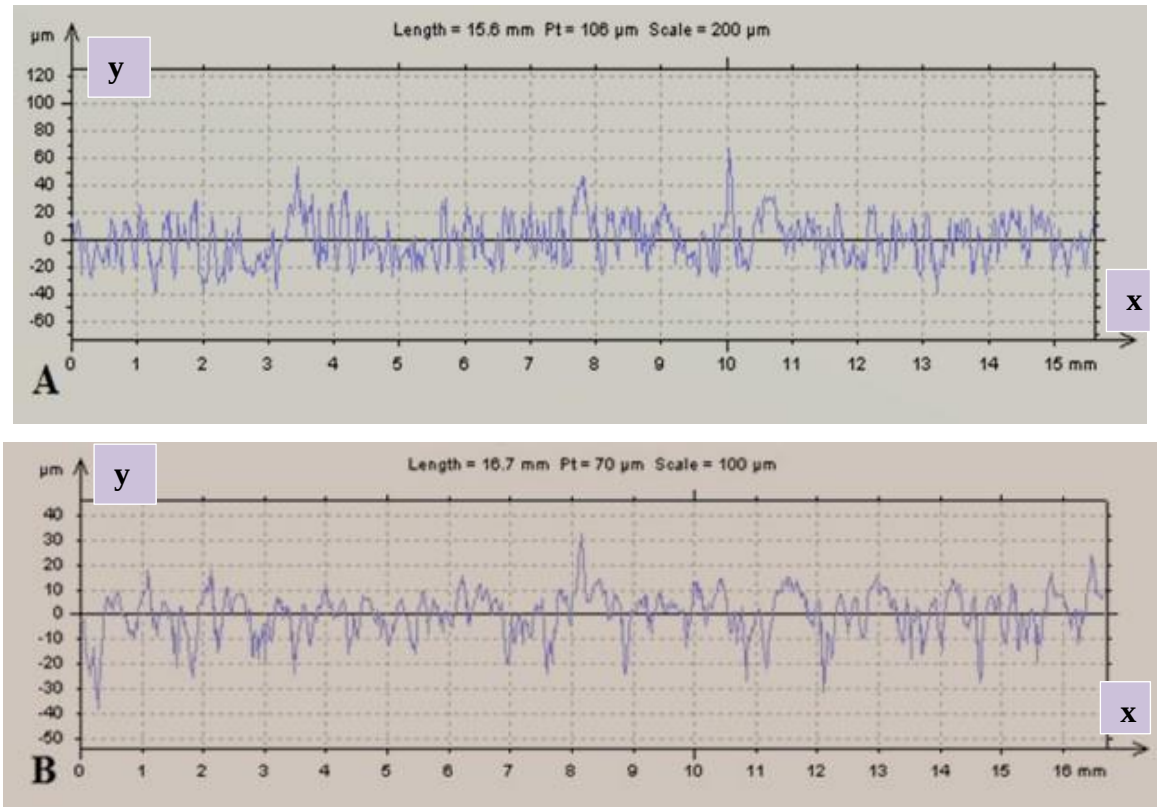

Fig 5. 6: The maximum height (Rt) of the as-built sample in the *zx* direction: a) parallel, and b) perpendicular, to the build direction.

The surface finish of the as built Ti6Al4V DMLS parts is shown in Figure 5.7. The large semi-melted particles have bonded onto the surfaces that are parallel to the build direction, whereas the surfaces perpendicular to the build direction (top surface) have few semi-melted particles and contain a smooth region that is associated with a rippled rough area. This explains why the *R*a values of the sample parallel surface are relatively higher than the perpendicular surface. Moreover, Figures 5.8a and 5.8b show the top surface, and demonstrates how the high speed movement of the laser at 1250 mm s^{-1} leads to pouring some of the molten material around the outer boundary and on the parallel surface of the samples. This molten material makes the powder particles adhere to the parallel surface of the sample, which was clear in the parallel surface images, as seen in Figures 5.7d. This leads to the production of sharp and prominent edges at the side of the sample edges (see Figure 5.8a), and this makes the upper surfaces of the samples those directly exposed to the laser semi-concave, due to having edges higher than the middle.

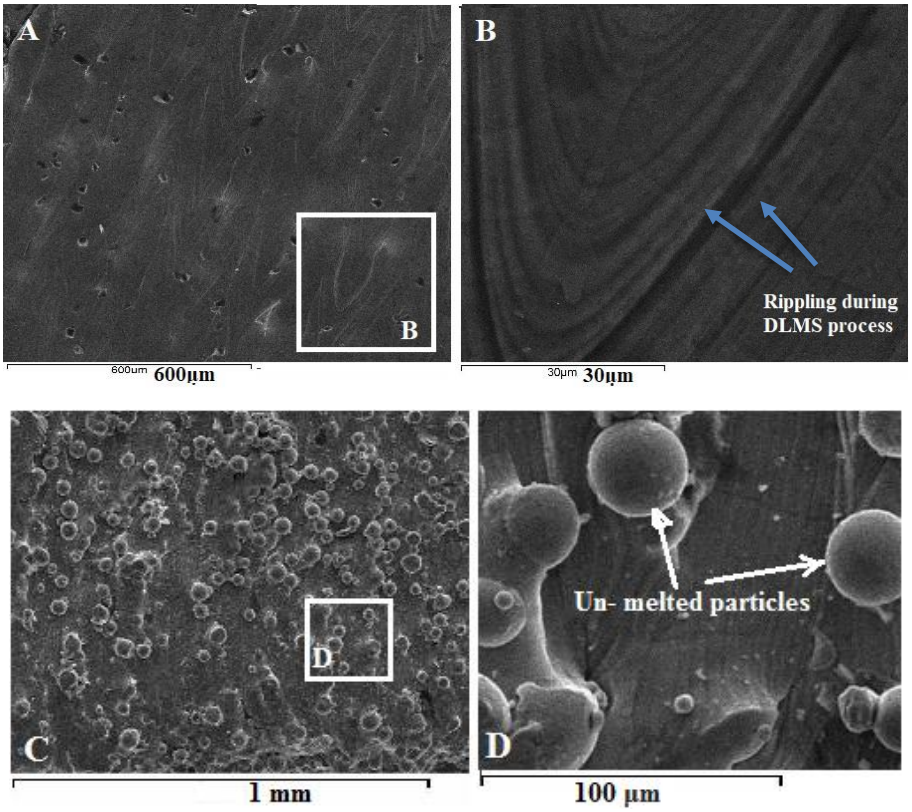

Fig 5.7: Typical surface finish of the as built Ti6Al4V DMLS parts revealing rippled rough area and unmelted powder particles (a, b) perpendicular, and (c, d) parallel, to build direction

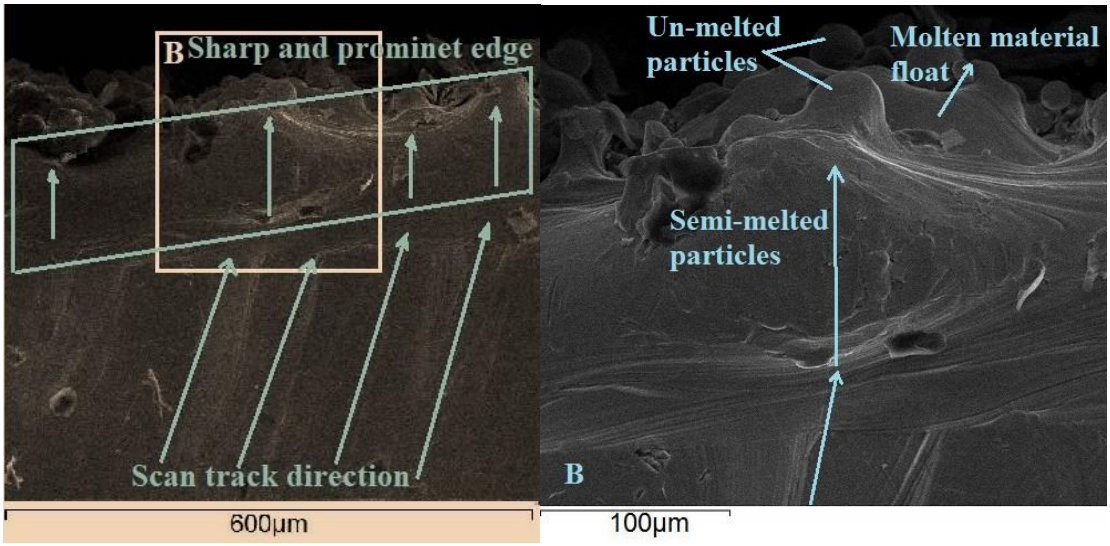

Fig 5.8: Show the prominent edges in the Ti6Al4V top surface of the parts produced by DMLS, (a) at 600 µm scale, and (b) at 100 µm scale.

Ti6Al4V is a common alloy used in the aerospace industries, and this is due to its excellent mechanical properties to weight ratio (Peters *et al*., 2003). Despite this, the surface finish of the part produced by DMLS is poor, and it usually requires a post process finishing operation for critical applications. For instance, the internal parts that are used in the aircraft engine (pipes, cylinders, etc.), and those parts may then leak some fluid and cause the risk of fire. According to previous research, a few approaches have been used to improve the surface finish. For instance, it small powder particles may be used for the part's fabrication. Alternatively, post-processing can be used, such as machining and polishing, to enhance the surface and reduce the roughness.

5.3.2 Microstructure analysis

Figures 5.9a, and 5.9b show the view of the microstructure of the top surface of as built Ti6Al4V, fabricated by DMLS. The top surface view reveals that a fully acicular α` phase of martensitic, is produced through the DMLS process. For more details about titanium phases, see Section 2.1. This production of an α` phase is probably due to the high temperature gradients that occurred (Murr *et al*., 2009). The side view in Figure 5.9c shows long columnar grains that are oriented in the build direction and up to 350 µm long, i.e., much longer than the layer thickness. These grains are identified as former β phases that grew epitaxially through the material during the melting and consolidation process. Columnar

grains with epitaxial growth on successive layers are due to the rapid cooling rate, as explained in Section 3.4.2 and Figure 3.9 (Seifi *et al*., 2016b).

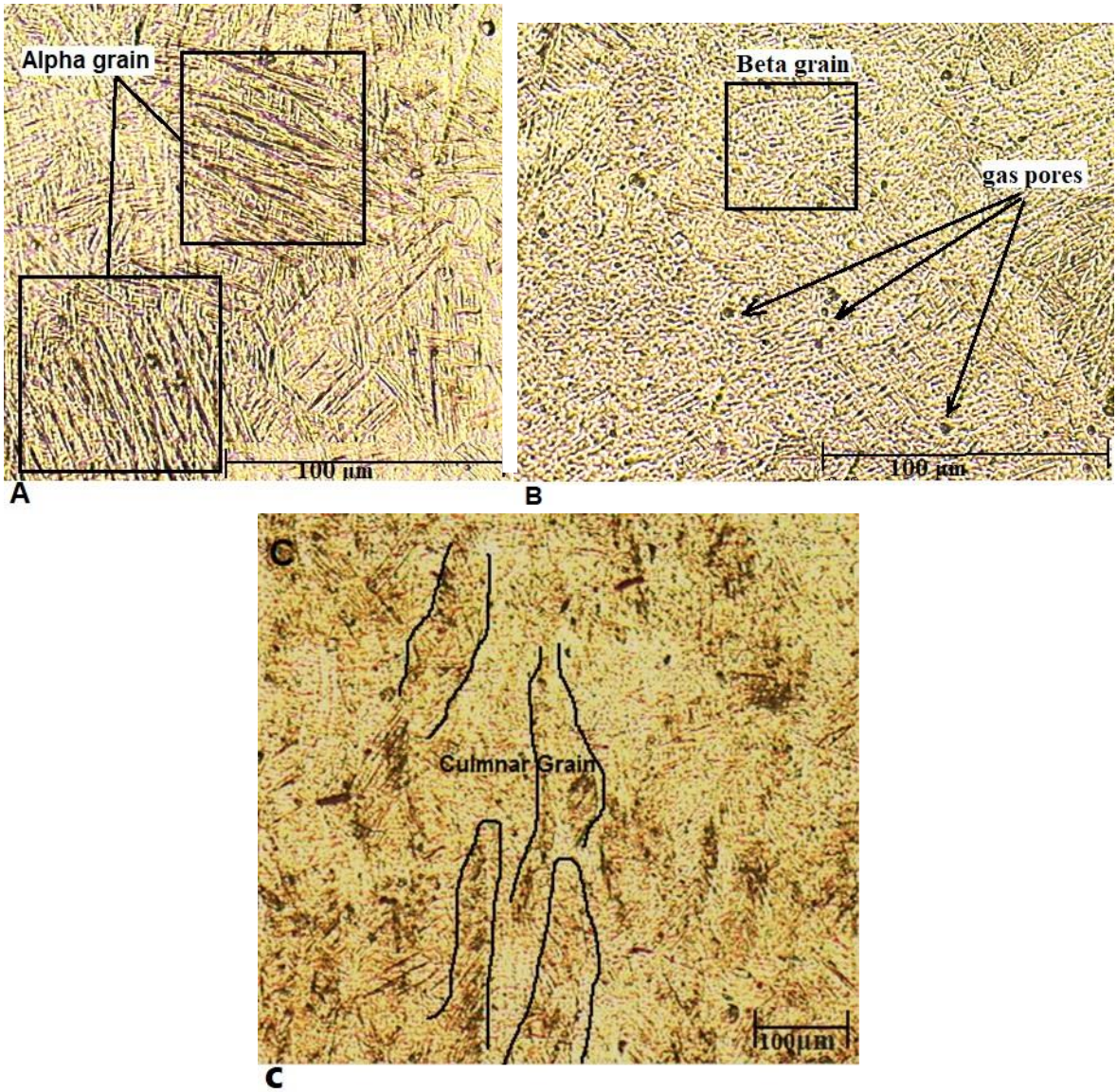

Fig 5. 9: Typical grain microstructures of as built samples of the Ti6Al4V alloy (A, B) top surface (C) side surface.

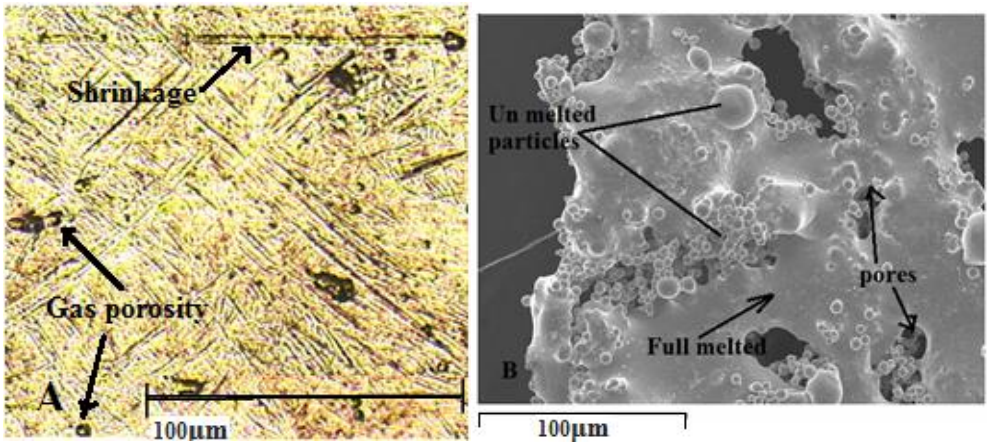

Fig 5. 10: Typical defects revealed in the Ti6Al4V DMLS component, a) gas pores, and shrinkage cavities, and, b) an SEM image of un-melted powder in the first few layers.

Small dark bands also appeared in the DMLS parts, as shown in Figure 5.9a. These are produced by the etching chemicals used on the Ti6Al4V parts. Figure 5.10a, reveals shrinkage cavities, and gas porosity in the DMLS parts that were trapped within the parts due to the rapid solidification rates at a high scan speed. At a very high scanning speed, the cooling rate is significantly higher, and so this is not preferable. The vulnerability to pore formation may be one of the reasons for the presence of unmelted powder in the first few layers (Figure 5.10b). The structure becomes more uniform and stable after the first few layers.

The interaction between the powder and the laser beam, the laser spot size and the scan velocity determine the size and behaviour of the melt pool. Consequently, it consolidates the microstructure. It has been revealed, through previous studies, that a large spot size (0.12 mm.) and a higher laser power (200 W) will produce a combination of equiaxed and columnar grains. While fully columnar grains will be produced, as in Figure 5.9c, when there is a small spot size and lower laser power, such as those used in this study, 0.1 mm. and 170 W, respectively (Kobryn and Semiatin, 2001, Lewis and Schlienger, 2000). High scan velocity 1250 mm s^{-1} will reduce the energy density input into the laser beam focused area and will result in a smaller melt pool, whereas a low scan velocity will produce a larger melt pool (Murr *et al*., 2012b). The grain size distribution is greater when the laser scanning is performed in different directions, such as by using a zigzag scanning strategy. The zigzag scanning strategy used in this study had a rotating angle of 67°, while it is smaller when there is deposition in the same direction, as revealed in Figures 5.9a, 5.9b and 5.9c (Dinda *et al*.,

2012). This increase in the grain size is due to the increase in the traverse speed and the incident energy. On the other hand, a higher cooling rate results in a martensitic structure and fine grains, which may enhance the mechanical properties of the Ti6Al4V parts.

5.3.3 Tensile and Hardness properties

The tensile properties (yield stress (Ys), UTS and % of strain) of the as built DMLS Ti6Al4V alloy are shown in Figure 5.11 and Table 5.3. The tensile stress was in three different directions: *xz*, *yx* and *zx*. The result indicates that there is no significant difference in ductility, yield strength, and UTS between the specimens built in the *xz* and *yx* orientations, and the *zx* specimen shows low values of elongation, yield strength, and UTS. This reveals that the samples which were built in the *xz* and *yx* directions have very similar properties. This isotropic behaviour is due to the same consolidation and fabrication, since the *xz* and *yx* directions were built horizontally on the base plate, and seemed to have the same strategy. The sharp edges, along with the semi-melted particles at the boundary of the *xz* and *yx* samples, also led to cracks being intiated and then propagated under the tensile load. However, the samples that were built in the *zx* direction presented lower values in the UTS and yield strength than did the others. This is because of the residual stress that remains in the *zx* parts higher than the residual stress in the *yx* and *xz* samples The different microstructure that occurs during the *zx* samples' production also influences the yield strength and UTS. This anisotropy in the mechanical properties has also been previously reported, as discussed in Section 3.4. Furthermore, the *zx* samples that were built in a vertical direction have the highest number of layers, and revealed shrinkage and some cracks that are aligned with scan tracks (seen in Figure 5.15). These defects make the crack initiate and propagate easily. A small number of pores was also presented in the samples, as seen Figure 5.3, and these have a negative effect on the mechanical properties of the parts produced.

The resulting ultimate tensile strength (UTS), and yielding stress (Ys) are relatively higher if compared to previous reports relating to the DMLS of the Ti6Al4V alloy (Chauke *et al*., 2013). However, the % of strain is relatively lower, and this could be due to flaws, such as internal and external pores, un-melted or semi-melted powder particles, and the high degree of roughness that was found in previous research. Additionally, the tensile testing data that were obtained in this study show a higher mechanical strength in comparison with the Aerospace Specification Metals of Ti6Al4V(AMS 4911) due to the high temperature

gradients that occur as result of the DMLS. For instance, AMS shows a 950 MPa UTS and 880 MPa yield strength (ASM, 2015), higher than the wrouth Ti6Al4V, see Section 3.4.1 (Table 3.1). Moreover, the results of aerospace specification metals are certified to ISO9001 and ISO9120 industry quality standards for samples fabricated by conventional processes. The improvement in ultimate tensile strength and yield strength could be attributed to the grain refinement in the DMLS parts due to the high temperature gradient and fast cooling rate.

The tensile values that have resulted from this study are higher than the conventionally quoted values because of the rapid cooling and consolidation employed during DMLS (or SLM), which leads to an improved microstructure. This phenomenon has previously been reported for various metallic materials, including Ti6Al4V, AISI 316 Stainless Steel and AlSi10Mg (Simonelli *et al*., 2014a, de Lima and Sankaré, 2014). Note that the ultimate tensile strength values in the *xz* and *yx* samples is higher than the yield strength of 100 MPa, indicating high strength with plastic deformation. The 55 MPa difference between the UTS and the yield strength of the samples built in the *zx* direction indicates a low strength with plastic deformation, due to some cracks being revealed, see Figure 5.15. All of these samples have a lower ductility in comparison to DMLS of Ti6Al4V, which is heat treated by a HIP, (Chauke *et al*., 2013, Gregolin *et al*., 2013). The crack path deviates during fracture; and this may be due to a poor alloying element in some of the zones of the α phase, causing rapid formation of cracks and the early failure of the material (Vrancken *et al*., 2012, Meier and Haberland, 2008). Thermal treatment may need to enhance the microstructure and to release the residual stress of the as-built Ti6Al4V alloy made by DMLS.

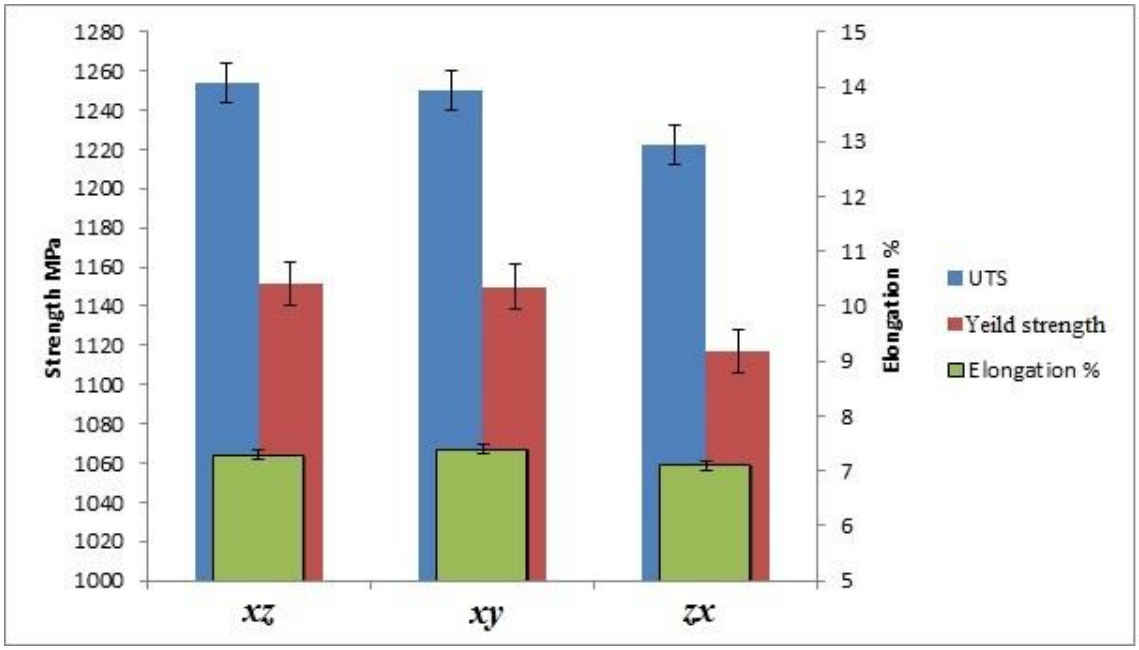

Fig 5.11: The graph for Ti6Al4V DMLS tensile specimens built to the net-dimensions in the *xz*, *yx*, and *zx* - build directions.

Table 5. 3: Mean tensile properties obtained from the as built Ti6Al4V made by DMLS.

As Built Sample	UTS (MPa) ±SD	Yield strength (MPa) ±SD	Elongation % ±SD
xz	**1254 ±7.2**	**1151 ±3.3**	**7.3 ± 0.4**
yx	**1250 ±9.3**	**1150 ±7.4**	**7.4 ±0.7**
zx	**1225 ±8.2**	**1117 ±2.4**	**7.1 ±0.5**

The graph in Figure 5.12 shows the average hardness value of Ti6Al4V. Hardness is the term used to describe the amount of energy required to permanently deform (stretch, bend, compress, etc.) a material. All of the samples were tested on both the cross-section surface and the top surface after polishing. The number of measurements for each sample was discussed in Section 4.5.3. The as-built condition specimens had hardness (Vicker's hardness) of 401.6 ±4 HV in the *xz* direction, with no significant difference in 400.3 ± 5.1 HV, in the *yx* direction. On the other hand, the *zx* direction records the smallest value (376.5 ± 5.2 HV), whereas a relatively lower hardness value may be due to a higher amount of porosity and the semi-melted particles that are presented in this orientation. The differences in the surface area of the layers built in the specimens with different building orientations will

also result in the differentiated thermal history of the consolidated metallic material. This thus leads to the difference in hardness values (Chlebus *et al*., 2011). The hardness values found in this study are higher than those values reported in conventional Ti6Al4V alloys for aerospace specification materials (ASM 4911) of 349 HV, and the Ti6Al4V parts fabricated by EBM (from 270HV to 370 HV) (Barreda *et al*., 2001). The hardness values in the samples of those built in the *xz* and *yx* directions are much superior to those of the Ti6Al4V parts made by SLM (306 HV) (Yu *et al*., 2007). The DMLS process, and its equipment, could be considered to be an excellent potential method for manufacturing high performance Ti6Al4V parts with controlled mechanical properties.

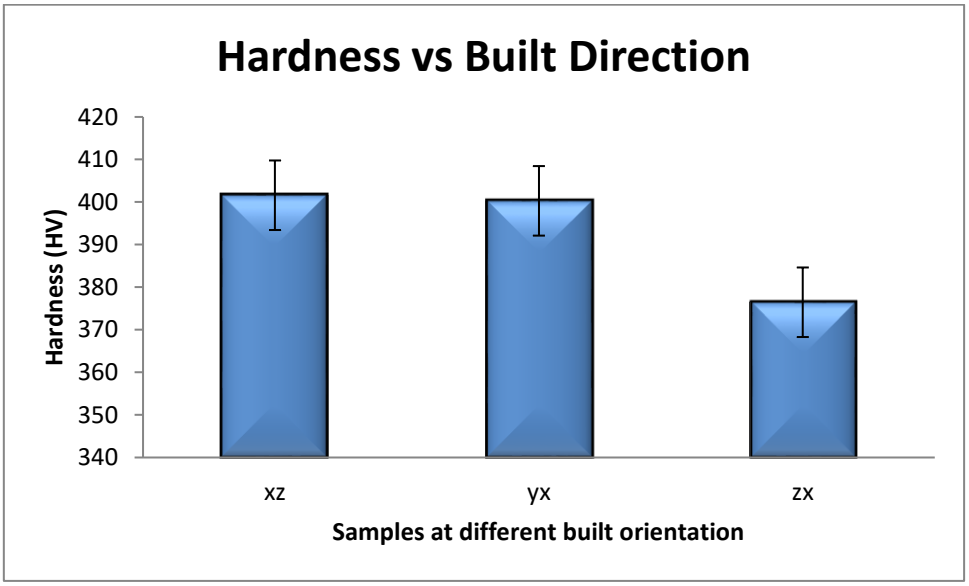

Fig 5.12: Vickers Hardness values for DMLS Ti6Al4V specimens built in the *xz*, *yx*, and *zx* - build directions.

5.3.4 Toughness and Fracture surface

Table 5.4 reveals that the Ti6Al4V fracture toughness values vary in samples built using different building directions. Samples built in the *xz* direction recorded the highest fracture toughness (132 MPa $m^{1/2}$), whereas the *yx* samples exhibited a medium value (118 MPa $m^{1/2}$ and the *zx* samples presented the lowest values (65 MPa $m^{1/2}$). For Ti6Al4V, the fracture toughness is in the order of 75 MPa $m^{1/2}$ (AMS 2015), and thus the DMLS samples have superior fracture toughness. This higher fracture toughness is probably related to the coarse-grained α` microstructure that formed during the high cooling rate. For more details about

titanium phases and structures see Section 2.1. These values of fracture toughness are also slightly higher if compared to previous research relating to Ti6Al4V made by EBM, which recorded 96.9 MPa $m^{1/2}$ in the horizontal direction, and 78.1 MPa $m^{1/2}$ in the vertical direction (Edwards *et al*., 2013). The present data are also higher than for Ti6Al4V alloys that were processed previously using different SLM processes that are discussed in the literature review, see Section 3.4.2. The fracture toughness values reported in this study are valid. For more details about their validity see Equation 3.1 and Section 3.4.2.

Table 5. 4: shows the Plane-Strain Fracture toughness values of Ti6Al4V made by DMLS.

Orientation	**K_{IC} (MPa $m^{1/2}$)**	**Stnd Dev ±**
xz	**132**	**2.6**
yx	**118**	**1.8**
zx	**65**	**3.1**

These toughness values highlight the dependence of the fracture toughness property on the samples' direction. The *xz* orientation was the highest value, sustaining toughness that was 50% greater than the *zx* direction, and 10% greater than the *yx* direction. The fracture toughness value of the *zx* direction samples represents 86%, in comparison to the fracture toughness value of the annealed Ti6Al4V (Welsch *et al*., 1993) (ASM, 2016). The low values in the *zx* direction were due to significant residual stress that remains in the non-equilibrium microstructure which is formed in several layers. Some induced defects, such as cracks, are shown in Figures 5.14 and 5.15. A very recent study by Seifi *et al* also reported that the texture, microstructure and some of the defects, vary with different machines, build orientations, and locations, thus affecting the magnitude of the fracture toughness (Seifi *et al*., 2016b).

The fracture surface evaluation revealed that different sizes of voids and cracking are present in samples *yx* and *zx*. The fracture surface of the *yx* sample (Figure 5.14) discloses a 35 μm crack length and an 8 μm crack width, while in the *zx* specimen a 68 μm crack length and 8 μm width length is revealed. This difference is due to the crack in the *zx* direction being between the two scan lines, and it is in alignment with the building layer. The regular voids, with average sizes of 4 μm, were clearly seen on the fracture surface of the samples in the *xz*, *yx* and *zx* directions (see Figures 5.14 and 5.15). Small pores with an average size of 2 μm were present in the fracture surfaces of all samples. These defects could be the reason for the

earlier fracturing and the low ductility, which reduce the fracture toughness value also. Dimples were observed in the *xz* and *yx* specimens (Figures 5.13 and 5.14), which are indicative of a ductile plastic failure in some regions.

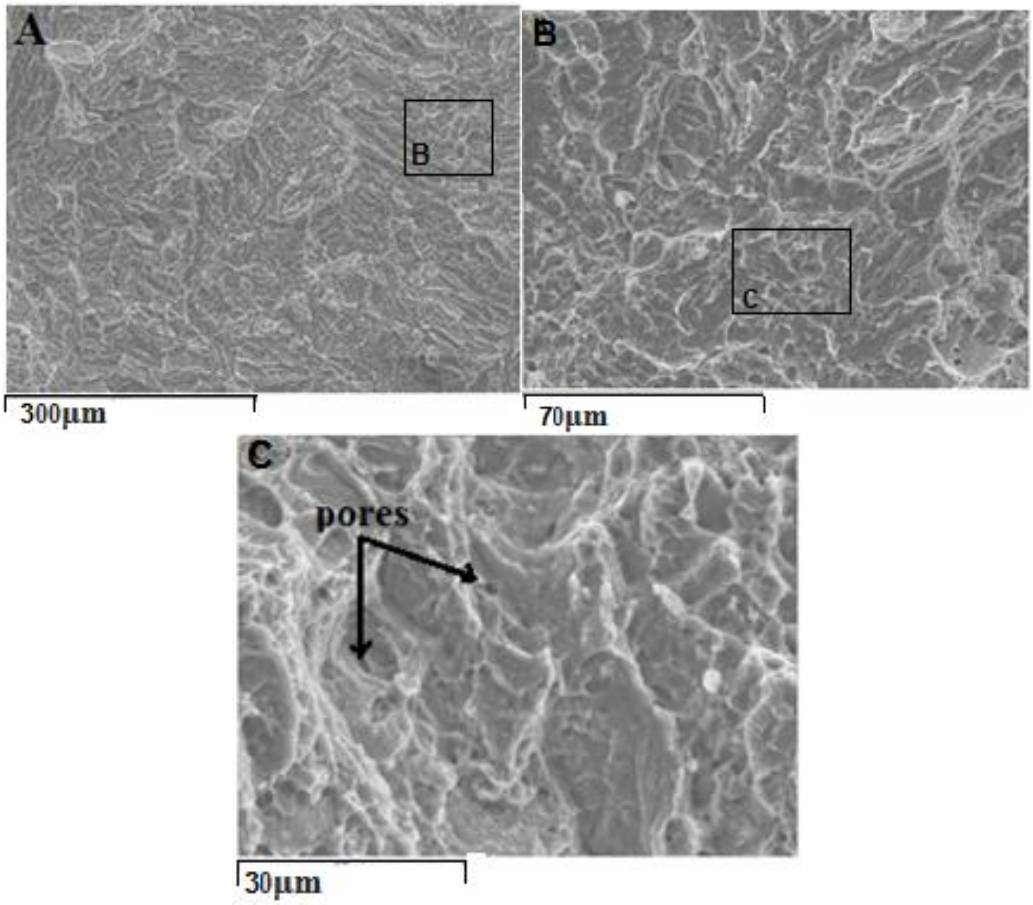

Fig 5.13: Typical SEM images of the fracture surfaces taken from the *xz* direction as built condition specimens at different magnifications.

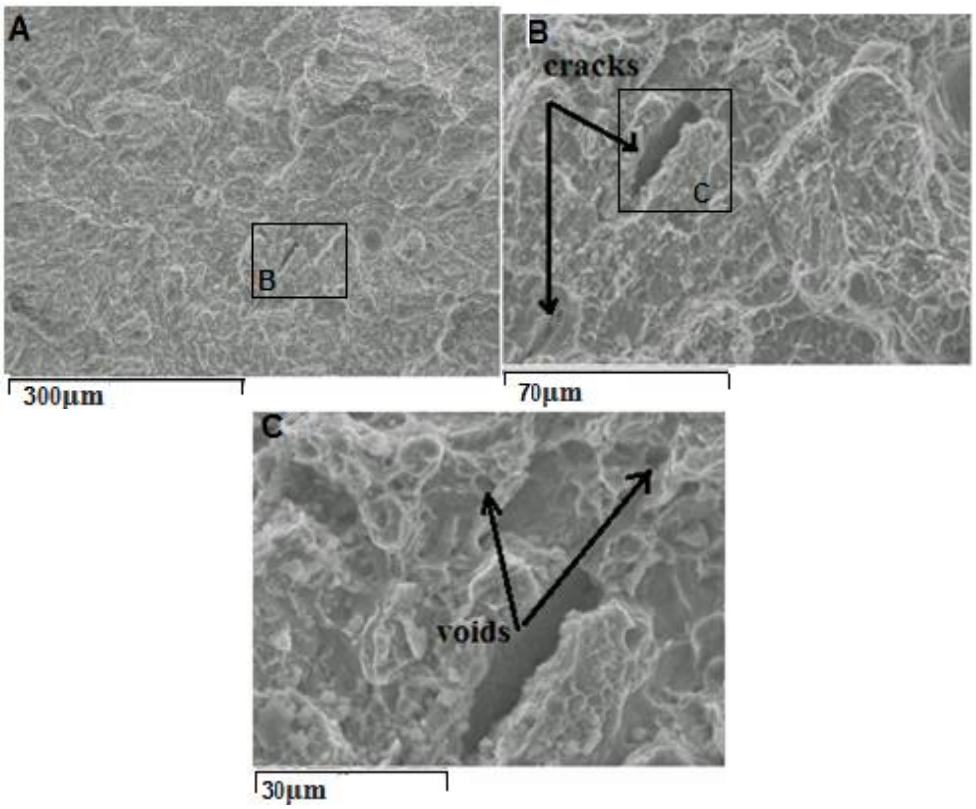

Fig 5.14: Typical SEM images of the fracture surface taken from the *yx* direction as built condition specimens at different magnifications.

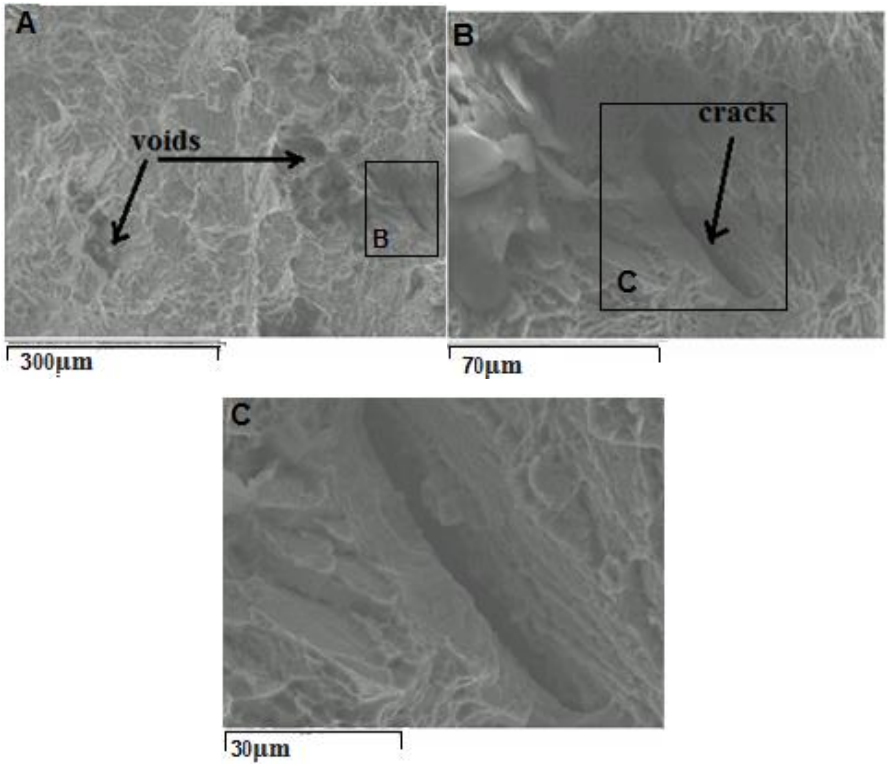

Fig 5.15: Typical SEM images of the fracture surface taken from the *zx* direction as built condition specimens at different magnifications.

It is believed that the surface roughness, and tensile strength, will have important effects on the fracture toughness results of the samples built in different directions. Microstructurally, Figure 5.9 reveals that the acicular needle of the martensitic structure in the DMLS samples is comparable to that of the wrought material. The microstructure observed in these parts is the same as that found in previous studies on the SLM of Ti6Al4V (Thijs *et al*., 2010, Edwards and Ramulu, 2014). The difference in the fracture toughness of the samples is in the three different directions that are affected by the microstructure of the parts produced. For instance, the crack present in the *zx* sample was aligned with a columnar grains structure, instead of that of the *xz* sample, which is perpendicular to the columnar grains' structure. This alignment eases the crack growth during the boundary of the α` grain. The *zx* direction samples were prone to more cracks than those in the *xz* and *yx* direction, and all of these cracks are aligned with the layer level as well as with a columnar grains' structure. The significant residual stress remaining in the *zx* samples was another reason to reduce the fracture toughness value. This is because, in the *zx* samples, the number of layers is too high, and the scanned area is smaller, which means the energy input that is applied to a region of powder is higher than the *yx* and *xz* samples. So the residual stress in the *zx* samples is the highest (King *et al*., 2014, Körner *et al*., 2013). However, suitable heat treatment can be applied to improve ductility by transforming the martensitic phase into α-β phase, and by reducing the internal stress and the enhancement of the ductility, since, typically, a ductility increase is also associated with a toughness increase.

Although it is hard to define the crack initiation site on the surface of each sample, it is assumed that the rough surface will play a role in this mechanism. The internal defects will also be the primary contributor to the crack initiation within the samples. Furthermore, the small amount of porosity that is embedded within the samples, shown in Figures 5.9 and 5.10, is still a key contributor to poor mechanical properties, since these pores serve as sites for crack initiation.

Table 5.3 reveals that the tensile properties of the Ti6Al4V parts produced by DMLS are higher than those for the wrought material, (Welsch *et al*., 1993). These values are also greater than those reported in previous studies on the SLM of Ti6Al4V (Edwards and Ramulu, 2014, Koike *et al*., 2011, Leuders *et al*., 2013). The high strength of these samples would suggest a promising fracture toughness performance, which is comparable to cast materials, since fracture toughness typically correlates to strength. However, the low ductility, 7.1%, would indicate the material's tendency towards brittle behaviour, which is related to the sensitivity to notches. In-depth material and microstructure characterisation and

the evaluation of samples built in different directions are thus essential in explaining why fracture toughness is reduced by loading in the columnar direction. Minimising the surface roughness by machining and polishing may also lead to slightly enhanced fracture toughness and mechanical performance. Future work could be carried out to investigate the influence of a rough surface on the fracture toughness properties.

5.4 Conclusion

This chapter has been investigated the density, surface quality, microstructure and mechanical properties of the components of the DMLS parts made using different building orientations. It has been illustrated that the effects of different build orientations influence the microstructures and the mechanical properties, especially the fracture toughness of the Ti6Al4V. The major findings are summarised below:

The density of the *xz*, *yx* and *zx* samples that are presented in this study exhibited the same value at 4.5 g cm^{-3} This value is also slightly higher than the annealed Ti6Al4V alloy, (grade 5) at 4.43 g cm^{-3}.

The surface roughness value, Ra, was found to be the same in all of the build directions. The surfaces parallel to the build direction in the *xz*, *yx* and *zx* samples were however found to be rougher than those on the surfaces that were perpendicular to the building direction.

The microstructure analysis in the three different building directions reveals a fully acicular α` of martensitic and long columnar grains that are oriented in the build directions, which are 350 μm long, due to high temperature gradients and a rapid cooling rate.

A small number of pores were present in all of the samples. They were of a small size and irregular in shape, and the shrinkage cavities that were revealed in the samples were built in the *zx* direction. Un-melted powder particles were presented in the first few layers only, and at the side edges of the samples, due to the very high scanning speed and cooling rates used to produce the samples.

The high speed movement of the laser beam makes the molten material move fast and adhere to the neighbouring particles surrounding the outer boundary of the parts, producing sharp and prominent edges.

The fracture toughness' of the DMLS Ti6Al4V materials that are evaluated in this research were higher than that of the cast material in the *xz* and *yx* directions, while they were slightly lower in the *zx* direction, due to cracks, porosity and surface finish. They were also slightly higher than those in the Ti6Al4V that were made by EBM, and this leads to superior mechanical properties of those made using the DMLS technique rather than those made with EBM (Edwards *et al.*, 2013) (Seifi *et al.*, 2016b).

The tensile strength of the as built samples was found to be higher than those of the wrought material. All of the samples also exhibited brittle fracture morphologies, which, linked to the martensitic phase, which was found in all of the build directions, as was expected, due to the high gradients of temperature that occur as a result of the DMLS process.

The influence of the surface roughness of the as-built condition samples on the fracture toughness property is not clear from this experimental procedure due to the porosity, cracks and the residual stresses that are present.

The mechanical properties change with the change in the microstructure due to the different build directions. Furthermore, the samples that were built in the vertical direction (parallel to the building direction) have a lower performance than those samples that were built in a horizontal direction (perpendicular to the building direction).

Low ductility indicates the high susceptibility of the Ti6Al4V to fracture. This, therefore, results in a requirement that more testing be done on samples with stress relief and less porosity.

Chapter 6: Effect of build orientation on the surface quality, microstructure and mechanical properties of selective laser melting 316L stainless steel

Chapter 6 studies the effect of different build direction on the parts quality and mechanical properties of 316L stainless steel processed by SLM. The process parameters for samples fabrication and the tests procedures are addressed in Section 6.2. Section 6.3 discussed the main result and compared to the previous literature of the same material made by SLM and conventional process. The most important findings are concluded and outlined in Section 6.4.

6.1 Introduction

Stainless steels are widely used as a feed powder material in SLM due to their comparatively low cost, their safety and their ease of use. 316L stainless steel is a common alloy that is used in aerospace applications due to its resistance to corrosion and its good specific strength (Yan *et al*., 2012). The SLM of 316L stainless steel was previously investigated in order to illustrate the effect of the process parameters on the density, the mechanical properties (Childs and Hauser, 2005, Childs *et al*., 2005), and in order to look for defects, such as porosity, cracks and balling, which were found to occur in SLM produced parts. Different SLM processing parameters, including laser power, scan speed, layer thickness, and hatch distance, have been examined in previous studies, however, the understanding of the inter-relationship between these parameters is still not clear, in particular, in relation to the effect of balling (Tolochko *et al*., 2004), the interaction mechanism between material and laser beam (Fischer *et al*., 2003), and the powder solidification on the substrate (Schoinochoritis *et al*., 2015). Earlier studies have yet to apply SLM to making 316 stainless steel parts with mechanical properties that are sufficient for use in applications (Zhang *et al*., 2011). There is also a limited characterisation of the critical mechanical properties for aerospace applications, particularly for fracture toughness, which hasn't been tested in different build directions (Kruth *et al*., 2010). So, there is a need for an in-depth and systematic study of the SLM processing of stainless steel for aerospace applications. This is essential, both in order to further improve the capability of SLM to process 316L, and for the resulting properties of parts for aerospace applications. A systematic study is required to provide a clear

understanding of the fundamental process mechanisms governing the resulting microstructure; and thus, the properties of 316L parts.

The research presented in this chapter has focused on the analysis of the mechanical properties and microstructures of SLM fabricated parts made with 316L steel, and, in particular, on the effect of build orientation on these properties. Firstly, the effect of build orientation on the toughness properties, strength and ductility of the SLM fabricated stainless steels was investigated. Secondly, the microstructure of the SLM parts was characterised, and their effects on the mechanical properties, in particular on fracture toughness, were evaluated. These measured properties were compared with previous research, providing an understanding of SLM processing for different metal alloys. The findings of this study provide new information about the use of the SLM process for the fabrication of stainless steel aerospace components.

6.2 Experimental Procedures

Fifteen sets of 316L stainless steel flat samples for tensile testing, and fifteen sets of SENB samples for fracture toughness testing, were produced, see Figure 6.1. The samples, made in three different build directions, were produced with a laser power of 180 W, a scan speed of 1600 mm s^{-1}, a layer thickness of 30 μm, and a scanning laser spot with a 75 μm diameter. The SLM machine had a base plate with axes *x* and *y*, and a build direction in the *z* axis. The naming convention uses two letters. The first letter is the axis of the machine, on which the longest axis of the sample lies. The second letter is the machine axis, on which the second longest sample axis lies.

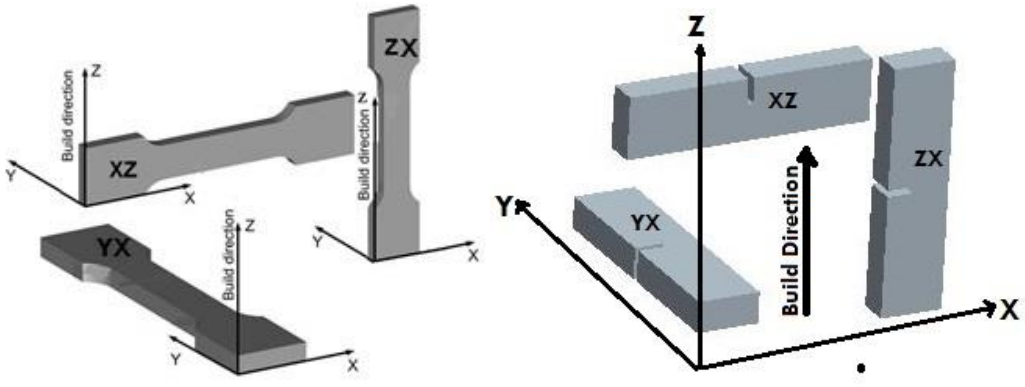

(a) (b)

Fig 6.1: The SLM fabrication of (a) tensile, and (b) fracture toughness testing samples produced at the *yx*, *xz* and *zx* building orientations

After removal from the plate, all the SLM fabricated samples were machined to remove the remaining support structure and they were then tested in an as-built condition; for more details see Section 4.4.1. For each direction, five specimens were built for tensile testing and five for fracture toughness testing. The densities of these specimens were evaluated by two methods, as explained in experimental measurements, Section 4.5.1. All the specimens were deformed until fracture during the tensile testing, and the toughness notched specimens were subjected to a three points test, under compression, to failure. These tests were carried out according to ASTM E8 and ASTM E399-9, for tensile and fracture toughness tests, respectively. For full details for the tests' specifications see the experimental measurements' Section, 4.5.4.

Metallographic investigations were carried out on the samples that were etched, as explained in Section 4.4.2. SEM and OM were used to characterise the surface morphology and microstructural features of the specimens. The surface roughness was measured for the as-built surfaces (top and side surface), as explained in Section 4.5.2. The average values of *R*a were obtained from both the parallel surface (side) and the perpendicular surface (top).

6.3 Result and discussion

6.3.1 Density Analysis

The same density, of 7.7gcm^{-3}, was found for for *yx*, *xz* and *zx* parts, with a standard deviation of ± 0.01. This result (7.7g cm^{-3}), for the SLM 316L stainless steel, accounts for 96% of the density of 8 g cm^{-3} for 316L stainless steels made by conventional production processes. On the other hand, the density results in this study are slightly lower in comparison to a previous study, which achieved 99% of the density of 8 g cm^{-3} (Yasa and Kruth, 2011) after some post process treatment was applied. Yasa and Kruth (2011) showed that the preheating temperature plays a major role in the SLM process, and high-density parts are made when preheating the powder bed to 200 °C. The laser re-melting may be another approach to enhance the density of SLM parts, as it reduces the porosity from 0.77% for the parts with no laser re-melting to 0.04% when the parameters are selected properly (Boisselier and Sankaré, 2012).

The effect of the build directions on the density of the SLM parts is very minimal. The samples that were built in the *zx* direction are exposed to semi-melted and loose particles that are bonded on their external surface boundaries after its exposure to, and interaction with, the scanning of the laser beam. The *zx* direction represents a larger building height and, consequently, there are a greater number of layers for these specimens. Each layer of the *zx* built group has a relatively smaller cross section than that of the *yx* and *xz* groups, and its external surface boundary is more likely to be bonded with the semi-melted particles.

In general, the SLM process is required to produce fully dense parts in order to meet strict mechanical property requirements for aerospace applications. However, it may be difficult to achieve complete metal powder densification during the SLM process, since there is no mechanical pressure applied to the metal powder, as in the moulding process. The metal powder densification during SLM is predominantly influenced by temperature, capillary force and gravity (Kruth *et al*., 2010). Gas bubbles can be entrapped in the powder material through the SLM's solidification. Hence, further research and development on SLM is still required in order to deliver high-density stainless steel components for aerospace applications. To provide an in-depth understanding of the laser material interaction mechanism, to manipulate the powder consolidation and to achieve enhanced densification, is also needed.

6.3.2 Surface and cross-section microstructure

Figure 6.2 shows different views (parallel and perpendicular to the build direction) of the *yx*, *xz*, and *zx* samples' microstructures. The scan tracks are clearly distinguishable in Figure 6.2 (b), and (c) through a few irregular pores that are caused by the process. The dark band areas are created due to sample preparation (etchant). The processed induced porosity occurs when the powder is distributed into the processing surface. This is because the powder particles have different diameters. Some particles are also not spherical, and these are intended to be consolidated into a layer of the correct height during the melting (Körner, 2013). The cross-section images show that the stainless steel powder particles also readily melt. Densification is clearly complete in the samples, and the overlapping (this phenomenon occurs when there is a short distance between the scan tracks) takes place between the scan tracks. This overlapping means that the additional heat was transferred from the melted track to the previously solidified track, leading to better consolidation and densification.

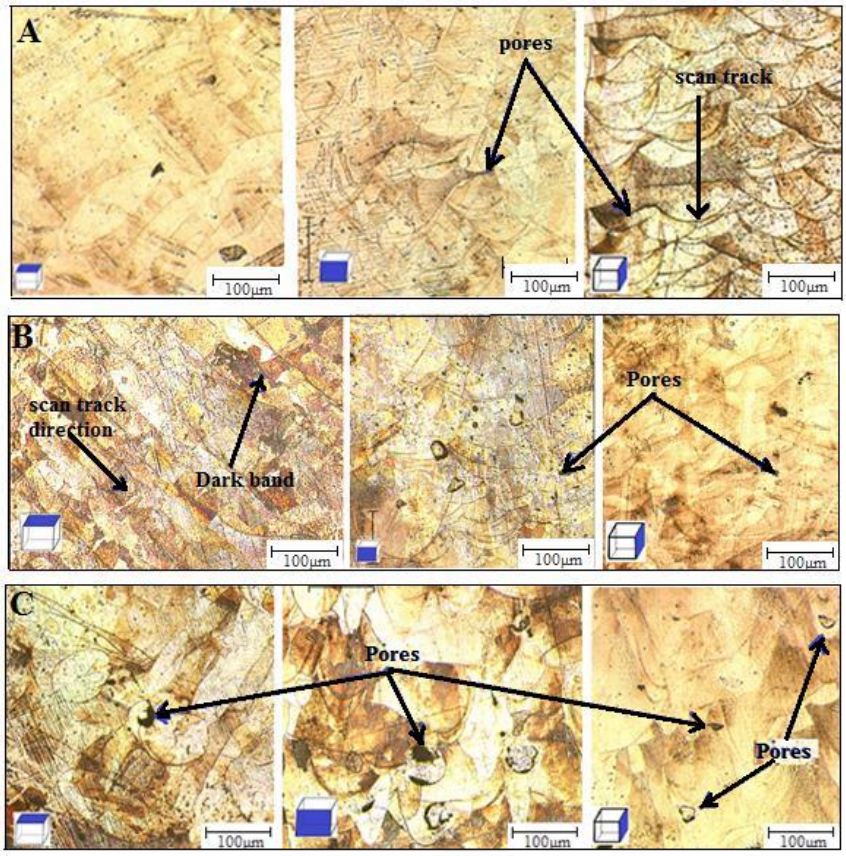

Fig 6.2: Typical metallography images showing parallel and perpendicular to build direction side wall views of 316L stainless steel SLM samples (polished and etched);(a) In the *yx*, (b) *xz*, and (c) the *zx* build directions.

Figure 6.3 presents the region between the scanning tracks of the material where the melting shows good diffusion. An anisotropic microstructure was observed along the different directions in this study. Fine dendritic structures are presented in the perpendicular to build direction (top surface) view in the very dense *xz* samples. These anisotropic and dendritic microstructures were confirmed by Gäumann *et al.*, who reported that the quality of metal parts formed by laser melting depends on the thermal gradient and growth speed (Gäumann *et al*., 1999). Rombouts also found similar microstructures had formed as a result of rapid solidification caused by a high cooling rate (Rombouts *et al*., 2006). The small pores found in samples can occur during the process and they are explained through two different resources: i) shrinkage, and ii) the composition of gas voids (balling) (Hao *et al*., 2009), for more details about shrinkage porosity, see Section 2.3.1. The irregular pores have a size up to 8µm in the *zx* samples. These pores are probably produced because of the shrinkage that occurs in the solidification process. Furthermore, Figure 6.3 reveals that the pores in the *zx* samples have

an irregular shape and appear more frequently than in samples built in the *yx* direction. Samples built in the *xz* direction reveal no pores in the same regions, implying good consolidation, which can be observed through the dendritic microstructure. This porosity may concentrate stress through mechanical loading, and this can increase during applied stress. Soboyejo reported that the growth of three dimensional defects may finally lead to a catastrophic failure in the structure and in engineering components (Soboyejo, 2002). Consequently, it is axiomatic that these pores affect the mechanical properties, especially the tensile strength, elongation and fracture toughness (this will be further clarified in Section 6.3.4).

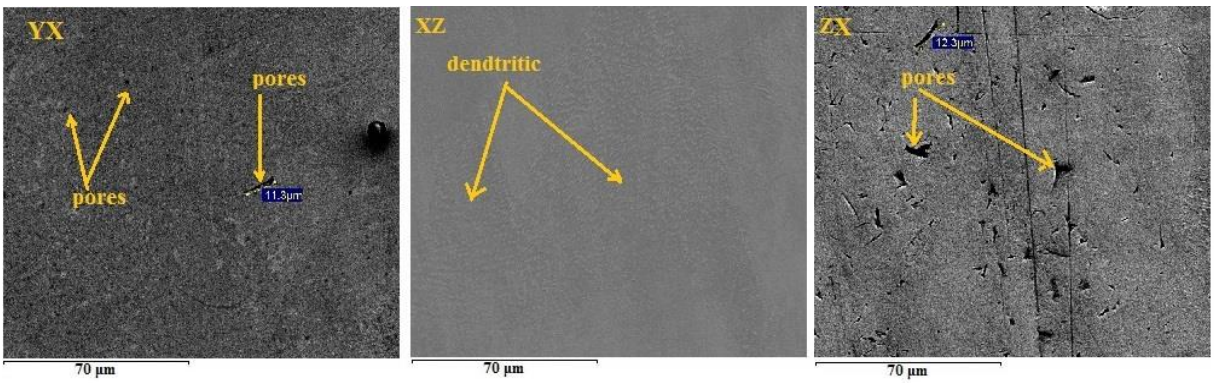

Fig 6.3: Typical SEM images for top side walls' views of 316L stainless steel parts built in the *yx*, *xz*, and *zx* directions. Images obtained at a 500× magnification.

Figure 6.4 presents the OM and SEM images of the *xz* build direction sample where the dendrite arms were normal to the surface. This structure showed that the solidification is dendritic or cellular, with a size of about 3 µm. In addition, Figure 6.4b shows higher magnification that reveals that the intercellular spacing is less than 1 µm, which contributes to the excellent strength that can be achieved, both in processed and aged conditions (Gu and Shen, 2009, Kruth *et al*., 2010, Cherry *et al*., 2015). Through previous research on SLM processing, Takalo *et al.* have found that these microstructures are common, and are formed as result of high thermal gradients and rapid solidification, due to a very high cooling rate. Their results also found that this microstructure helps to reduce crack nucleation at the pores between the scan tracks (Takalo *et al*., 1979). The mechanical properties significantly increase as a result of the amount of primary austenite dendrites in the multi alloy. This microstructure has been reported in previous studies, and this was explained by the relationship between the dendrites and the mechanical properties (Kaiser *et al*., 2013).

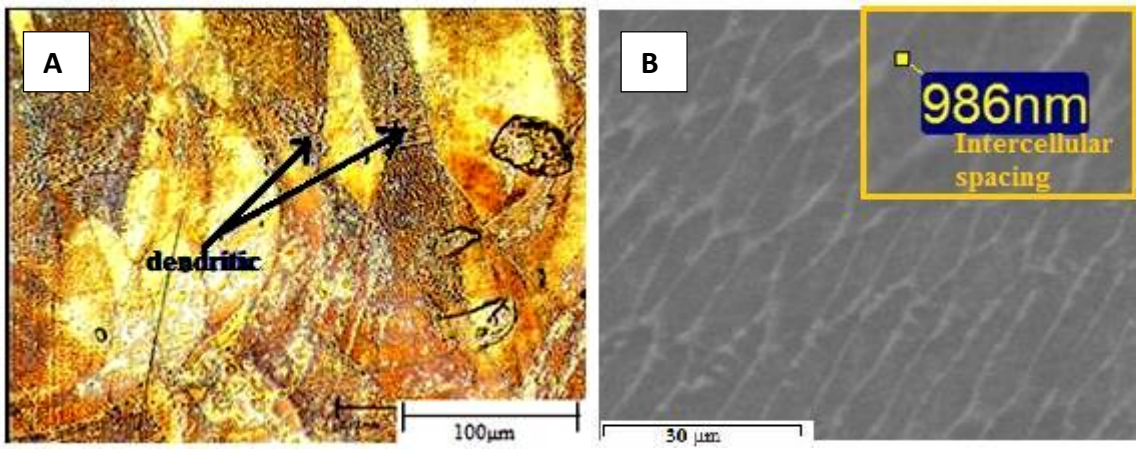

Fig 6. 4: Metallographic and SEM images of the microstructure of the *xz* build direction sample; (a) An OM (metallographic) image showing dendritic arms from the side view of the 316L sample, and (b) an SEM image at 1000 × magnification reveals dendritic arms.

To summarise, there is a correlation between dendrite arm spacing and mechanical properties, for instance, in the yield strength, hardness and ultimate tensile strength (Chirita *et al*., 2010). Generally, an improvement in the microstructure or grains leads to improved mechanical properties. The dendrite arm spacing was found to be significantly affected by the different cooling conditions (Ejiofor and Reddy, 1997). So, it is important to understand the microstructure of materials from different viewpoints, because the overlapping of the laser's scanning track can produce defects, such as cracks and voids. Such defects, when located at the interface between the rows (previous melting tracks) and scanning tracks, are known to produce a point that is vulnerable to crack growth, since the temperature gradient and local heat transfer conditions determine the grain growth in the parts that are produced by SLM (Kruth *et al*., 2010). This means that changes in the process parameter, as well as in the build direction, affect the microstructure of the parts, which leads to changes in the mechanical properties. These changes could be increased with an augmentation in the cooling rate, while the ductility is decreased gradually (Osorio *et al*., 2006, Mallapur *et al*., 2010, Kaiser *et al*., 2013).

6.3.3 Mechanical properties

6.3.3.1 Tensile test

Table 6.1 reveals the average of tensile test and Figure 6.5 reveals the tensile stress-strain curves for one test that were calculated for the *yx*, *xz* and *zx* build directions. The initial slope of the stress strain curve in this figure is usually called Young's modulus. The total elongation to failure, the ultimate and the yield strengths were determined after examination of the plastic and elastic parts of the curve. The total elongations were found to be between 35% and 41%, and these results agree with those from previous studies carried out by John and Yang *et al.* The ultimate tensile strength recorded a large difference from 564 MPa for the *zx* samples, to 695 MPa for the *xz* samples (standard deviation ±3 MPa) (John, 2001) (Yang *et al*., 2012b). The minimum value of UTS was recorded in the *zx* samples, because of the residual stress that remains in the parts, which influences the mechanical properties. The number of irregular pores and unique microstructures in the *zx* samples also influences the tensile properties. This variation in the microstructure related to the different build orientations causes the anisotropy (Vrancken, 2014, Leuders, 2014, Riemer, 2014). More details about the anisotropy for different build orientations were explained in Section 3.4.1. The presence of a weak region between the scanning tracks and the melted layers, where all the fractures occurred, can reduce the UTS value in the *zx* direction. On the other hand, the yield strength varied from 387 MPa, in the *zx* samples, to 423 MPa, in the *xz* samples. This value was larger than previously published values of 261 MPa (de Lima and Sankaré, 2014, John, 2001) and those for wrought 316L stainless steel (Yadroitsev, 2009).

This enhancement in the tensile properties was due to the proper selection of the process parameters. For example, the width of the hatch spacing (70 μm) was reasonable in order to ensure good consolidation. This contrasted to a value of 120 μm, which had been applied previously by de Lima and Sankaré, and which was to leave some gaps where the metal was un-melted, or partially melted, between the tracks. In Table 6.1, it was noted that the samples built in the *xz* direction showed the highest performance. This is due to their having fewer defects, such as irregular pores and finer grains (dendritic microstructures), as shown in Figures 6.4(a) and 6.4(b), and that are key factors in the enhancement of the properties of the metal, as discussed in Section 3.4.1 for an anisotropic microstructure. Generally, the tensile properties obtained in this experiment are high, if compared to previous studies, and they seem to be usable for aerospace applications. Consequently, the mechanical properties of the

SLM of 316L stainless steel depend not only on the material composition, but also on the build direction. In the meantime, it must be borne in mind that the defects, such as cracks and pores, which occur following the SLM process, can be reduced by post-process treatment and residual stress relief, in order to further improve the tensile strength and the fracture toughness. For more details about these treatments see Section 2.3.

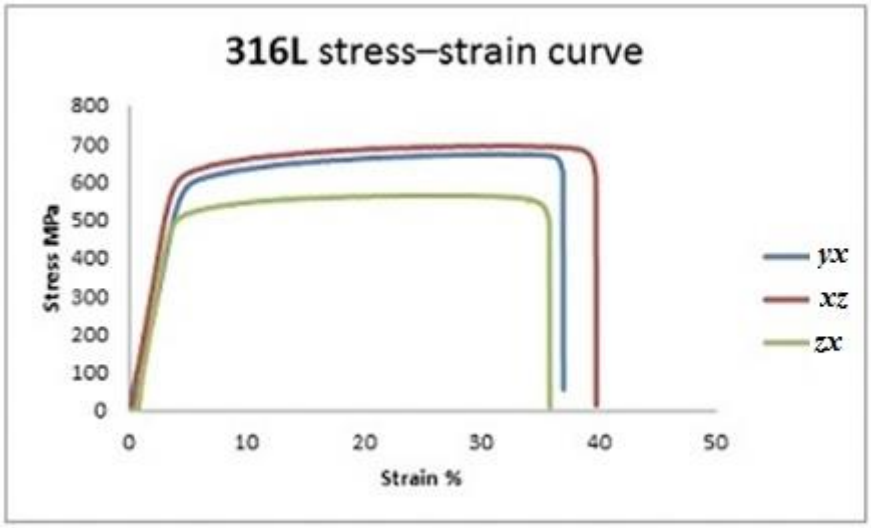

Fig 6.5: Tensile stress–strain curve for the SLM of 316L stainless steel built in different directions.

Table 6.1: Tensile properties obtained from the316L stainless steel made by SLM in different directions (±Stnd Dev).

As Built Samples	UTS (MPa)	Yield strength (MPa)	Elongation %
Yx	**668 ±3.4**	**397 ±4**	**37 ±1**
Xz	**695 ±2.1**	**423 ±3.3**	**41 ±1.9**
Zx	**564 ±2.5**	**387 ±1.8**	**35 ±0.6**
Wrought	**170-290**	**480-560**	**40**

6.3.3.2 Fracture toughness test

Fracture toughness results are presented in Table 6.2. These data were calculated according to the maximum flexural load by concentrating the stress in the area of the minimum cross section of the as built samples that were made in different build directions, (see Section 6.2

for test conditions). The fracture toughness varied between 145.5 MPa $m^{1/2}$ in the *zx* direction (standard deviation ± 1.1 MPa $m^{1/2}$) and 176 MPa $m^{1/2}$ in the *xz* direction (standard deviation ±0.9). These values are lower compared to the conventional method of austenitic stainless steel grade 316L, from 112 up to 278 MPa $m^{1/2}$ and for 316L annealed stainless steel at 210 MPa $m^{1/2}$ (Maloy *et al.*, 2001). These low values will probably be caused by the cracks, pores and voids in the parts produced, as well as by the residual stress that remains in the 316L parts after the SLM process. There are other reasons that affect the mechanical properties of materials, especially the fracture toughness and for more details see Section 3.4.2.

The differences in the fracture toughness values obtained in this study by the use of different build directions has been anticipated by previous investigations, as mentioned in Section 6.3.2. The tensile test results also showed that the samples built in the *xz* direction recorded the highest values of UTS and elongation, meaning that there is a larger area under the stress-strain curve, i.e., the material absorbs more energy before failure. These combined values enhance the fracture toughness of the parts built in the *xz* direction due to the fast cooling rate and the resulting dendritic grain structure (Seifi, 2016a). On the other hand, parts built in the *yx* and *zx* directions presented slightly lower values of fracture toughness than those built in the *xz* direction, because of the more prevalent and larger irregular pores and defects, especially in the samples built in the *zx* direction, as shown in Figure 6.6 in relation to the fracture surface, and which were subjected to loading perpendicularly to the build direction. The results in Table 6.2 reveal that the build orientation has a strong effect upon properties. For example, fracture toughness was smallest in the samples built in the *zx* direction, due to the defects present that are evident perpendicular to the build direction samples, which contribute to the reduction of the fracture toughness values. The microstructural variances along, and perpendicular to the build direction, can contribute to a decrease in the fracture toughness values (Seifi, 2016a). Furthermore, Figure 6.6(c) shows the fracture surface of the *zx* sample, which reveals process induced defects, such as pores, voids and cracks, present at the edge of the parts.

In summary, the toughness is the ability of a material to resist the growth of cracks. The key to toughness is also a good combination of high ductility and strength, and, according to the results obtained in this study these alloys appear to have properties matching these criteria.

Further treatments, such as a HIP, could reduce the amount of residual stress. Re-melting of parts is could also reduce the defects that are mentioned above.

Table 6.2: Mean fracture toughness of 316L stainless steel samples made by SLM in different build directions

As Built Sample	**Fracture toughness (**MPa $m^{1/2}$ **)**	**±Stnd Dev (**MPa $m^{1/2}$**)**
yx	**152.6**	**±1.16**
xz	**176**	**±0.9**
zx	**145.5**	**±1.1**

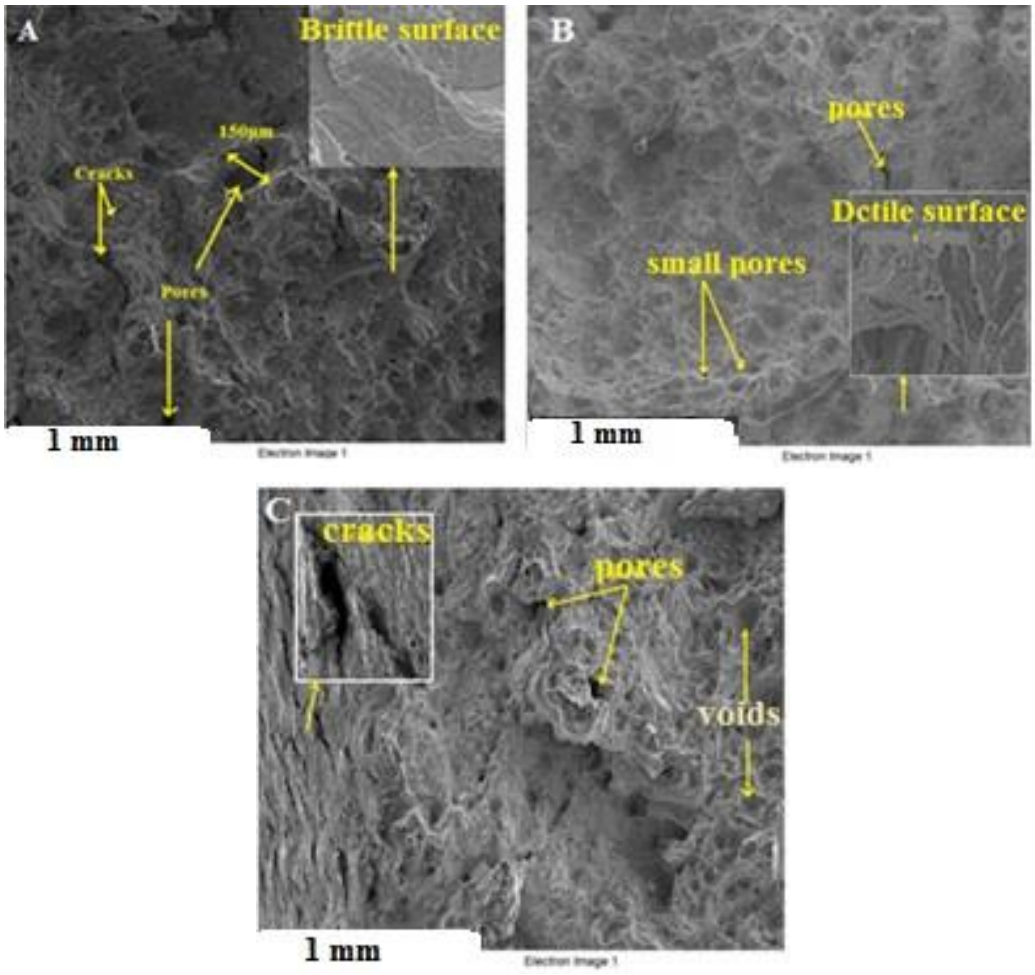

Fig 6.6: Typical SEM images at 30× .magnification of the fracture surface of 316L stainless steel samples made by SLM, in the (a) *yx*, (b) *xz*, and (c) *zx* build directions.

6.3.3.3 Vickers Hardness Test

The VH test for as-built samples, built in different orientations, was found to demonstrate small differences; 226 HV was found for the *yx* samples, and 221 HV, in the *xz* and *zx* samples. The *xz* build had the lowest value of hardness, which means that the samples that were built in this direction have more ductility than those built in other directions (as can be noticed in Figure 6.5). The parts built in the *zx* direction also have a low hardness due to porosity (see Table 6.7). The result presented in this study is similar to those found in conventional products that are made from this alloy, and those shown in a previous study of SLM 316L (Cherry *et al.*, 2015).

Table 6.3: Vickers Hardness result of 316L stainless steel.

Build Direction	**Vickers Hardness ±HV**	**±Stnd Dev HV**
yx	**226**	**1.0**
xz	**221**	**1.2**
zx	**221**	**1.1**

As defined in Section 5.3.3, hardness is the term used to describe the amount of energy required to permanently deform (stretch, bend, compress, etc.) a material. Toughness describes the energy required for fracture. It is often the case that hard materials are not tough, and vice versa (Osakada and Shiomi, 2006) In this study, the *xz* samples paradoxically showed the lowest hardness, as shown in Figure 6.7, but they also demonstrated the highest fracture toughness, as well as the highest strength and ductility values at 695 MPa and 41 %, respectively.

The low hardness samples achieve the highest fracture toughness, where the toughness is how much deformation a material can withstand before fracture. Hardness is a material's resistance to plastic deformation and, strength is a maximum amount of stress a material can withstand before deforming (Necking). Since the ductility increased by reducing the yielding point of the material, and from Figure 6.5, there is no big difference between the yielding point for the *xz* and *yx* samples, the *xz* samples achieve the highest strength and ductility.

Thus, the difference in ductility values between *xz* and *yx* samples could be due to the difference in the build strategies, which make a different in the plastic deformation stages (Uniform deformation stage or Necking deformation stage).

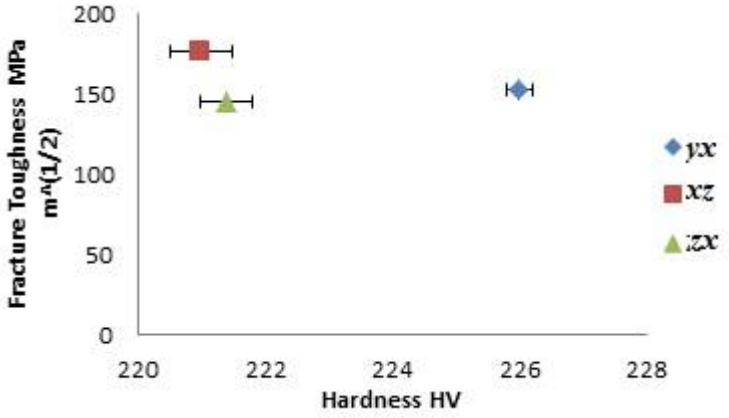

Fig 6.7: Fracture toughness of 316L stainless steel plotted against the hardness.

6.3.4 Surface quality

Figure 6.8 show that the surface roughness and the quality of the components produced by SLM of 316L stainless steel does not vary with build direction. Roughness does vary between surfaces parallel and perpendicular to the build direction. Perpendicular surfaces presented the highest values of roughness, with an average of Ra 4.25 μm (standard deviation of 0.5 μm), while surfaces parallel to the build direction had an average Ra of 3.1 μm (standard deviation of 0.2 μm). These differences are related to the occurrence of an elevated solidification ridge at the edge of the sample, see Figure 6.9a. These ridges may affect the dimensional accuracy of a part. However, the parallel surfaces were affected by partially melted powder particles that were clinging to the surface. Mumtaz and Hopkinson found that surface roughness was generated by the rippling effect that can occur during SLM, when the laser, moving the temperature gradient between the solidifying zone, produces a shear force on the liquid surface, which is contrasted by the surface tension force (Mumtaz and Hopkinson, 2010). This shear force results in the formation of residual rippling on the surface, as the relaxation process could not be fully realised on occasions, due to the extremely short solidification times of the melt pool, (Kruth *et al*., 2010, Strano *et al*., 2013b). These experimental results agree well with previous studies (Badrossamay and Childs, 2006, Rombouts *et al*., 2005, Chen *et al*., 2004), which showed that SLM has not yet

achieved a high surface quality of components. This is still one of the major drawbacks of the process, particularly in the fabrication of high performance aerospace components. This issue has to be further addressed by applying new process parameters, such as re melting, which has been applied previously, thus to reduce the surface roughness from 12 μm to 1.5 μm, as shown in Figure 6.9b (Kruth *et al.*, 2010). A number of other surface modifications can also be applied to reduce surface roughness, such as machining and etching oxidisation. The etching solution could be applied post-processing to enhance the surface quality. In this experiment, all the investigations were done for as-built samples, and without any re-melting, in order to reduce the energy consumed and the production costs.

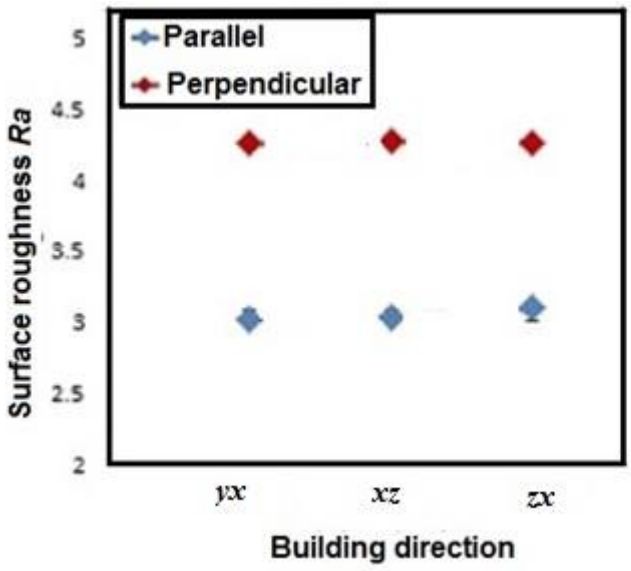

Fig 6.8: Effect of different build directions on the surface roughness of the SLM of 316L stainless steel parts made by SLM

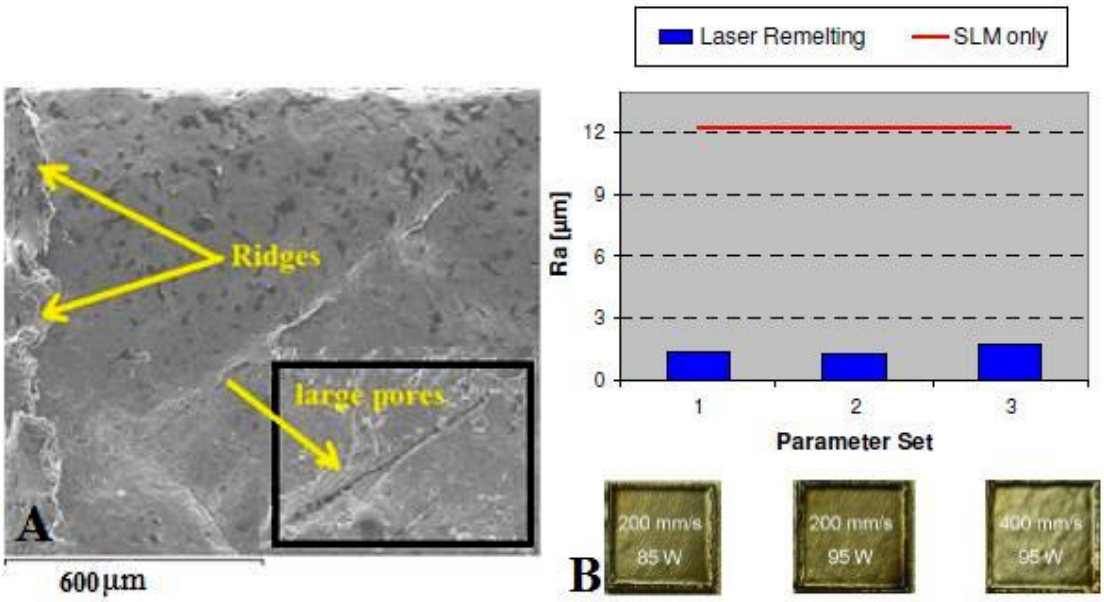

Fig 6.9: (a) A typical SEM image of an *yx* sample, and (b) Roughness values with and without laser i.e., -melting (Kruth *et al*., 2010).

6.3.5 The effect of microstructure and fabrication on the quality and mechanical properties

In terms of sample quality, the SLM process investigated in this study delivers a better surface roughness (Ra) on the surface that is parallel to the build direction. This means that the surfaces perpendicular to the laser are rougher, and this is due to the rippling effect, scan tracks and the elevated solidification ridges that arise at the edge of samples. Figure 6.9 summarises this by showing how the surfaces perpendicular to the laser have rough surfaces. However, here, these differences in surface quality are not related directly to mechanical properties. On the other hand, these results have proven that the build direction has an influence on the microstructure of the samples produced, as shown in Figures 6.2 and 6.3. This is because the samples built in the *zx* direction have more irregular pores with a length of from 10 to 15 µm (see Figure 6.10), and they also have more partially melted particles stacked onto the parallel surface because of the powder surrounding the samples. In contrast, samples manufactured in the *xz* direction present fewer pores and dendritic grains due to good consolidation (see Figure 6.2 and 6.4). Most pores had a spherical shape, with an average size of 8µm in all samples as shown in Figure 6.10 for the *zx* build direction sample. These microstructures gave a very clear indication of how to predict the mechanical properties of the samples. So, under these conditions, it can be concluded that the influence of the build

direction on mechanical properties is greater, due to the difference of the microstructure, especially in relation to the fracture toughness and the ultimate tensile strength.

The *xz* samples record the lowest value of hardness, which means the microstructure (the dendritic grains) have more ductility than the other samples in the *zx* and *yx* build directions, as well as high strength, see Table 6.2. This leads to a high fracture toughness value, due to the higher energy absorption of the material.

In the context of previous research, it can be concluded that the mechanical properties of the SLM of 316L stainless steel components are comparable to those made from conventional materials. (Cherry *et al.*, 2015, Kalu, 2013, Soboyejo, 2002). All of the results discussed in this experiment are only valid for the range of experimental processes that are considered in this study.

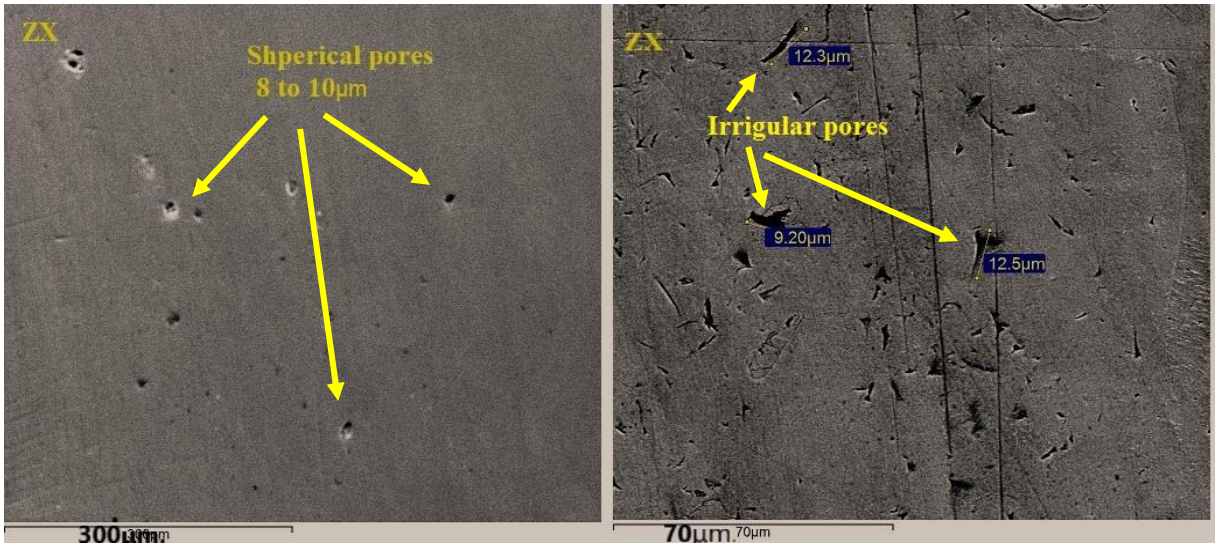

Fig 6.10: Typical SEM images reveal the pores size and shape of 316L stainless steel parts built in the yx, xz, and zx directions.

6.4 Conclusion

This chapter has been discussed the influences of density, surface quality, microstructure and mechanical properties of the components of the SLM parts made using different building orientations. The effects of different build orientations on the microstructures and the mechanical properties, especially the fracture toughness of the 316L stainless steel after it was fabricated by SLM have been concluded below, and the major findings have been summarised:

Samples fabricated in the *yx* and *zx* orientations present defects, such as pores and cracks, which affect the fracture toughness, strength and total elongation.

The density of the SLM parts is around 96%, in comparison with the conventional product in AISI 316L stainless steel.

The tensile and yield strengths are noted to be quite high, if compared to previous research. Special mention should also be given to the yield strength and the tensile strength, which are higher than those in conventional materials, while maintaining the high elongation values.

The minimum values of fracture toughness found in this study are 145.5 MPa $m^{1/2}$, and the maximum values are176 MPa $m^{1/2}$, at room temperature. These values are slightly higher than the minimum of (112 MPa $m^{1/2}$), for those in the conventional product (Maloy *et al*., 2001).

Vickers Hardness test results are similar to those found in conventional products made of this alloy, and the value of the hardness decreases with an increase in toughness.

The fracture surface and the microstructure show evidence of voids, cracks and pores in the samples produced in the *yx* and *zx* build orientations, and a few pores are present in samples with a *xz* build orientation, together with dendritic grains.

The orientation during the build affects the mechanical properties, particularly the fracture toughness. The weakest build strategy recorded was in the *zx* direction, due to the pores, voids and cracks that are present at the edges of the parts.

Dendritic grains appear in the *xz* parts due to a high temperature gradient and fast cooling, which seem to increase the toughness and ductility, although the number of pores decreases.

Most pores had aspherical shapes, with an average size of 8 μm in all parts, and in the *zx* built parts some irregular pores were present, with a length of from 10 to 15 μm.

Build orientation has a slight effect on surface roughness, with the *xz* built samples having 3.8Ra roughness, while this is increased to 4.7Ra in the *yx* and *zx* built parts. Further work, such as HIP treatment or re-melting, could improve the mechanical properties and surface roughness, and may reduce the internal stress.

With regard to the manufacture of stainless steel components for use in the aerospace industry, or in other industries where fracture toughness and strength are critical, it is clear that parts should be designed so they can be made in AM with the highest in-service load carried in the build direction *xz* direction. Furthermore, designers and manufacturers should be aware that, because of the inherent limitations of AM in surface roughness, parts will require subsequent heat treatments in order to solve stress concentration problems at sharp corners and fillets. Solidification ridges near sample edges mean that post-processing may be required if such features are critical.

Chapter 7: The influence of different build direction on the microstructure and Fatigue Crack Growth of 316L Stainless Steel made by SLM

This chapter is focused on the behaviour of 316L, made by SLM in new, different building directions under cyclical loading. Also, to understand the ability of the 316L stainless steel made by SLM to avoid early crack initiation to compensate for the remaining stress and porosity. Section 7.2 presents the experimental procedure including for samples fabrication and the FCG test. In Section 7.3.1, the results and discussion about the fatigue crack propagation test and the fracture mechanics experiments are addressed. The characteristics of the resulting microstructure to clarify the important factors of influence resulting from the microstructure and from fatigue crack propagation are addressed in Section 7.3.2. Section 7.4 summaries the main findings of this chapter.

7.1 Introduction

Fatigue crack growth is an important selection criterion for aerospace applications, because it is the final stage before the failure of the material during a gradual and irreversible reduction in residual strength due to the cyclical stresses that are experienced by an aircraft (Schijve, 1967). Currently, aerospace industries are focused on new processes that allow for the fabrication of larger parts, or of components with fairly high productivity, such as AM Technology. The advantage of this technology is in the high degree of design freedom and net shape. AM technologies are fast, and there is resource efficiency if compared to conventional methods. Consequently, AM technology offers great opportunities to meet the resource-efficient production of complex parts, particularly the SLM process, which employs a high energy laser source and metal powders (Schleifenbaum *et al*., 2011). Being able to use many different alloys to fabricate metal components, the success of the SLM process in recent years has mainly been attributed to a number of factors. New applications have been also discovered for SLM processes, e.g., the innovative fabrication of a moving coil cartridge using SLM (Riemer *et al*., 2014). In addition, these manufacturing processes have become more attractive, due to the increase in the productivity of the machines by the suppliers (Buchbinder *et al*., 2011). Finally, it has made a contribution through academic research in

order to innovate and to create a clean industrial environment (Thijs *et al*., 2013), The SLM processes through which you can manipulate the microstructure, as shown in recent research, can obtain mechanical properties similar to those of conventionally processed materials, as seen in Chapters 5 and 6. However, there are aspects that have strongly affected the mechanical properties of the components produced, for instance, internal stress resulting from high temperature gradients and high cooling rates, as well as pore defects that come with the parts produced, as discussed in Section 2.3. These defects have not been previously discussed, especially for components manufactured in different build directions, nor their effects on FCG and cyclical loading.

Different alloys have been processed using SLM, such as aluminium, titanium, steels and nickel alloys. Most of these studies that have been published have focussed on the process parameters, microstructure evaluation and material behaviour under constant loading. The fatigue properties of materials that have been processed using the DMLS and SLM methods are inadequately researched and require more study (Li *et al*., 2012, Van Hooreweder *et al*., 2012, Leuders *et al*., 2013, Riemer *et al*., 2014).

There are few studies available on stainless steel 316L, and those that are available mostly report on the effect of the remaining porosity and residual stress, the processing and effects of different surface modifications (Yasa and Kruth, 2011). There are a couple of published studies that demonstrate the FCG and HCF performance of stainless steel 316L processed by SLM (Riemer *et al*., 2014, Spierings *et al*., 2013). In addition, a recent review has summarized the FCG and HCF316L stainless steel parts produced by SLM; these studies have been discussed in Section 3.4.3. However, information on the effects of mechanical properties, crack initiation, and crack propagation under cyclical loading are needed for steel 316L components. The important questions in this chapter are: what building direction presents the highest ductility of 316L? How are these alloys able to avoid early crack initiation to compensate for the remaining stress and porosity? The current study is focused on answering this question and it investigates the behaviour of 316L, made by SLM in new, different building directions under cyclical loading. The FCG test and the fracture mechanics experiments were carried out, and the characteristics of the resulting microstructure were investigated by optical and scanning electron microscopy to clarify the important factors of influence resulting from the microstructure and from FCG.

7.2 Sample preparation and experimental methods

In this study, nine stainless steel 316L samples with standardized geometries were manufactured in three different building directions, *yx*, *xz* and *zx*, for the investigation of crack growth (see Figure 7.1). The samples were processed using SLM with a maximum power of 200W. Layers of 30 μm thickness were fabricated using a stainless steel 316L powder with a scan speed of 1600 mm s^{-1} , and a laser power of 180 W.

Analyses of crack growth behaviour in SLM samples were carried out using CT-samples (see Section 4.5.4 for design), manufactured according to ASTM E647-08 (Mohanty *et al*., 2010) with a crack length of 11.7 mm., specimen thickness of 5 mm and width of 26 mm. Three different directions were considered. Crack growth was determined parallel and perpendicular to the build direction, with a minimum of three samples being used for each test series. All tests were carried out using an INSTRON servo hydraulic 8874 testing machines at a frequency of 10 Hz, minimum load 0.6 KN, maximum load 6 KN, for a load cycle, and a stress intensity factor ratio of R = 0.1.

For the characterisation of the microstructure and fracture surface of all of the SLM samples an X-ray Diffraction (XRD) and SEM were used in this study.

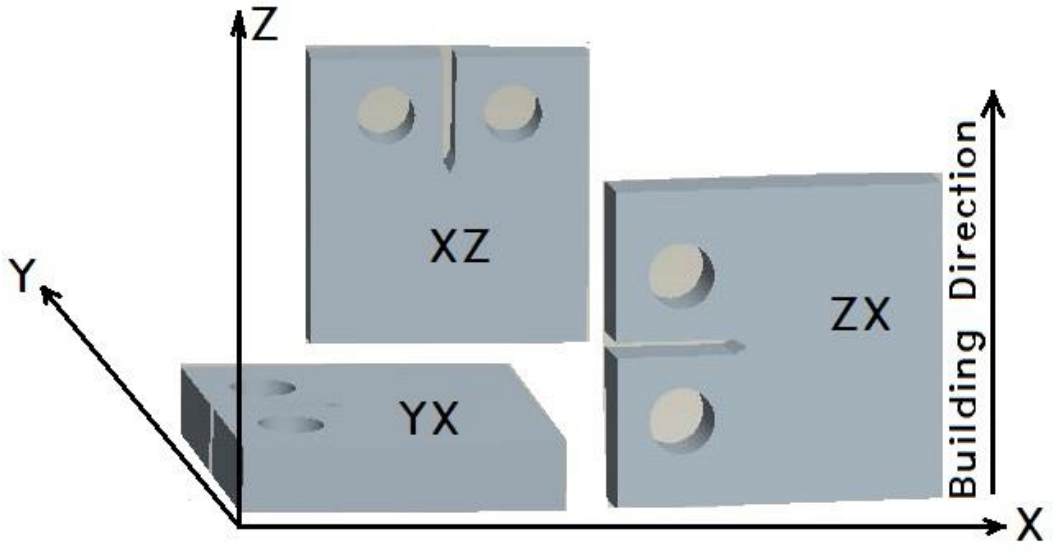

Fig 7.1: Schematic illustrations of CT samples in three different building directions for FC tests

7.3 Results and discussion

7.3.1 Fatigue crack growth and failure behaviour

Figure 7.2 shows the FCG data, the adjusted crack length values and the corresponding load cycles that were generated by the FCG testing. The total number of cycles prior to unstable crack growth was determined. The results obtained show different FCG behaviour for each orientation. The sample in the *zx* orientation revealed that the crack propagation perpendicular to the build direction withstood up to 600,000 cycles with no sign of cracking. Beyond this the cracks began to propagate to a length of 21 mm. at 1,550,000 cycles, and completely failed; thus, a cycle account of approximately 600,000 cycles was required to induce unstable crack propagation. The sample in the *xz* orientation, where a crack propagates parallel to the build direction, showed no sign of cracking up to 1,150,000 loading cycles. A crack then started to propagate gradually until 1,550,000 cycles with a 21mm length. This means that this build direction showed good ductility performance. The samples built in the *yx* orientation recorded that there were no signs of cracking up to 700,000 cycles, and only a small amount of cracking started with a length of 1 mm. at 800,000 cycles. After 820,000 cycles, the crack propagated suddenly to 18 mm. and the samples completely failed at 919,280 cycles. The samples in the *zx* and *xz* directions recorded the highest number of cycles, while the xy sample failure was noted at a low number of cycles and revealed that the crack growth behaviour was influenced by the different build directions; the build direction has been shown to affect the microstructure of the material produced, as described in Chapter 6 and Section 3.4.3. The non-uniform grain structure and the presence of induced process defects; such as residual stress, were the main reasons for the decrease in the fatigue life, especially in samples built in the *yx* orientation. It is obvious that the number of cycles required for complete failure in the *yx* sample decreased by approximately 30% in comparison to samples in the *zx* and *xz* orientations. Previous literature on the FCG for 316L stainless steel found that the finer grains resulted in a decrease in the FCG rate (Riemer *et al*., 2014). Consequently, the differences in the crack propagating behaviour between samples (see, Figure 3) with different building orientations must be clarified on a microstructural basis, emphasising the role of the grain shape and size (see Section 7.3.2).

7.3.2 Fracture surface and microstructure analysis

The SEM analysis highlights different fracture surfaces that are invariant in appearance to build directions (see Figure 7.5a-f). The fracture surfaces of both vertical and horizontal samples indicate the role played by the microstructural features on the ductility and strength of SLM built samples. The overall view of the FCG in the fracture surfaces of the vertical direction samples showed a ductile topography, see (Figures 7.5c, d, e and f) and (Figures 7.4a and 7.4b), which reveal the crack growth path and the microstructure of the samples. The fracture surfaces of the samples that were built in the *zx* direction show the main cause of fracture, micro cracks and voids, as is the case for typical SLM produced stainless steel parts (see Figures 7.5c and d) Plastic deformation coupled with shear deformation have been revealed in the fracture surfaces of *zx* samples because of the above work rate (the cyclical loading) of the alloy. The cracks propagate parallel to the build layers i.e. perpendicular to the build direction. It is also noted that the fatigue cracks that are initiated form shear slip bands, and these are followed by regions of stable crack propagation. Figures 7.5e and 7.5f reveal the fracture surfaces of samples in the *xz* series, which show that shallow dimples cover the overloading area, indicating the mechanism of the ductile rupture failure. The fracture surface is also free from any cracks or voids at low magnification, as seen in Figures 7.5e and 7.5f, which clearly distinguishes the region of crack initiation and the steady crack propagation with the final fracture. The samples that were built in the *xz* direction showed higher resistance to FCG.

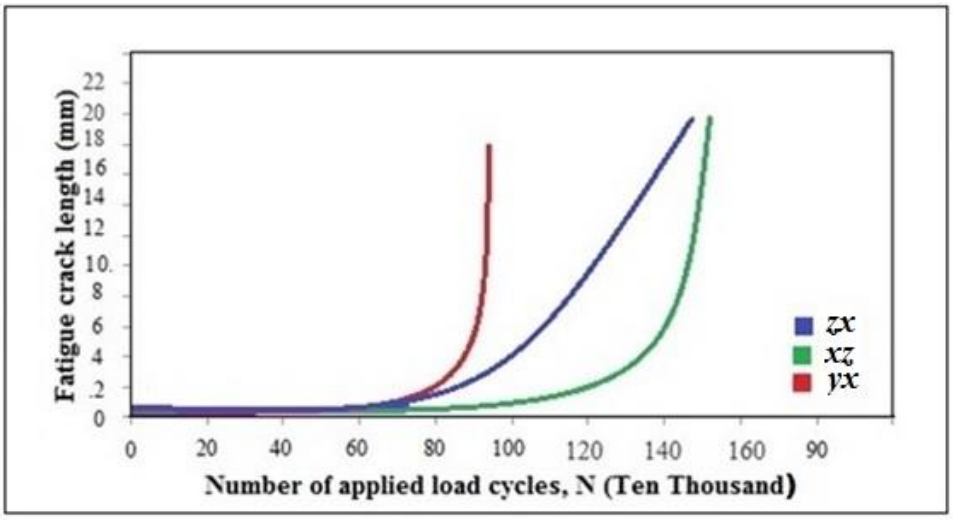

Fig 7.2: An FCG curves for 316L stainless steel samples produced in different build directions under cyclical loading.

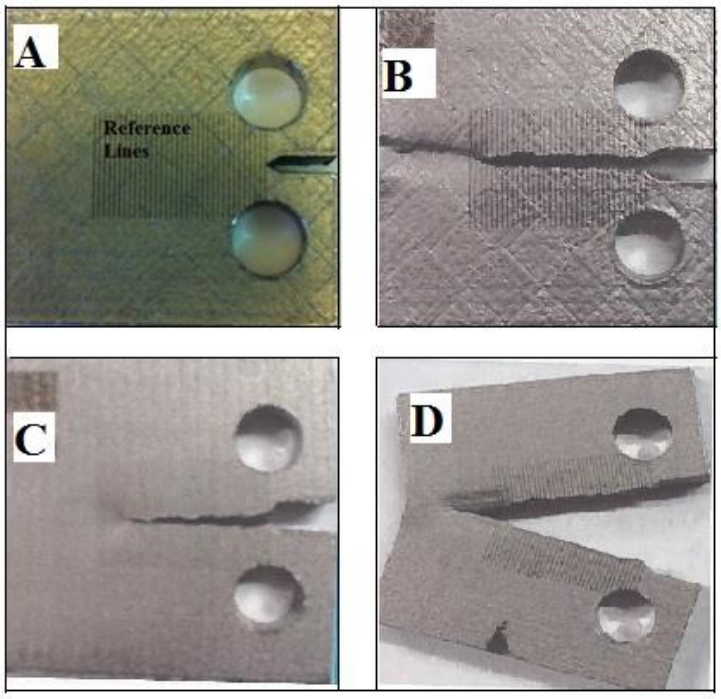

Fig 7.3: An FCG samples in different orientations (a) before testing, (b) *yx* orientation, (c) *xz* orientation, and (d) *zx* orientation after testing

The fracture surfaces of horizontally built samples reveal a fracture mode that is similar to those observed in the samples built in the vertical direction. Figures 7.5a and 7.5b show typical fracture surfaces of samples that were built in the *yx* direction. A mixed mode of ductile and brittle failure mechanisms was observed in these samples, and the voids present in some locations also act as crack initiation sites. Craters are also formed, and these are possibly caused by the pulling out of the material surrounding the voids. On the other hand, cleavage-like flat facets are present in the surface fractures of the *yx* samples, characteristic of brittle fracture (see Figure 7.4c). Previous studies have reported a similar fracture surfaces for austenitic stainless steel samples tested at a high strain rate (Ganesh *et al*., 2014, Tomota *et al*., 1998, Wang *et al*., 2008). In general, FCG is dependent on the initiation and growth of cracks, where crack initiation takes up much of the overall fatigue life (Oh *et al*., 2003). Crack initiation depends on various factors, for instance; microstructure, surface condition and the presence of secondary particles in the material, together with flaws (Rafi *et al*., 2013). However, in this study, the other reasons for crack initiation are likely to be due to the residual stress defect and the different build directions. These are factors that affect the fatigue life and can make fatigue failure easier in the case of the propagation of the crack perpendicularly to the build direction. In addition, the rapid cooling rate during SLM,

especially in the vertical direction samples, has a fine microstructure that leads to high toughness and stable crack growth during fatigue. More research is still required to understand the FCG of 316L stainless steel parts that are made by SLM using different processing and surface conditions.

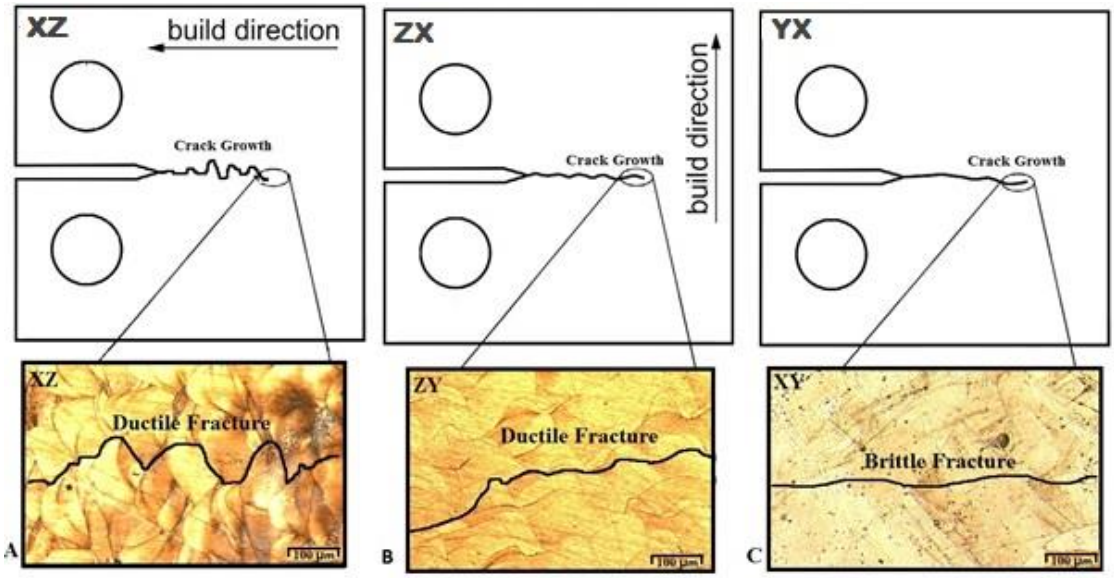

Fig 7.4: Shows crack path, microstructure and morphology dependent on building direction (a) *xz* orientation (b) *zx* orientation, and (c) *yx* orientation

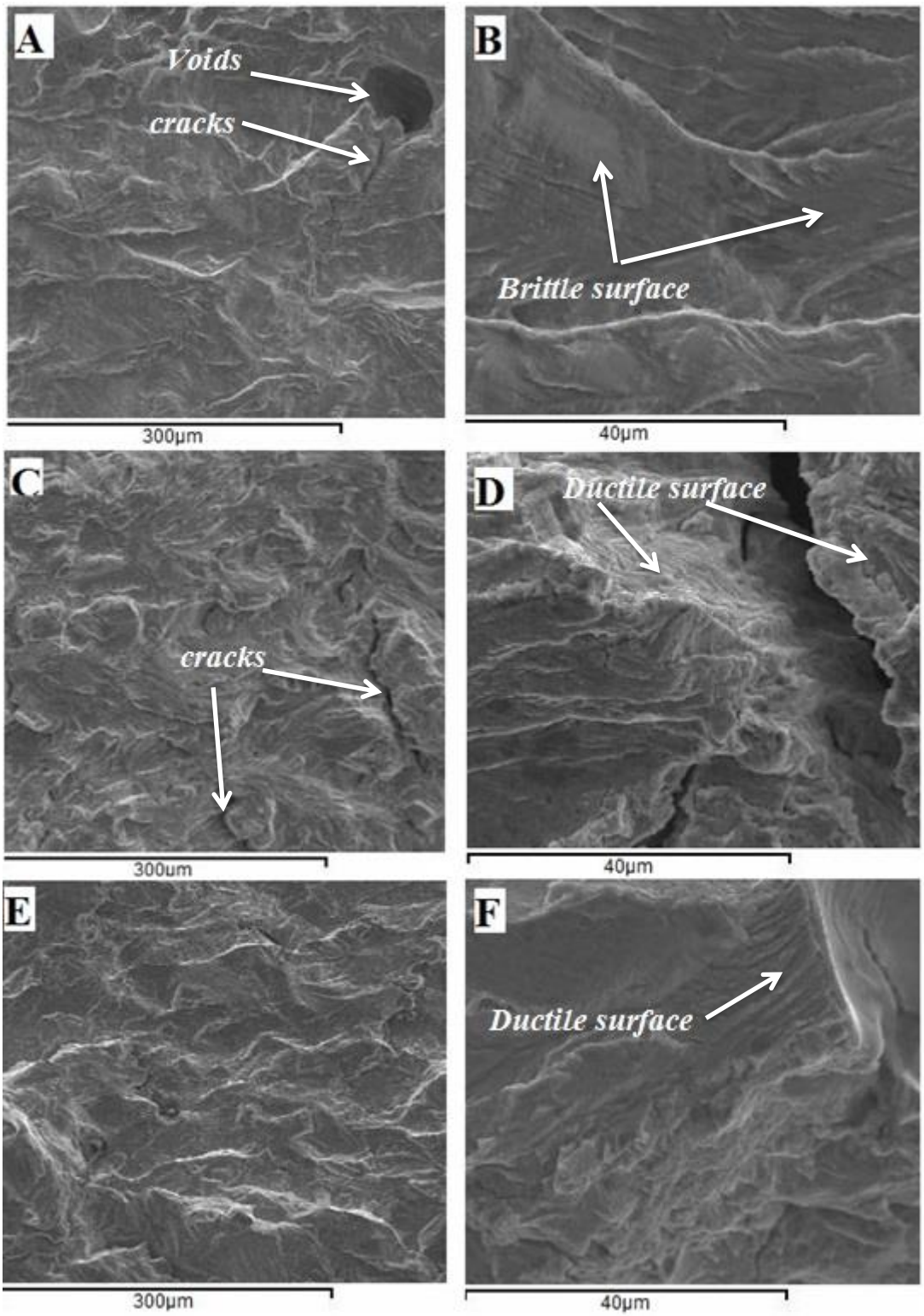

Figure 7.5: Typical SEM images of the 316L stainless steel fracture surfaces at different build directions. (A, B) in the *yx* direction, (C, D) in the *zx* orientation, and (E, F) in the *xz* orientation

7.4 Conclusions

The main study in this chapter was to evaluate the FCG behaviour of 316L stainless steel manufactured by SLM. Tests for the crack initiation, crack growth, microstructure and defects were conducted. After analysing the outcomes, the following conclusions can be drawn:

A high number of cycles were recorded in the samples that were built in the *zx* and *xz* orientation, and the *yx* sample revealed a low number of cycles, which meant that the crack growth behaviour is influenced by different microstructures in different build directions.
Ductility was higher than for other comparable materials, notably those built in the vertical orientation. These samples also have a fine microstructure leading to good fatigue performance, because of the rapid cooling rate during the SLM process.

The fatigue life of samples built in the *yx* orientation decreased by approximately 30% in comparison to those samples that were built in the *zx* and *xz* orientations. This is attributed to the non-uniform grain structure, which is due to the different build orientations, and defects produced during the process, such as a presence of cracks, pores and the internal stress that remains.

The fatigue life is affected by different build directions, which can make failure easier in the case of crack growth that runs perpendicularly to the build direction, and the highest resistance to FCG samples was shown in the *xz* orientation. It is recommended that uses of such components should be restricted to those built in the *zx* and *xz* directions.

The fracture surfaces of the SLM 316L stainless steel samples reveal that plastic deformation is coupled with the shear deformation in the *zx* orientation sample, while cleavage present in the *yx* orientation sample is characteristic of a brittle fracture.

Chapter 8: Fracture toughness and the tensile strength of 316L stainless steel cellular lattice structures manufactured using the selective laser melting technique.

Chapter 8 evaluates the manufacturability of 316L stainless steel cellular structure and the effect of different build orientations on mechanical properties of 316L stainless steel cellular structure made by SLM. The evaluation is given to the cellular structure for lightweight applications to provide understanding on their geometrical and mechanical characterisation. Also, is present a new method is presented to predict the fracture toughness of SLM 316L cellular structure by using Ashby and Gibson micromechanical modelling. The design procedure and software tools used for generating cellular structure are presented in Section 8.2.1. The samples fabrication and mechanical tests procedure are addressed in Sections 8.2.2 and 8.2.3, respectively. The result and discussion are addressed in Section 8.3, which include the effect of different build direction on density, tensile and fracture toughness of 316L cellular structure. Finally, the major findings are summarised in section 8.4.

8.1 Introduction

Today, most of the research into aerospace applications tends to be focused on increasing energy efficiency and reducing fuel consumption and exhaust emissions. Extensive efforts are still needed, however, to find ways of reducing the components' overall material consumption and weight, thereby saving increasingly scarce natural resources and saving fuel consumption. Many previous studies have examined the use of high specific strength materials for this purpose, such as magnesium, aluminium, titanium and high strength steels (Brungs, 1997, Boyer, 1996, Kuziak *et al.*, 2008). Other research has focused on structural design adaptations to the actual loading condition, such as sandwich design, which helps to reduce weight by stiffness or by reducing the numbers of joining elements (Degischer, 2009). These strategies still however require highly complex geometries to be reliably produced, and in practice this confronts the manufacturing method with substantial challenges.

Additive Manufacturing Technologies, such as the SLM technique, allow complex 3D lattice structures to be produced (Osakada and Shiomi, 2006, Yan *et al*., 2012) while also reducing the time and costs of production. Parthasarathy (Parthasarathy *et al*., 2010) has found that AM technologies allow flexibility of design and provide very few feature sizes for the fabricating of closed or open cell structures with locally variable stiffness and optimized compatibility. Currently, there is great demand for lightweight components in aerospace applications in order to reduce the rate of fuel consumption and carbon emissions, and this requires more effort to improve the performance of the lightweight structures that are produced. In the aerospace sector, Ti6Al4V alloys are also promising, due to their balanced and well-studied properties. Current studies on lightweight structures in the field of AM have investigated the influence of process parameters on the quality of the parts produced, such as laser power and scanning speed, or the layer thickness of powder and the resulting mechanical behaviour (Yadroitsev and Smurov, 2010).

Lattice structures are well known, and their excellent low density and thus good specific properties, are used widely in the aerospace and other transport sectors (Thijs, 2013, Su, 2003, Ghosh, 2011). There are commercial suppliers of metallic lattice materials. The porous nature of these materials means they require a different set of manufacturing processes, tending to make them more expensive than conventional alternatives, such as honeycombs or advanced alloy solids. The influence of cell size and volume fraction on the quality of the parts and their effect on mechanical behaviour have also been explored (Hussein *et al*., 2013) (Yan *et al*., 2012). A few studies have addressed the failure mode and the mechanical performance of different 3D metallic AM lightweight structures (McKown *et al*., 2008). Brenne *et al*. studied the local deformation behaviour of cellular structures in order to investigate the failure characteristics of the parts that are subjected to uniaxial loading (Brenne *et al*., 2013).

In this context, the present study has sought to investigate the local failure mechanism of a cellular 316L stainless steel structure that is manufactured by SLM under uniaxial tension loading. A fracture toughness test was conducted in order to evaluate the effect of utilising different build directions for the 316L AM cellular parts. The results obtained from the fracture toughness tests were compared with the Ashby and Gibson model(Gibson and Ashby, 1999). The tensile strength and the elongation of the 316L stainless steel cellular structure were also addressed. The SEM, X-ray Computed Tomography, and OM were used

to examine the microstructural changes in both tensile test samples and SENB samples during fracture.

8.2 Experimental Procedure

8.2.1 Materials and cellular lattice structure design

All of the cellular lattice structure samples were made from a 316L stainless steel powder with an average particle size of 30 ± 10μm. The powder was almost spherical in shape, which led to good flow ability. This sample also had a narrow distribution of particle sizes and some irregular particles sticking to it, with the smaller sizes between 3 to 10μm, which resulted in a rough surface, as discussed in Section 4.1.2 and shown in Figure 4.2. The CAD software provided by Simpleware Ltd, UK, was used to generate the cellular lattice structure samples with the gyroid unit cell model, as shown in Figure 8.1. The gyroid unit cell (see Figure 8.1a) and the lattice structures, were mathematically defined, and studied at different cell sizes and volume fractions (Yan *et al*., 2012, Olurin *et al*., 2000), which process circular struts and spherical cores with the self-supported feature extending the capability of SLM to produce cellular lattice structures. The volume fraction, or volume percentage, of the solid material in the cellular lattice structure, with the same volume of 15%, was used in all periodic lattice structures at different building directions. The cell sizes were also kept constant at 3mm, as shown in Figure 8.1b & c.

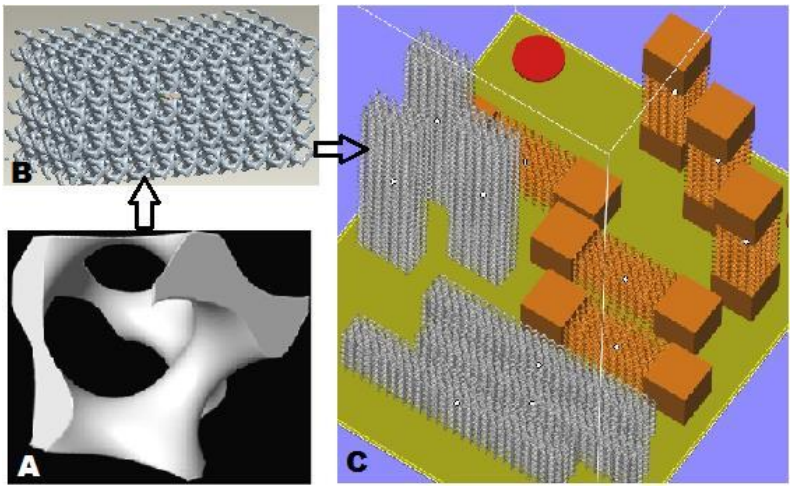

Fig 8.1: (A) CAD models of gyroid unit cell, (B) periodic cellular lattice structures, and (C) typical CAD models of samples at different design directions and their position on the platform.

8.2.2 The selective laser melting process

The SLM fabricating process was carried out on a concept laser (M1, ES Technology Ltd, UK). The SLM machine used a fibre laser with a wavelength of 1060 nm, a nominal power of 200W and a focussing diameter of between 50 to 200 μm. The laser power, scanning speed and layer thickness were 200 W, 7 m s^{-1} and 0.03 mm. respectively. Six gyroid cellular lattice structures with dimensions of 10 × 20 × 80 mm. for the SENB test, and another six with dimensions of 15 × 15 × 60 mm. were built on a base plate by the SLM process. All samples were cut off from the base plate using wire cutters (Electrical Discharge Machine EDM) - see Figure 6.2.

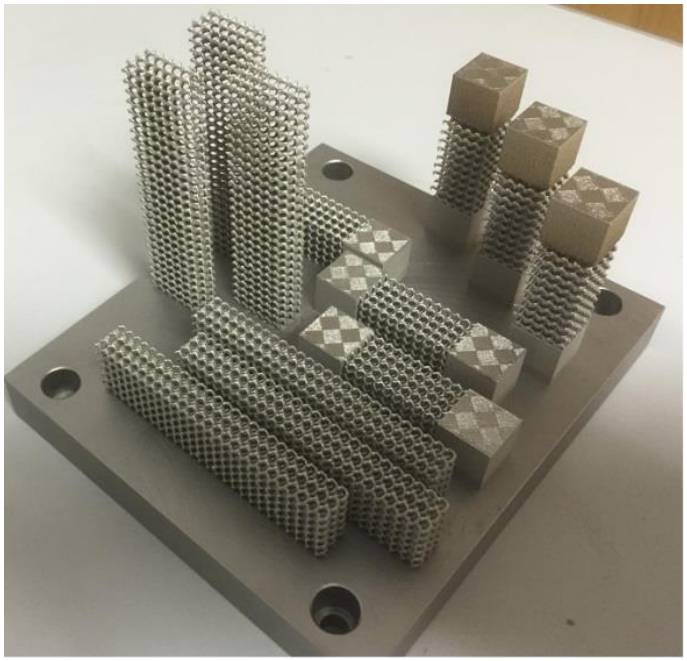

Fig 6.2: Periodic cellular lattice structures of 316L stainless steel samples in different building directions on the platform.

8.2.3 Measurements and mechanical tests

A micro-CT scanner was used to scan the lattice structure samples both before and after the mechanical testing, and two dimensional slice images were collected. Software (VGstudio MAX2.1) was used to reconstruct the three dimensional models of the manufactured lattice structure samples to determine their internal defects and the solid strut volume. The SEM was used to characterise the failure behaviour, the strut deformation and the size of the cellular lattice structure samples. An OM was used to investigate the morphologies of the

manufactured samples of the cellular lattice structures. More details about these measurements were explained in Section 4.5. The density, and the relative density, of the solid struts of the lattice cellular structures were measured. Six samples, manufactured in parallel and perpendicular to the build direction, were deformed under uniaxial tension using a 3300 Dual column universal material testing machine (Instron Instruments Ltd, UK) at a constant rate of loading 0.5 mm min^{-1}. The fracture toughness test was carried out at room temperature using an Instron hydraulic machine at a constant displacement 0.5 mm min^{-1}, the machine's model and the tests' specification were explained in Chapter 4, and for more details see Section 4.5.4. This test method was for Mode I (opening mode and pre-cracked specimens) of loading, and all data were recorded and measured to estimate the fracture toughness of the cellular lattice structures.

8.3 Results and discussion

8.3.1 Effect of different build direction on the density of the lattice structure and the solid struts

The density of the solid struts and the density of the lattice structure within the gyroid cellular structures, with different building directions, are shown in Figure 8.3. The solid strut density 7.7 g cm^{-3} was found in both the vertical and horizontal directions; while, for the lattice structures, the densities were found to be 1.35 g cm^{-3} with a standard deviation of 0.014 g cm^{-3} for both samples and they were built in both the vertical and horizontal directions. For comparison, the density of cast 316L is 8.0 g cm^{-3} (Ji *et al*., 2001). The relative density of the solid struts vs bulk cast density is thus ~96%. This low value in the relative density is confirmed by the cross-section of the CT scan image in Figure 8.4, which indicates few pores inside the struts of the lattice structure. Compared to previous studies (Yan *et al*., 2012) on the same type and size of unit cell, these results remain great. increased density could thus be achieved by optimising the processing parameters of the SLM process and the higher the density of the struts, the smaller the unit cell sizes they present (Yan *et al*., 2012).

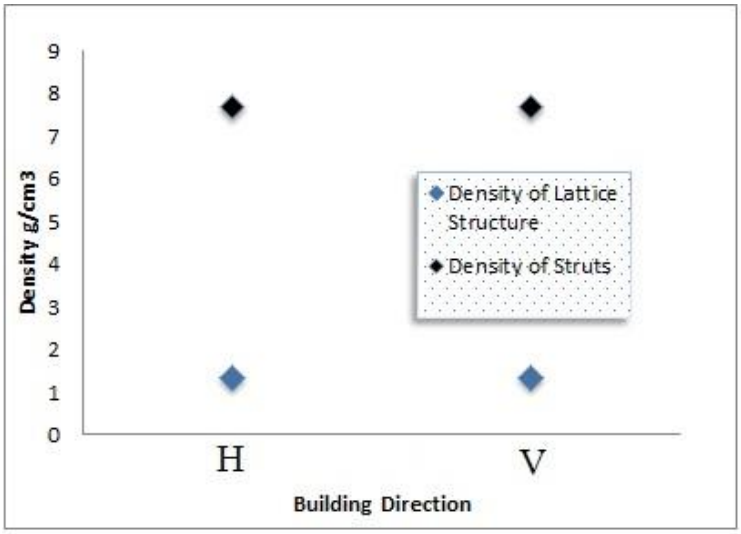

Fig 8.3: Variation of the struts' and lattice structure densities with different build directions.

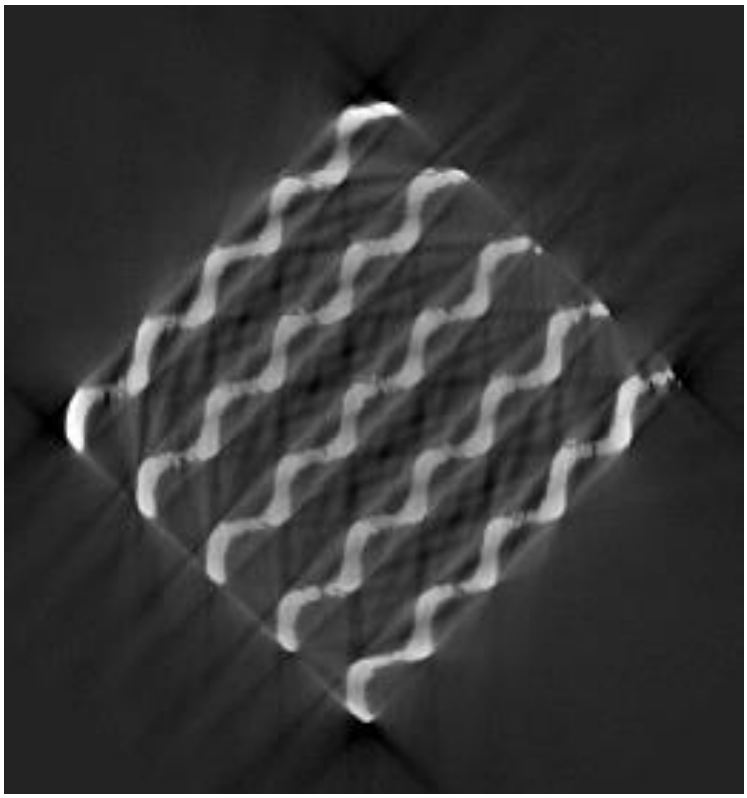

Fig 8.4: Cross section images from the micro-CT scans of the gyroid cellular lattice structures with a volume fraction of 15% and a unit cell size of 3 mm made by SLM.

8.3.2 Effect of different building direction on the strength and elongation of the lattice structure

The stress-strain curves of the tensile tests on the gyroid cellular lattice structures, with the same volume fraction of 15% and the unit cell size of 3mm, are shown in Figure 8.5. The ultimate tensile strength of bulk cast 316L is 485 MPa, and it is a ductile (Maloy *et al*., 2001), Yadroitsev, 2009). From the very beginning of the loading, the stress increases in a concave fashion and show a linear region with a high degree of linearity. This behaviour may be attributed to a good consolidation of the material. Further indication of this was there was no distortion nor defects when the samples were cut off the base plate (McKown *et al*., 2008).

The images in Figure 8.6 show the difference between the built samples and the elongation behaviour of the lattice structure samples after tensile loading. No brittle failure is visible in the photographs. The deformation throughout the testing process was a steady and smooth progression; the struts of the unit cells rotated by approximately 45°, and the alignment with the direction of the uniaxial tension load applied to the samples is attributed to the circular struts and the sphere core of the of the unit cell, as seen in Figure 8.6b. Furthermore, the area of the built samples (225 mm^2) was reduced after the tensile test to 174 mm^2 for the samples built in a vertical direction, and 169 mm^2 for the samples built in a horizontal direction; this is due to the constriction of the struts to each other and to their being expanded longitudinally.

This can be attributed to the sudden change in density and, thus, stiffness - forming a stress concentration. An SEM picture of a strut end, Figure 8.7, which shows an SEM image of a fracture strut, indicates that there was yield, ductile surface and some voids present. The centre of the sample, in Figure 8.6b, clearly shows how the end constraints affect the deformation of the cellular solid, and that the centre section is clearly not dominated by the constraint at the sample ends.

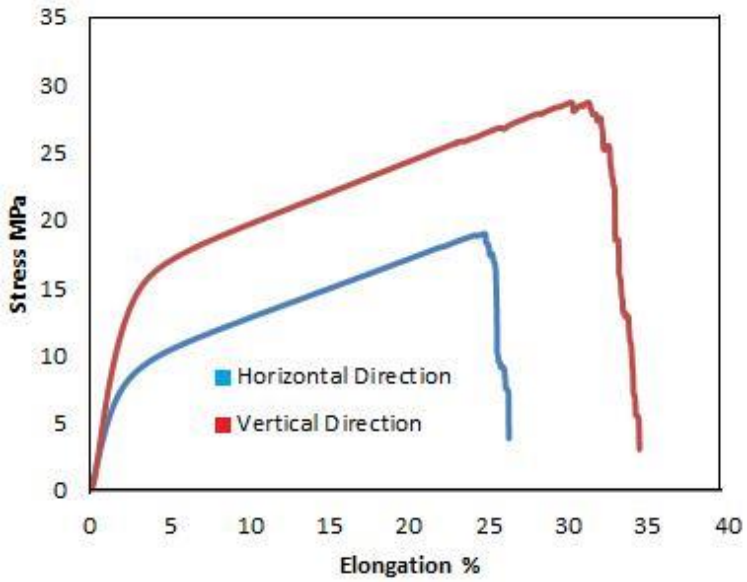

Fig 8.5: Stress-strain curves of the tensile tests on the cellular lattice structures with 15% of volume fraction and 3mm. of unit cell size.

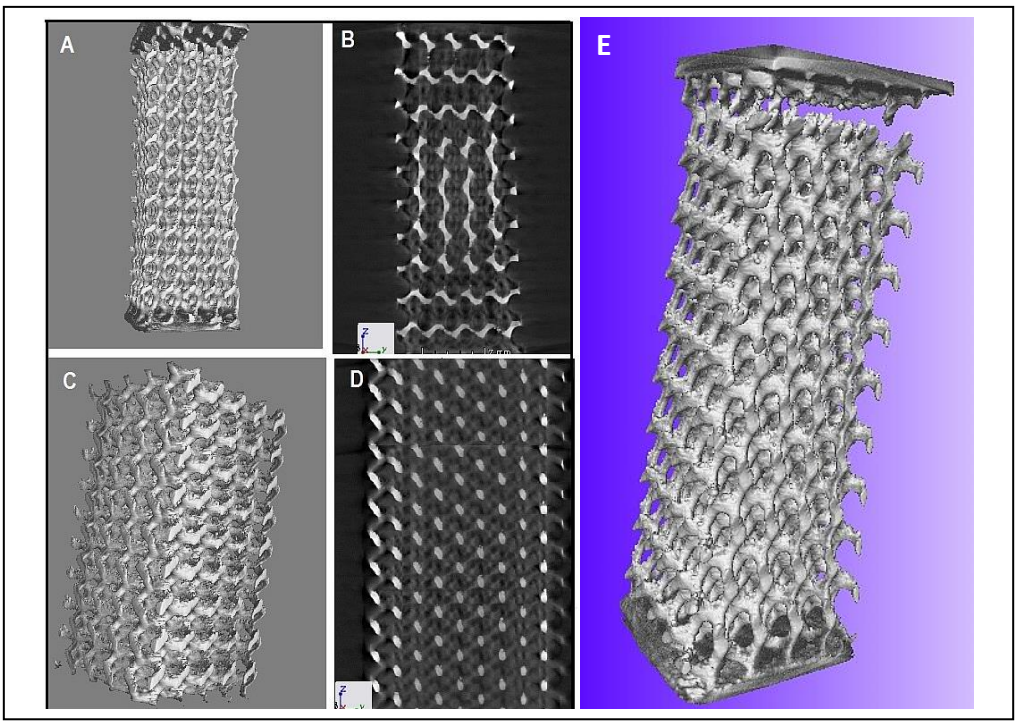

Fig 8.6: CT scans of the cellular lattice structure before and after a tensile test. Figures 8.6A and 8.6E show the sample after testing, with the detail of the rupture clearer in 8.6E. Figure 8.6B is a 2D slice through the sample after rupture, showing the rotation of internal struts. Figures 8.6C and 8.6D show the sample before testing, with B showing the internal struts in the initial un-rotated configuration.

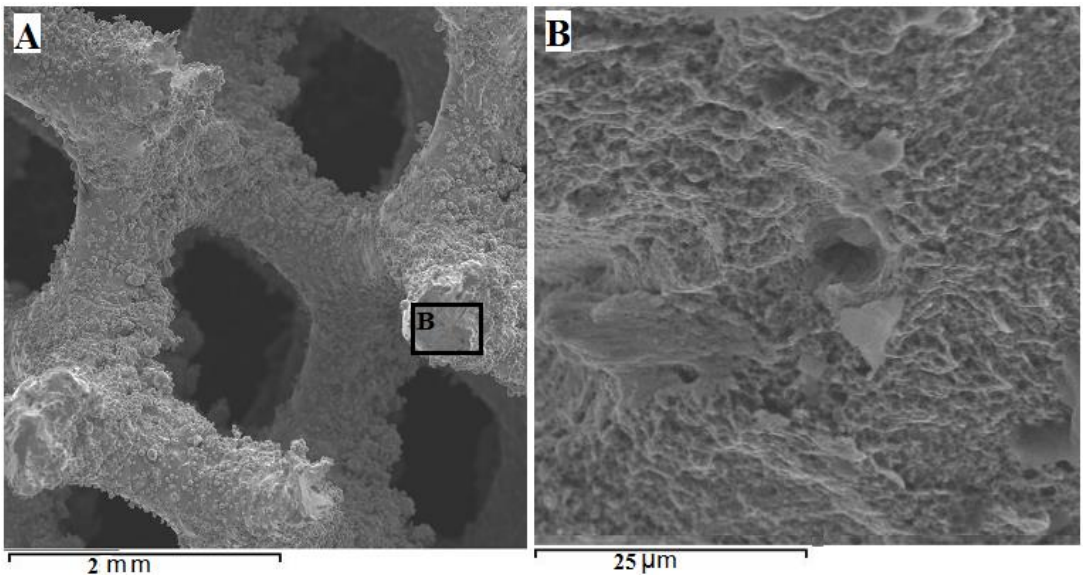

Fig 8.7: Typical SEM image of a fracture strut, at (a) 45 × magnification, and (b) 1000 × magnification, which reveal some voids and ductile fracture

Table 8.1, reveals the ultimate tensile strength, the yield strength and the elongation of the cellular lattice structures with the same volume fraction and unit cell size, 15% and 3mm., respectively. The mechanical properties of the cellular lattice structures samples that were built in a vertical orientation are higher than those built in the horizontal direction. This increase in the tensile properties is approximately 66%, and it can be attributed to the tension load direction that was applied parallel to the vertical building direction. This means the vertical struts in the vertical building direction samples that are subject to tensile tension are stronger than those built horizontally. In the samples that were built in the horizontal direction, the horizontal struts were subjected to tension load. This can cause weak struts because there was little overlap between the successive melted layers, leading to a fracture of the struts and ultimately of the structure when subjected to load. Consequently, the increase of unit cell size leads to an increase in the diameter of the struts. Thus the horizontal struts become very weak, due to the deformation of material without a support structure. The higher mechanical properties of the gyroid cellular lattice structure also further prove that the struts that are oriented parallel to the building direction, and which are perpendicular to the baseplate, have been well fabricated by SLM technology.

Table 8.1: Tensile properties obtained from the cellular lattice structures of 316L stainless steel with the same volume fraction (15%), and unit cell 3 mm. made by SLM at different building orientations.

As Built Samples	UTS (MPa) ±Stdev	yield strength (MPa) ±Stdev	Elongation % ±Stdev
Vertical	**28.5 ±0.5**	**13 ±1**	**31 ±0.9**
Horizontal	**19 ±1**	**6 ±1**	**24.5 ±0.5**
Bulk cast 316L	**485**	**170**	**40**

8.3.3 Effect of different build direction on the fracture toughness of the cellular lattice structure

Figure 8.8 shows two typical loads–displacement curves of a three point bend fracture toughness test on cellular lattice structures when built in either the vertical or the horizontal directions. For both build directions highly irregular load-elongation curves were obtained, where the curves fluctuate up and down, which mean the load increase and decrease up to 100N after reaching the maximum load. This was expected from the periodic cellular structures, where strut failure occurs, and the sample therefore becomes weak after losing a set of struts, causing the load to descend. Ductile fracture was observed in all the tested samples, and plastic deformation was also confirmed during the test. For SENB samples with L/W = 4, the fracture toughness value was calculated using the following equation (Olurin *et al*., 2000, Quintana-Alonso *et al*., 2010, Marsavina and Linul, 2010):

$$K_Q = P_Q \frac{f\left(\frac{a}{W}\right)}{BxW^{\frac{1}{2}}} \qquad (8.1)$$

Where ($0<a/W<1$) andP_Q, B, *W, a, L,* are the load, specimen thickness, specimen width, crack length and span respectively.

All of the tests were valid for plane strain conditions, and the fracture toughness was considered $K_{IC}=K_Q$ after conducting the validity check, as discussed in Section 3.4.2 by using Equation 3.1.

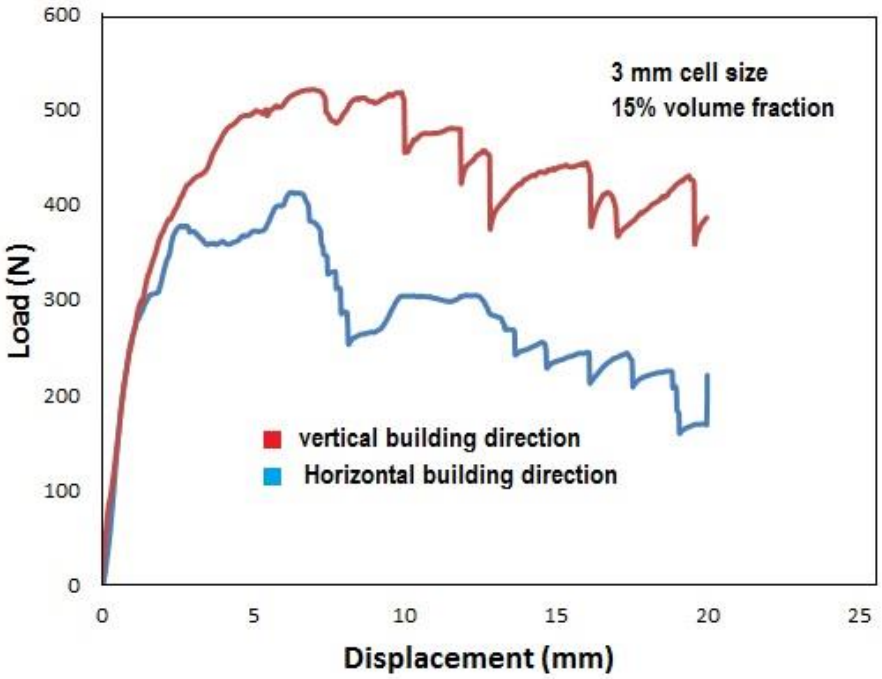

Fig 8.8: Load – displacement curves for different building directions of the cellular structure with the same volume fraction (15%) and cell size (3mm.).

The maximum and minimum values of fracture toughness are 4.3 MPa $m^{1/2}$ with a vertical build direction, and 3.3 MPa $m^{1/2}$ with a horizontal build direction. For comparison, the fracture toughness of bulk cast 316L is 112 to 278 MPa $m^{1/2}$ (Maloy *et al*., 2001). The fracture toughness result obtained from the SENB test was expected from the tensile test. As mentioned in Section 8.3.2, because the perpendicular struts in the vertical build direction samples are stronger (stiffness) than those in the horizontal; this means that these perpendicular struts are more vulnerable to the process of bending. Conversely, in the horizontal build direction samples, it was the horizontal struts that were the most vulnerable to the process of bending, due to the deformation during the fabrication process, as seen in Figure 8.9(a) for a horizontal build direction sample, and (b) for a vertical direction sample, which reveal larger crack lengths.

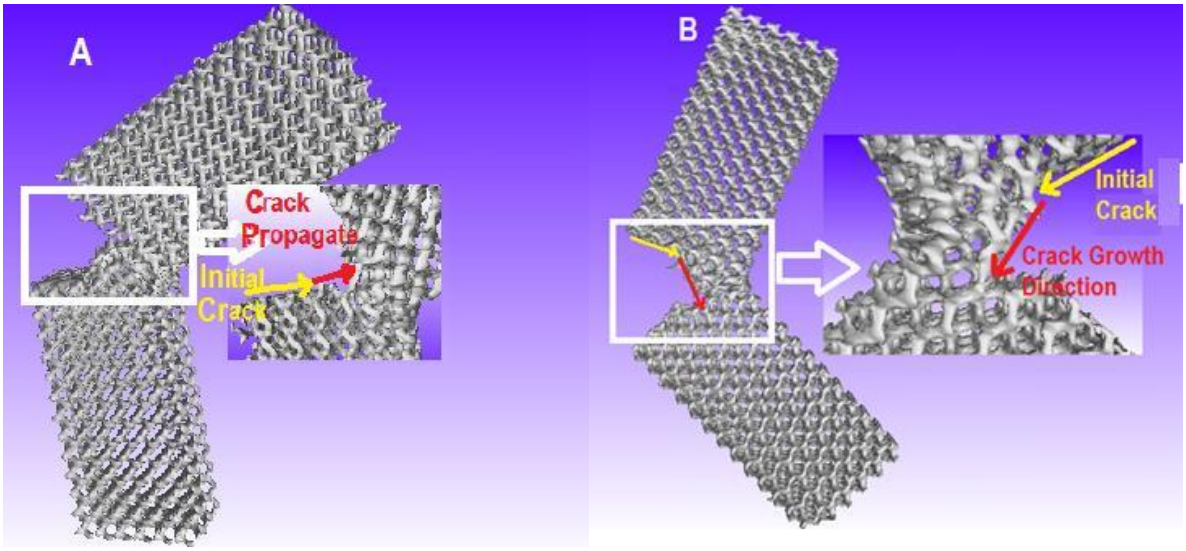

Fig 8.9: Images of the fracture toughness test samples (a) in the horizontal build direction, and, (b) the vertical build direction

Figure 8.10 compares the SENB test result for fracture toughness in different build directions with the Ashby and Gibson micromechanical model. It can be seen that for both build directions there was a difference between the SENB test values and the Ashby and Gibson model predictions; this difference was smaller in the vertical build direction samples, (0.2 MPa $m^{1/2}$), however, than in the horizontal build direction samples (0.5 MPa $m^{1/2}$). This difference is normal is was expected from tensile test, as that there is a variation in the ultimate tensile strength between the different build directions, as seen in Table 1, which reveals that the vertical build direction samples recorded higher tensile properties than the Ashby and Gibson model, as a function of the density and fracture strength of the cellular structures. The difference in fracture toughness between the Ashby and Gibson model and the SENB tested values may also be attributed to the roughness of the strut surfaces and the residual stress remaining in the SLM samples (Yan *et al.*, 2014b). In additional, the Ashby and Gibson model used in this study is based on Cubic unit cell. The constant value (C) was used in Ashby and Gibson model (equation 8.2) to predict the fracture toughness of cellular structures is 0.65, for more details see discussion part in Section 10.1. The struts that were subjected to a tension load in the horizontal direction were weaker than those in the vertical direction, and this was due to the different build direction, see Figure 8.2.

Equation 8.2 (Gibson and Ashby, 1999) sets out a micromechanical model to predict the fracture toughness of an open cell lattice structure. This model relates the fracture toughness K_{IC} to the tensile strength of the cell walls σ_{fs} , the dimension of cell *l* and the relative density ρ^*/ρ_s.

$$\frac{K_{Ic}^*}{\sigma_{fs}\sqrt{\pi l}} = C\,(\rho^*/\rho_s)^m \qquad (8.2)$$

where C is a constant value equal to 0.65.

Extensive studies of micromechanical models for lightweight and cellular materials have been presented by Gibson and Ashby (Ashby and Medalist, 1983, Gibson and Ashby, 1999), and Mills (Mills, 2007).

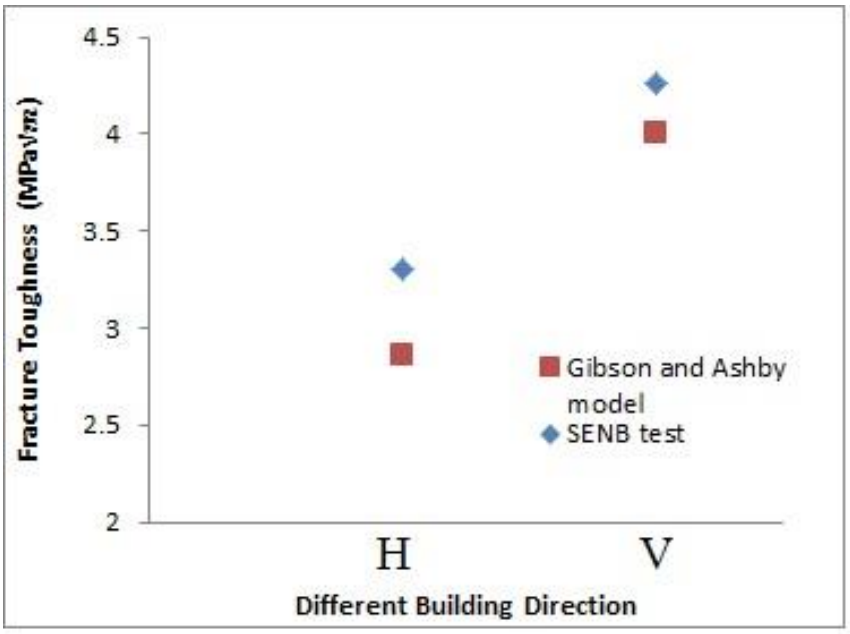

Fig 8.10: Experimental results of fracture toughness K_{IC}versus micromechanical models for cellular lattice structure of 316L stainless steel in different building directions with a constant cell size of 3mm. and a volume fraction of 15%.

8.4 Conclusion

This study investigates the fracture toughness and tensile strength of 316L periodic cellular lattice structures that are fabricated by SLM. The effect of different build directions on the density, tensile strength and fracture toughness properties of the cellular lattice structure were investigated. The following observations were made:

The cellular lattice structure's density was found at 1.35 g cm^{-3} , for both vertical and horizontal building directions, while the relative density of the solid struts in both building directions was found 96.%.

The ultimate tensile and yield strength in the vertical building direction samples are approximately 60% higher than those samples that were built in the horizontal build direction. The elongation of the samples that were built in the vertical direction is also approximately 40% higher than that of the samples built in the horizontal direction. This is because the struts of unit cells that were built horizontally were weaker than the struts that were built in the vertical building direction, which was parallel to the building direction.

All the tensile samples eventually fractured close to the solid end plate, where the struts join the non-cellular end tabs, and this was due to the sudden change in density, and thus stiffness, which formed a stress concentration.

The fracture toughness of the 316L stainless steel cellular lattice structure was 4.3 MPa $m^{1/2}$ and 3.3 MPa $m^{1/2}$ in the vertical and horizontal build directions, respectively. This is due to the weaker struts in the horizontal build direction. Fracture toughness is strongly dependent on build direction, with other possible parameters influencing the fracture toughness being the strut density and the loading rate.

The Ashby and Gibson micromechanical model that is used in this study is a useful tool to predict the fracture toughness of cellular lattice structure materials, and records small difference between the micromechanical model and the SENB results from 0.2 to 0.5 MPa $m^{1/2.}$

Chapter 9: Effect of the different cell size and build direction on the fracture toughness and strength of lightweight 316L stainless steel cellular lattice structures processed by selective laser melting

This chapter is evaluating the manufacturability of 316L cellular structure made by SLM at different cell sizes and build direction. Also, the effect of different cell sizes of 316L stainless steel cellar structure on fracture toughness and tensile strength properties is addressed. The mechanical property results are compared with Ashby and Gibson micromechanical model results. The design procedure and software tools used for generating cellular structure are presented in Section 9.2. The samples fabrication and mechanical tests procedure also are addressed in Sections 9.2. The result and discussion are addressed in Section 9.3, which include the effect of different build direction and cell sizes on density, tensile and fracture toughness of 316L cellular structure. Finally, the major findings are given in section 9.4.

9.1 Introduction

Lightweight metal cellular structures can offer high performance, for instance, good impact energy absorption, high strength accompanied by low weight, and good acoustic and thermal insulation properties (Nakajima, 2007, Williams and Rosen, 2007, Williams *et al*., 2011), thus finding uses in aerospace structures (Zhou *et al*., 2004). Metal cellular structures are divided into two common types: periodic cellular lattice structures (uniform structure or repeating unit cell) and stochastic porous structures (with a random distribution of open or closed voids) (Yan *et al*., 2014a). Structures made by SLM methods can possess relatively complex geometries, enjoy wide design freedom, and exhibit the functionality to meet advanced applications. Previous research has investigated the manufacturability and mechanical properties of stainless steel cellular lattice structures with different cell sizes and unit cell geometries (Yadroitsev *et al.*, 2009, Tsopanos *et al.*, 2010). For instance, colleagues of Yan (Yan *et al*., 2012) recently evaluated the manufacturability and properties of 316L stainless steel cellular structures, finding that gyroid type unit cells are able to self-support without excessive deformation during manufacture in a wide range of unit cell seizes, specifically 2 - 8 mm. The same authors go on to examine AlSiMg alloy periodic cellular

structures that are made by direct metal sintering (Yan *et al*., 2014a), and found the compressive modulus and strength were positively correlated with the volume fraction, showing good agreement with predictions from the Gibson-Ashby model (Yan e*t al*., 2014b). Considering applications in aerospace, where fracture toughness is considered a vitally important property, there are unfortunately no reports dealing with fracture toughness for any periodic metallic cellular lattice structures (although there is one report on foamed aluminium) (Yan *et al*., 2015). It is known that cell size and build direction strongly influence mechanical properties (Gibson and Ashby, 1999), so it is of some importance to establish their effects on fracture toughness if considering such structures for use within Aerospace. This chapter evaluates the manufacturability of cellular lattice structures and the effect of unit cell size and build directions on tensile and fracture toughness properties.

9.2 Experimental procedure

All of the cellular lattice structure samples were made from a 316L stainless steel powder with an average particle size of 30 ±10μm. The material, and the design, that were used in this chapter were the same as that in Chapter 6 for a 3 mm. cell size (Alsalla *et al*., 2016). The 15% of volume fraction, or the volume percentage of the solid material in the cellular lattice structure, was used in all of the periodic lattice structures in different building directions, and the cell sizes were used in different ranges of 3 mm, 4 mm, and 6 mm. The SLM fabricating process was carried out on a concept laser (M1, ES Technology Ltd, UK). The SLM machine used a fibre laser at 1060 nm wavelengths, with a nominal power of 200W and a focussing diameter of between 50 to 200 μm. The laser power, scanning speed and layer thickness were 200 W, 7 m s^{-1} and 0.03 mm, respectively. Six gyroid cellular lattice structures with dimensions of 10 × 20 × 80 mm. for the SENB test, and another six with dimensions of 15 × 15 × 60 mm., were built for the different cell sizes and different building directions on a base plate using the SLM process, and they were cut from the base plate using wire cutters (Electrical Discharge Machine EDM) - see Figure 9.1.

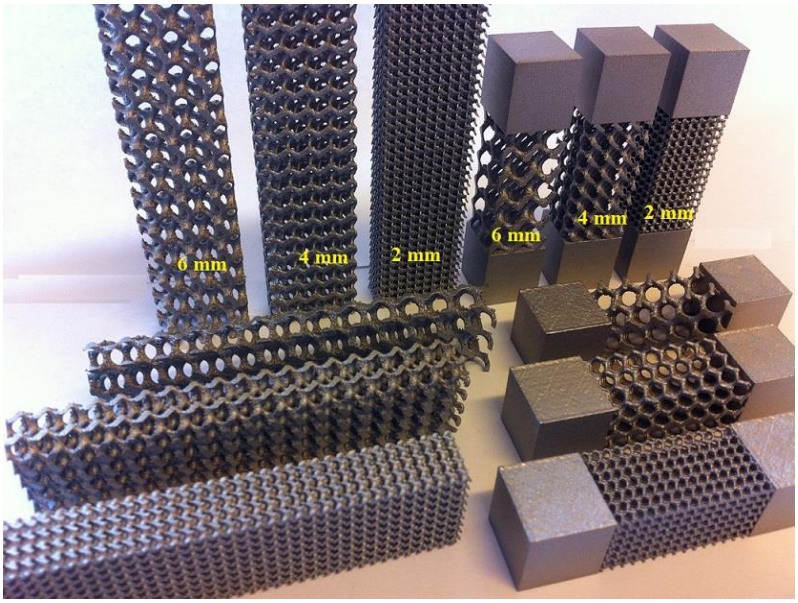

Fig 9.1: Periodic cellular lattice structures of 316L stainless steel samples at different cell sizes and building directions after they had been removed from the platform.

A micro-CT scanner (Benchtop CT 160Xi, X-Tek) at a voltage of 120KV, was used to scan the lattice structure samples before and after the mechanical testing, and two dimensional slice images were collected. The software (VGstudio MAX2.1) was used to reconstruct the three dimensional models of the manufactured lattice structure samples in order to determine the internal defects and the solid strut volume. An OM (Dino-lite Digital Microscope) was used to investigate the morphologies of the manufactured samples of the cellular lattice structures. The density and the relative density of the solid struts of the lattice cellular structures were measured. All tensile samples, both in parallel and perpendicularly to the building direction, were pulled under uniaxial tension tests using an Instron universal material testing machine at a constant loading rate of 0.5 mm. min^{-1}. The Mode I (opening mode and pre-cracked specimens) fracture toughness test (ASTM E399) was carried out at room temperature using an Instron hydraulic testing machine, and all data were recorded and measured to estimate the fracture toughness of the cellular lattice structures in different building directions and cell sizes, ASTM E399 (ASTM., 2016), more detail about the test machines and set up have been given in the experimental procedure chapter in Section 4.5.

9.3 Results and discussion

9.3.1 Effect of different cell sizes and building directions on the density of lattice structures and solid struts

The density of the solid struts and the density of the lattice structure within the gyroid cellular structures, with different cell sizes and building directions, are shown in Figure 9.2. No difference in density was recorded between the horizontal and vertical direction samples. The solid struts' densities at 2, 4 and 6 mm. cell sizes, are 7.9, 7.5 and 7.2 g. cm^{-3}, respectively, and they were measured in both the vertical and horizontal directions with a standard deviation of 0.03; while, in the lattice structures, the densities of the 2, 4, 6 mm. cell size were measured as 1.63, 1.3 and 1.1 g cm^{-3}, respectively, with a standard deviation of 0.010 for both samples, and they were built in both the vertical and horizontal directions. For comparison, the density of cast 316L is 8.0 g cm^{-3} (Ji *et al*., 2001). The relative density of the 2 mm. samples of solid struts vs. bulk cast density is thus 98.75%, whereas the 6mm. cell size sample had a relative density of 90%. This decrease in the relative density is confirmed by the cross-section of the CT scan and the SEM images in Figures 9.3 and 9.4, which show a small number of pores inside the struts of the lattice structures in the samples of 4 and 6 mm. cell sizes, and very few pores in the samples of 2 mm cell sizes. It is clear that the density of the cellular structures, and the struts themselves, decreases with an increase in the cell size. The relative sparsity of pores in the smaller unit cell size samples may be attributed to the short scan vector length during the fabrication process, which means that the cross section area of the struts became smaller as the unit cell size decreased, see Figure 9.3. Higher densities could thus be achieved by optimising the SLM process processing parameters for the smaller unit cell sizes, (Nakajima, 2007).

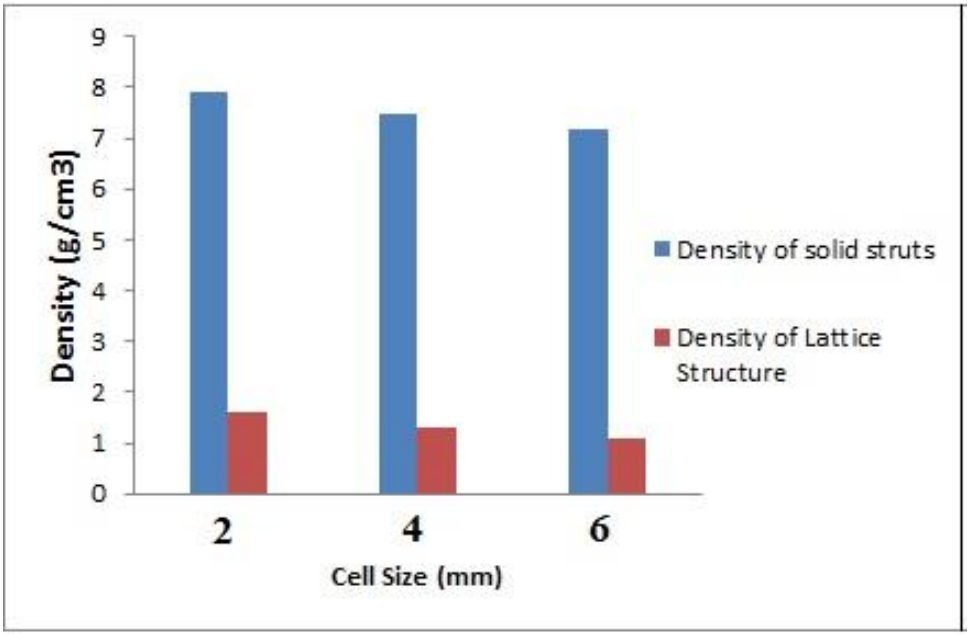

Fig 9.2: Shows the variation of the struts' density and the lattice structure density with different cell sizes and building directions

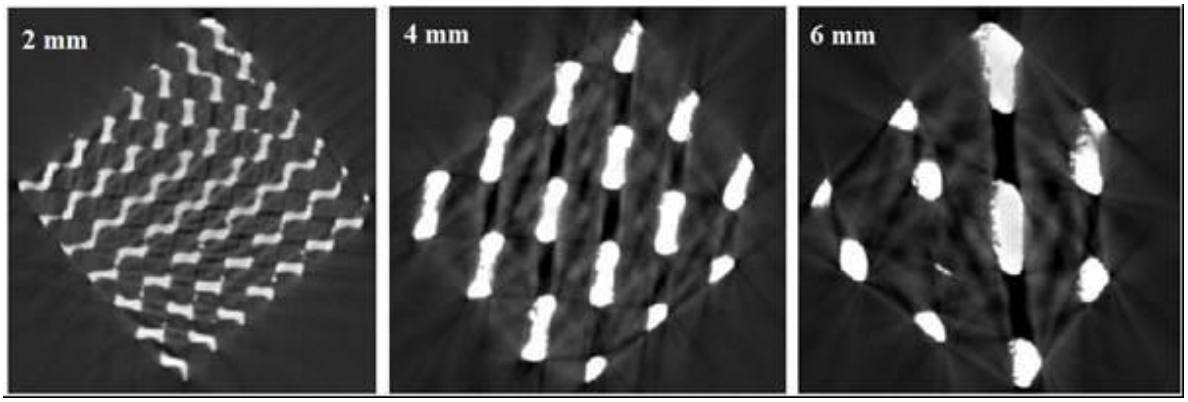

Fig 9.3: Cross section images from the micro-CT scans of the gyroid cellular lattice structures with the volume fraction of 15% and unit cell sizes of 2, 4 and 6 mm. made by SLM.

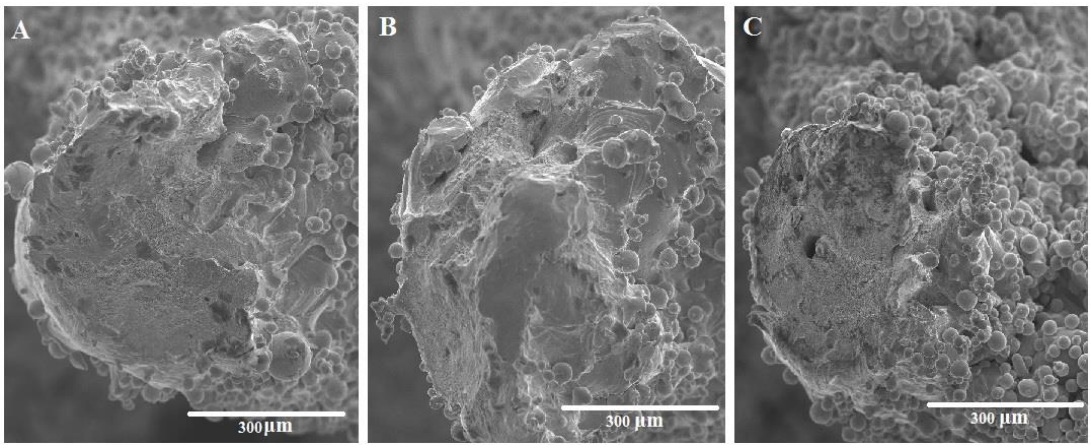

Fig 9.4: SEM images of a fracture: struts at 200 × magnification, (a) 2 mm. cell size sample, (b) 4 mm, cell size sample, and (c) 6 mm cell size sample.

9.3.2 The effect of the different cell sizes and build directions on the strength and elongation of the lattice structure

The stress-strain curves of the tensile tests on the gyroid cellular lattice structures, with the same volume fraction of 15% and the unit cell sizes 2mm, 4mm and 6mm in the vertical and horizontal building directions, are shown in Figures 9.5a and 9.5b. from the stress/strain curves in Figures 9.5a and b, it is observed that the stress/strain curves in the horizontal build direction reveal an elastic region with a fairly high degree of linearity, followed by strain hardening that is extended up to ultimate strength, and finally to failure. It is also found that the lattice structure in the horizontal building direction offers lower tensile properties than the lattice structure in the vertical building direction, although both of them have the same cell sizes: 2 mm, 4 mm and 6 mm, and the same volume fraction of 15%. The struts of the horizontal samples which were subjected to less tension load than the vertical struts but had early failure because deformation through the SLM process is more likely to occur. Moreover, the samples with 6 mm cell size have overhang which require support structure while the samples with 2 mm cell size have a less overhang but their horizontal struts diameter are very thin in the middle (thickness approximately 6 to 8 layers rather than the vertical struts with the same thickness but several layers). The comparisons of the tensile test results show that the ultimate tensile strength and the yield strength decrease with an increase in the unit cell size of the lattice structure in both the horizontal and vertical building

direction, while the elongation increases with an increase in the unit cell size of the lattice structure for both the vertical and the horizontal building directions, see Table 9.1.

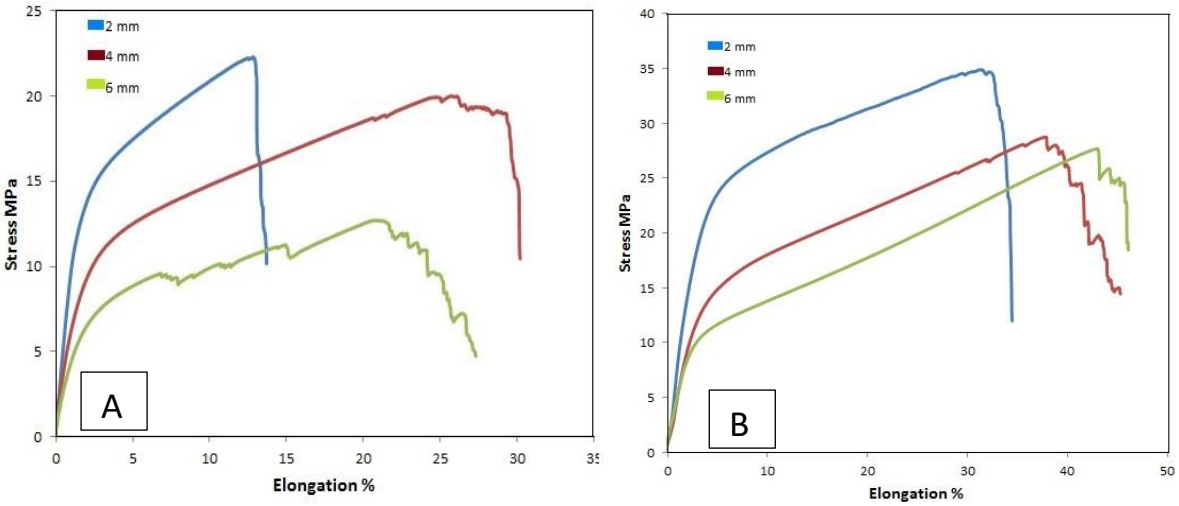

Fig 9.5: Stress-strain curves of the tensile tests on the cellular lattice structures with 15% of volume fraction and 2, 4 and 6 mm. unit cell sizes, (a) in the horizontal building direction, (b) in the vertical building direction.

The lattice structures were built in the horizontal direction, and the 2 mm. cell size exhibits the highest values of UTS and yield strength, which are 23.39 MPa and 12.29 MPa, respectively, while the lattice structures that were built in 4 mm. reveal the UTS and yield strength are 20.13 MPa and 9.77 MPa, and the lattice structure samples that were built in 6 mm. reveal the UTS and yield strength are 12.25 MPa and 6.5 MPa, respectively. The elongations of the samples that were built in the horizontal direction at 2 mm, 4 mm. and 6 mm. are 21.9 %, 25.11% and 26%, respectively, see Table 9.1. On the other hand, in the lattice structures that were built in the vertical direction, the 2 mm. cell size exhibits the highest values of UTS and yield strength, which are 34.97 MPa and 22.22 MPa, respectively, while the lattice structures that were built in 4 mm. reveal the UTS and yield strength are 29.46 MPa and 13.48 MPa, and the lattice structure samples that were built in 6 mm. reveal the UTS and yield strength are 27.68 MPa and 6.8 MPa, respectively. The elongations of the samples that were built in a horizontal direction at 2 mm, 4 mm and 6 mm are 33 %, 40 % and 43.8 %, respectively, see Table 9.1.

Table 9.1: Tensile properties obtained from the cellular lattice structures of 316L stainless steel with the same volume fraction (15%) and unit cell (2, 4 and 6 mm.) made by SLM

Cell Size	Direction	UTS (MPa)	Yield Strength (MPa)	Elongation (%)
2 mm	**Vertical**	**34.97**	**22.22**	**33**
	Horizontal	**22.39**	**12.29**	**21.97**
4 mm	**Vertical**	**29.47**	**13.48**	**40**
	Horizontal	**20.13**	**9.8**	**25.1**
6 mm	**Vertical**	**27.68**	**6.8**	**43.87**
	Horizontal	**12.85**	**6.5**	**26.1**

The images in Figure 9.6 show that the ductile failure and deformation throughout the testing process occurred in a steady and smooth progression, the struts of the unit cells rotating by approximately 45˚, and the alignment with the direction of uniaxial tension load applied to the samples is attributed to the circular struts and the sphere core of the unit cell, as shown in Chapter 8. All the samples' areas are reduced due to the construction of the struts and the relationships to each other, and they expanded longitudinally after tensile test, the samples that were built at the 6 mm. cell size recorded the smallest area after tensile testing, while the samples that were built at the 2 mm. cell sizes recorded the highest area. This was to be expected from the elongation data in Table 9.1, as the samples that were built at 6 mm. for both the vertical and horizontal, reveal the highest value of elongation. From Figure 9.7 it can be seen that the samples that were built at the 2 mm. and 4 mm. cell sizes fractured close to the solid end plate, where the struts join the non-cellular end tabs, while the samples that were built at the 6 mm. cell size fractured in the middle of samples. This can be attributed to the sudden change in density and stiffness- forming a stress concentration in the samples of the 2 mm. and 4 mm. cell size. This difference in fracture position can be attributed to the differences in struts dimeters, which lead to a stress concentration between the solid plate and the lattice structure of the 2 mm cells because there is change in density for the solid material volume. For the lattice structure samples with 4 mm cells, the fracture and stress concentration again occur at the interface between the solid plate and cellular structure, see Figure 9.7. The samples were built with 6 mm cell have the largest struts diameter which means they are strongest and most tightly joined to the sold plate, this means the fracture

does not occur at the interface between cells and solid plat but at some distance from the solid surface, as seen in Figure 9.7, in the cellular structure sample where the stress concentration is formed in the middle and the area of sample reduced by the tension load.

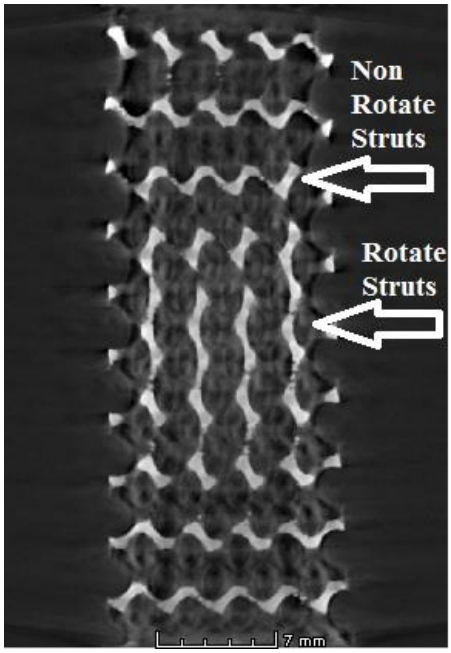

Fig 9.6: Shows the CT scan (single 2D slice) of the cellular lattice structure after a tensile test showing the rotation of the internal struts

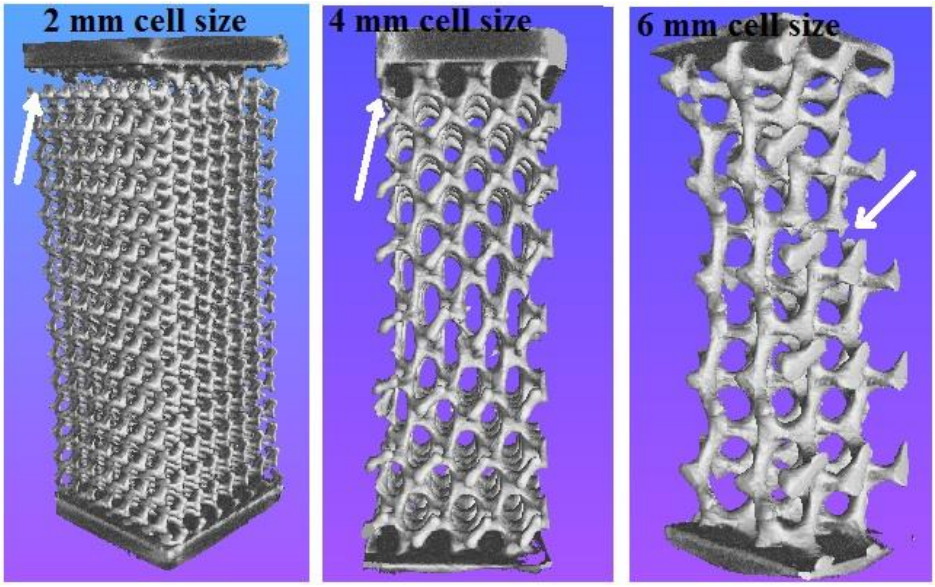

Fig 9.7: Reconstructed 3D CT scans of the cellular lattice structure samples at different cell sizes after a tensile test, with the details of the rupture shown more clearly

From the results obtained, it is thus clear that the low mechanical properties of the tensile test are due to the weakness of the struts. Because there was little overlap between the successive melted layers during fabrication the struts and therefore the structures are weaker under loading, especially if the cell size is increased, and thus likely to fracture early. Consequently, the increase of the unit cell size lead to an increase of strut diameter. This result is based on fixed volume fraction of 15%, and when the volume fraction is set constant and the cell size is increased, the number of cells in the volume decreased and the struts become thicker. Consequently, the horizontal struts become very weak due to the deformation without a support structure. The higher mechanical properties of the gyroid cellular lattice structure further proves that the struts oriented parallel to the building direction and the struts perpendicular to the baseplate, have been well fabricated by SLM technology, at this small cell size.

9.3.3 The effect of different cell sizes and building directions on the fracture toughness of the cellular lattice structure

Figures 9.8a and 9.8b show the typical load–displacement of a three point bend fracture toughness test on the cellular lattice structure samples at different cells sizes (2 mm. 4 mm. and 6 mm.) built in either the vertical or horizontal direction. For all samples, over the whole range of cell sizes and build directions, nonlinear stress-strain curves were obtained wherein the load varied by between 50 and 100N after reaching the maximum load. This was to be expected because of the nature of the strut failure, with subsequent weakening after losing a number of struts and drop off in load. Ductile fracture was observed in all the tested samples, and plastic deformation was also confirmed during the test, see Figure 9.4.

The fracture toughness values were calculated for SENB samples with L/W = 4 as shown in Chapters 6 and 8 (Alsalla *et al*., 2016), and all of the tests were valid for plain strain conditions and the fracture toughness was considered $K_{IC}=K_Q$ after conducting the following validity check:

$$A, B, (W-a) \geq 2.5\left(\frac{K_Q}{\sigma_{ys}}\right)^2 \quad (9.1)$$

The maximum fracture toughness values in this study were recorded in the samples built with the 2 mm. cell size, in both the horizontal and vertical building direction, which are 5.4 MPa

$m^{1}/_{2}$ and 5.8 MPa $m^{1/2}$, respectively, while the minimum fracture toughness values were recorded in the samples that were built with a cell size of 6 mm., which are 2.1 MPa $m^{1/2}$ in the horizontal directions and 2.6 in the vertical directions. For comparison, the fracture toughness of bulk cast 316L is 112 to 278 MPa $m^{1/2}$ (Miracle *et al*., 2001, Committee, 1997).

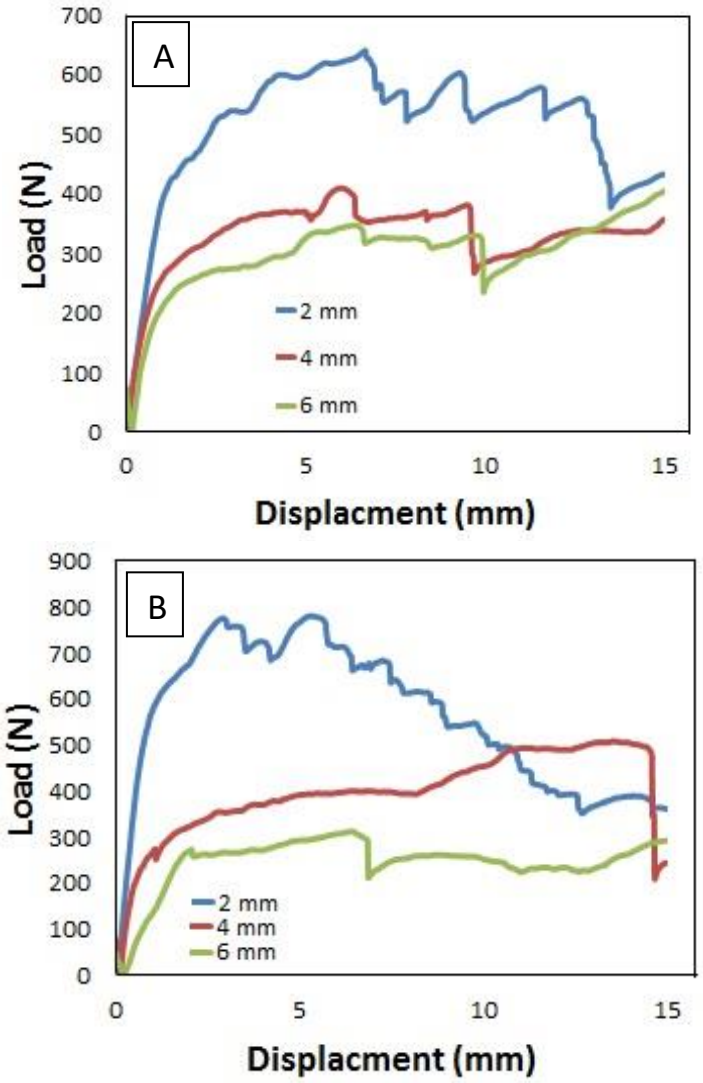

Fig 9.8: Load – displacement curves for different building direction of cellular structures with the same volume fraction (15%) and cell sizes (2, 4 and 6 mm, in the (a) horizontal building direction, and (b) the vertical building direction

From the tensile test result in Section 9.3.2, the fracture toughness values obtained from the SENB were expected, because the perpendicular struts in the samples that were built in the vertical direction were stronger that those struts that were built in the horizontal direction, meaning that these struts were more vulnerable to the process of bending. In contrast, in the horizontal build direction samples, it was the horizontal struts that were the most vulnerable

to the process of bending, due to deformation during the fabrication process, as discussed in Chapter 8 and by Alsalla *et al* (Alsalla *et al*., 2016). The fracture toughness result obtained in this study is less than the 15% of the fracture toughness of bulk cast 316L (16 MPa $m^{1/2}$ to 41 MPa $m^{1/2}$), which does not obey the scaling laws.

Figures 9.9a and 9.9b show that the increase of cell sizes in the cellular structure samples results in a decrease in the fracture toughness values for both in the horizontal and vertical building directions. This means that the fracture toughness increases with cell size and decreases at a constant volume fraction, and the fracture toughness decreases with cell size and increases at a constant volume fraction. These results are expected from the tensile tests, which reveal that the tensile ultimate and yield strengths increase as the unit cells of cellular structures decrease, and vice versa, at a constant volume fraction, see the Section 9.3.2.

Figures 9.9a and 9.9b compare the SENB test results for the fracture toughness of the cellular lattice structure in the different build directions and cell sizes with the Ashby and Gibson micromechanics model. It can be seen that for both build directions at the different cell sizes there was a difference between the SENB test values and the Ashby and Gibson model predictions. However, this difference was smaller for both the horizontal and vertical samples built with a 2 mm. cell size, and which recorded a difference of 1 MPa $m^{1/2}$. The samples built with the 4 mm. cell size recorded a difference of 0.4 MPa $m^{1/2}$, and the samples built with the 6 mm. cell size recorded a difference of 0.3 MPa $m^{1/2}$. From these results it can therefore be said that the difference in the fracture toughness value between the SENB test and the Ashby and Gibson model decrease with an increase in the size of the unit cells of the cellular structure samples, and vice versa. This could be expected considering the variation in the ultimate tensile strength between the different build directions and the different cell sizes, as seen in Figures 3a and 3b, which reveal that the vertical build direction samples and the small cell size recorded higher tensile strength than the Ashby and Gibson model, as a function of the density and fracture strength of the cellular structures. The difference in fracture toughness between the Ashby and Gibson model and the SENB tested values may also be attributed to the Ashby and Gibson model used in this study is based on Cubic unit cell as discussed in chapter 8 Section 8.3. The constant value (C) was used in Ashby and Gibson model (equation 9.2) to predict the fracture toughness of cellular structures is 0.65, for more details see discussion part in Section 10.1. The struts that were subjected to a tension load in the horizontal direction were weaker than those in the vertical direction, due to the different build direction (Alsalla *et al*., 2016).

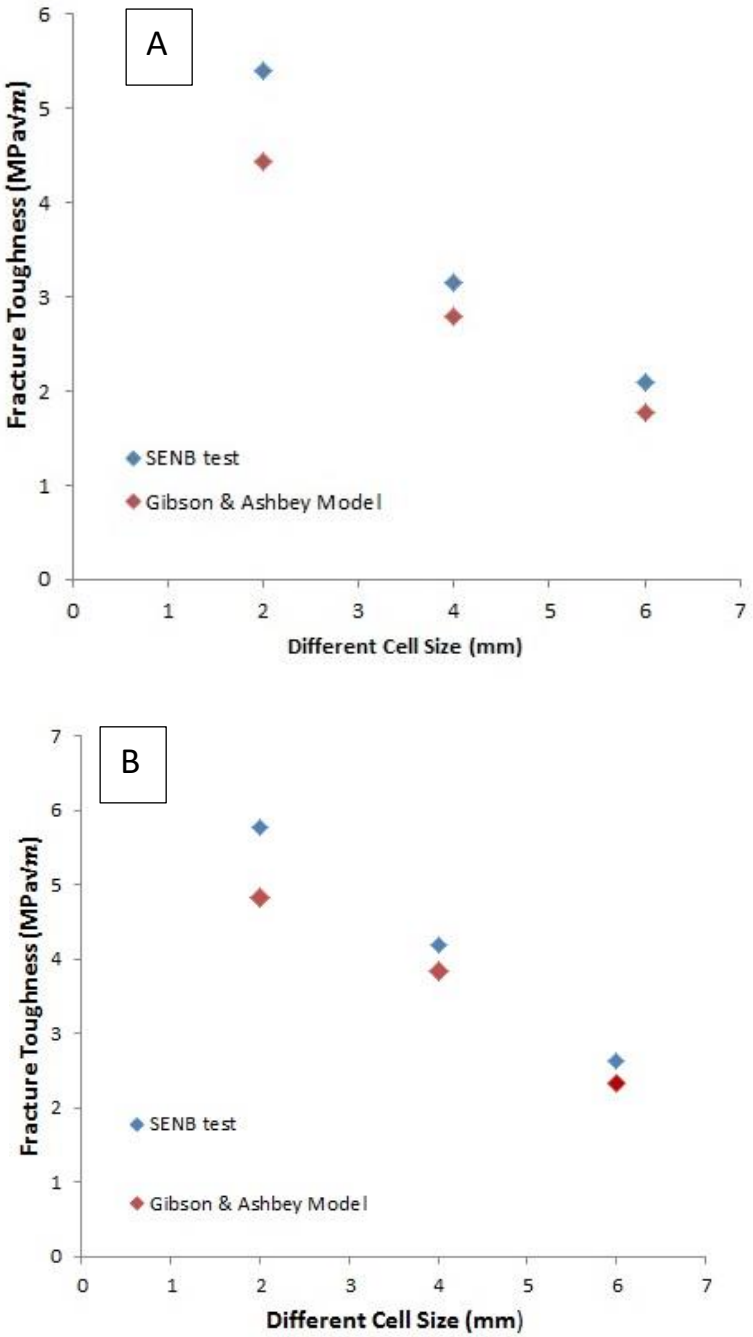

Fig 9.9: Experimental results of fracture toughness K_{Ic}versus micromechanical models for the cellular lattice structure of 316L stainless steel at different cell sizes (2, 4 and 6 mm.), with a constant volume fraction of 15%, at (a) the horizontal building direction, and (b) the vertical building direction

Furthermore, Figure 9.10 shows the fracture toughness sample fracture points, the perpendicular struts in the vertical build direction samples were stronger than those in the horizontal, meaning that these struts were more vulnerable to the process of bending.

Conversely, in the horizontal build direction samples, it was the horizontal struts that were the most vulnerable to the process of bending, due to deformation during the fabrication process, which meant they were weaker than the vertical struts and the cracks propagated quickly. The difference between the Ashby and Gibson model and the SENB test could be attributed to the density of the bulk cast 316L that was used in the model for all of the samples, instead of the density of the solid struts of each sample, and the properties changed with changes in the cell size during the laser melting.

Equation 9.2 (Gibson and Ashby, 1999) sets out a micromechanical model to predict the fracture toughness of an open cell lattice structure. This model relates the fracture toughness K_{IC} to the tensile strength of the cell walls σ_{fs} , the dimension of cell l and the relative density ρ^*/ρ_s.

$$\frac{K_{Ic}^*}{\sigma_{fs}\sqrt{\pi l}} = C\,(\rho^*/\rho_s)^m \qquad (9.2)$$

where C has a constant value equal to 0.65

Extensive studies of micromechanical models for lightweight and cellular materials are presented by Gibson and Ashby (Ashby and Medalist, 1983) and Mills (Mills, 2007).

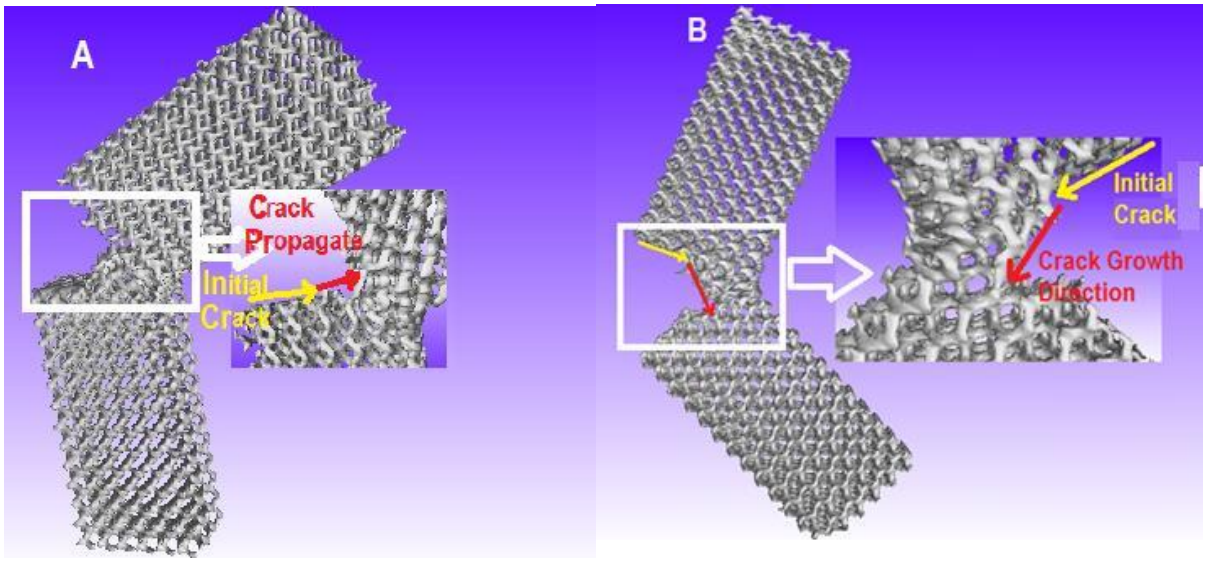

Fig 9.10: Shows the fracture toughness test samples, (a) in the horizontal building direction, and (b) in the vertical building direction (Alsalla *et al*., 2016)

9.4 Conclusion

This chapter has been investigated the density, fracture toughness and tensile strength of 316L periodic cellular lattice structures made by SLM. The effect of different cell sizes and build directions on the density, tensile strength and fracture toughness properties of the periodic cellular lattice structure, were investigated. The major findings of this study are:

That the maximum density of cellular lattice structure was found at 1.63 g cm^{-3} of the 2 mm. cell size samples for both the vertical and horizontal building directions, and the minimum was found at 1.1 g cm^{-3} of the 6 mm. cell size samples.

The maximum solid strut density was found at 7.9 g cm^{-3} of the 2 mm. cell size samples, while the minimum solid strut density was found at 7.2 g $cm^{-3}$of the 6 mm.' cell size samples.

Both the relative density of the solid struts and the cellular lattice structures' density increase with a decrease in the cell size, but they are unaffected by the different building directions.

The ultimate tensile and yield strength in the vertical building direction samples are higher than in those samples that were built in the horizontal building direction at all of the different cell sizes, while the ultimate tensile and yield strength of periodic cellular lattice structures increases with a decrease in the cell size of the lattice structure for both the vertical and horizontal building direction samples.

The elongation of the samples that were built in the vertical direction is higher than that of the samples built in the horizontal building direction, and the elongation of the periodic cellular lattice structure increases with an increase in the cell size of the cellular lattice structure samples for both the vertical and horizontal building directions. This is because the struts of the unit cells that were built horizontally were weaker than the struts that were built in the vertical building direction, which was parallel to the building.

The tensile samples that were built at the 2 and 4 mm. cell sizes, for both the vertical and horizontal building directions, eventually fractured close to the sold end plate, where the struts join the non-cellular tabs, due to the sudden change in density, and therefore stiffness, so forming a stress concentration, while the 6 mm. samples fractured in the middle of the samples.

The fracture toughness of the 316L stainless steel cellular lattice structure increased with a decrease in the cell size of the cellular lattice structure samples in both the vertical and horizontal building directions.

The fracture toughness of the 316L stainless steel cellular lattice structure in the vertical building direction samples is higher than those that were built in the horizontal building direction

The maximum difference in fracture toughness values between the SENB results and the Ashby and Gibson micromechanical model was recorded 1 MPa $m^{1/2}$ at 2 mm. cell size samples, while the minimum difference in fracture toughness value was recorded as 0.3 MPa $m^{1/2}$ in the 6 mm. cell size samples, for both samples built in the vertical and horizontal building directions.

The Ashby and Gibson micromechanical model used in this study is a useful tool with which to predict the fracture toughness.

Discussion, Findings and Recommendations

Chapter 10: Discussion, Conclusions and Future Work

10.1 Discussion

The focus of this research was to investigate how well the SLM and DMLS of titanium and steel alloys perform as fabrication methods for aerospace structures. This research demonstrates the mechanical properties of bulk titanium alloy and stainless steel and cellular lattice structures of stainless steel that are manufactured by AM. The results can help engineers and designers to identify appropriate mechanical properties and macroscopic morphology, along with process parameters, for the best use in aerospace components.

The primary goal of this research was to investigate the critical mechanical properties of these AM parts of Ti6Al4V and 316L Stainless steel alloys, such as their fracture toughness and FCG in different building directions, as well as the effect of different cell sizes and build directions on the fracture toughness and local failure mechanism of 316L Stainless steel cellular structures under uniaxial tension loading were investigated. A secondary aim was to use modelling in material analysis to understand experimental investigation. The following steps illustrate and summarize the approach, which was taken in this thesis:

- The DMLS and SLM techniques were identified as being appropriate AM processes for the manufacture of aerospace parts with advanced and complex geometries, particularly those using high strength materials. The excellent performance of sample geometries manufactured using these processes is shown in Chapters 5 and 6, e.g., the tensile strength and the fracture toughness for both titanium alloy and steel that are produced in AM is higher than that produced by conventional methods, see Tables 5.3, 5.4, 6.1 and 6.2. The AM technology is as good and promises good mechanical properties.

- Microstructure and failure behaviour were investigated to allow comparison to previous literature. A small amount of porosity was found along with cracks, shrinkages and voids in the fracture surfaces of samples.
- Investigation of the effect of different build direction and cell size on the density, surface roughness, hardness, fracture toughness, strength and FCG properties was

undertaken to allow comparison with the existing literature. The results of tests show these samples are superior in comparison to others as discussed in chapter 3 Section 3.3

- Comparison was made of the mechanical properties of cellular lattice structured to the Ashby and Gibson micromechanical models. It indicates that the Ashby and Gibson model can be used to guide and predict trends in fracture toughness.

- However, it is important to note that, for the stainless steel alloy used in this PhD project. The Concept laser machine was not suited to producing mixture powder of stainless steel or when mixed with other alloying elements. It is just suited to standard stainless steel and iron.

DMLS of Ti6Al4V

From the summary of Chapter 5, it can be concluded that the yield and ultimate tensile strength for the DMLS process Ti6Al4V exceeded the minimum limit that is given by AMS 4911 for aerospace specification Ti6Al4V. The DMLS process has given the average YS and UTS for failure of 1148 MPa ±15 and 1235 MPa ±17, respectively, which were higher than the 880 MPa YS and 950 MPa UTS for the aerospace titanium specification (AMS 2015). In addition, the performance of all of the specimens in all of the different build directions exceeded the minimum specification that is defined for standard annealed Ti6Al4V. However, there was no significant variation in the tensile specimens with the same position in the build chamber, but in terms of the different build direction, the DMLS specimens were affected by the direction in the plane of the bed, which reveal that the low properties were in the z direction specimens. On the other hand, the elongation found in this research was relatively lower, at 7.3%. Overall, in comparison to the previous results reported by Al-Bermani *et al* and Facchini *et al* (Al-Bermani *et al*., 2010, Facchini *et al*., 2009), they report lower YS and UTS and higher ductility than this result. This may be due to the preheating temperature that was used in their experiments, leading to a coarsening of the α plates and transform to prior β phase in the microstructure (Al-Bermani *et al*., 2010). This result slightly increased the elongation of the fractures and decreased the strength.

From the results presented in Chapter 5 (accepted in rapid prototyping journal) , it can also be seen that the fracture toughness property of the DMLS specimens exceeded the standard annealed Ti6Al4V test data and showed better average results 105 MPa $m^{1/2}$. This means that the DMLS has superior mechanical properties to other AM processes, which can be attributed to the coarse grained α microstructure. On the other hand, the presence of pores may be the reason for earlier fracturing and low ductility. From this investigation, it is clear that components that are made from titanium by DMLS are appropriate for use in aerospace applications where stresses are applied perpendicularly to the build direction.

SLM of 316L stainless steel

To understand the effect of the different build directions on the mechanical properties of 316L stainless steel made by SLM, a set of specimens were produced and tested according to the ASTM standard, in three different build directions, in order to find the best direction for offering higher efficiency. From the results presented in Chapters 6 (also in Alsalla *et al*,. 2017) and 7, it can be seen that the specimens that where built in the vertical direction and parallel to the build direction, show lower properties than others that were built in the horizontal direction and parallel to the build direction for all of the tests undertaken in this study.

In comparison to wrought materials and to that report in the literature, these results indicate better or best performance in terms of tensile strength, fracture toughness and FCG. The tensile properties of specimens produced by SLM gave average UTS values of 642 MPa, YS values of 402 MPa, and elongation values of 37%. These values are higher than the minimum specification required for the tensile properties of the 316L austenitic stainless steel that is used in aerospace applications. The fracture toughness for all specimens gave average values of 157 MPa $m^{1/2}$, which exceeded the minimum limit for the standard test data and showed better toughness performance, if compared to the annealed 316L stainless steel and the reports of previous literature (Maloy *et al*., 2001). In the SLM of 316L stainless steel, the specimens failed to survive 1,550,000 cycles along the different build directions, and it was only the specimens that were built in the vertical direction and parallel to the build direction that have earlier crack propagation than the other specimens in the horizontal direction, this is due to non-uniform grain structure and the presence of pores, which are the main reasons for the decrease in the fatigue life, as discussed in Chapter 7. This enhancement was due to the proper selection of the process parameter, which gave a finer grained microstructure in the specimens produced, and this result is considered good.

Since these structures demonstrate a high performance relative to existing cast structures it is likely that lightweight 316L components made by SLM may offer significant fuel efficiency savings for airline companies vs cast steel. Candidate structures for replacement with SLM made parts include exhaust components, high temperature engines and structural parts, e.g. the SLM-manufactured Airbus A380 bracket. In the example of the Airbus bracket the weight was reduced from 1.09 kg to 380 grams, and reductions such as this can have significant effects on fuel costs and CO_2emissions over the long term such as an aiframe's life span.

Ti6Al4V and stainless steel 316L: comparison and influence of different build directions

From the results discussed in Chapters 5 and 6, some differences can be highlighted between Ti6Al4V and 316L stainless steel that is manufactured by SLM under similar build directions:

(i) Both materials are sensitive to the build-up of internal stress

(ii) Stainless steel 316L appears to be more prone to the occurrence of mechanical anisotropy, both in the parallel to build direction (*zx*) and in the two perpendicular directions (*xz*, *yx*).

(iii) Both materials appear to show the occurrence of microstructural anisotropy in relation to "lack of fusion or melting and porosity" defects, both in the parallel to build direction (*zx*) and in the two perpendicular directions (*xz*, *yx*).

While the SLM technique has certain benefits, it also faced a number of problems, such as porosities that are due to entrapped gas, a lack of fusion and the poor wetting of a new layer on the previous solidified material (Alcisto, 2011, Frazier, 2010, Herderick, 2011). Another key problem of SLM is that the structure undergoes fast cooling once the laser beam leaves the melting of the fusing zone, thus producing out of equilibrium microstructures. The high residual stress may rise due to the high thermal gradients (Herderick, 2011) and the construction of a new layer upon cooling is constrained by the previous layers (NIST, 2013). This result support previous publication were they also reported that the thermal history of SLM parts show that the thermal conductivity is likely to play a role in the build-up of internal stresses (Mani, 2014, NIST, 2013). These various factors can affect the properties of metallic parts that are manufactured by SLM, and produce anisotropy of the mechanical properties (Vilaro, 2011, Zheng, 2008, Kobryn, 2001).

SLM of 316L stainless steel cellular lattice structure

To meet these objectives, the effect of different build directions and cell sizes on the 316L stainless steel manufactured by SLM was addressed in Chapter 8 (Alsalla *et al*,. 2016) in order to explore how best to improve structural performance for strength/weight and fracture toughness. The results show that the YS, UTS, elongation and fracture toughness properties of 316L stainless steel cellular structures increase with a decreasing cell size in the cellular lattice structure for both the vertical and horizontal building directions, while the YS, UTS, elongation and fracture toughness properties in the vertical building direction specimens are higher than those specimens that were built in the horizontal direction. The difference in fracture toughness between materials produced in the experimental tests and the Ashby and Gibson micromechanical model was recorded as 1 MPa $m^{1/2}$ at the 2 mm cell size, and this decreased with an increase in the cell size for both the vertical and horizontal building direction. The result generated by comparing the Ashby and Gibson model and experimental results show that the model slightly under-predict the fracture toughness and tensile property for 316L stainless steel cellular structures. The approach in these analyses is to identify a unit cell and assume a deformation mode leading to failure. The Ashby and Gibson model used in this study is based on Cubic unit cell, as seen in Figure 10.1, where the deformation is controlled by the bending of the individual struts within the unit cell. The unit cell shape (gyroid) used in this study is more complex than that cubic unit cell shown in Figure 10.1, but it deforms and fail by same mechanism, and can be using dimensional arguments which meet all constants arising from the specific cell geometry. The constant value (C) was used in Ashby and Gibson model (equation 8.2 Section 8.3.3) to predict the fracture toughness of cellular structures is 0.65. This value was applied for cubic unit cell and could be required further modify and improve the accuracy to comply with different shapes of units cells. Generally, the Ashby and Gibson model can be used to guide and predict trends in fracture toughness. Understanding the build direction allows users to properly design sandwich structures, which make excellent use of lattices as low cost, and which have corrosion resistant low density cores.

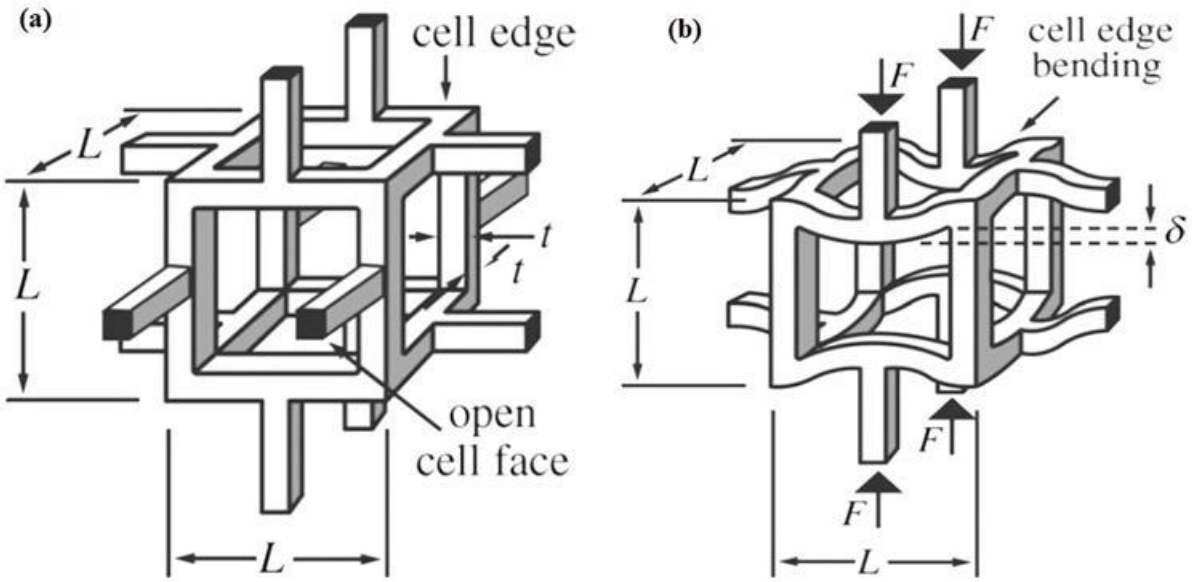

Fig 10.1: A cubic model for an open-cell foam showing the edge length, l, and edge thickness, t (Gibson and Ashby, 1999).

Comparison of the mechanical properties of bulk and cellular structure of stainless steel 316L

Table 10.1 reveals the percentage of the mechanical properties of the cellular structure parts compared to those of the bulk parts for stainless steel 316L manufactured by SLM. This comparison is especially noted in the tensile and fracture toughness of perpendicular and parallel to build direction parts. All tests were carried out in a similar specification and at room temperature, as discussed in Section 4.5.4. From Table 10.1, it can be seen that the mechanical properties of a cellular structure manufactured at 15% of volume fraction don't meet the 15% of mechanical properties for the bulk parts, this could be attributed to the type of unit cell (Gyroid). The Gyroid unit cell was selected for this study due to its self-supporting properties during the manufacturing process, but it has different strut diameters, especially in the middle, where it was very much thinner than at the corners and the sides. The Figure 9.10 in Chapter 9 showed that the crack was quickly propagated along the weak struts (thin side). On the other hand, there is no big difference in the elongation and the cellular structures' parts that are manufactured at 15% volume fraction and 6 mm. cell size, these reveal little higher elongation than the bulk samples, because of the ductility struts' deformation. The tensile and fracture toughness result that has been obtained in this study are

less than the 15% of the fracture toughness and tensile of bulk cast 316L, which don't obey scaling laws.

Table 10.1: comparison of mechanical properties between bulk and cellular structures of 316L stainless steel made in the same build direction

316L	Build direction and cell size		UTS (MPa)	Yield strength (MPa)	Elongation %	Fracture toughness (MPa $m^{1/2}$)
Bulk	**Horizontal**		**695**	**423**	**41**	**152.6**
	Vertical		**564**	**387**	**35**	**145.5**
Cellular structure	**Horizontal**	**2 mm**	**22.4 (3.2%)**	**12.3 (3.0%)**	**21.9 (53%)**	**5.4 (3.5%)**
		4 mm	**20.1 (2.9%)**	**9.8 (2.3%)**	**25.1 (61%)**	**3.3 (2.2%)**
		6 mm	**12.9 (1.9%)**	**6.5 (1.5%)**	**26 (63%)**	**2.1 (1.4%)**
	Vertical	**2 mm**	**34.9 (6.4%)**	**22.2 (5.7%)**	**33 (94%)**	**5.8 (4%)**
		4 mm	**29.5 (5.4%)**	**13.5 (3.5%)**	**40 (114%)**	**4.2 (2.8%)**
		6 mm	**27.7 (5.1%)**	**6.8 (1.7%)**	**43.9 (125%)**	**2.6 (1.8%)**

10.2 Conclusion

This research has investigated the manufacturability and mechanical properties of Ti4V6Al and 316L stainless steel processed by AM. The 316L stainless steel used in this research was based on bulk and cellular lattice structure parts, while the Titanium based on bulk parts only. Comprehensive experimental tests were carried out at different build direction using standard available 316L stainless steel and Ti6Al4V metal powders. All the experiments were performed in commonly used AM systems (SLM M1 Concept laser and DMLS EOSINT M280). The SolidWork and SimpleWare software were used to design the parts built and transferred the files into STL files. The mechanical tests performed according to ASTM standard. The first work focused on Ti6Al4V alloy to allow observation and study of a material has been used previously in AM, then moved on to the 316L Stainless steel, which is costly effective material to find the proper build direction achieve the best mechanical

properties in both bulk and cellular lattice structure parts that would be able to show the strengths and fracture resistance comparable to high performance aerospace grade Stainless Steel. The primary contributions of this PhD are:

- The DMLS of the ti6Al4V process showed more consistent and homogenous static properties in all of the build directions, and meet the minimum specification required for wrought and annealed Ti6Al4V, except in relation to the elongation. All of the DMLS of titanium samples were found to have the same surface roughness, but were slightly rougher in parallel to the build direction surfaces. The microstructure analysis shows fully the acicular α` of martensitic, and the long columnar grains that are oriented in the building direction, which are 350 μm long, due to high temperature gradients and a rapid cooling rate giving a small number of pores. The high speed movement of the laser beam makes the molten material adhere to the neighbouring particles that surround the outer boundary of the parts and produce sharp and prominent edges at the side of the part's edges. Build direction is not an important factor in structures made using Ti6Al4V.
- The Ti-6Al-4V test pieces produced using the DMLS process exhibited better fracture toughness values in the *yx* and *xz* direction, and lower values in the *zx* samples, in comparison to the annealed Ti6Al4V, while the tensile strength was found to be higher than that in the wrought material. In addition, low ductility and brittle fracture were found in all of the samples, which were linked to the martensitic phase, and this was expected due to the high gradients of temperature that occur as a result of the DMLS process. AM is thus seen to enhance the performance of materials.
- The current SLM 316L stainless steel bulk parts have been shown to be able to compete with the wrought material, and the effect of the different build directions on the strength are seen to be quite high in comparison to previous research, as well as being higher than those in conventional material, while they maintain the high elongation values. The fracture toughness results are, on average, values from 145.5 MPa $m^{1/2}$ to 176 MPa $m^{1/2}$ at room temperature, if compared to conventional material, but the Vickers' Hardness Test shows results that are similar to those of conventional material.
- The surface roughness of the SLM of 316L stainless steel parts shows different values, for instance, the *xz* direction parts proved to be the smoothest, while the *yx* and *zx* orientation parts are rougher, and there are fewer cracks and pores present in the *xz*

parts than those in the *yx* and *zx* orientations. The dendrites' grain present in *xz* orientation parts are due to the high temperature gradient and fast cooling rate, also increased the toughness and ductility and decreased the number of pores. From a fracture toughness point of view, roughness was problematical and the parts may require secondary polishing for other reasons.

- With regard to the manufacture of 316L stainless steel components for use in the aerospace industry and other industries where fracture toughness and strength are critical, it is clear that parts should be designed so they can be made by AM with the highest in- service load carried in the build direction, the *xz* direction. Furthermore, designers and manufacturers should be aware that, because of the inherent limitations of ALM in surface roughness, parts will require subsequent heat treatments in order to solve stress concentration problems at sharp corners and fillets. Solidification ridges near the sample edges mean that post-processing may be required if such features are critical.
- The FCG of the 316L stainless steel parts that were produced by SLM showed a good fatigue performance. However, a high number of cycles were recorded in the *xz* and *zx* orientation parts when compared to the *yx* orientation parts, which means the crack growth behaviour is influenced by different microstructures in different build directions. This was attributed to the presence of pores and non-uniform grains in the *yx* orientation parts, which can make the crack propagate more easily than in the *xz* orientation parts. It is therefore advisable to select vertical orintation for components that are subjected to high cyclical loads.
- In the manufacturability of the 316L stainless steel cellular structure it was found that this is good in SLM and this can be attributed to the curved struts that form the Gyroid unit cell, this means that the unit cells are self-supported in a wider range of cell sizes and volume fractions. Both the relative density of the solid struts and the cellular lattice structure density increase with a decrease in the cell size, but they are unaffected by the different building directions. The UTS, yield strength and elongation of the parts produced increase with a decrease in the cell size of the lattice structure in both the vertical and horizontal building directions, while these properties, in the vertical building direction, are higher than those that are built in the horizontal building direction. The tensile parts were built at 2, 3, and 6 mm. cell sizes in both the vertical and horizontal building directions, and eventually fractured in the middle

parts, in particular where the struts are thin. This was due to the sudden change in density, and therefore the stiffness that formed a stress concentration. It is therefore advisable to select smaller pore sizes for cellular structure components.

- The fracture toughness of the 316L stainless steel cellular lattice structure in the vertical building direction gives parts higher than those that were built in the horizontal building direction, while the fracture toughness of the 316L stainless steel cellular lattice structure increase with a decrease in the cell size in both the vertical and horizontal building direction for parts.
- The Ashby and Gibson micromechanical model that was used in this study is able to predict trends in the fracture toughness, with the maximum difference between the SENB result and the Ashby and Gibson micromechanical model being recorded at 1 MPa $m^{1/2}$ in the 2 mm cell size samples, while the minimum difference in fracture toughness value was recorded at 0.2 MPa $m^{1/2}$ in the 6 mm cell size samples, in both the vertical and horizontal building directions. This very good agreement between experiments and modelling underpins the usefulness of the Ashby and Gibson model in the design of materials to estimate the fracture toughness of the cellular structure made by AM.
- The mechanical properties change with the change in the microstructure due to the different build directions and the orientation during the build, which affects the mechanical properties, particularly the fracture toughness. The weakest build strategy recorded in the bulk parts produced was in the *zx* direction (vertical), because of the pores, voids and cracks that are present at the edges of the parts and aligned with the solidified layers, but the weakest build strategy recorded in the cellular lattice structure parts that were produced was in the horizontal direction. This is because the struts of unit cells that were built horizontally were weaker than the struts that were built in the vertical building direction, which was parallel to the building.
- The tensile and fracture toughness of 316L stainless steel cellular structures result that has been obtained in this study are less than the 15% of the tensile and fracture toughness of bulk cast 316L, which don’t obey scaling laws.
- The fracture toughness of 316L and titanium parts produced by AM is enhanced in comparison to literature.

10.3 Future work

There is still a lot of work to be done in the optimization and design of materials for the aerospace sector. From the work presented in this thesis, further areas of research are suggested as follows:

- The SLM and DMLS machines in the lab were able to process standard powders of stainless steel but couldn't process a mixed powder of different stainless steel grades. An obvious next step would be to process stainless steel mixtures with PH 17-4, and with typical alloying elements, e.g. Cu, Si, Mg., as well as mixture titanium with Cu, in order to increase the ductility of 316L stainless steel and reduce the cost of the processing material.
- Alternative materials and alloys, which the study has used in this thesis, could also be applied to different materials, such as 6061Al alloy as a standard material and mixed with typical alloying elements, i.e., Cu, Zn, Si, Mg and Li. It can be mixed with two or more powders at the same time.
- A modelling study of the influence of process parameters and build direction, to check for changes in solidification behaviour in the SLM and DMLS powder bed processes, would be an important study. Simulation and modelling of process- property relationships in the SLM and DMLS processes, in order to produce parts with fewer defects by optimising the final microstructures would be fruitful. To develop a statistical model that includes the influence of the laser's angle and beam on the consolidation behaviour would improve the reliability of the model and could help to optimize the process parameters in terms of reducing and predicting the residual stress, this represents an interesting topic on which to focus, and it could reduce the experimental work quantity that is required in order to evaluate the residual stress.
- More specimens, with different cell types and thicknesses, can be tested in order to observe their effect on fracture toughness and FCG properties.
- Defects and semi-melted powder present in parts produce poor flow behaviour of powders, and this can affect the performance and quality of DMLS and SLM made components. In order to increase part quality, powders could be heat treated before DMLS or SLM in order to improve the flowability and favour the degassing of the contaminants that can potentially be adsorbed on the powder surface.
- This thesis has studied the relationship between the AM parts and microstructure development. More characterization could be used to investigate the relationship by

using a numerical model that is capable of predicting the temperature that is experienced by the layers in relation to the laser scan speed and energy density. This could be used to predict the grain growth direction under different process parameters, especially in titanium alloy, and would allow further control of the microstructure and the mechanical behaviour of the parts produced. This numerical thermal model would be good in order to estimate the cooling rate of each layer after solidification, and it can decrease the fast cooling rates of AM to reduce the thermal stress that occurs through AM and to produce more desirable microstructure specimens.

- Further on non-destructive testing is required so as to evaluate the quality of the specimens and to detect the critical size of the pores and their relation to life prediction as well as to determine the real porosity in the specimens. The effect of the powder distribution and powder particle size on the manufacturability of the parts would be a good area on which to focus in future works.
- The effect of the surface roughness on the mechanical properties of the cellular lattice structure is not considered in this research, and it will be important to focus future work on this in order to design high performance lightweight components, and to investigate the effect of rough surface on crack growth. the design and manufacturing of low density cellular lattice structures with various cell shapes, volume fractions and orientations that are gained from different metallic powders while using the DMLS and SLM processes so as to help the designer to use the right cell shape, size and volume fraction for the particular application is also needed.
- An optimization project could be run to identify the best build direction from a manufacturability point of view, so as to improve the mechanical properties. Proper care should be used during the post processing of samples and, when cleaned, the very low volume fractions should reduce the risk of binding loose powders to the cell struts.
- Further work, such as the HIP treatment or re-melting, could improve the mechanical properties, surface roughness and may reduce the internal stress.

References

ABOULKHAIR, N. T., EVERITT, N. M., ASHCROFT, I. & TUCK, C. 2014. Reducing porosity in AlSi10Mg parts processed by selective laser melting. *Additive Manufacturing,* 1**,** 77-86.

ADAM, G. A. & ZIMMER, D. 2015. On design for additive manufacturing: evaluating geometrical limitations. *Rapid Prototyping Journal,* 21**,** 662-670.

AEROSPACE, S. 2010. Titanium Alloy Casting, Investment Ti6Al-4V Hot Isostatic Pressed, Anneal Optional. *AMS* 4991D-2010.

AL-BERMANI, S., BLACKMORE, M., ZHANG, W. & TODD, I. 2010. The origin of microstructural diversity, texture, and mechanical properties in electron beam melted Ti-6Al-4V. *Metallurgical and materials transactions a,* 41**,** 3422-3434.

ALCISTO, J., ENRIQUEZ, A., GARCIA, H., HINKSON, S., STEELMAN, T., SILVERMAN, E., VALDOVINO, P., GIGERENZER, H., FOYOS, J. & OGREN, J. 2011. Tensile properties and microstructures of laser-formed Ti-6Al-4V. *Journal of Materials Engineering and Performance*, 20, 203-212.

ALSALLA, H., HAO, L. & SMITH, C. 2016. Fracture toughness and tensile strength of 316L stainless steel cellular lattice structures manufactured using the selective laser melting technique. *Materials Science and Engineering: A,* 669**,** 1-6.

ALSALLA, H. S., C. W., &. HAO, L., 2017. Effect of build orientation on the surface quality, microstructure and mechanical properties of selective laser melting 316L stainless steel. *Rapid prototyping journal*, Vol:24.

ARISOY, Y. M., CRIALES, L. E., ÖZEL, T., LANE, B., MOYLAN, S. & DONMEZ, A. 2016. Influence of scan strategy and process parameters on microstructure and its optimization in additively manufactured nickel alloy 625 via laser powder bed fusion. *The International Journal of Advanced Manufacturing Technology***,** 1-25.

ASHBY, M. F. & MEDALIST, R. M. 1983. The mechanical properties of cellular solids. *Metallurgical Transactions A,* 14**,** 1755-1769.

ASM International. Handbook Committee. 1998. Volume 7 of ASM Handbook: Powder Metal Technologies and Applications.

AMS. 2015. Aerospace Metals Specifications. http://www.aerospacemetals.com/ June, 7, 2017

ASTM award for refractory metals engineer. Metal Powder Report. Volume 69, Issue 4, July–August 2014, Page 8

ASTM International. 2003. ASTM E399-90 Standard Test Method for Plane-Strain Fracture Toughness of Metallic Materials

ASTM International. 2009. ASTM E8/E8M - 09 Standard Test Methods for Tension Testing of Metallic Material

ASTM International. 2016. Standard Specification for Additive Manufacturing File Format (AMF) Version 1.2, ASTM International, West Conshohocken, PA, 2016, www.astm.org

ASTM 2012. ASTM Standard F2792-12a,"Standard Terminology for Additive Manufacturing Technologies", *ASTM International, West Conshohocken*, . PA, 2012, DOI: 10.1520/F2792-10 , www.astm.org.

ASTM 2016. Guide for orientation and location dependence mechanical properties for metal additive manufacturing. *ASTMWork ItemWK49229*.

ATKINS 2007. Manufacturing a Low Carbon Footprint. *Loughborough University Project* N0012J.

ATKINS Project.2009 a low-carbon manufacturing solution. *Loughborough University Project. funded by Technology Strategy Board (TSB). Accessed 22-01-18.* www. atkins-project.com.

ATZENI, E. & SALMI, A. 2015. Study on unsupported overhangs of AlSi10Mg parts processed by Direct Metal Laser Sintering (DMLS). *Journal of Manufacturing Processes,* 20**,** 500-506.

AUMUND-KOPP, C. & PETZOLDT, F. 2008. Laser Sintering of parts with complex internal structures. *Advances in Powder Metallurgy & Particulate Materials***,** 8-12.

AZMAN, A., AYUB, R., ARSHAD, M. M., NORHAFIEZAH, S., FATHIL, M., KAMARUDIN, M., NURFAIZ, M. & HASHIM, U. Controlling growth rate of ultra-thin Silicon Dioxide S by incorporating nitrogen gas during dry thermal oxidation. Semiconductor Electronics (ICSE), 2014 *IEEE International Conference on*, 2014. IEEE, 392-395.

BACCHEWAR, P., SINGHAL, S. & PANDEY, P. 2007. Statistical modelling and optimization of surface roughness in the selective laser sintering process. *Proceedings of the Institution of Mechanical Engineers, Part B: Journal of Engineering Manufacture,* 221**,** 35-52.

BADDOO, N. 2008. Stainless steel in construction: A review of research, applications, challenges and opportunities. *Journal of Constructional Steel Research,* 64**,** 1199-1206.

BADROSSAMAY, M. & CHILDS, T. Layer formation studies in selective laser melting of steel powders. *Proc. SFF Symp., Austin, Texas, USA*, 2006. 268-279.

BARREDA, J., SANTAMARıA, F., AZPIROZ, X., IRISARRI, A. & VARONA, J. 2001. Electron beam welded high thickness Ti6Al4V plates using filler metal of similar and different composition to the base plate. *Vacuum,* 62**,** 143-150.

BARRINGTON, N. & BLACK, M. 2001. Aerospace materials and manufacturing processes at the millennium. *Series in Materials Science and Engineering***,** 1.

BASAK, A., ACHARYA, R. & DAS, S. 2016. Additive Manufacturing of Single-Crystal Superalloy CMSX-4 Through Scanning Laser Epitaxy: Computational Modeling, Experimental Process Development, and Process Parameter Optimization. *Metallurgical and Materials Transactions A,* 47**,** 3845-3859.

BAUEREIB, A., SCHAROWSKY, T. and KORNER, C., 2014. Defect generation and propagation mechanism during additive manufacturing by selective beam melting. *Journal of Materials Processing Technology,* 214(11), pp.2522-2528.

BECKER, T. H., BECK, M. & SCHEFFER, C. 2015. Microstructure and mechanical properties of direct metal laser sintered Ti-6Al-4V. *South African Journal of Industrial Engineering,* 26**,** 1-10.

BEUTH, J., FOX, J., GOCKEL, J., MONTGOMERY, C., YANG, R., QIAO, H., SOYLEMEZ, E., REESEEWATT, P., ANVARI, A. & NARRA, S. Process mapping for qualification across multiple direct metal additive manufacturing processes. *Proceedings of SFF Symposium., Austin, TX*, Aug, 2013. 12-14.

BOISSELIER, D. & SANKARÉ, S. 2012. Influence of powder characteristics in laser direct metal deposition of SS316L for metallic parts manufacturing. *Physics Procedia,* 39**,** 455-463.

BOURELL, D., STUCKER, B., SPIERINGS, A., HERRES, N. & LEVY, G. 2011. Influence of the particle size distribution on surface quality and mechanical properties in AM steel parts. *Rapid Prototyping Journal,* 17**,** 195-202.

BOYER, R. 1996. An overview on the use of titanium in the aerospace industry. *Materials Science and Engineering: A,* 213**,** 103-114.

BRADBURY, J. March 2012. AM engineer at Airbus Filton, personal consultation.

BRANDL, E., HECKENBERGER, U., HOLZINGER, V. & BUCHBINDER, D. 2012. Additive manufactured AlSi10Mg samples using Selective Laser Melting (SLM): Microstructure, high cycle fatigue, and fracture behavior. *Materials & Design,* 34**,** 159169.

BRENNE, F., NIENDORF, T. & MAIER, H. 2013. Additively manufactured cellular structures: Impact of microstructure and local strains on the monotonic and cyclic behavior under uniaxial and bending load. *Journal of Materials Processing Technology,* 213**,** 1558-1564.

BREZNY, R. & GREEN, D. J. 1990. The effect of cell size on the mechanical behavior of cellular materials. *Acta metallurgica et materialia,* 38**,** 2517-2526.

BRICE, C. A. & HOFMEISTER, W. H. 2013. Determination of bulk residual stresses in electron beam additive-manufactured aluminum. *Metallurgical and Materials Transactions A,* 44**,** 5147-5153.

BRIF, Y., THOMAS, M. & TODD, I. 2015. The use of high-entropy alloys in additive manufacturing. *Scripta Materialia,* 99**,** 93-96.

BRUNGS, D. 1997. Light weight design with light metal castings. *Materials & Design,* 18**,** 285-291.

BUCHBINDER, D., SCHLEIFENBAUM, H., HEIDRICH, S., MEINERS, W. & BÜLTMANN, J. 2011. High power selective laser melting (HP SLM) of aluminum parts. *Physics Procedia,* 12**,** 271-278.

CAIN, V., THIJS, L., VAN HUMBEECK, J., VAN HOOREWEDER, B. & KNUTSEN, R. 2015. Crack propagation and fracture toughness of Ti6Al4V alloy produced by selective laser melting. *Additive Manufacturing,* 5**,** 68-76.

CALIGNANO, F. 2014. Design optimization of supports for overhanging structures in aluminum and titanium alloys by selective laser melting. *Materials & Design,* 64**,** 203-213.

CALIGNANO, F., LORUSSO, M., PAKKANEN, J., TREVISAN, F., AMBROSIO, E. P., MANFREDI, D. & FINO, P. 2016. Investigation of accuracy and dimensional limits of part produced in aluminum alloy by selective laser melting. *The International Journal of Advanced Manufacturing Technology***,** 1-8.

CAMPBELL JR, F. C. 2011. *Manufacturing technology for aerospace structural materials,* Elsevier.

CAMPBELL, S., GALLOWAY, A., RAMSEY, G. & MCPHERSON, N. A potential solution to GMAW gas flow optimisation. Trends in Welding Research 2012: *Proceedings of the 9th International Conference,* 2013. ASM International, 453.

CARON, R. & STALEY, J. 1997. Effects of composition, processing, and structure on properties of nonferrous alloys. *Materials Park, OH: ASM International, 1997.***,** 383-415.

CARTER, L. N., ATTALLAH, M. M. & REED, R. C. 2012. Laser powder bed fabrication of nickel-base superalloys: influence of parameters; characterisation, quantification and mitigation of cracking. *Superalloys 2012***,** 577-586.

CAULFIELD, B., MCHUGH, P. & LOHFELD, S. 2007. Dependence of mechanical properties of polyamide components on build parameters in the SLS process. *Journal of Materials Processing Technology,* 182**,** 477-488.

CHALLIS, V. J., XU, X., ZHANG, L. C., ROBERTS, A. P., GROTOWSKI, J. F. & SERCOMBE, T. B. 2014. High specific strength and stiffness structures produced using selective laser melting. *Materials & Design,* 63**,** 783-788.

CHAUKE, L., MUTOMBO, K. & KGOMO, C. 2013. Characterization of the direct metal laser sintered Ti6Al4V Components.

CHEN, L., HUANG, J., LIN, C., PAN, C., CHEN, S., YANG, T., LIN, D., LIN, H. & JANG, J. 2017. Anisotropic response of Ti-6Al-4V alloy fabricated by 3D printing selective laser melting. *Materials Science and Engineering: A,* 682**,** 389-395.

CHEN, X., XIE, J. & FOX, P. 2004. Direct laser remelting of iron with addition of boron. *Materials science and technology,* 20**,** 715-719.

CHERRY, J., DAVIES, H., MEHMOOD, S., LAVERY, N., BROWN, S. & SIENZ, J. 2015. Investigation into the effect of process parameters on microstructural and physical properties of 316L stainless steel parts by selective laser melting. *The International Journal of Advanced Manufacturing Technology,* 76**,** 869-879.

CHILDS, T. & HAUSER, C. 2005. Raster scan selective laser melting of the surface layer of a tool steel powder bed. *Proceedings of the Institution of Mechanical Engineers, Part B: Journal of Engineering Manufacture,* 219**,** 379-384.

CHILDS, T., HAUSER, C. & BADROSSAMAY, M. 2005. Selective laser sintering (melting) of stainless and tool steel powders: experiments and modelling. *Proceedings of the Institution of Mechanical Engineers, Part B: Journal of Engineering Manufacture,* 219**,** 339-357.

CHIRITA, G., STEFANESCU, I., CRUZ, D., SOARES, D. & SILVA, F. 2010. Sensitivity of different Al–Si alloys to centrifugal casting effect. *Materials & Design,* 31**,** 2867-2877.

CHLEBUS, E., KUŹNICKA, B., KURZYNOWSKI, T. & DYBAŁA, B. 2011. Microstructure and mechanical behaviour of Ti—6Al—7Nb alloy produced by selective laser melting. *Materials Characterization,* 62**,** 488-495.

CHOI, J.-W., KIM, H.-C. & WICKER, R. 2011. Multi-material stereolithography. *Journal of Materials Processing Technology,* 211**,** 318-328.

CHOI, S. & SANKAR, B. 2003. Fracture toughness of carbon foam. *Journal of Composite Materials,* 37, 2101-2116.

CHRIS CAREY, O. I., SIR DAVID KING, 2013. Advanced aerospace materials: past, present and future. *Oxford University's Smith School of Enterprise and the Environment.*

CHU, C., GRAF, G. & ROSEN, D. W. 2008. Design for additive manufacturing of cellular structures. *Computer-Aided Design and Applications,* 5**,** 686-696.

COMMITTEE, A. I. H. 1997. *ASM handbook: Materials selection and design,* CRC Press.

CONTREPOIS, Q. & LECOMTE-BECKERS, J. 2011. Rapidly solidified microstructure of 3D parts fabricated by selective laser melting (SLM)-Examples of stainless steel 316L and titanium Ti-6Al-4V.

DADBAKHSH, S. & HAO, L. 2012. Effect of Al alloys on selective laser melting behaviour and microstructure of in situ formed particle reinforced composites. *Journal of alloys and compounds,* 541**,** 328-334.

DADBAKHSH, S., HAO, L., JERRARD, P. & ZHANG, D. 2012a. Experimental investigation on selective laser melting behaviour and processing windows of in situ reacted Al/Fe 2 O 3 powder mixture. *Powder technology,* 231**,** 112-121.

DADBAKHSH, S., HAO, L. & SEWELL, N. 2012b. Effect of selective laser melting layout on the quality of stainless steel parts. *Rapid Prototyping Journal,* 18**,** 241-249.

DAHAR, M. S., SEIFI, S. M., BEWLAY, B. & LEWANDOWSKI, J. J. 2015. Effects of test orientation on fracture and fatigue crack growth behavior of third generation as-cast Ti–48Al–2Nb–2Cr. *Intermetallics,* 57**,** 73-82.

DAHOTRE, N. B. & HARIMKAR, S. P. 2008. Laser-Based Rapid Prototyping Processes. *Laser Fabrication and Machining of Materials***,** 353-411.

DAS, S. 2003. Physical aspects of process control in selective laser sintering of metals. *Advanced Engineering Materials,* 5**,** 701-711.

DE LIMA, M. S. F. & SANKARÉ, S. 2014. Microstructure and mechanical behavior of laser additive manufactured AISI 316 stainless steel stringers. *Materials & Design,* 55**,** 526-532.

DEGISCHER, H. P. 2009. *Leichtbau: Prinzipien, Werkstoffauswahl und Fertigungsvarianten,* John Wiley & Sons.

DEWIDAR, M., DALGARNO, K. & WRIGHT, C. 2003. Processing conditions and mechanical properties of high-speed steel parts fabricated using direct selective laser sintering. *Proceedings of the Institution of Mechanical Engineers, Part B: Journal of Engineering Manufacture,* 217**,** 1651-1663.

DINDA, G., DASGUPTA, A. & MAZUMDER, J. 2012. Evolution of microstructure in laser deposited Al–11.28% Si alloy. *Surface and Coatings Technology,* 206**,** 2152-2160.

DING, D., PAN, Z., CUIURI, D. & LI, H. 2015. Wire-feed additive manufacturing of metal components: technologies, developments and future interests. *The International Journal of Advanced Manufacturing Technology,* 81**,** 465-481.

DOUTRE, P.-T., MORRETTON, E., VO, T. H., MARIN, P., POURROY, F., PRUDHOMME, G. & VIGNAT, F. 2017. Comparison of some approaches to define a CAD model from topological optimization in design for additive manufacturing. *Advances on Mechanics, Design Engineering and Manufacturing.* Springer.

Dursun, T. and Soutis, C., 2014. Recent developments in advanced aircraft aluminium alloys. *Materials & Design*, 56, pp.862-871.

EDWARDS, P., O'CONNER, A. & RAMULU, M. 2013. Electron beam additive manufacturing of titanium components: Properties and performance. *Journal of Manufacturing Science and Engineering,* 135**,** 061016.

EDWARDS, P. & RAMULU, M. 2014. Fatigue performance evaluation of selective laser melted Ti–6Al–4V. *Materials Science and Engineering: A,* 598**,** 327-337.

EDWARDS, P. & RAMULU, M. 2015. Effect of build direction on the fracture toughness and fatigue crack growth in selective laser melted Ti-6Al-4 V. *Fatigue & Fracture of Engineering Materials & Structures,* 38**,** 1228-1236.

EISEN, W., FERGUSON, B., GERMAN, R., IACOCCA, R., LEE, P., MADAN, D., MOYER, K., SANDEROW, H. & TRUDEL, Y. 1998. Powder metal technologies and applications.

EJIOFOR, J. & REDDY, R. 1997. Developments in the processing and properties of particulate Al-Si composites. *Jom,* 49**,** 31-37.

ELAHINIA, M., MOGHADDAM, N. S., ANDANI, M. T., AMERINATANZI, A., BIMBER, B. A. & HAMILTON, R. F. 2016. Fabrication of NiTi through additive manufacturing: A review. *Progress in Materials Science,* 83**,** 630-663.

EVANS, A. G., HUTCHINSON, J. & ASHBY, M. 1998. Multifunctionality of cellular metal systems. *Progress in Materials Science,* 43**,** 171-221.

FACCHINI, L., MAGALINI, E., ROBOTTI, P. & MOLINARI, A. 2009. Microstructure and mechanical properties of Ti-6Al-4V produced by electron beam melting of pre-alloyed powders. *Rapid Prototyping Journal,* 15**,** 171-178.

FACCHINI, L., MAGALINI, E., ROBOTTI, P., MOLINARI, A., HÖGES, S. & WISSENBACH, K. 2010. Ductility of a Ti-6Al-4V alloy produced by selective laser melting of prealloyed powders. *Rapid Prototyping Journal,* 16**,** 450-459.

FETONI, A. R., DE BARTOLO, P., ERAMO, S. L. M., ROLESI, R., PACIELLO, F., BERGAMINI, C., FATO, R., PALUDETTI, G., PETROSINI, L. & TROIANI, D. 2013. Noise-induced hearing loss (NIHL) as a target of oxidative stress-mediated damage: cochlear and cortical responses after an increase in antioxidant defense. *Journal of Neuroscience,* 33**,** 4011-4023.

FISCHER, P., ROMANO, V., WEBER, H. P., KARAPATIS, N. P., BOILLAT, E. & GLARDON, R. 2003. Sintering of commercially pure titanium powder with a Nd:YAG laser source. *Acta Materialia,* 51**,** 1651-1662.

FODRAN E, W. K. 2015. Surface finish enhancement for the electron beam direct digital manufacturing of Ti-6Al-4V alloy structural components. *Tech. Rep., Armament Research, Development and Engineering Center,Weapons Software Engineering Center, Ben´et Lab.*

FRAZIER, W. E. 2010. Direct digital manufacturing of metallic components: vision and roadmap. 21st Annual International Solid Freeform Fabrication Symposium, Austin, TX, Aug, 2010. 9-11.

FRAZIER, W. E. 2014. Metal additive manufacturing: a review. *Journal of Materials Engineering and Performance,* 23**,** 1917-1928.

FU, C. & GUO, Y. 2014. Three-dimensional temperature gradient mechanism in selective laser melting of Ti-6Al-4V. *Journal of Manufacturing Science and Engineering,* 136**,** 061004.

Gammon, L.M., Briggs, R.D., Packard, J.M., Batson, K.W., Boyer, R. and Domby, C.W., 2004. Metallography and microstructures of titanium and its alloys. *ASM Handbook,* 9, pp.899-917

GAJALAKSHMI, S. & SRIRAM, K. 2015. Investigation of mechanical behavior of ultra light weight nano composite for aero-crafts. *International Journal of Science and Research (IJSR),* 4**,** 1892-1895.

GANESH, P., KAUL, R., SASIKALA, G., KUMAR, H., VENUGOPAL, S., TIWARI, P., RAI, S., PRASAD, R. & KUKREJA, L. 2014. Fatigue crack propagation and fracture toughness of laser rapid manufactured structures of AISI 316L stainless steel. *Metallography, Microstructure, and Analysis,* 3**,** 36-45.

GÄUMANN, M., HENRY, S., CLETON, F., WAGNIERE, J.-D. & KURZ, W. 1999. Epitaxial laser metal forming: analysis of microstructure formation. *Materials Science and Engineering: A,* 271**,** 232-241.

GEBHARDT, A., SCHMIDT, F.-M., HÖTTER, J.-S., SOKALLA, W. & SOKALLA, P. 2010. Additive manufacturing by selective laser melting the realizer desktop machine and its application for the dental industry. *Physics Procedia,* 5**,** 543-549.

GHANI, S., ZAKARIA, M., HARUN, W. & ZAULKAFILAI, Z. Dimensional accuracy of internal cooling channel made by selective laser melting (SLM) And direct metal laser sintering (DMLS) processes in fabrication of internally cooled cutting tools. *MATEC Web of Conferences,* 2017. EDP Sciences, 01058.

GHOSH, S. K. & SAHA, P. 2011. Crack and wear behavior of SiC particulate reinforced aluminium based metal matrix composite fabricated by direct metal laser sintering process. *Materials & Design,* 32**,** 139-145.

GIBSON, I., ROSEN, D. & STUCKER, B. Additive Manufacturing Technologies Rapid Prototyping to Direct Digital Manufacturing. 2010. *Springer.*

GIBSON, L. J., ASHBY, M. & SOLIDS, C. 1997. Structure and properties. *Cellular Solids***,** 307-308.

GIBSON, L. J. & ASHBY, M. F. 1999. Cellular solids: structure and properties, *Cambridge university press.*

GNÄUPEL-HEROLD, T., SLOTWINSKI, J., MOYLAN, S., CHIMENTI, D. E., BOND, L. J. & THOMPSON, D. O. Neutron measurements of stresses in a test artifact produced by laser-based additive manufacturing. *AIP Conference Proceedings,* 2014. AIP, 1205-1212.

GOCKEL, J. & BEUTH, J. 2013. Understanding Ti-6Al-4V microstructure control in additive manufacturing via process maps. *Solid Freeform Fabrication Proceedings, Austin, TX, Aug***,** 12-14.

GOCKEL, J., BEUTH, J. & TAMINGER, K. 2014. Integrated control of solidification microstructure and melt pool dimensions in electron beam wire feed additive manufacturing of Ti-6Al-4V. *Additive Manufacturing,* 1**,** 119-126.

GONG, H., RAFI, K., GU, H., STARR, T. & STUCKER, B. 2014. Analysis of defect generation in Ti–6Al–4V parts made using powder bed fusion additive manufacturing processes. *Additive Manufacturing,* 1**,** 87-98.

GREGOLIN, R. F., BARBOSA, F. M., DE CAMARGO ZAVAGLIA, C. A. & TOKIMATSU, R. C. 2013. DEVELOPMENT AND MECHANICAL CHARACTERIZATION OF A MANDIBULAR PROSTHESIS IN TITANIUM ALLOY FABRICATED BY DIRECT METAL LASER SINTERING (*DMLS*).

GREITEMEIER, D., DALLE DONNE, C., SYASSEN, F., EUFINGER, J. & MELZ, T. 2016. Effect of surface roughness on fatigue performance of additive manufactured Ti–6Al–4V. *Materials Science and Technology,* 32**,** 629-634.

GU, D. & SHEN, Y. 2009. Balling phenomena in direct laser sintering of stainless steel powder: metallurgical mechanisms and control methods. *Materials & Design,* 30**,** 2903-2910.

GUAN, K., WANG, Z., GAO, M., LI, X. & ZENG, X. 2013. Effects of processing parameters on tensile properties of selective laser melted 304 stainless steel. *Materials & Design,* 50**,** 581-586.

HAO, L., DADBAKHSH, S., SEAMAN, O. & FELSTEAD, M. 2009. Selective laser melting of a stainless steel and hydroxyapatite composite for load-bearing implant development. *Journal of Materials Processing Technology,* 209**,** 5793-5801.

HAUSER, C., SUTCLIFFE, C., EGAN, M. & FOX, P. 2005. SPIRAL GROWTH MANUFACTURING (SGM)–A CONTINUOUS ADDITIVE MANUFACTURING TECHNOLOGY FOR PROCESSING METAL POWDER BY SELECTIVE LASER MELTING. *Proc. Solid Freeform Fabrication***,** 1-12.

HERDERICK, E. 2011. Additive manufacturing of metals: A review. *Materials Science & Technology,* 1413-1425.

HERDERICK, E. D. 2016. Additive Manufacturing in the Minerals, Metals, and Materials Community: Past, Present, and Exciting Future. *JOM,* 68**,** 721-723.

HOPKINSON, N., HAGUE, R. & DICKENS, P. 2006. *Rapid manufacturing: an industrial revolution for the digital age*, John Wiley & Sons.

HUANG, Y., JIVRAJ, J., ZHOU, J., RAMJIST, J., WONG, R., GU, X. & YANG, V. X. 2016. Pulsed and CW adjustable 1942 nm single-mode all-fiber Tm-doped fiber laser

system for surgical laser soft tissue ablation applications. *Optics Express,* 24**,** 16674-16686.

HUNT, E. J., ZHANG, C., ANZALONE, N. & PEARCE, J. M. 2015. Polymer recycling codes for distributed manufacturing with 3-D printers. *Resources, Conservation and Recycling,* 97**,** 24-30.

HUSSEIN, A., HAO, L., YAN, C., EVERSON, R. & YOUNG, P. 2013. Advanced lattice support structures for metal additive manufacturing. *Journal of Materials Processing Technology,* 213**,** 1019-1026.

INAGAKI, I., TAKECHI, T., SHIRAI, Y. & ARIYASU, N. 2014. Application and features of titanium for the aerospace industry. *Nippon Steel & Sumitomo Metal Technical Report,* 106**,** 22-27.

JERRARD, P., HAO, L. & EVANS, K. 2009. Experimental investigation into selective laser melting of austenitic and martensitic stainless steel powder mixtures. *Proceedings of the Institution of Mechanical Engineers, Part B: Journal of Engineering Manufacture,* 223**,** 1409-1416.

JI, C. H., LOH, N. H., KHOR, K. A. & TOR, S. B. 2001. Sintering study of 316L stainless steel metal injection molding parts using Taguchi method: final density. *Materials Science and Engineering: A,* 311**,** 74-82.

JIA, Q. & GU, D. 2014. Selective laser melting additive manufacturing of Inconel 718 superalloy parts: Densification, microstructure and properties. *Journal of Alloys and Compounds,* 585, 713-721.

JOHN, F. 2001. Ready: LIA Handbook of Laser Materials Processing. *Laser Institute of America Magnolia Publishing Inc***,** 181-183.

JOHNS, D. March 2009. AM manager at Airbus Filton, personal consultation.

JONES, D. R. & ASHBY, M. F. 2005. *Engineering materials 2: an introduction to microstructures, processing and design,* Butterworth-Heinemann.

KAISER, R., WILLIAMSON, K., O'BRIEN, C., RAMIREZ-GARCIA, S. & BROWNE, D. 2013. The influence of cooling conditions on grain size, secondary phase precipitates and mechanical properties of biomedical alloy specimens produced by investment casting. *Journal of the mechanical behavior of biomedical materials,* 24**,** 53-63.

KALU, I. 2013. *Numerical Modeling Of Wellbore Instability (SHEAR Failure) Using Fracture Mechanics Approach.*

KELLENS, K., YASA, E., RENALDI, R., DEWULF, W., KRUTH, J.-P. & DUFLOU, J. Energy and resource efficiency of SLS/SLM processes (keynote paper). *SFF Symposium* 2011, 2011. 1-16.

KEMPEN, K., THIJS, L., VRANCKEN, B., BULS, S., VAN HUMBEECK, J. & KRUTH, J. Producing crack-free, high density M2 Hss parts by selective laser melting: pre-heating the baseplate. Proceedings of the 24th international solid freeform fabrication symposium. *Laboratory for freeform fabrication, Austin,* TX, 2013. 131-139.

KHAING, M., FUH, J. & LU, L. 2001. Direct metal laser sintering for rapid tooling: processing and characterisation of EOS parts. *Journal of Materials Processing Technology,* 113**,** 269-272.

KHANNA, N. & DAVIM, J. 2015. Design-of-experiments application in machining titanium alloys for aerospace structural components. *Measurement,* 61**,** 280-290.

KING, D. & CAREY, C. 2009. Advanced aerospace materials: past, present and future. *Aviation and the Environment,* 22**,** 27.

KING, W. E., BARTH, H. D., CASTILLO, V. M., GALLEGOS, G. F., GIBBS, J. W., HAHN, D. E., KAMATH, C. & RUBENCHIK, A. M. 2014. Observation of keyhole-mode laser melting in laser powder-bed fusion additive manufacturing. *Journal of Materials Processing Technology,* 214**,** 2915-2925.

KOBRYN, P. & SEMIATIN, S. 2001. The laser additive manufacture of Ti-6Al-4V. *JOM,* 53**,** 40-42.

KOBRYN PA, S. S. 2001. Mechanical properties of laser-deposited Ti-6Al-4V. *In Solid Freeform Fabrication Proceedings,* pp. 179–86. Austin: Univ. Tex.

KOIKE, M., GREER, P., OWEN, K., LILLY, G., MURR, L. E., GAYTAN, S. M., MARTINEZ, E. & OKABE, T. 2011. Evaluation of titanium alloys fabricated using rapid prototyping technologies—Electron beam melting and laser beam melting. *Materials,* 4**,** 1776-1792.

KÖRNER, C., BAUEREIß, A. & ATTAR, E. 2013. Fundamental consolidation mechanisms during selective beam melting of powders. *Modelling and Simulation in Materials Science and Engineering,* 21**,** 085011.

KRAKHMALEV, P., FREDRIKSSON, G., YADROITSAVA, I., KAZANTSEVA, N., DU PLESSIS, A. & YADROITSEV, I. 2016. Deformation behavior and microstructure of Ti6Al4V manufactured by SLM. *Physics Procedia,* 83, 778-788

KRAKHMALEV, P., YADROITSAVA, I., FREDRIKSSON, G. & YADROITSEV, I. Microstructure of SLM manufactured 316L and 420 grades stainless steel. *RAPDASA* 2014, 2014.

KRUTH, J.-P., BADROSSAMAY, M., YASA, E., DECKERS, J., THIJS, L. & VAN HUMBEECK, J. Part and material properties in selective laser melting of metals. *Proceedings of the 16th international symposium on electromachining*, 2010.

KRUTH, J.-P., FROYEN, L., VAN VAERENBERGH, J., MERCELIS, P., ROMBOUTS, M. & LAUWERS, B. 2004. Selective laser melting of iron-based powder. *Journal of Materials Processing Technology,* 149**,** 616-622.

KRUTH, J.-P., LEVY, G., KLOCKE, F. & CHILDS, T. 2007. Consolidation phenomena in laser and powder-bed based layered manufacturing. *CIRP Annals-Manufacturing Technology,* 56**,** 730-759.

KUCHEROV, L. & RYVKIN, M. 2014. Fracture toughness of open-cell Kelvin foam. *International Journal of Solids and Structures,* 51**,** 440-448.

KURGAN, N. 2013. Effects of sintering atmosphere on microstructure and mechanical property of sintered powder metallurgy 316L stainless steel. *Materials & Design,* 52**,** 995-998.

KURZYNOWSKI, T., CHLEBUS, E., KUŹNICKA, B. & REINER, J. Parameters in selective laser melting for processing metallic powders. SPIE LASE, 2012. *International Society for Optics and Photonics*, 823914-823914-6.

KUZIAK, R., KAWALLA, R. & WAENGLER, S. 2008. Advanced high strength steels for automotive industry. *Archives of civil and mechanical engineering,* 8**,** 103-117.

LEUDERS, S., LIENEKE, T., LAMMERS, S., TRÖSTER, T. & NIENDORF, T. 2014. On the fatigue properties of metals manufactured by selective laser melting–The role of ductility. *Journal of Materials Research,* 29**,** 1911-1919.

LEUDERS, S., THÖNE, M., RIEMER, A., NIENDORF, T., TRÖSTER, T., RICHARD, H. & MAIER, H. 2013. On the mechanical behaviour of titanium alloy TiAl6V4 manufactured by selective laser melting: Fatigue resistance and crack growth performance. *International Journal of Fatigue,* 48**,** 300-307.

LEUTENECKER-TWELSIEK, B., KLAHN, C. & MEBOLDT, M. 2016. Considering Part Orientation in Design for Additive Manufacturing. *Procedia CIRP,* 50**,** 408-413.

LEVY, G. N., SCHINDEL, R. & KRUTH, J.-P. 2003. Rapid manufacturing and rapid tooling with layer manufacturing (LM) technologies, state of the art and future perspectives. *CIRP Annals-Manufacturing Technology,* 52**,** 589-609.

LEWANDOWSKI, J. J. & SEIFI, M. 2016. Metal additive manufacturing: a review of mechanical properties. *Annual Review of Materials Research,* 46**,** 151-186.

LEWIS, G. K. & SCHLIENGER, E. 2000. Practical considerations and capabilities for laser assisted direct metal deposition. *Materials & Design,* 21**,** 417-423.

LEYENS, C. & PETERS, M. 2003. Titanium and titanium alloys: fundamentals and applications, *John Wiley & Sons,page 9*.

LI, P., WARNER, D., FATEMI, A. & PHAN, N. 2016. Critical assessment of the fatigue performance of additively manufactured Ti–6Al–4V and perspective for future research. *International Journal of Fatigue,* 85**,** 130-143.

LI, R., LIU, J., SHI, Y., DU, M. & XIE, Z. 2010. 316L stainless steel with gradient porosity fabricated by selective laser melting. *Journal of Materials Engineering and Performance,* 19**,** 666-671.

LI, S., MURR, L. E., CHENG, X., ZHANG, Z., HAO, Y., YANG, R., MEDINA, F. & WICKER, R. 2012. Compression fatigue behavior of Ti–6Al–4V mesh arrays fabricated by electron beam melting. *Acta Materialia,* 60**,** 793-802.

LI, X., KANG, C., HUANG, H. & SERCOMBE, T. 2014. The role of a low-energy–density re-scan in fabricating crack-free Al 85 Ni 5 Y 6 Co 2 Fe 2 bulk metallic glass composites via selective laser melting. *Materials & Design,* 63**,** 407-411.

LIAO, Y., LI, H. & CHIU, Y. 2006. Study of laminated object manufacturing with separately applied heating and pressing. *The International Journal of Advanced Manufacturing Technology,* 27**,** 703-707.

LINDEMANN, C., REIHER, T., JAHNKE, U. & KOCH, R. 2015. Towards a sustainable and economic selection of part candidates for additive manufacturing. *Rapid Prototyping Journal,* 21**,** 216-227.

LIU, Z., ZHANG, D., SING, S., CHUA, C. & LOH, L. 2014. Interfacial characterization of SLM parts in multi-material processing: Metallurgical diffusion between 316L stainless steel and C18400 copper alloy. *Materials Characterization,* 94**,** 116-125.

LLC, D. M. 2013. EOS M 280- Direct Metal Laser-Sintering. *3DPARTS Manufacturing LLC,* [online].

LOUVIS, E., FOX, P. & SUTCLIFFE, C. J. 2011. Selective laser melting of aluminium components. *Journal of Materials Processing Technology,* 211**,** 275-284.

LU, S., TANG, H., NING, Y., LIU, N., STJOHN, D. & QIAN, M. 2015. Microstructure and mechanical properties of long Ti-6Al-4V rods additively manufactured by selective

electron beam melting out of a deep powder bed and the effect of subsequent hot isostatic pressing. *Metallurgical and Materials Transactions A,* 46**,** 3824-3834.

MAKOANA, N., MOLLER, H., BURGER, H., TLOTLENG, M. & YADROITSEV, I. 2016. Evaluation of single tracks of 17-4PH steel manufactured at different power densities and scanning speeds by selective laser melting. *South African Journal of Industrial Engineering,* 27**,** 210-218.

MALLAPUR, D., RAJENDRA UDUPA, K. & KORI, S. 2010. Influence of grain refiner and modifier on the microstructure and mechanical properties of a 356 alloy. *International Journal of Engineering Science and Technology,* 2**,** 4487-4493.

MALOY, S., JAMES, M., WILLCUTT, G., SOMMER, W., SOKOLOV, M., SNEAD, L., HAMILTON, M. & GARNER, F. 2001. The mechanical properties of 316L/304L stainless steels, Alloy 718 and Mod 9Cr–1Mo after irradiation in a spallation environment. *Journal of Nuclear Materials,* 296**,** 119-128.

MANFREDI, D., CALIGNANO, F., KRISHNAN, M., CANALI, R., AMBROSIO, E. P., BIAMINO, S., UGUES, D., PAVESE, M. & FINO, P. 2014. Additive manufacturing of al alloys and aluminium matrix composites (AMCs). *Light Metal Alloys Applications,* 11**,** 3-34.

MANI, M., LYONS, K. W. & GUPTA, S. 2014. Sustainability characterization for additive manufacturing. *Journal of research of the National Institute of Standards and Technology,* 119, 419.

MARKL, M., AMMER, R., RÜDE, U. & KÖRNER, C. 2015. Numerical investigations on hatching process strategies for powder-bed-based additive manufacturing using an electron beam. *The International Journal of Advanced Manufacturing Technology,* 78**,** 239-247.

MARSAVINA, L. & LINUL, E. 2010. Fracture toughness of polyurethane foams, Experiments versus micromechanical models. *Proceedings of ECF18, Dresden*.

MATSUMOTO, M., SHIOMI, M., OSAKADA, K. & ABE, F. 2002. Finite element analysis of single layer forming on metallic powder bed in rapid prototyping by selective laser processing. *International Journal of Machine Tools and Manufacture,* 42**,** 61-67.

MCDONALD, K. 2015. *Thermal management during direct laser deposition (DLD) of Ti-6Al-4V components.* University of Birmingham.

MCKOWN, S., SHEN, Y., BROOKES, W., SUTCLIFFE, C., CANTWELL, W., LANGDON, G., NURICK, G. & THEOBALD, M. 2008. The quasi-static and blast

loading response of lattice structures. *International Journal of Impact Engineering,* 35**,** 795-810.

MCNUTT, P. A. 2015. *An investigation of cracking in laser metal deposited nickel superalloy CM247LC.* University of Birmingham.

MEIER, H. & HABERLAND, C. 2008. Experimental studies on selective laser melting of metallic parts. *Materialwissenschaft und Werkstofftechnik,* 39**,** 665-670.

MERTENS, A., CONTREPOIS, Q., DORMAL, T., LEMAIRE, O. & LECOMTE-BECKERS, J. Ti alloys processed by selective laser melting and by laser cladding: microstructures and mechanical properties. Proc. 12 th European Conference on Space Structures, *Materials and Environmental Testing, Noordwijk, The Netherlands* (ESA SP-691, 2012.

MERTENS, A., REGINSTER, S., PAYDAS, H., CONTREPOIS, Q., DORMAL, T., LEMAIRE, O. & LECOMTE-BECKERS, J. 2014. Mechanical properties of alloy Ti–6Al–4V and of stainless steel 316L processed by selective laser melting: Influence of out-of-equilibrium microstructures. *Powder Metallurgy,* 57**,** 184-189.

MILLS, N. 2007. Polymer foams handbook: engineering and biomechanics applications and design guide, *Butterworth-Heinemann.*

MIRACLE, D. B., DONALDSON, S. L., HENRY, S. D., MOOSBRUGGER, C., ANTON, G. J., SANDERS, B. R., HRIVNAK, N., TERMAN, C., KINSON, J. & MULDOON, K. 2001. *ASM handbook,* ASM international Materials Park, OH, USA.

MOHAMMADHOSSEINI, A., FRASER, D., MASOOD, S. & JAHEDI, M. 2013. Microstructure and mechanical properties of Ti–6Al–4V manufactured by electron beam melting process. *Materials Research Innovations,* 17**,** s106-s112.

MOHANTY, J., VERMA, B. & RAY, P. 2010. Determination of fatigue crack growth rate from experimental data: a new approach. *International Journal of Microstructure and Materials Properties,* 5**,** 79-87.

MONROY, K. P., DELGADO, J., SERENO, L., CIURANA, J. & HENDRICHS, N. J. 2014. Effects of the Selective Laser Melting manufacturing process on the properties of CoCrMo single tracks. *Metals and Materials International,* 20**,** 873.

MORROW, W., QI, H., KIM, I., MAZUMDER, J. & SKERLOS, S. 2007. Environmental aspects of laser-based and conventional tool and die manufacturing. *Journal of Cleaner Production,* 15**,** 932-943.

MUMTAZ, K. & HOPKINSON, N. 2009. Top surface and side roughness of Inconel 625 parts processed using selective laser melting. *Rapid Prototyping Journal,* 15**,** 96-103.

MUMTAZ, K. & HOPKINSON, N. 2010. Selective laser melting of Inconel 625 using pulse shaping. *Rapid Prototyping Journal,* 16**,** 248-257.

MURR, L., QUINONES, S., GAYTAN, S., LOPEZ, M., RODELA, A., MARTINEZ, E., HERNANDEZ, D., MARTINEZ, E., MEDINA, F. & WICKER, R. 2009. Microstructure and mechanical behavior of Ti–6Al–4V produced by rapid-layer manufacturing, for biomedical applications. *Journal of the mechanical behavior of biomedical materials,* 2**,** 20-32.

MURR, L. E., GAYTAN, S., CEYLAN, A., MARTINEZ, E., MARTINEZ, J., HERNANDEZ, D., MACHADO, B., RAMIREZ, D., MEDINA, F. & COLLINS, S. 2010. Characterization of titanium aluminide alloy components fabricated by additive manufacturing using electron beam melting. *Acta Materialia,* 58**,** 1887-1894.

MURR, L. E., GAYTAN, S. M., RAMIREZ, D. A., MARTINEZ, E., HERNANDEZ, J., AMATO, K. N., SHINDO, P. W., MEDINA, F. R. & WICKER, R. B. 2012a. Metal fabrication by additive manufacturing using laser and electron beam melting technologies. *Journal of Materials Science & Technology,* 28**,** 1-14.

MURR, L. E., MARTINEZ, E., AMATO, K. N., GAYTAN, S. M., HERNANDEZ, J., RAMIREZ, D. A., SHINDO, P. W., MEDINA, F. & WICKER, R. B. 2012b. Fabrication of metal and alloy components by additive manufacturing: examples of 3D materials science. *Journal of Materials Research and technology,* 1**,** 42-54.

NAKAI, M. & ETO, T. 2000. New aspect of development of high strength aluminum alloys for aerospace applications. *Materials Science and Engineering: A,* 285**,** 62-68.

NAKAJIMA, H. 2007. Fabrication, properties and application of porous metals with directional pores. *Progress in Materials Science,* 52**,** 1091-1173.

NIST 2013. ‘‘Measurement Science Roadmap for Metal-Based Additive Manufacturing,’’. US Department of Commerce, National Institute of Standards and Technology, Prepared by Energetics Incorporated, May 2013.

OH, J., KIM, N. J., LEE, S. & LEE, E. W. 2003. Correlation of fatigue properties and microstructure in investment cast Ti-6Al-4V welds. *Materials Science and Engineering: A,* 340**,** 232-242.

OLAKANMI, E. 2013. Selective laser sintering/melting (SLS/SLM) of pure Al, Al–Mg, and Al–Si powders: Effect of processing conditions and powder properties. *Journal of Materials Processing Technology,* 213**,** 1387-1405.

OLAKANMI, E., COCHRANE, R. & DALGARNO, K. 2015. A review on selective laser sintering/melting (SLS/SLM) of aluminium alloy powders: Processing, microstructure, and properties. *Progress in Materials Science,* 74**,** 401-477.

OLURIN, O., FLECK, N. & ASHBY, M. 2000. Deformation and fracture of aluminium foams. *Materials Science and Engineering: A,* 291**,** 136-146.

OSAKADA, K. & SHIOMI, M. 2006. Flexible manufacturing of metallic products by selective laser melting of powder. *International Journal of Machine Tools and Manufacture,* 46**,** 1188-1193.

OSORIO, W. R., GOULART, P. R., GARCIA, A., SANTOS, G. A. & NETO, C. M. 2006. Effect of dendritic arm spacing on mechanical properties and corrosion resistance of Al 9 Wt Pct Si and Zn 27 Wt Pct Al alloys. *Metallurgical and Materials Transactions A,* 37**,** 2525-2538.

PARTHASARATHY, J., STARLY, B., RAMAN, S. & CHRISTENSEN, A. 2010. Mechanical evaluation of porous titanium (Ti6Al4V) structures with electron beam melting (EBM). *Journal of the mechanical behavior of biomedical materials,* 3**,** 249-259.

PARTNET, C. 2009. Sand Casting. *retrieved Oct,* 7.

PETERS, M., KUMPFERT, J., WARD, C. H. & LEYENS, C. 2003. Titanium alloys for aerospace applications. *Advanced Engineering Materials,* 5**,** 419-427.

PINKERTON, A. J. 2007. Matching the additive process and parameters to the purpose. *AILU Technology Workshop,* Rotherham, UK.

POLMEAR, I. 2006a. Light metals: from traditional alloys to nanocrystals. *Elsevier, Oxford*.

POLMEAR, I. J. 2006b. Light alloys: From traditional alloys to nanocrystals.

PRASHANTH, K., SCUDINO, S., KLAUSS, H., SURREDDI, K. B., LÖBER, L., WANG, Z., CHAUBEY, A., KÜHN, U. & ECKERT, J. 2014. Microstructure and mechanical properties of Al–12Si produced by selective laser melting: Effect of heat treatment. *Materials Science and Engineering: A,* 590**,** 153-160.

QI, H., YAN, Y., LIN, F. & ZHANG, R. 2007. Scanning method of filling lines in electron beam selective melting. *Proceedings of the Institution of Mechanical Engineers, Part B: Journal of Engineering Manufacture,* 221**,** 1685-1694.

QIU, C., ADKINS, N. J. & ATTALLAH, M. M. 2013. Microstructure and tensile properties of selectively laser-melted and of HIPed laser-melted Ti–6Al–4V. *Materials Science and Engineering: A,* 578**,** 230-239.

QUINTANA-ALONSO, I., MAI, S., FLECK, N., OAKES, D. & TWIGG, M. 2010. The fracture toughness of a cordierite square lattice. *Acta Materialia,* 58**,** 201-207.

RAFI, H. K., STARR, T. L. & STUCKER, B. E. 2013. A comparison of the tensile, fatigue, and fracture behavior of Ti–6Al–4V and 15-5 PH stainless steel parts made by selective laser melting. *The International Journal of Advanced Manufacturing Technology,* 69**,** 1299-1309.

REHME, O. & EMMELMANN, C. 2010. *Cellular design for laser freeform fabrication*, Cuvillier Göttingen. ., Leibniz information centre for science and technology University Library, Germany. Series: Schriftenreihe Lasertechnik; 4; 1-298. ISBN: 978-3-86955-273-6. www.tib.eu

RICKENBACHER, L., ETTER, T., HÖVEL, S. & WEGENER, K. 2013. High temperature material properties of IN738LC processed by selective laser melting (SLM) technology. *Rapid Prototyping Journal,* 19**,** 282-290.

RIEMER, A., LEUDERS, S., THÖNE, M., RICHARD, H., TRÖSTER, T. & NIENDORF, T. 2014. On the fatigue crack growth behavior in 316L stainless steel manufactured by selective laser melting. *Engineering Fracture Mechanics,* 120**,** 15-25.

ROMBOUTS, M., FROYEN, L., BOURELL, D. & KRUTH, J. Roughness after laser melting of iron based powders. *Proc. 2nd Int. Conf. on Advanced Research in Virtual and Rapid Prototyping VRAP, Leiria, Portugal*, 2005. 329-335.

ROMBOUTS, M., KRUTH, J.-P., FROYEN, L. & MERCELIS, P. 2006. Fundamentals of selective laser melting of alloyed steel powders. *CIRP Annals-Manufacturing Technology,* 55**,** 187-192.

SACRISTÁN, R., VEREDAS, G., BONJOCH, I., PEÑALVA, I., CALDERÓN, E., ALBERRO, G., BALART, D., SARRIONANDIA-IBARRA, A., PÉREZ, V. & IBARRA, A. 2014. Fuskite® preliminary experimental tests based on permeation against vacuum for hydrogen recovery as a potential application in Pb15. 7Li loop systems. *Fusion Engineering and Design,* 89**,** 1551-1556.

SAFDAR, A., HE, H., WEI, L.-Y., SNIS, A. & CHAVEZ DE PAZ, L. E. 2012. Effect of process parameters settings and thickness on surface roughness of EBM produced Ti-6Al-4V. *Rapid Prototyping Journal,* 18**,** 401-408.

SAMES, W., MEDINA, F., PETER, W., BABU, S. & DEHOFF, R. Effect of process control and powder quality on Inconel 718 produced using electron beam melting. Proceedings of the 8th International Symposium on Superalloy 718 and Derivatives, 2014. *John Wiley & Sons*, 409.

SANTOS, E. C., SHIOMI, M., OSAKADA, K. & LAOUI, T. 2006. Rapid manufacturing of metal components by laser forming. *International Journal of Machine Tools and Manufacture,* 46**,** 1459-1468.

SANTOS, E., OSAKADA, K., SHIOMI, M., KITAMURA, Y. & ABE, F. 2004. Microstructure and mechanical properties of pure titanium models fabricated by selective laser melting. Proceedings of the institution of mechanical engineers, part c: *journal of mechanical engineering science*, 218, 711-719.

SATHYAJITH, S. Effect of Laser Peening without Coating on 316L austenitic stainless steel. IOP Conference Series: *Materials Science and Engineering,* 2015. IOP Publishing, 012152.

SAVALANI, M. M. & PIZARRO, J. M. 2016. Effect of preheat and layer thickness on selective laser melting (SLM) of magnesium. *Rapid Prototyping Journal,* 22**,** 115-122.

SCHAFFER, G., SERCOMBE, T. & LUMLEY, R. 2001. Liquid phase sintering of aluminium alloys. *Materials Chemistry and Physics,* 67**,** 85-91.

SCHIJVE, J. 1967. Significance of fatigue cracks in micro-range and macro-range. *Fatigue Crack Propagation.* ASTM International.

SCHLEIFENBAUM, H., DIATLOV, A., HINKE, C., BÜLTMANN, J. & VOSWINCKEL, H. 2011. Direct photonic production: towards high speed additive manufacturing of individualized goods. *Production Engineering,* 5**,** 359-371.

SCHOINOCHORITIS, B., CHANTZIS, D. & SALONITIS, K. 2015. Simulation of metallic powder bed additive manufacturing processes with the finite element method: A critical review. *Proceedings of the Institution of Mechanical Engineers, Part B: Journal of Engineering Manufacture***,** 0954405414567522.

SEIFI, M., CHRISTIANSEN, D., BEUTH, J., HARRYSSON, O. & LEWANDOWSKI, J. J. Process mapping, fracture and fatigue behavior of Ti-6Al-4V produced by EBM additive manufacturing. Proceedings of World Conference on Titanium, 13th, 2016a. *TMS/Wiley Warrendale, PA/Hoboken,* NJ, 1373-77.

SEIFI, M., DAHAR, M., AMAN, R., HARRYSSON, O., BEUTH, J. & LEWANDOWSKI, J. J. 2015. Evaluation of orientation dependence of fracture toughness and fatigue crack propagation behavior of as-deposited ARCAM EBM Ti-6Al-4V. *Jom,* 67**,** 597-607.

SEIFI, M., SALEM, A., BEUTH, J., HARRYSSON, O. & LEWANDOWSKI, J. J. 2016b. Overview of materials qualification needs for metal additive manufacturing. *JoM,* 68**,** 747-764.

SENTHILKUMARAN, K., PANDEY, P. M. & RAO, P. 2007. DFM and Process Planning Issues in Selective Laser Sintering.

SHANG, Y., YUAN, Y., ZHANG, Y., LI, D. & LI, Y. Investigation into Effects of Scanning Speed on in Vitro Biocompatibility of Selective Laser Melted 316L Stainless Steel Parts. *MATEC Web of Conferences, 2017*. EDP Sciences, 01009

SHAPIRO, A., BORGONIA, J., CHEN, Q., DILLON, R., MCENERNEY, B., POLIT-CASILLAS, R. & SOLOWAY, L. 2016. Additive Manufacturing for Aerospace Flight Applications. *Journal of Spacecraft and Rockets***,** 952-959.

SHIFENG, W., SHUAI, L., QINGSONG, W., YAN, C., SHENG, Z. & YUSHENG, S. 2014. Effect of molten pool boundaries on the mechanical properties of selective laser melting parts. *Journal of Materials Processing Technology,* 214**,** 2660-2667.

SHIOMI, M., OSAKADA, K., NAKAMURA, K., YAMASHITA, T. & ABE, F. 2004. Residual stress within metallic model made by selective laser melting process. *CIRP Annals-Manufacturing Technology,* 53**,** 195-198.

SIMCHI, A. 2004. The role of particle size on the laser sintering of iron powder. *Metallurgical and Materials Transactions B,* 35**,** 937-948.

SIMONELLI, M., TSE, Y. & TUCK, C. 2014a. Effect of the build orientation on the Mechanical Properties and Fracture Modes of SLM Ti–6Al–4V. *Materials Science and Engineering: A,* 616**,** 1-11.

SIMONELLI, M., TSE, Y. Y. & TUCK, C. 2014b. Effect of the build orientation on the Mechanical Properties and Fracture Modes of SLM Ti–6Al–4V. *Materials Science and Engineering: A,* 616**,** 1-11.

SOBOYEJO, W. 2002. *Mechanical properties of engineered materials*, CrC Press.

SOCHALSKI-KOLBUS, L., PAYZANT, E. A., CORNWELL, P. A., WATKINS, T. R., BABU, S. S., DEHOFF, R. R., LORENZ, M., OVCHINNIKOVA, O. & DUTY, C. 2015. Comparison of residual stresses in Inconel 718 simple parts made by electron beam melting and direct laser metal sintering. *Metallurgical and Materials Transactions A,* 46**,** 1419-1432.

SOE, S., RYAN, M., MCSHANE, G. & THEOBALD, P. 2015. Energy Absorbing Characteristics of Additively Manufactured TPE Cellular Structures.

SONG, B., DONG, S., ZHANG, B., LIAO, H. & CODDET, C. 2012. Effects of processing parameters on microstructure and mechanical property of selective laser melted Ti6Al4V. *Materials & Design,* 35**,** 120-125.

SPIERINGS, A., STARR, T. & WEGENER, K. 2013. Fatigue performance of additive manufactured metallic parts. *Rapid prototyping journal,* 19**,** 88-94.

STEEN, W. M. 1991. Laser surface treatment. *Laser Material Processing.* Springer.

STEEN, W. M. & MAZUMDER, J. 2010. Laser automation and in-process sensing. *Laser Material Processing.* Springer.

STRANO, G., HAO, L., EVERSON, R. & EVANS, K. 2013a. A new approach to the design and optimisation of support structures in additive manufacturing. *The International Journal of Advanced Manufacturing Technology,* 66**,** 1247-1254.

STRANO, G., HAO, L., EVERSON, R. M. & EVANS, K. E. 2013b. Surface roughness analysis, modelling and prediction in selective laser melting. *Journal of Materials Processing Technology,* 213**,** 589-597.

SU, W., ERASENTHIRAN, P. & DICKENS, P. M. 2003. Investigation of fully dense laser sintering of tool steel powder using a pulsed Nd: YAG (neodymium-doped yttrium aluminium garnet) laser. *Proceedings of the Institution of Mechanical Engineers, Part C: Journal of Mechanical Engineering Science,* 217**,** 127-138.

SU, X. & YANG, Y. 2012. Research on track overlapping during selective laser melting of powders. *Journal of Materials Processing Technology,* 212**,** 2074-2079.

SUN, Y., MOROZ, A. & ALRBAEY, K. 2014. Sliding wear characteristics and corrosion behaviour of selective laser melted 316L stainless steel. *Journal of materials engineering and performance,* 23, 518-526.

SVENSSON 2009a. Ti6Al4V manufactured with electron beam melting (EBM):mechanical and chemical properties. *In Proceedings from the Materials&Processes for MedicalDevices Conference,* Novelty, OH: ASM Int**,** pp. 189–94.

SVENSSON, M. 2009b. Ti6Al4 V manufactured with Electron Beam Melting (EBM): mechanical and chemical properties. *Aeromat 2009',* Dayton, OH, .

TAKALO, T., SUUTALA, N. & MOISIO, T. 1979. Austenitic solidification mode in austenitic stainless steel welds. *Metallurgical Transactions A,* 10**,** 1173-1181.

TAKEDA, K., KAJIMURA, H. & MIYAHARA, M. 2006. Austenitic stainless steel. *Google Patents.*

THIJS, L., KEMPEN, K., KRUTH, J.-P. & VAN HUMBEECK, J. 2013. Fine-structured aluminium products with controllable texture by selective laser melting of pre-alloyed AlSi10Mg powder. *Acta Materialia,* 61**,** 1809-1819.

THIJS, L., VERHAEGHE, F., CRAEGHS, T., VAN HUMBEECK, J. & KRUTH, J.-P. 2010. A study of the microstructural evolution during selective laser melting of Ti–6Al–4V. *Acta Materialia,* 58**,** 3303-3312.

THOMPSON, M. K., MORONI, G., VANEKER, T., FADEL, G., CAMPBELL, R. I., GIBSON, I., BERNARD, A., SCHULZ, J., GRAF, P. & AHUJA, B. 2016. Design for Additive Manufacturing: Trends, opportunities, considerations, and constraints. *CIRP Annals-Manufacturing Technology,* 65**,** 737-760.

TIAMIYU, A., ESKANDARI, M., NEZAKAT, M., WANG, X., SZPUNAR, J. & ODESHI, A. 2016. A comparative study of the compressive behaviour of AISI 321 austenitic stainless steel under quasi-static and dynamic shock loading. *Materials & Design,* 112**,** 309-319.

TOLOCHKO, N. K., MOZZHAROV, S. E., YADROITSEV, I. A., LAOUI, T., FROYEN, L., TITOV, V. I. & IGNATIEV, M. B. 2004. Balling processes during selective laser treatment of powders. *Rapid Prototyping Journal,* 10**,** 78-87.

TOLOSA, I., GARCIANDÍA, F., ZUBIRI, F., ZAPIRAIN, F. & ESNAOLA, A. 2010. Study of mechanical properties of AISI 316 stainless steel processed by "selective laser melting", following different manufacturing strategies. *The International Journal of Advanced Manufacturing Technology,* 51**,** 639-647.

TOMOTA, Y., XIA, Y. & INOUE, K. 1998. Mechanism of low temperature brittle fracture in high nitrogen bearing austenitic steels. *Acta materialia,* 46**,** 1577-1587.

TSOPANOS, S., MINES, R., MCKOWN, S., SHEN, Y., CANTWELL, W., BROOKS, W. & SUTCLIFFE, C. 2010. The influence of processing parameters on the mechanical properties of selectively laser melted stainless steel microlattice structures. *Journal of Manufacturing Science and Engineering,* 132**,** 041011.

UNOCIC, R. & DUPONT, J. 2004. Process efficiency measurements in the laser engineered net shaping process. *Metallurgical and materials transactions B,* 35**,** 143-152.

VAN BAEL, S., CHAI, Y. C., TRUSCELLO, S., MOESEN, M., KERCKHOFS, G., VAN OOSTERWYCK, H., KRUTH, J.-P. & SCHROOTEN, J. 2012. The effect of pore geometry on the in vitro biological behavior of human periosteum-derived cells seeded on selective laser-melted Ti6Al4V bone scaffolds. *Acta biomaterialia,* 8**,** 2824-2834.

Vander Voort, G.F., Lucas, G.M. and Manilova, E.P., 2004. Metallography and microstructures of stainless steels and maraging steels. *ASM Handbook*, 9,pp. 670-700.

VAN HOOREWEDER, B., MOENS, D., BOONEN, R., KRUTH, J. P. & SAS, P. 2012. Analysis of fracture toughness and crack propagation of Ti6Al4V produced by selective laser melting. *Advanced Engineering Materials,* 14**,** 92-97.

VAN NOORT, R. 2012. The future of dental devices is digital. *Dental materials,* 28**,** 3-12.

VILARO, T., COLIN, C. & BARTOUT, J.-D. 2011. As-fabricated and heat-treated microstructures of the Ti-6Al-4V alloy processed by selective laser melting. *Metallurgical and Materials Transactions A,* 42**,** 3190-3199.

VILLANUEVA, D. E., JUNIOR, F., PLAUT, R. & PADILHA, A. 2006. Comparative study on sigma phase precipitation of three types of stainless steels: austenitic, superferritic and duplex. *Materials Science and Technology,* 22**,** 1098-1104.

VRANCKEN, B., CAIN, V., KNUTSEN, R. & VAN HUMBEECK, J. 2014. Residual stress via the contour method in compact tension specimens produced via selective laser melting. *Scripta Materialia,* 87**,** 29-32.

VRANCKEN, B., THIJS, L., KRUTH, J.-P. & VAN HUMBEECK, J. 2012. Heat treatment of Ti6Al4V produced by Selective Laser Melting: Microstructure and mechanical properties. *Journal of Alloys and Compounds,* 541**,** 177-185.

WANG 2011. Characteristics and technology of stainless steel parts research by selective laser melting. *Dissertation for the Doctoral Degree. Guangzhou:,* South China University of Technology.

WANG, S., YANG, K., SHAN, Y. & LI, L. 2008. Plastic deformation and fracture behaviors of nitrogen-alloyed austenitic stainless steels. *Materials Science and Engineering: A,* 490**,** 95-104.

WANG, X., GONG, X. & CHOU, K. 2015. Scanning speed effect on mechanical properties of Ti-6Al-4V alloy processed by electron beam additive manufacturing. *Procedia Manufacturing,* 1**,** 287-295.

WANHILL, R. & BARTER, S. 2011. Fatigue of beta processed and beta heat-treated titanium alloys, Springer Science & Business Media

WANHILL, R. & BARTER, S. 2012. Metallurgy and microstructure. Fatigue of Beta Processed and Beta Heat-treated Titanium Alloys. *Springer*.New York. ISSN2191-530X. pages 11-19

WAUTHLE, R., AHMADI, S. M., YAVARI, S. A., MULIER, M., ZADPOOR, A. A., WEINANS, H., VAN HUMBEECK, J., KRUTH, J.-P. & SCHROOTEN, J. 2015. Revival of pure titanium for dynamically loaded porous implants using additive manufacturing. *Materials Science and Engineering*: C, 54, 94-100.

WEI, Q., LI, S., HAN, C., LI, W., CHENG, L., HAO, L. & SHI, Y. 2015. Selective laser melting of stainless-steel/nano-hydroxyapatite composites for medical applications: Microstructure, element distribution, crack and mechanical properties. *Journal of Materials Processing Technology,* 222**,** 444-453.

WELSCH, G., BOYER, R. & COLLINGS, E. 1993. *Materials properties handbook: titanium alloys,* ASM international.

WILLIAMS, C. & ROSEN, D. 2007. Manufacturing cellular materials via three-dimensional printing of spray-dried metal oxide ceramic powder. *Virtual and Rapid Manufacturing: Advanced Research in Virtual and Rapid Prototyping***,** 331.

WILLIAMS, C. B., COCHRAN, J. K. & ROSEN, D. W. 2011. Additive manufacturing of metallic cellular materials via three-dimensional printing. *The International Journal of Advanced Manufacturing Technology,* 53**,** 231-239.

WILLIAMS, C. B., MISTREE, F. & ROSEN, D. W. Investigation of additive manufacturing processes for the manufacture of parts with designed mesostructure. ASME 2005 International Design Engineering Technical Conferences and Computers and Information in Engineering Conference, 2005. *American Society of Mechanical Engineers*, 353-364.

WOHLERS, T. T. & CAFFREY, T. 2015. *Wohlers report 2015: 3D printing and additive manufacturing state of the industry annual worldwide progress report*, Wohlers Associates.

XAVIOR, M. A. & ADITHAN, M. 2009. Determining the influence of cutting fluids on tool wear and surface roughness during turning of AISI 304 austenitic stainless steel. *Journal of materials processing technology,* 209**,** 900-909.

YADROITSEV, I., BERTRAND, P. & SMUROV, I. 2007. Parametric analysis of the selective laser melting process. *Applied surface science,* 253**,** 8064-8069.

YADROITSEV I, E. A. 2009. Mechanical properties of samples fabricated by selective laser melting. *In: Proceedings of 14èmes Assises Européennes du Prototypage & Fabrication Rapide. Paris,*.

YADROITSEV, I., SHISHKOVSKY, I., BERTRAND, P. & SMUROV, I. 2009. Manufacturing of fine-structured 3D porous filter elements by selective laser melting. *Applied Surface Science,* 255**,** 5523-5527.

YADROITSEV, I. & SMUROV, I. 2010. Selective laser melting technology: from the single laser melted track stability to 3D parts of complex shape. *Physics Procedia,* 5**,** 551-560.

YADROITSEV, I. & SMUROV, I. 2011. Surface morphology in selective laser melting of metal powders. *Physics Procedia,* 12**,** 264-270.

YAN, C., HAO, L., HUSSEIN, A., BUBB, S. L., YOUNG, P. & RAYMONT, D. 2014a. Evaluation of light-weight AlSi10Mg periodic cellular lattice structures fabricated via direct metal laser sintering. *Journal of Materials Processing Technology,* 214**,** 856-864.

YAN, C., HAO, L., HUSSEIN, A. & RAYMONT, D. 2012. Evaluations of cellular lattice structures manufactured using selective laser melting. *International Journal of Machine Tools and Manufacture,* 62**,** 32-38.

YAN, C., HAO, L., HUSSEIN, A., YOUNG, P., HUANG, J. & ZHU, W. 2015. Microstructure and mechanical properties of aluminium alloy cellular lattice structures manufactured by direct metal laser sintering. *Materials Science and Engineering: A,* 628**,** 238-246.

YAN, C., HAO, L., HUSSEIN, A., YOUNG, P. & RAYMONT, D. 2014b. Advanced lightweight 316L stainless steel cellular lattice structures fabricated via selective laser melting. *Materials & Design,* 55**,** 533-541.

YAN, X. & GU, P. 1996. A review of rapid prototyping technologies and systems. *Computer-Aided Design,* 28**,** 307-318.

YANG, J., OUYANG, H., XU, C. & WANG, Y. 2012a. Top surface quality research for direct metal laser fabrication. *Rapid Prototyping Journal,* 18**,** 4-15.

YANG, Y., LU, J.-B., LUO, Z.-Y. & WANG, D. 2012b. Accuracy and density optimization in directly fabricating customized orthodontic production by selective laser melting. *Rapid Prototyping Journal,* 18**,** 482-489.

YASA, E., DECKERS, J. & KRUTH, J.-P. 2011a. The investigation of the influence of laser re-melting on density, surface quality and microstructure of selective laser melting parts. *Rapid Prototyping Journal,* 17**,** 312-327.

YASA, E. & KRUTH, J.-P. 2011. Microstructural investigation of Selective Laser Melting 316L stainless steel parts exposed to laser re-melting. *Procedia Engineering,* 19**,** 389-395.

YASA, E., KRUTH, J.-P. & DECKERS, J. 2011b. Manufacturing by combining selective laser melting and selective laser erosion/laser re-melting. *CIRP Annals-Manufacturing Technology,* 60**,** 263-266.

YAVARI, S. A., WAUTHLÉ, R., VAN DER STOK, J., RIEMSLAG, A., JANSSEN, M., MULIER, M., KRUTH, J.-P., SCHROOTEN, J., WEINANS, H. & ZADPOOR, A. A. 2013. Fatigue behavior of porous biomaterials manufactured using selective laser melting. *Materials Science and Engineering*: C, 33, 4849-4858.

YU, C., YANG, L., SHEN, C., LUAN, B. & PERNG, T. 2007. Corrosion behavior of thermohydrogen processed Ti6Al4V. *Scripta materialia,* 56**,** 1019-1022.

ZAEH, M. F. & BRANNER, G. 2010. Investigations on residual stresses and deformations in selective laser melting. *Production Engineering,* 4**,** 35-45.

ZÄH, M. F. & LUTZMANN, S. 2010. Modelling and simulation of electron beam melting. *Production Engineering,* 4**,** 15-23.

ZHANG, L. C., KLEMM, D., ECKERT, J., HAO, Y. L. & SERCOMBE, T. B. 2011. Manufacture by selective laser melting and mechanical behavior of a biomedical Ti–24Nb–4Zr–8Sn alloy. *Scripta Materialia,* 65**,** 21-24.

ZHANG, S. 2014. *Location Analysis of 3D Printer Manufacturing Industry.* Columbia University.

ZHANG, S., LIN, X., CHEN, J. & HUANG, W. 2009. Heat-treated microstructure and mechanical properties of laser solid forming Ti-6Al-4V alloy. *Rare metals,* 28**,** 537.

ZHAO, H., ANTONYSAMY, A., MEYER, J., CIUCA, O., WILLIAMS, S. & PRANGNELL, P. Automated Multi-Scale Microstructure Heterogeneity Analysis of Selective Electron Beam Melted TiAl6V4 Components. *TMS 2015 144th Annual Meeting & Exhibition,* 2015. Springer, 429-436.

ZHENG, B., ZHOU, Y., SMUGERESKY, J., SCHOENUNG, J. & LAVERNIA, E. 2008. Thermal behavior and microstructure evolution during laser deposition with laserengineered net shaping: part II. *Experimental investigation and discussion. Metallurgical and Materials Transactions A,* 39, 2237-2245.

ZHOU, J., SHROTRIYA, P. & SOBOYEJO, W. 2004. On the deformation of aluminum lattice block structures: from struts to structures. *Mechanics of Materials,* 36**,** 723-737.

ZHOU, X., WANG, D., LIU, X., ZHANG, D., QU, S., MA, J., LONDON, G., SHEN, Z. & LIU, W. 2015. 3D-imaging of selective laser melting defects in a Co–Cr–Mo alloy by synchrotron radiation micro-CT. *Acta Materialia,* 98**,** 1-16.